CHARACTERISATION AND OPTIMISATION OF HYBRID POLYMER / METAL OXIDE PHOTOVOLTAIC DEVICES

by

Punniamoorthy Ravirajan

Centre for electronic Material and Device
Dept. of Physics, Blackett Laboratory
Imperial College London
University of London

Thesis submitted to the University of London
for the degree of Doctor of Philosophy

September, 2004

BIBL. LONDIN.

For my beloved parents

ACKNOWLEDGEMENT

I would like to express my profound gratitude to my supervisors Dr. Jenny Nelson and Prof. Donal Bradley for their excellent guidance, encouragement and invaluable suggestions. In particular, I am most grateful to Jenny for her all comments and advice in connection with the writing of this thesis and our publications. The submission of this thesis within three years has been made possible because of her excellent guidance. I would also like to thank Jenny for always having time for discussions on my results.

I wish to thank Dr. James Durrant for his stimulating discussions and for providing the opportunity to work in his lab. I also wish to thank Dr. Saif Haque for guiding my first steps in sample fabrication and characterization in James's laboratory and later for his useful discussions. I am grateful to Dr. Emillio Palomares and Alex Green for helping me in the preparation of TiO_2 pastes and supplying their metal oxides paste, to Dr. Ana Peiro, for her technical assistance with scanning electron microscopy measurements and supplying her metal oxides paste and to Yeni Astuti for her assistance in cyclic voltammetry measurements.

My thanks go to Dr. Dmitry Poplavskyy for his guidance on Kelvin probe, electroabsorption spectroscopy measurements, to Dr. Mili Eppler for guiding my first steps in device fabrications and to Dr. Theo Kreouzis for teaching me the time of flight technique. I wish to extend my thanks to all the EXSS group, Marilu, Stelios, Youngkyoo, Jingsong, Roberto, George, Katie, Jo, Marc, Patrick., Felix, Sachetan, Rosie, James K, Jamie, Edmond, Carl, Simon, Martina. M., James D., Martina P., Alex, Ruth, Aris, Miguel, Mariano, Boon and many others for their helpful company in the clean room and laboratory and for making my life at work enjoyable.

I am grateful to The Dow Chemical Company, Merck NBSC Ltd and Prof. H. H. Horhold for providing the polymer samples and to Dr. J. M. Kroon for supplying a TiO_2 paste sample. Special thanks go to the Commonwealth Scholarship Commission for a Commonwealth Scholarship and to the University of Jaffna for granting my study leave.

My endless gratitude goes to my parents, brothers, sister and all of my former teachers for their help and encouragements with my education so far. Among them, I am deeply thankful to my parents for their extreme attention to my education. Without their help and encouragement, I would not have such an opportunity for a scholarship and a chance to interact with such intellectuals. I thank my brother and his wife in London for their advice and help rendered here for the last three years. Last, but certainly not least, I am grateful to my wife and our little sons for their strong support and company.

ABSTRACT

This thesis addresses the factors that limit the performance of hybrid metal oxide/polymer photovoltaic devices and the optimisation of device design. We first present a novel, multi-layer design for hybrid TiO_2/polymer devices. The design consists of layers of dense TiO_2 (~50nm), porous nanocrystalline TiO_2 (~100nm), dip-coated polymer, spin-coated polymer and poly(ethylenedioxythiophene)/polystyrene sulphonate(PEDOT:PSS). The porous layer improves the short circuit current density, J_{SC}. The dip-coating step improves polymer infiltration and device fill factor. The PEDOT:PSS layer improves charge collection, and also improves fill factor by minimising the energy mismatch at the polymer/metal interface.

We have studied the relationship between device performance and polymer optoelectronic properties using several thiophene and *p*-phenylene-vinylene based polymers in the multi-layer structure. We find that J_{SC} is limited primarily by the polymer absorption coefficient and exciton diffusion length, rather than by its hole-transport properties. High mobility slightly improves both fill factor and open circuit voltage V_{OC}.

We have studied the effect of porous TiO_2 microstructure and thickness, and alternative metal oxides. Device performance is improved when the pore diameter is similar to the polymer exciton diffusion length, and when the relative volumes of TiO_2 and polymer and the active layer thickness are optimised. An optimised device produced peak external quantum efficiency ≈ 40 %, $J_{SC} > 2$ mAcm^{-2}, V_{OC} of 0.64 V and fill factor of 0.43 in Air Mass 1.5 illumination (100 mWcm^{-2}) resulting in an efficiency of 0.58 %. Replacing the TiO_2 layer with nanocrystalline SnO_2 produced a device efficiency of 0.17 %, the first reported for polymer/SnO_2 devices.

The electron mobility of porous TiO_2 is low (10^{-7} - 10^{-6} cm^2/Vs) and depends on the film morphology. Sputter-deposited columnar TiO_2 films have higher electron mobility than porous colloidal films. The results suggest that further device improvement can be achieved using columnar nanocrystalline metal oxides.

Contents

1.0 Introduction and literature review..... 08

1.1 Motivation..... 08

1.2 Aim and layout of the thesis..... 10

1.3 Photovoltaic effect in conjugated polymer..... 11

1.4 Photovoltaic effect in donor-acceptor heterojunctions..... 13

1.5 Photovoltaic characterisation 16

1.6 Series and shunt resistance of a photovoltaic device..... 20

1.7 Review of previous work of organic solar cells..... 22

1.8 Review of previous work on hybrid metal oxide / polymer device... 29

1.9 Summary..... 41

2.0 Materials and Experimental techniques..... 42

2.1 Materials..... 42

2.2 Sample fabrication 46

2.3 UV-VIS optical absorption spectroscopy..... 49

2.4 Transient absorption spectroscopy..... 51

2.5 Exciton diffusion length measurements..... 55

2.6 Cyclic voltammetry..... 56

2.7 Time-of-flight (TOF) technique..... 57

2.8 Electrical characterisation..... 63

2.9 The Kelvin probe technique..... 64

2.10 Electro-absorption spectroscopic technique..... 67

3.0 Optimising the design of hybrid polymer / TiO_2 devices..... 69

3.1 Abstract 69

3.2 Charge generation in single layer and bi-layer devices..... 70

3.3 Charge collection with different top electrodes 72

3.4 Charge separation and recombination kinetics 76

3.5 Polymer penetration into porous TiO_2 by melt processing..... 79

3.6 Influence of device thickness and interfacial area..... 82

3.7 Effect of light intensity..... 86

3.8 Improvement of fill factor by dip treatment..... 89

3.9 Effect of interfacial step at polymer / metal interface..... 94
3.10 PEDOT:PSS as hole collector..... 97
3.11 Summary..... 99

4.0 Influence of polymer optoelectronic properties..... 100
4.1 Abstract..... 100
4.2 Introduction..... 101
4.3 Optoelectronic properties of the polymers..... 101
4.3.1 Polymer absorption and adsorption on to TiO_2..... 102
4.3.2 Hole mobility of the polymers..... 103
4.3.3 Ionisation potential of the polymers..... 106
4.3.4 Exciton diffusion length of the polymers..... 107
4.4 Charge recombination kinetics and polymer infiltration 110
4.5 Effect of PEDOT:PSS layer..... 112
4.6 Influence of polymer optoelectronic properties 115
4.6.1 Effect of spectral absorbance 115
4.6.2 Importance of exciton diffusion length of polymer..... 116
4.6.3 Influence of hole mobility of the polymer..... 117
4.7 Summary..... 119

5.0 Effect of TiO_2 microstructure and of type of metal oxide 120
5.1 Abstract.....120
5.2 The effect of type of metal oxides 122
5.2.1 SEM Images.....122
5.2.2 Photovoltaic performance..... 123
5.2.3 Effect of metal oxide and dye treatments..... ...125
5.3 Effect of TiO_2 microstructure.....131
5.3.1 SEM Images of the TiO_2 films..... 131
5.3.2 Polymer uptake..... 132
5.3.3 Charge recombination kinetics 133
5.3.4 J-V characteristics..... 134
5.4 Role of hole and electron blocking layers.....141
5.5 Optimising active layer thickness.....143
5.6 Summary.....149

6.0 Charge transport in porous TiO_2.....150

6.1 Abstract..... 150

6.2 Introduction..... 151

6.3 Experimental details.....152

6.4 Results and discussions..... 154

6.4.1 TOF measurements of colloidal films.....154

6.4.2 Heterogeneous field distribution model.....157

6.4.3 Effect of morphology on electron mobility of porous TiO_2.. 160

6.4.3.1 XRD measurements.....161

6.4.3.2 SEM measurements.....162

6.4.3.3 TOF measurements..... 162

6.5 Summary 164

7.0 Conclusion and Future Works..... 165

7.1 Conclusion 165

7.2 Suggestion for Future works.....168

References 170

Appendix - List of publications and conference abstracts.....184

Chapter 1

Introduction and literature review

This chapter explains the principle of operation of organic photovoltaic devices, and reviews previous work on organic photovoltaic devices in general and hybrid TiO_2 / polymer photovoltaic devices in particular.

1.1 Motivation

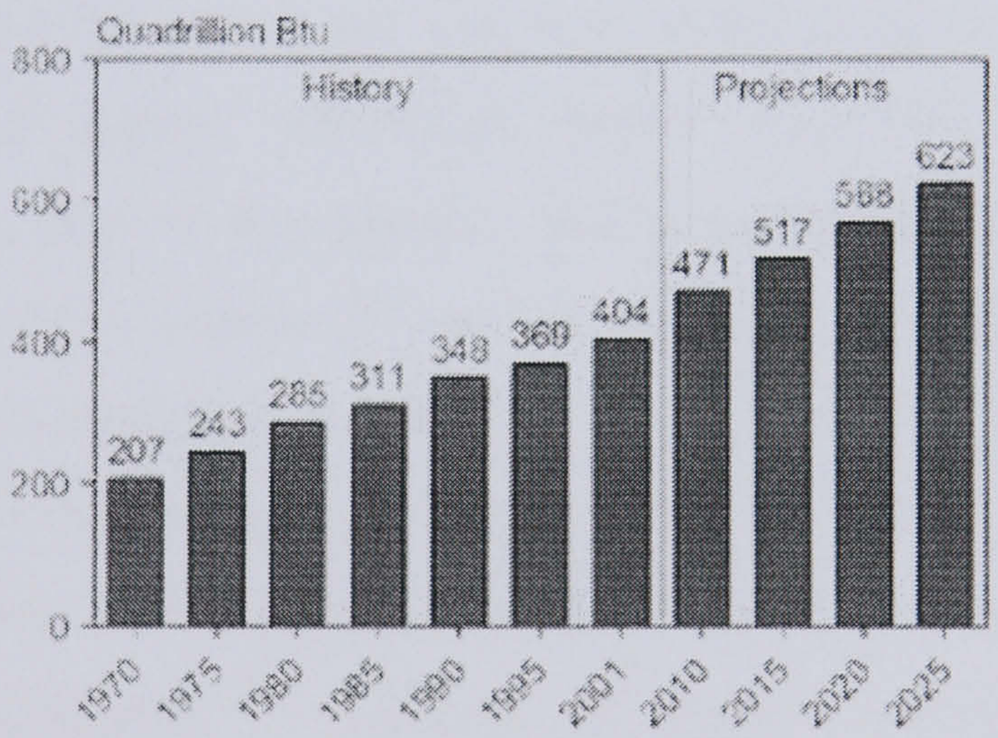


Figure 1.1 [1]*World (primary) energy consumption, 1970 - 2025*

World energy consumption is expected to rise by more than 50 % over the next two decades[1] (see Figure 1.1), while production of oil will soon begin to decline possibly as soon as 2008[2]. Since the traditional fossil fuel energy sources are finite and release waste products into the environment, alternative energy sources such as wind, hydroelectric, tidal, solar thermal and solar photovoltaic are in increasing demand. Regarding electricity supply, photovoltaic electricity is one of the best alternatives to fossil fuel produced power due to the following advantages over other alternative energy sources. First, photovoltaic energy conversion is the only process which converts

light energy directly into electricity without any intermediate stage. Second, the solar energy received by the earth is 8×10^{17} MJ every year[3] which is ~14,000 times greater than the annual world wide electricity consumption (5.6×10^{13} MJ[4]). A suitable calculation shows that with 10 % efficient photovoltaic (PV) devices of 0.3 % total land area of Sahara desert is sufficient to supply world electricity needs. In addition, photovoltaic modules do not require any cooling water system, have no moving parts, require little maintenance and are silent in operations[5].

The photovoltaic industry based on silicon PV devices (solar cells) is in a phase of rapid expansion, growing at over 30 % per annum over recent years[6]. Traditional silicon PV devices offer solar power conversion efficiencies between 15 % (typical module) and 25 % (best PV device), close to the fundamental limit of 29 % for silicon[7]. However, the relatively high cost of manufacturing these cells: the high temperatures required, very sophisticated vacuum technology and numerous lithographic steps, has prevented them from widespread use. The system costs are high (over 6 $ / Watt in 2002[6]) and reducing largely through economies of scale. For more rapid uptake of PV technology, we need to find new materials or very different manufacturing routes. These aspects have prompted the search for low cost alternatives to silicon. One of these alternatives is the new organic technology, which offers low cost, low weight, low material requirements, ease of manufacture, mechanical flexibility and a large field of application[8-11]. In principle, organic PV devices can also be produced in several colours and even be transparent in the visible enabling semi-transparent windows, roof lighting or automobile sunroofs that generate electricity from solar light.

Power conversion efficiencies exceeding 4 % have been reported in several organic device configurations[12,13]. Although all-organic systems such as polymer – fullerene blends are receiving high interest, these systems suffer from poor photo-stability of the two organic components and poor mechanical stability of the active layers through phase segregation. One promising alternative approach is to use a nanostructured *inorganic* semiconductor as the electron transport component [9,14,15]. Electron transporting metal oxides such as titanium dioxide (TiO_2) are attractive materials in this context on account of their low cost, good stability, ease of fabrication and the potential that exists for controlling their film morphology on the nano-scale[8]. Effective charge separation in metal oxide–conjugated polymer composites has been demonstrated and such hybrid materials are attracting growing interest[16-23] for use in photovoltaics. However, the highest power conversion efficiency value reported for

such systems prior to this work is 0.18 % under 1 sun (100 $mWcm^{-2}$)[16], substantially lower than the highest efficiency for conjugated polymer-fullerene solar cells.

1.2 Aim and layout of the thesis

This thesis addresses several factors that determine the photovoltaic performance of hybrid metal oxide/polymer photovoltaic device, presents criteria for optimisation of such systems, and reports a power conversion efficiency of 0.58 % for an optimised TiO_2 / polymer device under 1 sun. The thesis is divided into seven chapters.

Chapter 2 describes the details of the materials and experimental techniques, including UV-VIS optical absorption spectroscopy, transient absorption spectroscopy, cyclic voltammetry, Kelvin probe, electroabsorption spectroscopy, electrical characterisation and time of flight techniques that have been used in this work.

Chapter 3 addresses the effects of the following factors: annealing, surface treatments, layer thickness, interfacial area, light intensity and energy step at the polymer-metal interface, on the performance of fluorene-thiophene copolymer / TiO_2 photovoltaic devices.

Chapter 4 explores the influence of the optoelectronic properties of the polymer on the device performance and the effect of PEDOT:PSS layer on charge collection. The study focuses on a series of high hole-mobility MEH-PPV based polymers and a bi-thiophene polymer in contact with nanocrystalline TiO_2 films.

Chapter 5 examines the effect of modifying the properties of the porous metal oxide layer on the performance of metal oxide / polymer devices. We address the effect of the microstructure of the TiO_2 film, the film thickness, the type of metal oxide (TiO_2, ZnO and SnO_2), and of treatment of the TiO_2 surface with an alumina coating or a dye coating. An optimised device produced the highest overall power conversion efficiency to date, of 0.58 % under 1 sun. The corresponding external quantum efficiency was 40 % at the maximum absorption of the polymer

Chapter 6 reports charge transport studies of nanostructured TiO_2 films prepared by different routes (sol-gel and physical deposition methods) and the relation of transport properties to microstructure and chemical environment

Chapter 7 concludes the results and outlines directions for future work.

1.3 Photovoltaic effect in conjugated polymer

Conjugated polymers are organic molecules with repeating structural units attached to each other by alternative single and double carbon-carbon bonds. The single bond is so-called σ-bond, while the double bond contains a σ-bond and a π-bond. The characteristics of the π-bonds are the source of the electronic properties of these polymers. In this alternating chain of single and double bonds, the molecular p_z orbitals constituting the π-bonds are overlapped and spread over the entire molecule, and the electrons in this molecular orbital are delocalized along the whole molecular chain. The quantum mechanical overlap of the p_z orbitals on two neighbouring C atoms produces two orbitals, a bonding (π) orbital and an antibonding (π*) orbital[11]. The lower energy π-orbital produces the occupied molecular orbital and the higher energy π*-orbital forms unoccupied orbital. When polymer molecules come together to form a solid, the electronic structure of the solid can be represented as shown in figure 1.1 (a). The simplified electronic structure of a conjugated polymer solid can therefore be represented as shown in Figure 1.1(b). The top of the occupied states and bottom of the unoccupied states are known as the highest occupied molecular orbital (HOMO) and the lowest unoccupied molecular orbital (LUMO).

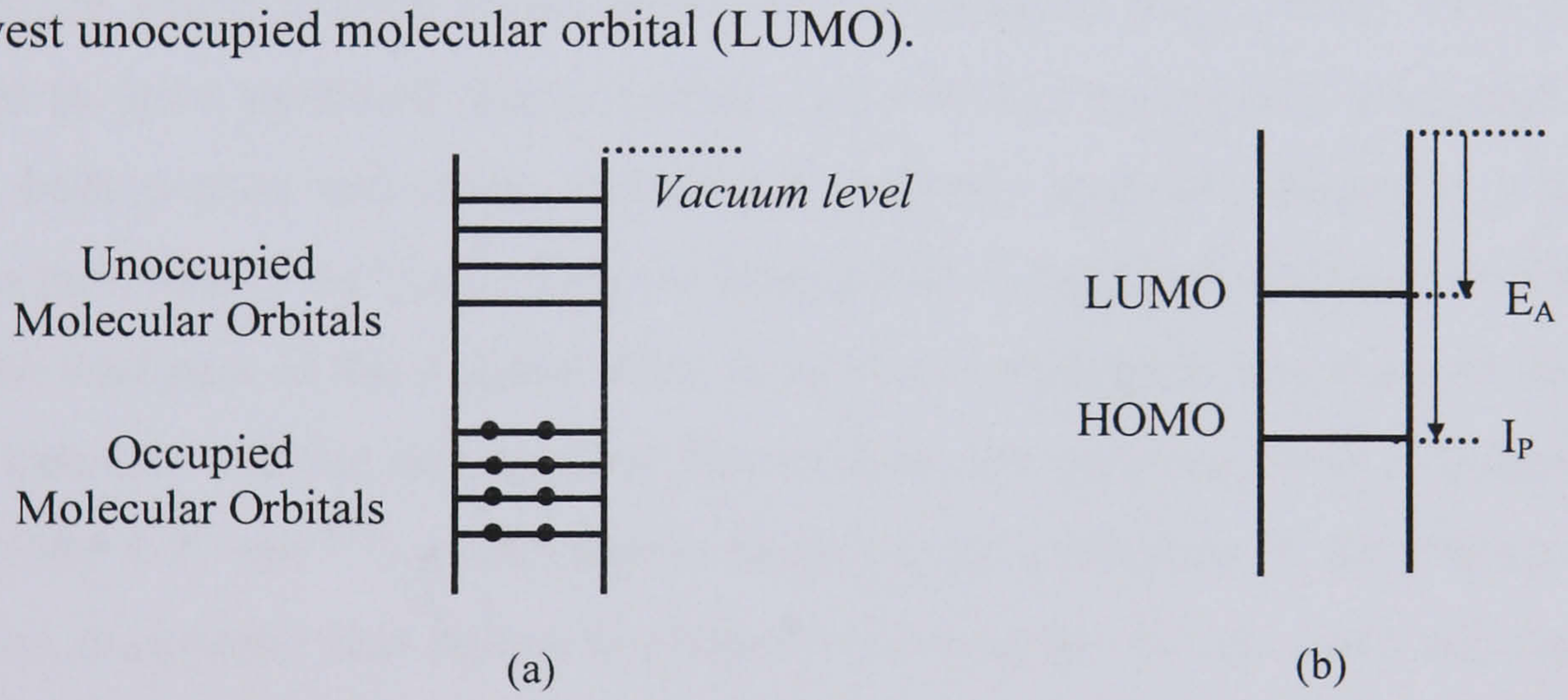


Figure 1.1 *(a) Electronic structure of a polymer solid (b) simplified electronic structure of the solid*

The energy separation between the HOMO energy state and the LUMO energy state corresponds to the energy gap that determines the optical properties of conjugated polymer materials[24]. Most conjugated polymers have energy gaps between 1.5 to 3 eV[11], which makes them ideal candidates for photovoltaic and LED application[25]. The *ionization energy* (I_P) and the *electron affinity* (E_A) of a polymer are defined as the energy separation of the HOMO and LUMO from the vacuum level respectively[24].

In these conjugated polymers, absorption of light with energy equal to or above the energy gap promotes an electron to the LUMO level from the HOMO level, leaving a hole in the HOMO level. The photogenerated electron and hole in conjugated polymers are bound together by coulomb and lattice interactions. The electron-hole binding is usually strong, of order of 0.5 eV[9,11] that is more than 20 times higher the room temperature thermal energy (kT ~ 0.026 eV) and so the charge separation necessary for the photovoltaic effect does not necessarily result from the absorption of light. This electron-hole pair is called an *exciton*, which is generally confined to a region of a polymer chain. The operation of the photovoltaic effect requires dissociation of the exciton to form an electron-hole pair before their recombination. In principle, exciton dissociation in conjugated polymers may be achieved by sandwiching a polymer layer between two metal contacts, known as *electrodes*, one with high work function and the other with low work function. However, the electric field set up in the polymer layer due to the asymmetry of the work functions of the electrodes, known as the *built-in field,* is not enough for efficient exciton dissociation in most polymers. Instead the exciton diffuses within the polymer layer until it reaches near the polymer / electrode interface where exciton dissociation or recombination may occur[9]. This built-in-field helps to drive separated charge carriers towards their appropriate electrodes. We note that both exciton and charge transport in polymer materials usually requires *hopping* from molecule to molecule. If the exciton diffusion length of the polymer is comparable to the thickness of the polymer film, most of the photogenerated excitons should reach the interface without recombining. But exciton diffusion ranges in polymers are short, typically 5-20 nm[19,26], which limits charge carrier generation in the polymer film. The region in polymer that allows photogenerated excitons to dissociate and the separated charges to reach their electrodes is often called the *active region*. Thus, only light absorbed in the active region can contribute to the photocurrent. The inefficient charge separation can be overcome by introducing a donor-acceptor heterojunction[27,28].

1.4 Photovoltaic effect in donor-acceptor heterojunction combination

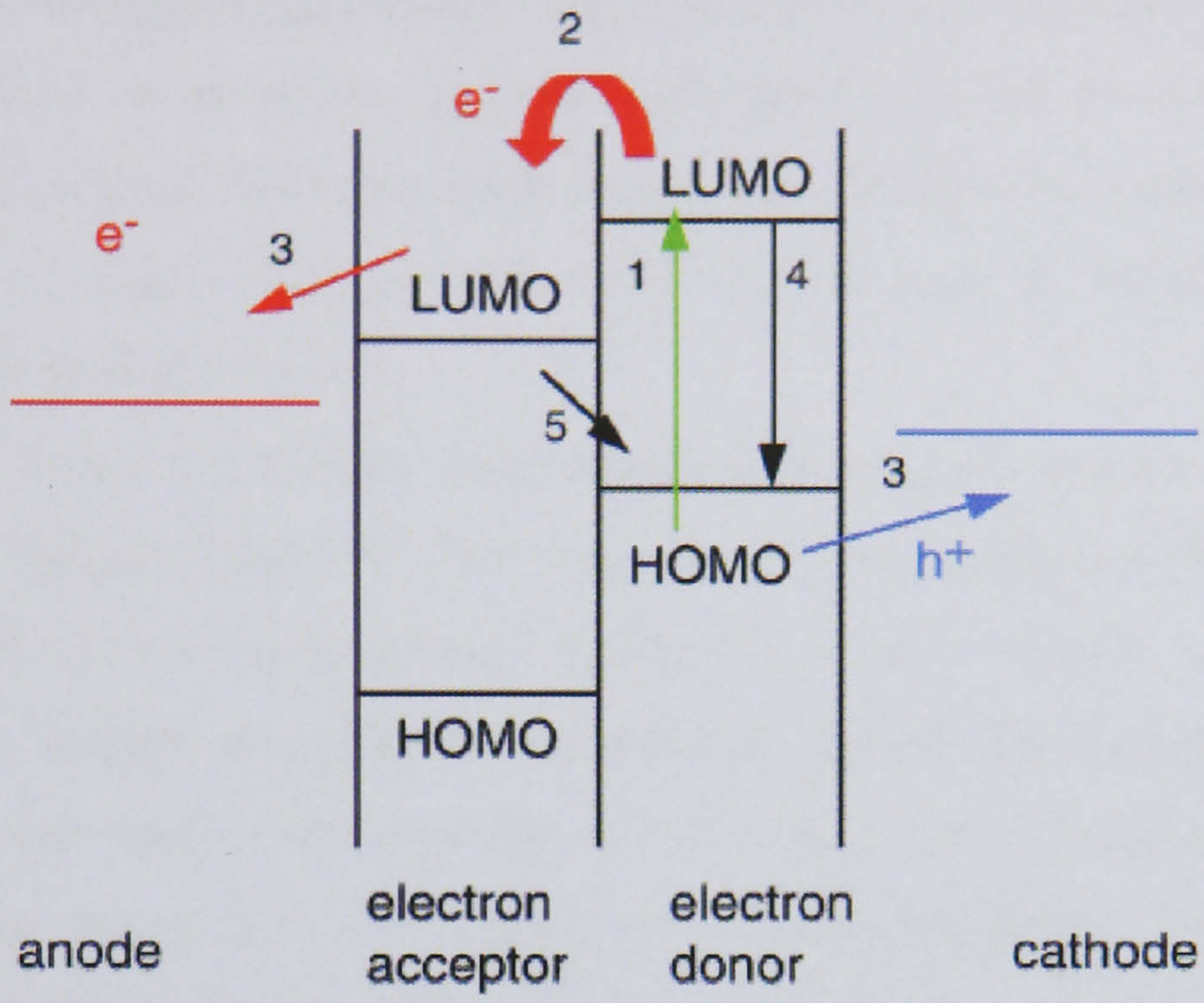


Figure 1.2 *(Figure from Ref.[9]) Schematic energy band diagram of a donor-acceptor heterojunction photovoltaic device and the corresponding details of the processes and losses is indicated in flow chart in Figure 1.3.*

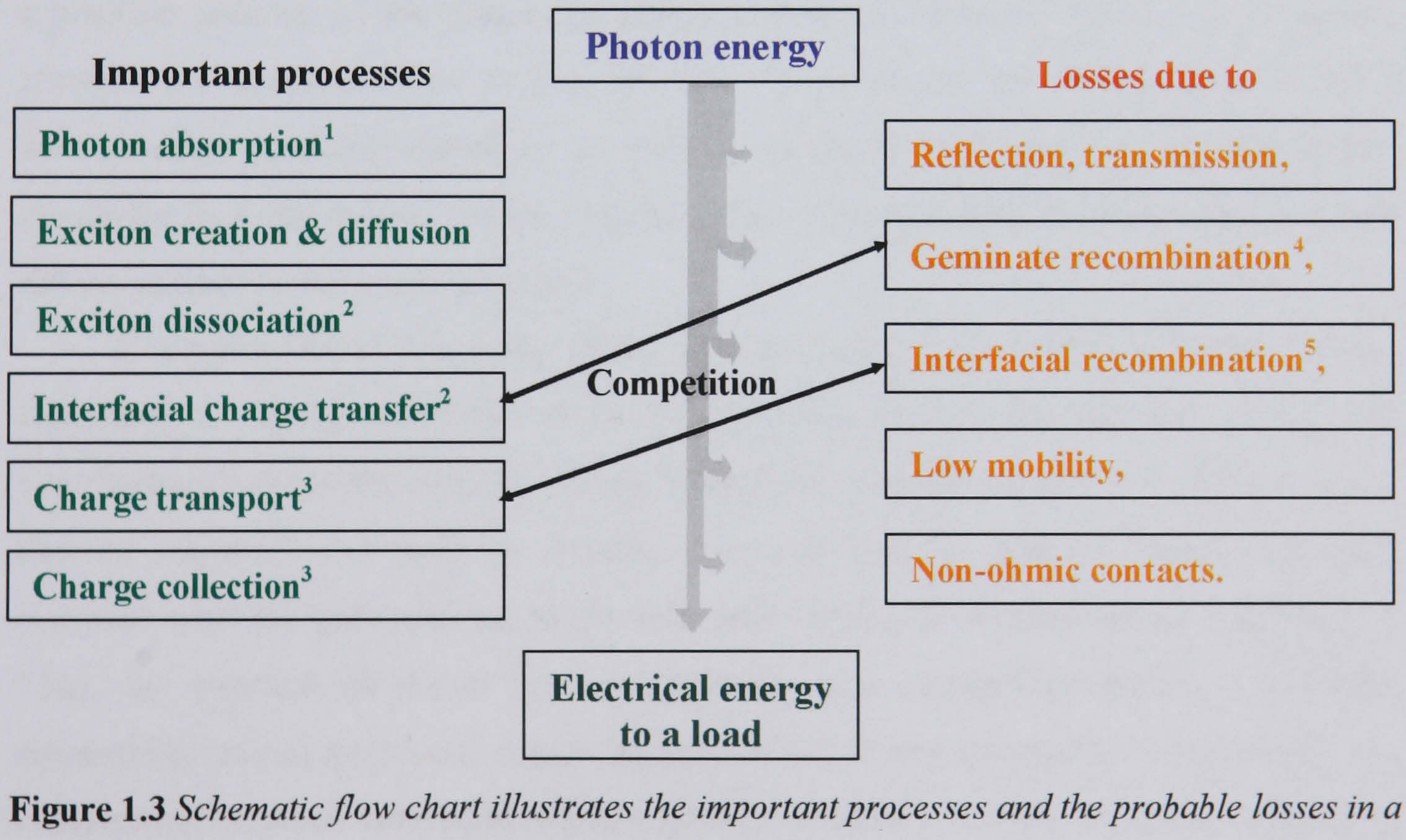


Figure 1.3 *Schematic flow chart illustrates the important processes and the probable losses in a photovoltaic device. The arrows represent the competitions between the important processes and the losses. Numbers refer to processes in Figure 1.2.*

There are two types of donor-acceptor heterojunction device structures, namely bi-layer structures [29], and blend structures[28,30]. Previous work and details of these structures will be discussed in section 1.7. In this section, we will discuss the principle

of operation of this type of system. In this system, one of the materials should be an electron acceptor with good electron-mobility and the other is electron donor with good hole-mobility. Since most of the polymers are poor electron conductors, in some devices inorganic semiconductor materials are used as the electron acceptor. Thus, there are two types of donor-acceptor junctions: organic–organic heterojunctions and inorganic-organic heterojunctions.

Figure 1.2 shows a schematic band diagram of a donor-acceptor heterojunction, while Figure 1.3 shows a schematic flow chart showing the important processes and the probable losses in a photovoltaic device. Absorption of light in one or both materials of this combination, creates an exciton in the polymer film(s). The exciton then diffuses through the polymer film(s) and may find a site where it can dissociate into separate charges, otherwise the exciton will recombine. This recombination is called *geminate recombination*. If both electron affinity and ionization potential are greater in one material (the electron acceptor) than the other (the electron donor) and the difference is greater than the exciton binding energy, then *exciton dissociation* is chemically favourable. The dissociated *charge*s, then *transfer* to the respective materials by leaving a positive *polaron* on the donor and negative polaron on the acceptor. The separated *charge*s are *transport*ed to their respective electrodes by an electric field or by a concentration gradient created by asymmetry of the work function of the electrodes; otherwise they recombine before reaching the electrodes. The *collected charges* then deliver current to the external circuit

It is unavoidable that some of the charge carriers will recombine before charge separation or charge collection when they traverse through the cell and so will not contribute current to the external circuit. Therefore, the photocurrent generation in these devices depends how well the interfacial charge transfer and the charge transport compete with the geminate recombination and interfacial recombination respectively. Thus, the function of theses devices depends upon competition between geminate recombination and interfacial charge transfer which is key for exciton dissociation, and competition between interfacial recombination and transport which is the key for charge collection.

Although losses due to reflection and transmission are significant in thin organic films, these losses are not normally dominant compared to recombination. These losses can be reduced in a better device design. In order to reduce recombination, the charges have to be transported quickly. Both high mobility hole conducting donor materials and

acceptor materials are ideal. For efficient charge collection good non-blocking contacts between the semiconducting materials and the electrodes are essential. One of the electrodes is transparent to allow light into the device. Indium Tin Oxide (ITO) (mixture of In_2O_3 (90 %) and SnO_2 (10 %) with a wide band gap of 3.7 eV and a Fermi-level between 4.5 and 4.9 eV) coated glass substrates are widely used as the transparent electrode. In some cases, a transparent layer of poly (sterenesulfonate) (PSS) doped poly (3,4-ethylenedioxythiophene) (PEDOT:PSS) is spin coated on top of ITO to improve ohmic and physical contact between the electrode and the photoactive polymer layer[31]. The top electrode materials are metals such as Al, Ca and Au. LiF layer is also used to reduce effective work function of top contact. Several other metals are used in devices such as Pt, C, Hg, In etc. The work function of the top electrode materials can be found in Table 1.1[32,33]. The values are for poly-crystalline materials. The work function of the electrode materials on top of a polymer film need not be the same. It has been reported that the effective work function of evaporated Au on top of polymer is different from the nominal values[34-36]. Recent electro-absorption studies[37] indicate that the work function of the evaporated Au on polymer is smaller than expected from the nominal work function.

Table 1.1[32] *Work function of the elements in polycrystalline form*

IA	IIA	IIIB	IVB	VB	VIB	VIIB		VIII		IB	IIB	IIIA	IVA	VA	VIA
Li	Be											B	C	N	O
2.9	4.98											4.45	5.0	-	-
Na	Mg											Al	Si	P	S
2.75	3.66											4.28	4.85	-	-
K	Ca	Sc	Ti	V	Cr	Mn	Fe	Co	Ni	Cu	Zn	Ga	Ge	As	Se
2.30	2.87	3.5	4.33	4.3	4.5	4.1	4.5	5.0	5.15	4.65	4.33	4.2	5.0	3.75	5.9
Rb	Sr	Y	Zr	Nb	Mo	Tc	Ru	Rh	Pd	Ag	Cd	In	Sn	Sb	Te
2.16	2.59	3.1	4.05	4.3	4.6	-	4.71	4.98	5.12	4.26	4.22	4.12	4.42	4.55	4.95
Cs	Ba	La	Hf	Ta	W	Re	Os	Ir	Pt	Au	Hg	Ti	Pb	Bi	Po
2.14	2.7	3.5	3.9	4.25	4.55	4.96	4.83	5.27	5.65	5.1	4.49	3.84	4.25	4.22	-
Fr	Ra	Ac	Th	Pa	U										
-	-	-	3.4	-	3.63										
			Ce	Pr	Nd	Pm	Sm	Eu	Gd	Tb	Dy	Ho	Er	Tm	Yb
			2.9	-	3.2	-	2.7	2.5	3.1	3.0	-	-	-	-	-

1.5 Photovoltaic characterization

The characteristics of a photovoltaic device can be described by its current-voltage curve. Figure 1.4 shows the J-V characteristic of a photovoltaic device. Performance of the photovoltaic device is normally described by in terms of power conversion efficiency and sometimes also in terms of the photocurrent quantum efficiency spectrum. Good quantum efficiency does not guarantee good photovoltaic energy conversion, but it is a prerequisite[38]. It is essential to measure power conversion efficiency under standard conditions for comparison of different solar cells. The power conversion efficiency measurements are normally taken under air mass 1.5 (AM1.5) simulated irradiation at an irradiance of 100 $mWcm^{-2}$ and temperature of 25 ^0C (sun's emission spectrum at air mass 1.5, after travelling 1.5 times through the Earth's atmosphere)[39], while monochromatic power conversion efficiency and photocurrent quantum efficiency are measured using monochromatic light, at a lower irradiance.

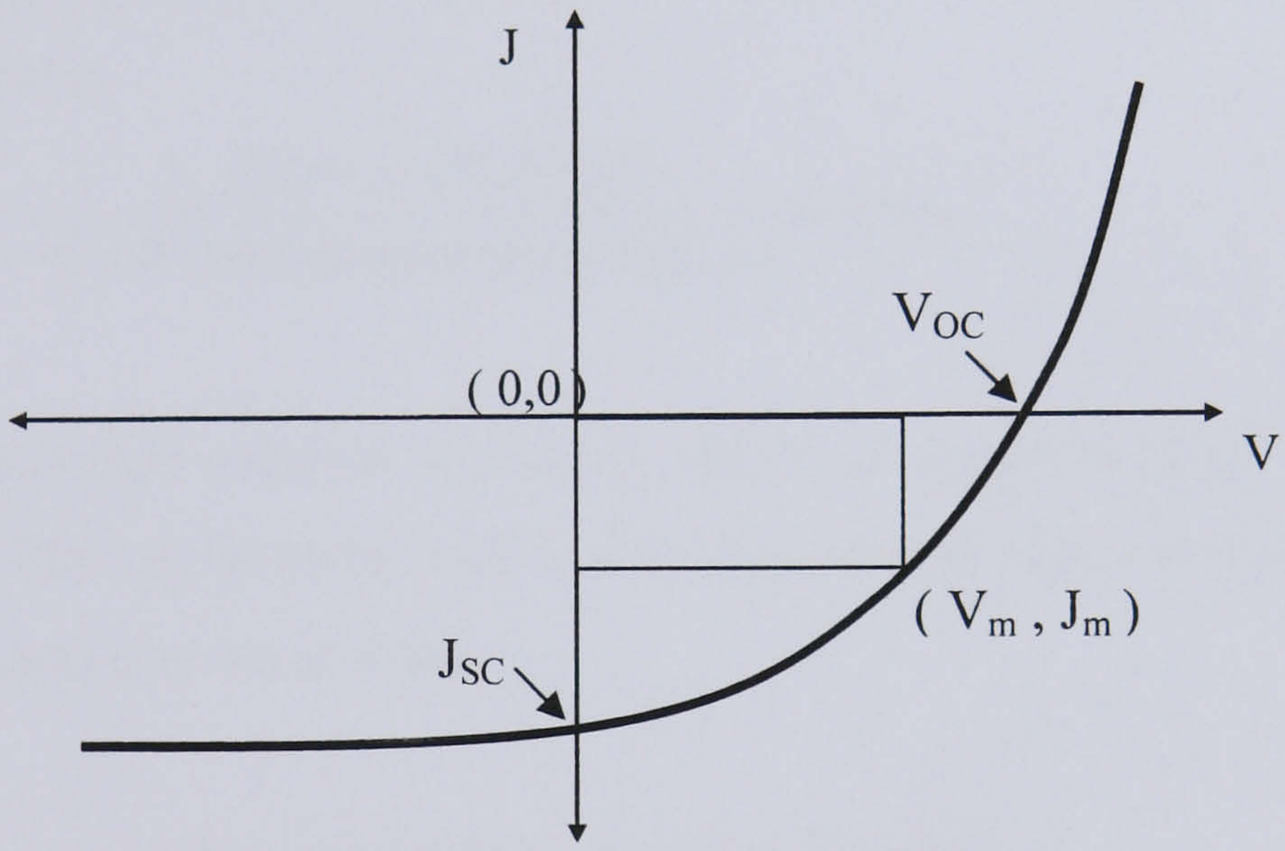


Figure 1.4 *Typical current density– voltage (J-V) characteristics of a photovoltaic device under illumination*

The power conversion efficiency of the device is defined as follows:

$$\eta = \frac{\text{Maximum Output Power density}}{\text{Total Incident Power density}} \times 100\ \% \qquad (1.1)$$

$$\eta = \frac{J_m\ V_m}{\text{Total Incident Power density}} \times 100\ \% \qquad (1.2)$$

where the maximum output power density of the device is given by the product J_mV_m, where J_m is the current density and V_m is the voltage at peak power. The values of J_m and V_m can be obtained from the J-V curve of the device, where the product J-V is

maximum at the point where $V = V_m$ along the curve. The short circuit current density, J_{SC} of the device is defined as the current density through the device when the applied voltage is zero, while the open circuit voltage, V_{OC} is the voltage developed in the device when the current through the device is zero. The power conversion efficiency expression can also be written as follows in term of these parameters:

$$\eta = \frac{J_{SC}\, V_{OC}\, FF}{\text{Total Incident Power density}} \times 100\,\% \qquad (1.3)$$

where the FF is called fill factor of the device and is defined as

$$FF = \frac{J_m\, V_m}{J_{SC}\, V_{OC}} \qquad (1.4)$$

The monochromatic power conversion efficiency of the device at a wavelength λ can also be written as

$$\eta(\lambda) = \frac{J_{SC}(\lambda)\, V_{OC}(\lambda)\, FF(\lambda)}{\text{Total incident power density}(\lambda)} \times 100\,\% \qquad (1.5)$$

The external quantum efficiency (EQE) of a photovoltaic device is the ratio between the flux of electrons collected in the external circuit and the flux of incident photon at a particular wavelength, λ.

$$\text{EQE}(\lambda) = \frac{Flux\ of\ electrons\ in\ external\ circuit}{Flux\ of\ incident\ photons} \qquad (1.6)$$

$$\text{Flux of incident photons per unit area} = \frac{P_{in}(\lambda)}{E_{Ph}(\lambda)} \qquad (1.7)$$

$$\text{i.e. Flux density of incident photons} = \frac{P_{in}(\lambda)}{E_{Ph}(\lambda)}$$

where $E_{Ph}(\lambda)$ is the energy of a photon and can be written as $E_{Ph}(\lambda) = \frac{hc}{\lambda}$ and $P_{in}(\lambda)$ is the total incident power per unit area at incident light of wavelength λ.

$$\text{Flux density of electron in the external circuit per unit area} = \frac{J_{SC}}{e}$$

$$\text{EQE}\,(\lambda) = \frac{J_{SC}}{P_{in}(\lambda)}\,\frac{hc}{e\lambda} = \frac{1240\,(\text{J C}^{-1}\,nm)\,J_{SC}\,(mA\,cm^{-2})}{P_{in}(mW\,cm^{-2})\,\lambda\,(\text{nm})} \qquad (1.8)$$

The intensity of the monochromatic light, $P_{in}\ (\lambda)$ is normally monitored by a calibrated silicon photodiode. The short circuit photocurrent density of the silicon diode, J_{SC}^{Si} and its spectral response $SR_{Si}\ (\lambda)$ give the intensity of the light.

$$\text{P}_{\text{in}}\,(\,\lambda) = \frac{J_{SC}^{Si}(\lambda)}{SR_{Si}(\lambda)} \qquad (1.9)$$

The external quantum efficiency, EQE (λ) of the device can also be written as follows:

$$\text{EQE}\,(\lambda) = \left[\frac{J_{SC}^{Si}}{P_{in}(\lambda)}\,\frac{hc}{e\lambda}\right]\frac{J_{SC}}{J_{SC}^{Si}} = \text{EQE}_{\text{Si}}\,(\lambda)\,\frac{J_{SC}}{J_{SC}^{Si}} \qquad (1.10)$$

where $\text{EQE}_{\text{Si}}\,(\lambda)$ is the EQE of the calibrated silicon photodiode.

The *internal* quantum efficiency (IQE) of the device is defined as the ratio between the flux of electrons collected in the external circuit and the flux of *absorbed* photons at a particular wavelength, λ. Suppose the absorbance in non active layers of the device is negligible, then IQE can be written as

$$\text{IQE}\,(\lambda) = \frac{\text{EQE}}{[\,1 - \text{R} - \text{T}\,]} \qquad (1.11)$$

where R is the reflectivity of the device, and T is the transmittance.

Yoshino *et al.*[40] investigated a donor-acceptor heterojunction and suggested an expression for monochromatic power conversion efficiency, η by considering the conversion steps we discussed in the section 1.3.

$$\eta = \frac{N_{exc}}{N_{ph}} \times \frac{N_{ct}^{e-h}}{N_{exc}} \times \frac{N_{free}^{e-h}}{N_{ct}^{e-h}} \times \frac{eV_{OC}}{h\nu} \times FF \qquad (1.12)$$

$$= \alpha(\omega) \times \varphi_{ex} \times \phi_{e\text{-}h} \times \xi_{en} \times \text{FF}$$

where,

N_{exc} - number of electron–hole pairs (excitons)

N_{ph} - number of photons

N_{ct}^{e-h} - number of interfacial composite charge transfer (ct) excitons

N_{free}^{e-h} - number of excitons that undergo charge separation

$\alpha(\omega)$ - Efficiency of photon collection

φ_{ex} - The quantum efficiency of the excitonic dissociation

$\phi_{e\text{-}h}$ - quantum yield of free electrons in acceptor parts and holes in donor parts

ξ_{en} - energetic factor

FF - Fill factor

$\frac{eV_{OC}}{h\nu}$ - The fraction of absorbed photon energy that can be converted to electrical energy

The power conversion efficiency of a device depends on several parameters, such as photon collection efficiency, exciton dissociation efficiency, charge transfer yield, fill factor and photon-electron conversion efficiency.

Most room for improvement of polymeric photovoltaics lies in extending the range of quantum efficiency spectrum more on red and improving the fill factor. The series and shunt resistance of a photovoltaic device strongly influence the photovoltaic parameters of the device and we will discuss this in the next section.

1.6 Series and shunt resistance of a photovoltaic device

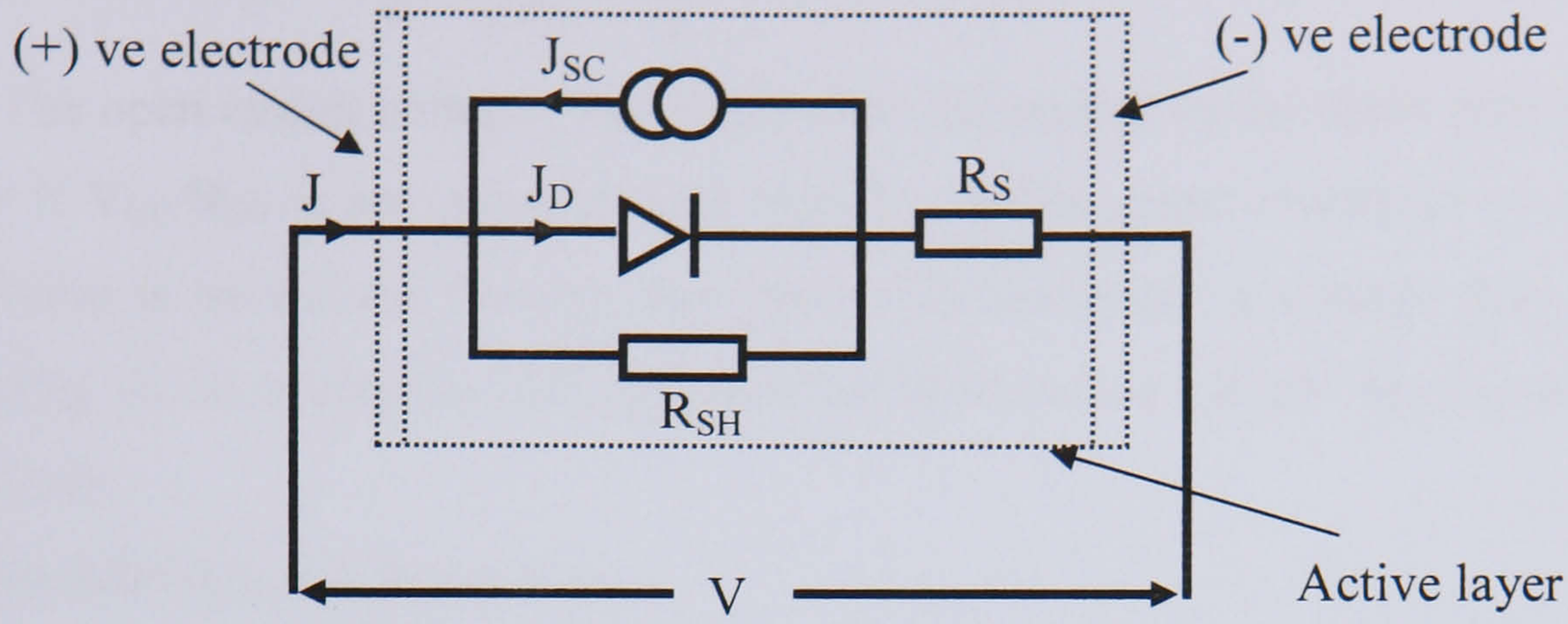


Figure 1.5 *Equivalent circuit diagram of a photovoltaic device under illumination*

Figure 1.5 shows the equivalent circuit diagram of an inorganic photovoltaic device used to describe its electrical behaviour. Although the physical processes of organic based photovoltaic devices may be different from inorganic solar cells, the main loss mechanisms are same and the above equivalent circuit can be assumed for organic based photovoltaic devices. The circuit contains a current source, a diode, a series resistance R_S and a shunt resistance, R_{SH}. The series resistance arises from the resistance of the device materials to current flow and the effects of low mobility of the device materials and transport layer thickness. The shunt resistance arises from leakage of current through the device. This may be due to recombination of charge carriers.

In the presence of these resistances, the current density of the device under illumination and applied bias voltage V can be written as

$$J = J_0\left[\exp\left\{\frac{q(V - AJR_S)}{nkT}\right\} - 1\right] + \frac{V - AJR_S}{AR_{SH}} - J_{SC} \qquad (1.13)$$

where AJ, represents the current throughout the whole device, AJ_0 stands for the reverse current of the diode, n is the ideality factor of the diode (typically lies between 1 and 2 for Si or GaAs diodes), and J_{SC} is the light generated current density of the device.

For an ideal diode, $R_S = 0$, $R_{SH} = \propto$ and $n = 1$,

$$J = J_0\left[\exp\left\{\frac{qV}{kT}\right\} - 1\right] - J_{SC} \qquad (1.14)$$

At the open circuit voltage condition of a device under illumination

$V = V_{OC}$ and $J = 0$,

$$V_{OC} = \frac{nkT}{q}\ln\left[\frac{J_{SC} - V_{OC}/AR_{SH}}{J_0} + 1\right] \qquad (1.15)$$

$$V_{OC} = \frac{kT}{q} \ln\left[\frac{J_{SC}}{J_0} + 1\right] \text{ for ideal device} \quad (1.16)$$

The open circuit voltage, V_{OC} is therefore influenced by the shunt resistance of the device if V_{OC}/R_{SH} is not much smaller than J_{SC}, while series resistance is unimportant since there is no current flowing through it that can create a voltage drop. However, increasing series resistance will decrease the short-circuit current density as shown in Figure 1.6.

Suppose both R_{SH} and R_S are low,

$$J = J_0\left[\exp\left\{\frac{qV}{kT}\right\} - 1\right] + \frac{V}{AR_{SH}} - J_{SC} \quad (1.17)$$

$$\frac{dAJ}{dV} = \frac{q}{nkT} J_0 \exp\left\{\frac{qV}{kT}\right\} + \frac{1}{R_{SH}} \quad (1.18)$$

At the short-circuit point ($V = 0$, $J = J_{SC}$)

$$\frac{dAJ}{dV} = \frac{qJ_0}{nkT} + \frac{1}{R_{SH}} \approx \frac{1}{R_{SH}} \quad (1.19)$$

Since the term V/R_{SH} in the equation 1.17 vanishes at short circuit condition, the shunt resistance has no effect on J_{SC}. However, decreasing shunt resistance may reduce the V_{OC}.

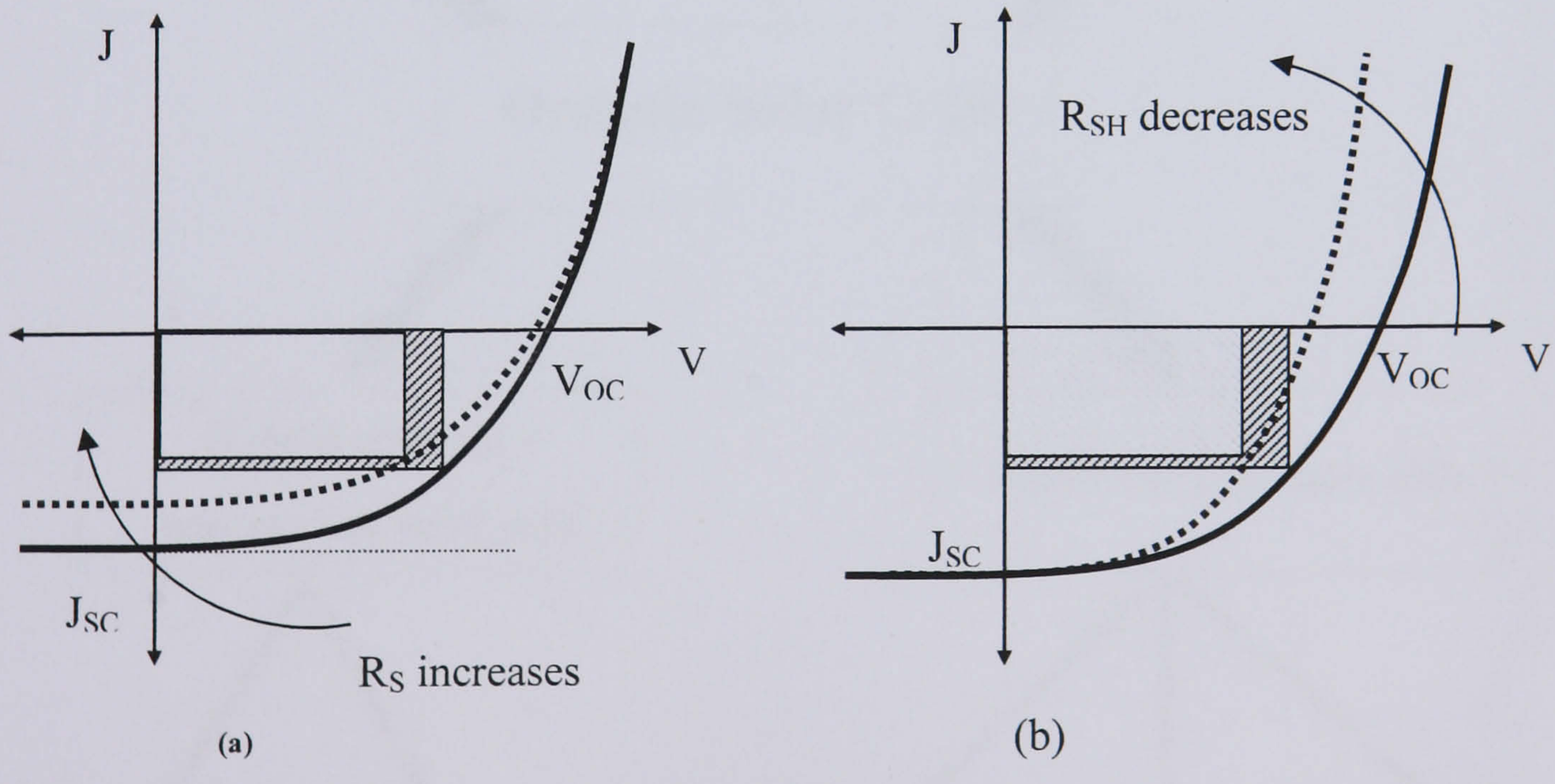


Figure 1.6[41] *The effect of (a) increasing series resistance and (b) decreasing shunt resistance*

The V_{OC} is not only affected by R_{SH}, but also is affected by the ratio between the short circuit current and reverse saturation current, temperature and ideality factor of the device. According to the diode model, reducing the dark current (current flows across a device under bias in the dark) would offer higher open circuit voltage.

1.7 Review of previous work on organic solar cells

Organic solar cells defined here as solar cells which use at least one molecular material in the active layer, have been a focus of considerable research over the last decade. There are four major classes (see, Figure 1.7) of molecular solar cells in the literature namely, dye sensitized nanocrystalline metal oxide solar cells, polymer blend solar cells, molecular film solar cells and hybrid polymer / nanocrystal solar cells.

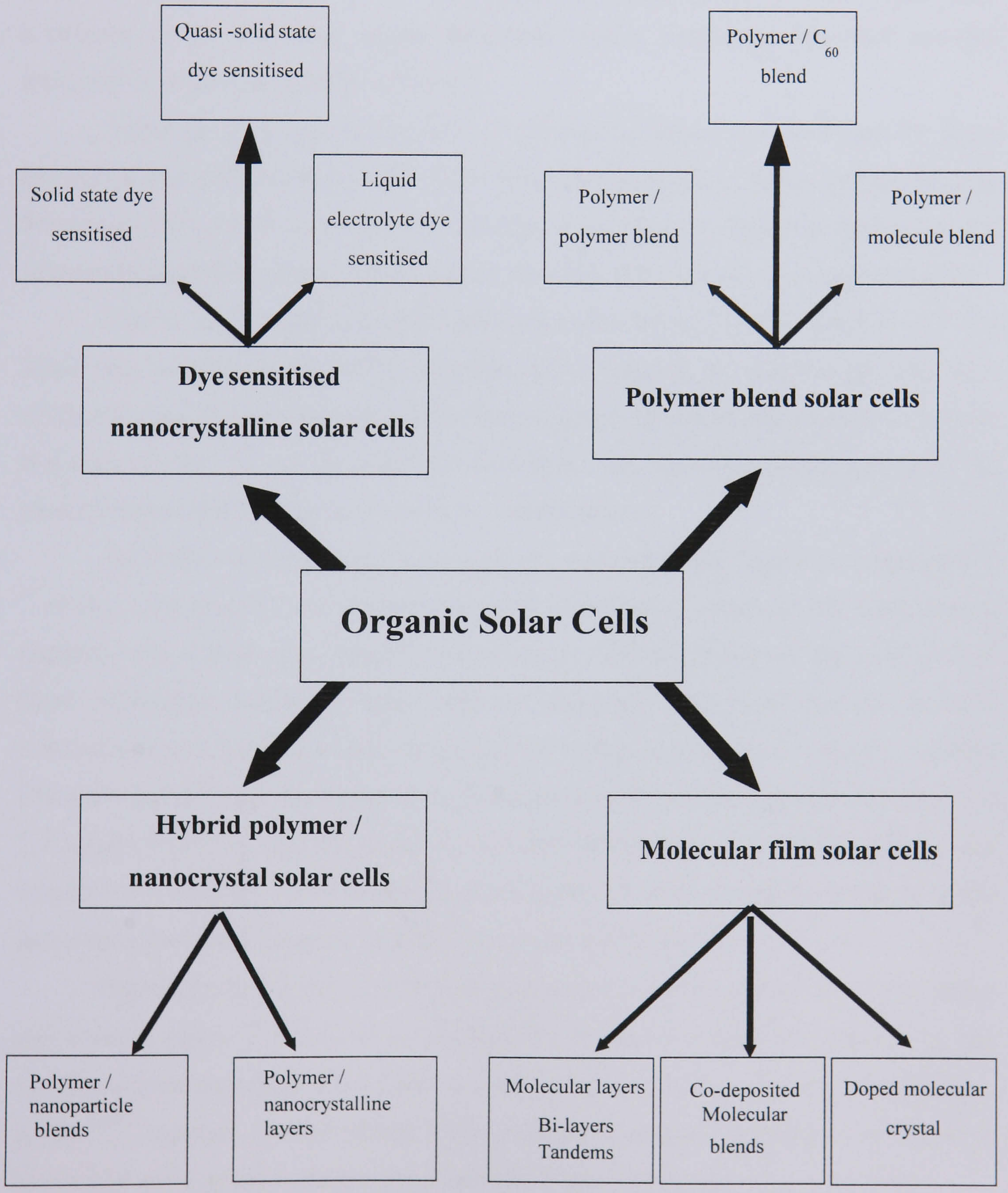


Figure 1.7 Overview *of different classes and their sub classes of organic solar cells.*

1.7.1 Dye sensitized solar cells

Amongst all molecular solar cells, the highest power efficiencies so far have been reported for liquid electrolyte dye sensitized nanocrystalline TiO_2 solar cells. Michael Grätzel's group[42] reported 10-11 %, efficiency at AM 1.5 standard solar spectrum for such type of a solar cell. Several attempts to replace TiO_2 with other metal oxides, SnO_2, ZnO, Nb_2O_5, have not been very successful, until Tennakone's group[43] reported 8 % efficiency photochemical solar cell made from a porous film consisting of a mixture of tin and zinc oxides sensitized with a ruthenium bipyridyl complex measured at direct sunlight (90 $mWcm^{-2}$).

Although good power conversion efficiencies have been achieved for these electrolyte and photochemical solar cells, there are a number of disadvantages, such as the requirement of encapsulation of the device to prevent electrode drying up and chemically aggressive redox system, which limit the cell from practical applications.

Cao *et al.*[44] reported a quasi-solid state photochemical cell employing a dye sensitized, nanocrystalline TiO_2 electrode and a polymer gel electrolyte. The cells exhibited open circuit voltages and fill factors comparable with liquid electrolyte cells but lower power efficiencies of 3-5 % under white light. Quasi-solid state version of the photochemical cell also requires complex encapsulation.

Solid-state dye-sensitized solar cells are currently under intense investigation[45-47] as they offer practical advantages compared to electrolyte solar cell. The electrolyte is replaced with a solid state organic hole transport material. However, the efficiency of these solid-state sensitized solar cells is drastically decreased due to the low conductivity and mobility of the charge carriers in the organic hole-conductor. Michael Grätzel's group[47] recently reported a solid-state dye-sensitized solar cell based on 2,2 7,7-tetrakis(N,N-di-p-methoxyphenyl-amine)-9,9-spiro-bifluorene with overall power conversion efficiency 3.2 % under air mass (AM) 1.5 illumination by performing the dye adsorption in the presence of silver ions in the dye solution.

Recombination is the main loss of mechanism in dye-sensitised solar cell. James and Jenny's group [48-53] intensively studied the charge recombination kinetics in dye sensitised nanocrystalline TiO_2 films or cells using transient absorption spectroscopy. Jenny [54-56] reported several Monte Carlo simulation studies of charge recombination kinetics in such systems and electron transport in nanocrystalline TiO_2 electrodes.

1.7.2 Molecular film solar cells

In molecular film organic solar cells, the active layers are cast by vacuum deposition techniques. In 1986, Tang[29]demonstrated solar cell action in molecular bi-layers, which were vacuum deposited. In this pioneering work, Tang reported a power conversion efficiency of about 1 % for a bi-layer solar cell of copper phthalocyanine (CuPc) and a perylene dye under simulated AM 2 illumination. Thelakkat *et al.*[57] recently reported that the power efficiency of this bi-layer device can be improved by depositing an additional thin TiO_2 layer. They reported a power conversion efficiency of 1.4 % at 82 $mWcm^{-2}$ in a three layer device which consisted of copper pathalocyanine (CuPc), a perylene dye and an additional thin TiO_2 layer. All three layers including the thin layer of TiO_2 were deposited by chemical vapour deposition. The authors discuss the effect of additional TiO_2 in terms of energy band diagram. The higher efficiency of the three-layer device may be attributed to the additional TiO_2 layer, which reduces the band-offset for electron injection and also functions as an effective hole-blocking electron-transport layer.

Efficient photon harvesting in organic thin films solar cell could be achieved by incorporating an exciton-blocking layer (EBL) between the photoactive organic layers and the metal cathode. Forrest's group[58] reported a power conversion efficiency, η of 2.4 % for a vacuum deposited ultra thin organic device consisting of thin layers of CuPc, 3,4,9,10-perylenetetracarboxylic bis-benzimidazole (PTCBI) and a blocking layer. The blocking layer transports electrons to the cathode from the adjoining acceptor layer while effectively blocking excitons in the lower-energy-gap acceptor layer from recombining at the cathode. They recently reported[59] an improved device, which shows a η of 3.6 % under AM1.5 spectral illumination of 150 $mWcm^{-2}$. The device structure is the same as the previous one but with C_{60} as electron transporter and an additional PEDOT: PSS layer on top of the ITO. It is interesting to note that the introduction of the PEDOT: PSS layer causes a shift of photocurrent characteristics by a voltage $\Delta V = 0.5$ V (see Figure 1.8). The PEDOT:PSS layer improves the ohmic contact for holes and increases the charge separating built-in voltage by 0.5 V, leading to improved collection of the photogenerated carriers at higher positive voltages, and hence, an increased η. It had already been reported[60] that built-in voltage increases by 0.5 V when a PEDOT:PSS film is incorporated between the ITO electrode and a polymer layer which supports the Forrest's group observation.

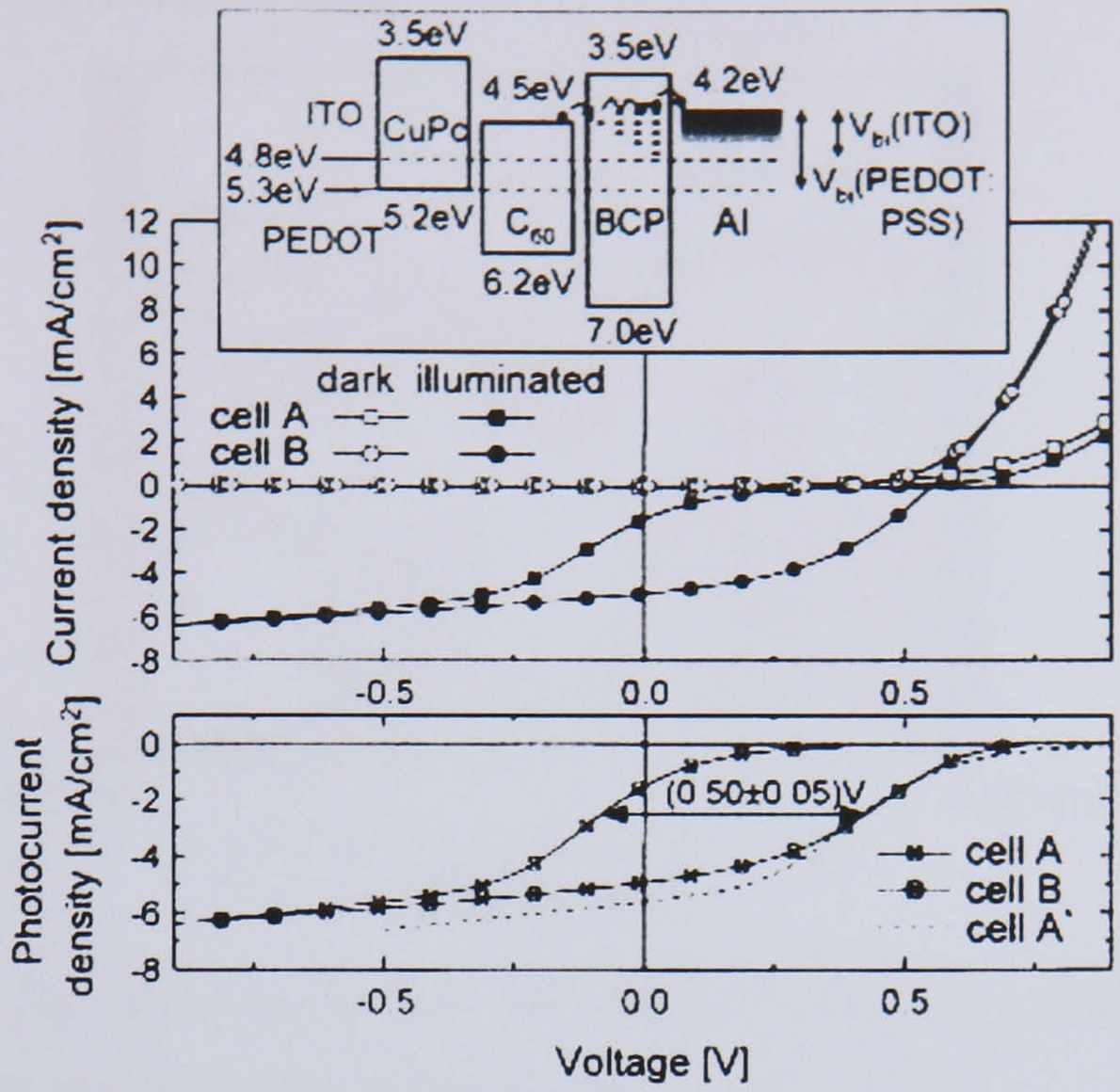


Figure 1.8 [59] ***Upper panel****: Effect of the PEDOT:PSS layer on the J-V characteristics of anode / CuPc / C_{60} / BCP / Al devices under AM 1.5G illumination with an intensity of 100 mW/cm^2, where the anode is either ITO (cell A, squares), or ITO / PEDOT:PSS (cell B, circles).* ***Lower panel:*** *Effect of the PEDOT:PSS layer on the photocurrent–voltage characteristics of the same devices The photocurrent is the difference between the I–V curves taken in the dark and under illumination. Also shown is the photocurrent of cell A shifted by V = +0.50 V (cell A*, dashed line), which overlaps with the photocurrent curve of cell B.*

In case of C_{60} and CuPc , the photocurrent contribution of C_{60} is generated mainly between 400 and 550 nm, while the CuPc layer contributes from 550 to 750 nm. The spectral response of the combined system is excellent and so an efficient device resulted in this combination.

Even though the thin film vacuum / vapour deposited solar cells show good power conversion efficiency, on account of the cost of vacuum deposition, the fabrication cost of molecular film solar cells is high compared to solar cell made by cheap solution processing technique.

1.7.3 Polymer blend solar cells

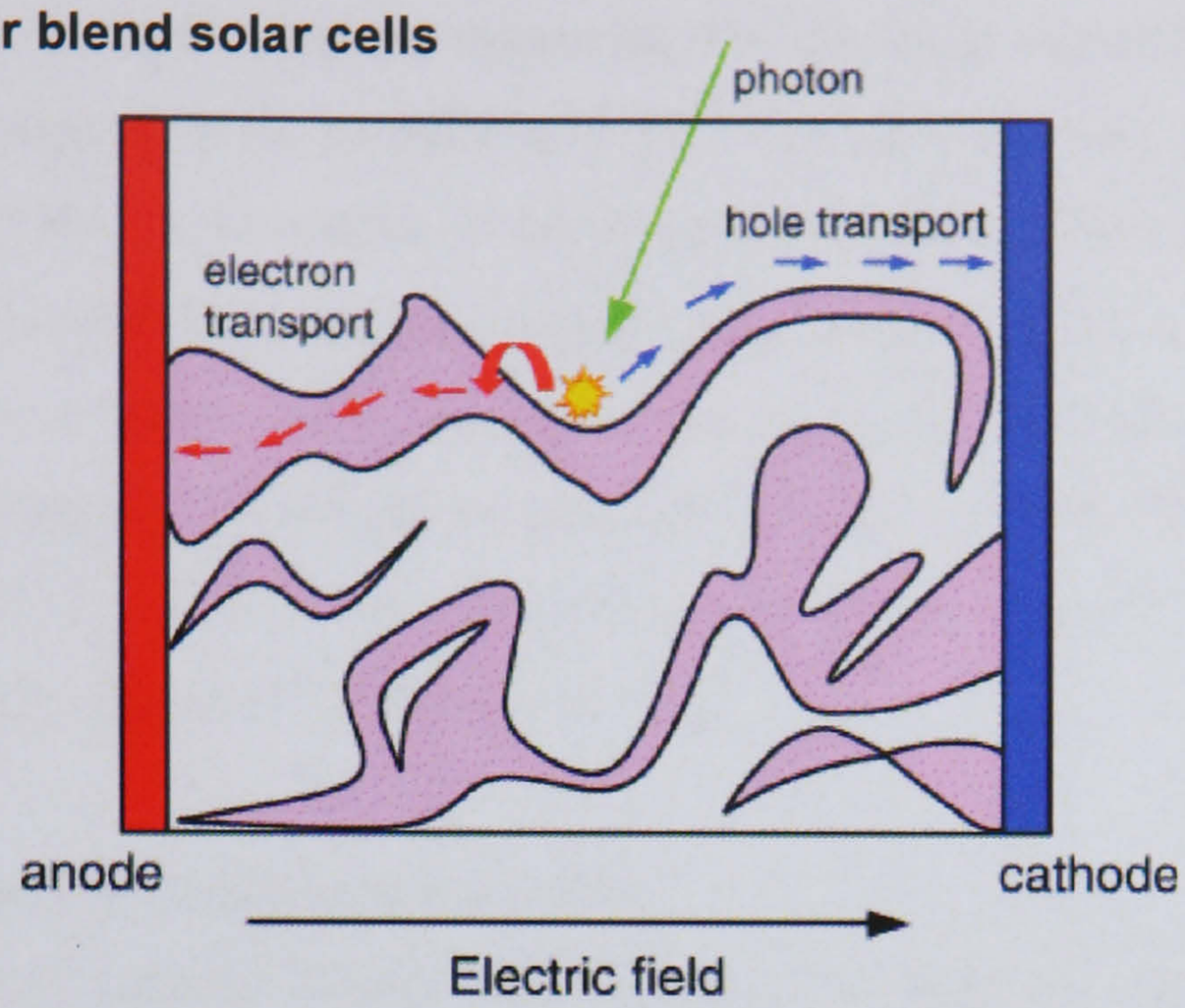


Figure 1.9 [9] *Schematic shows how the charge carriers may reach the electrodes after dissociation of an exciton at a polymer / polymer interface.*

All the solid-state organic solar cells discussed so far are planar devices. In planar devices the interfacial area is limited. A breakthrough for polymer solar cells was the introduction of the bulk heterojunction. In 1995, two independent groups reported[27] that an increase of several orders of magnitude in quantum efficiency can be obtained by mixing an electron conducting component with a hole conducting polymer. These blends of polymer produce three-dimensional heterojunctions and lead to efficient charge generation within the whole film.

Solar cells based on blends of methanofullerenes with PPV derivative, and more recently, polythiophenes, polymers have been investigated. Recent reports[12,61,62] on polymer / PCBM blend devices reported a power conversion efficiency of over 3 %. In a blend structure, the length scale of the blend may be similar to the exciton diffusion length. A relatively fine scale is therefore favourable for photogenerated excitons to diffuse to an interface and dissociate. Figure 1.9 illustrates how the separated carriers may travel to the contacts, if a continuous path is available. It is essential to have continuous paths for the transport of separated charges to the contact. Even though isolated domains of either donor or acceptor materials would be optically active, these are electrically inactive which reduce the efficiency of the solar cells. Therefore for optimum performance each material must provide a continuous path for transport of separated charges to the electrodes[9].

Friend's group[63] successfully designed a laminated polymer structure for solar cell application. The laminated structure consists of two interpenetrating layers of the

donor and the acceptor polymer materials. The structure was prepared by pressing two separately prepared films of MEH-CN-PPV [a cyano derivative of poly(*p*-phenylene vinylene)]: POPT [a derivative of polythiophene] (19:1) blend on low work function electrode (aluminium or calcium coated glass substrate) and a POPT:MEH-CN-PPV (19:1) blend on high work function electrode (ITO or PEDOT:PSS substrate) at elevated temperature. The EQE of a device with Au / PEDOT:PSS and Ca electrodes reaches 29 % at 480 nm and calculated power conversion efficiency for a simulated solar spectrum AM 1.5 (77 mW/cm^2) is 1.9 %.

1.7.4 Polymer / nanocrystal solar cells

Electron mobility values and stability of most of the organic materials used in organic solar cells are extremely poor compared to inorganic materials used in inorganic solar cells. Poor electron mobility causes much current loss due to recombination. Incorporating good electron transporters into hole-conducting organic material should reduce the recombination. The limitation of charge transport may be overcome by combining hole-conducting polymers with inorganic semicondutors such as CdSe, TiO_2, ZnO and SnO_2.

In 1996, Neil Greenham, working in Paul Alivisatos's group[64], reported an organic / inorganic composite solar cell consisting of a mixture of cadmium selenide nanocrystals and MEH-PPV polymer. They observed an enhancement in photocurrent yield attributed to photoinduced electron transfer from the MEH-PPV to the nanocrystals and found EQE of 12 % and power conversion efficiency of 0.6 % at 514 nm for device consisted of 90 wt % CdSe nanocrystals (5 nm diameters). The corresponding power conversion efficiency was about 0.1 % under AM 1.5 conditions (80 $mWcm^{-2}$).

Six year after the above observation of PV action in blends of CdSe nanocrystals and MEH-PPV polymer, Paul Alivisatos' group[14] improved power conversion efficiency, of 1.7 % under A.M. 1.5 solar conditions, for a CdSe / polymer solar cell, using CdSe nanorods and a high hole-mobility polymer, poly-3 (hexylthiophene) (P3HT). The nanorods are single crystallites. Electron transport within the rods is therefore fast. The optimum cell consisted 90 wt % of CdSe nanorods of 7 nm diameter and 60 nm lengths.

A nanostructured metal oxide such as TiO_2, ZnO and SnO_2 combined with a conjugated hole-transporting polymer is another interesting material combination Metal

oxides offer good electron transport properties, excellent physical and chemical stability and fabrication via facile techniques. Moreover they offer the possibility of control of the microstructures in order to create a large and stable interfacial area when coated with a polymer film.

Efficient charge transfer to TiO_2 from several polymers has been reported[16-23,65-68]. However, the power conversion efficiency of solar cells made from nanostructured TiO_2 and hole transporting polymers is low compared to the best organic solar cells. Nevertheless, there is plenty of room for improvement of this system. A better understanding of the factors affecting test devices, may lead to improvements in this device system. Previous studies on this system will be reviewed in more detail since they are the basis for our work.

1.8 Review of previous work on hybrid metal oxide / polymer device

Although nanocrystalline metal oxides such as TiO_2 have been intensively studied for use in dye-sensitised solar cells for more than a decade, hybrid polymer / metal oxide combinations have been studied for solar energy conversion only in recent years, but with growing interest.

The capability of organic materials to act as sensitizers of TiO_2 for visible light have been reported[16-23,66-73] for several conjugated polymers such as MEH-PPV[1], PA-PPV[2], BFB[3], MDMO-PPV[4], and PATs { PATs = Poly(3-alkylthiophenes), where alkyl = butyl, hexyl, dodecyl or octadecyl }. The MEH-PPV / TiO_2 combination is one of the best-studied systems for hybrid metal oxide / polymer photovoltaic devices in the literature.

1.8.1 Evidence for exciton dissociation at MEH-PPV / TiO_2 interface

In 1998, Savenije and co-workers[19] first reported evidence for dissociation of excitons at the MEH-PPV / TiO_2 interface and electron injection into the conduction band of TiO_2. They successfully made a working TiO_2 / MEH-PPV device with ITO and Hg as electrons and holes-collecting electrodes respectively. A thin film (80 nm) of anatase TiO_2 was deposited on the ITO by chemical vapour deposition yielding very smooth and transparent layers. A solution of MEH-PPV in $CHCl_3$ was spin coated on top of the flat TiO_2 layer. The device showed poor EQE of 3 % around 500 nm. Nevertheless this study showed that on excitation of the MEH-PPV polymer, electrons are injected into the conduction band of the TiO_2. Furthermore, capacitance measurements showed that a depletion layer was formed at the interface of the bi-layer, analogous to an inorganic p / n heterojunction. The authors further estimated the exciton diffusion length in this spin-coated MEH-PPV polymer to be 20 ± 3 nm by comparing photoluminescence of polymer layers with different thicknesses on ITO and flat TiO_2 layer substrates at the wavelength corresponding to maximum luminescence.

1.8.2 PPV / TiO_2 blends

Soon after the first report on TiO_2 / MEH-PPV, Salafsky and co-workers[67] focused on blends of TiO_2 nanocrystals and PPV. They used the time resolved microwave conductivity (TRMC) technique to show that excitons generated in PPV would dissociate at the TiO_2 / MEH-PPV interface to transfer electrons to the TiO_2 nanocrystals.

---

[1] poly [2-methoxy-5-(2'-ethyl-hexyloxy) para-phenylene vinylene], [2]poly(N-phenylimino-1,4-phenylene-1,2-ethenylene-1,4-(2,5-dioctoxy)-phenylene-1,2-ethenylene-1,4-phenylene), [3]Poly(9,9'-dioctylfluorene-co-bis-N,N'-(4- butylphenyl)-bis-N,N'-henylbenzididine, [4]poly[2-m methoxy-5-(2'-

In 1999, Salafsky[68] prepared and characterised ultra thin (100 nm) TiO_2 nanocrystal / PPV composite devices containing different weight % (0 to 67) of TiO_2 (20 nm particle diameter) in the polymer. The author prepared composite layers by spin coating the solution of the TiO_2 / PPV mixture onto an ITO substrate. The mixture was prepared by mixing the TiO_2 nanocrystals (75 % anatase) / methanol (at pH 2) into a methanol solution of a sulfonium precursor of PPV. The film was then heated in vacuum or under flowing nitrogen at 150-200 ^{0}C to convert the precursor into PPV. Photoluminescence (PL) studies on composites of these PPV with TiO_2 nanocrystals revealed that there is significant quenching of polymer fluorescence even with 5 wt. % of nanocrystals. However, the external quantum efficiencies reached only 1-2 % in the wavelength range 400 to 500nm but over 10 % below 387 nm for the ITO / PPV:TiO_2 / Al devices with 20 wt. % TiO_2. The response between 400 and 500 nm is due to the polymer, and the response in the blue to the TiO_2 nanocrystals. The high EQE obtained below 387 nm is not useful for harvesting solar radiation. The device produced a J_{SC} of less than 40 $\mu A/cm^2$ under white light illumination (100 $mWcm^2$). The lower J_{SC} is attributed due to poor charge transport through the blend containing amorphous TiO_2 domains and / or isolated TiO_2 or polymer domains.

Salafsky combined his experimental results with a hopping model for charge transport in a nanocrystal lattice. The combined study indicated that most photogenerated excitons lead to charge separation at the interface between the polymer and the nanocrystals, for compositions above 20-wt % TiO_2, but the electron collection efficiency is limited by fast recombination.

In the same year, Carter and co-workers[21] reported a study of MEH-PPV / TiO_2 devices comparing blends and layered structures. The blend structure was a polymer / nanoparticle composite film made by simply spin casting a MEH-PPV / TiO_2 nanoparticle mixture (70 % by weight of TiO_2 to polymer). The mixture was prepared either by first dispersing the nanoparticles in p-xylene, and then adding this mixture to the MEH-PPV / p-xylene solution, or by adding the nanoparticles directly to the MEH-PPV / p-xylene solution. The former technique resulted in better dispersion of the nanoparticles in the final film. In the layered structure, the porous TiO_2 nanocrystalline layers of thickness of 4-6 μm were made by coating an ITO glass substrate with a viscous TiO_2 water solution that is spread onto the substrate and annealed for 30 min at 500 °C to fuse the nanoparticles. A thin layer of the polymer was deposited on the porous layer by usual spin coating technique. Au electrode deposited by thermal

evaporation in layered structure sample as hole collecting electrode, while Ca electrode deposited for the blend structure as electron collecting electrode. In forward bias, a two-order magnitude increase in photoconductivity, along with sharp photocurrent saturation, was observed in the layered structure in contrast to blends where no enhancement occurs. Poor charge transfer from nanoparticles to polymer in blend device may be due to isolation of individual particle within polymer. On the other hand, layered devices show a peak external quantum efficiency of 4 % and open circuit voltage of 0.7 V. The poor power quantum efficiency may be due to thicker TiO_2 layer (4-6 μm), lager size of TiO_2 particles (80 nm) which limits interfacial area and insufficient penetration of the polymer into the pores of the TiO_2.

1.8.3 Evidence for creation of polaron and their kinetics

The above studies showed clear evidence for the dissociation of excitons in MEH-PPV and PPV polymers at the interface with TiO_2 and electron injection into the conduction band of TiO_2. However, the characteristics of photogenerated hole (polarons) in the polymers in contact with TiO_2 were not studied in detail until 1999.

In 1999, Janssen and co-workers[66] successfully applied photoinduced absorption (PIA) spectroscopy and photoinduced electron spin resonance (ESR) spectroscopy to provide direct spectral evidence for the photoinduced creation of polarons in MEH-PPV as well as in poly[2-methoxy-5-(3′,7′-dimethyl-octyoxy)-*p*-pheneylene vinylene] (MDMO-PPV) and P3HT polymers in contact with nanocrystalline TiO_2. This study further showed that photoexcitons present in this material system are long-lived.

In 2000, Savenije and co-workers[65] again focused on the TiO_2 / MEH-PPV bi-layer system to study charge separation and device performance. A flash-photolysis time-resolved microwave conductivity technique was used to monitor charge separation between a smooth electron beam deposited anatase TiO_2 film (80nm) and spin coated layers of a MEH-PPV polymer (20-140 nm thick), exciting the polymer at 544 nm. The quantum efficiency of electron injection into the TiO_2 from photons absorbed in the polymer layer was calculated by comparing the conductivity resulting from 544 nm irradiation with that from direct band gap excitation of the anatase layer at 308 nm. The peak quantum efficiency is about 6 % for polymer thickness range of 30-50 nm. The sensitisation efficiency for the interfacial electron transfer from a soluble PPV to TiO_2 was estimated to reach 60 %, when the thickness of the polymer film is below the exciton diffusion length (approx. 20 nm).

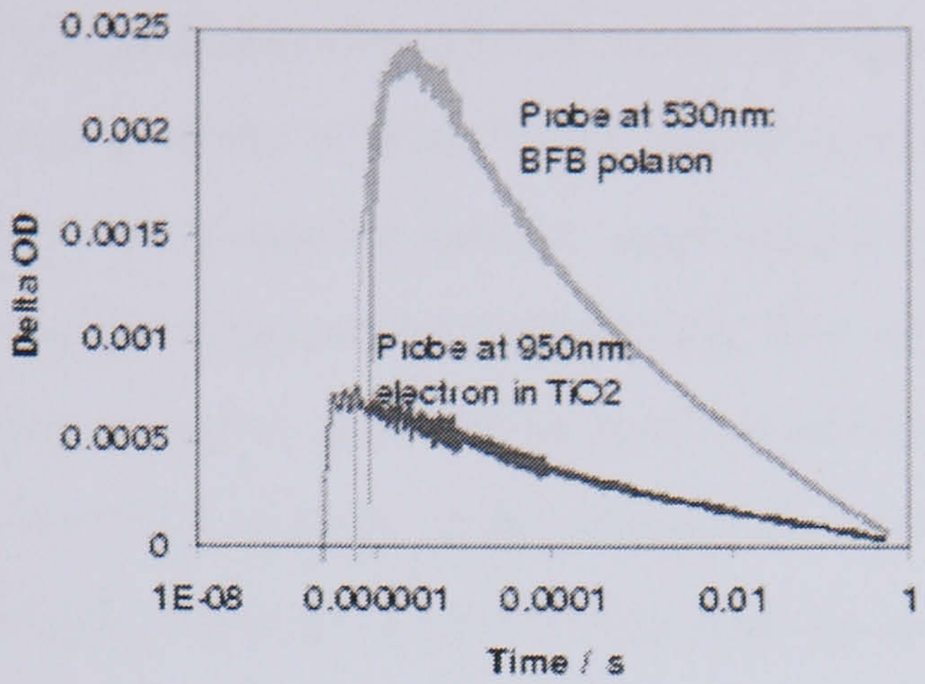


Figure 1.10 [74]*Transient absorbance decays due to charge species (electron and polaron) in a BFB / TiO_2 composite upon photoexcitation by a laser pulse at 400 nm. Absorbance bands centred at 530 nm and 950 nm correspond to the BFB polaron and the electron in the TiO_2 respectively. The half-life for recombination is around 1 ms, indicating that separated species are long-lived.*

In 2002, our group at Imperial College[74] successfully applied nanosecond-microsecond transient absorption spectroscopy (TAS) in a composite containing high hole mobility BFB polymer and porous TiO_2. TAS is a useful technique for monitoring both the charge separation yield and the charge recombination kinetics in molecular photovoltaic devices[46,49,75,76]. Figure 1.10 shows that recombination between the polaron in the BFB polymer and electron in the TiO_2 is relatively slow with a half-life of around 1ms, which is comparable with the recombination time in dye-sensitised films at short circuit. The high ΔOD values shown in the Figure 1.10 corresponding to high charge transfer yields, is achieved in the TiO_2 / BFB structure, when the extinction coefficient of the polymer is taken into account.

1.8.4 Fast electron transfer from MEH-PPV to TiO_2

Anderson *et al.*[77] applied femtosecond IR transient absorption spectroscopy on a MEH-PPV / TiO_2 composite and showed that the electron-transfer from the excited MEH-PPV polymer to the TiO_2 nanoporous thin film occurs on a time scale of 100 fs, which is comparable with polymer / fullerene solar cells. They further observed that the charge-separated species in this composite are long-lived.

1.8.5 Surface modification of TiO_2

Gratzel's group[78] investigated the influence of TiO_2 surface modification on dark J-V characteristics of TiO_2 / polymer bi-layer structures. They modified the

heterojunction of TiO_2 and spiro-MeOTAD[5] small molecules via surface adsorption of para–substituted benzoic acids with different dipole moments and reported that para-functionalised benzoic acids can be used to systematically modify the current-voltage characteristics of organic-inorganic heterojunctions. The device behaviour was shown to be consistent with the variation of the work function of the modified TiO_2 surface. This effect is attributed due to a change in the interfacial energy step at the TiO_2 / spiro-MeOTAD interface induced by the dipole moment of the adsorbed benzoic acids.

1.8.6 Efficient MEH-PPV / TiO_2 devices

In 2001, Fan and co-workers[23] reported an efficient MEH-PPV / TiO_2 device with ITO and Au as electrodes. The TiO_2 layers of 50 nm thicknesses were prepared on ITO glass substrate using sol-gel and dip coating techniques followed by sintering at 450^0C for 30 minutes. The polymer layer of thickness 80nm was spin coated on top of the TiO_2 layer before deposition of Au electrode. The device shows a peak EQE of 9.5 % and monochromatic power conversion efficiency of 1.6 % at 500 nm. This was the highest reported peak EQE for TiO_2 / MEH-PPV devices. The better device performance may be attributed to reduced active layer thicknesses and better charge collection by the Au electrode in place of the Hg electrode used by Savenije and co-workers. Fan et al. observed that the photovoltaic properties of the device remained constant for a test period of one year in dark.

In the same year, Carter and co-workers[16] reported the effect of polymer thickness, hole-mobility, and morphology on the performance of ITO / TiO_2 / MEH-PPV / Au devices. Figure 1.11 shows the J-V characteristics of the ITO / TiO_2 / MEH-PPV/Au devices with different polymer layer thicknesses. The fill factor increases with decreasing polymer thickness at a constant light intensity. The poor fill factor for thicker sample at a constant light intensity may be due higher resistive losses. Note the shape of the photocurrent curve close to open circuit voltage. Three types of TiO_2 layers were prepared in order to investigate the effect of TiO_2 morphology: sintered sol-gel (dense layer), non-sintered sol-gel (dense layer), and anatase nanoparticle (purchased from Solaronix) layers. They observed higher J_{SC} and EQE for sintered dense layer devices comparable to their non-sintered counter parts. Device made using TiO_2 nanoparticle layers show significant improvement in device performance compared to dense layer devices. The improvement may be due to increased surface area.

---

[5] 2,2' 7,7'-tetrakis(N,N-di-p-methoxyphenylamine)-9,9'-spiro-bifluorene

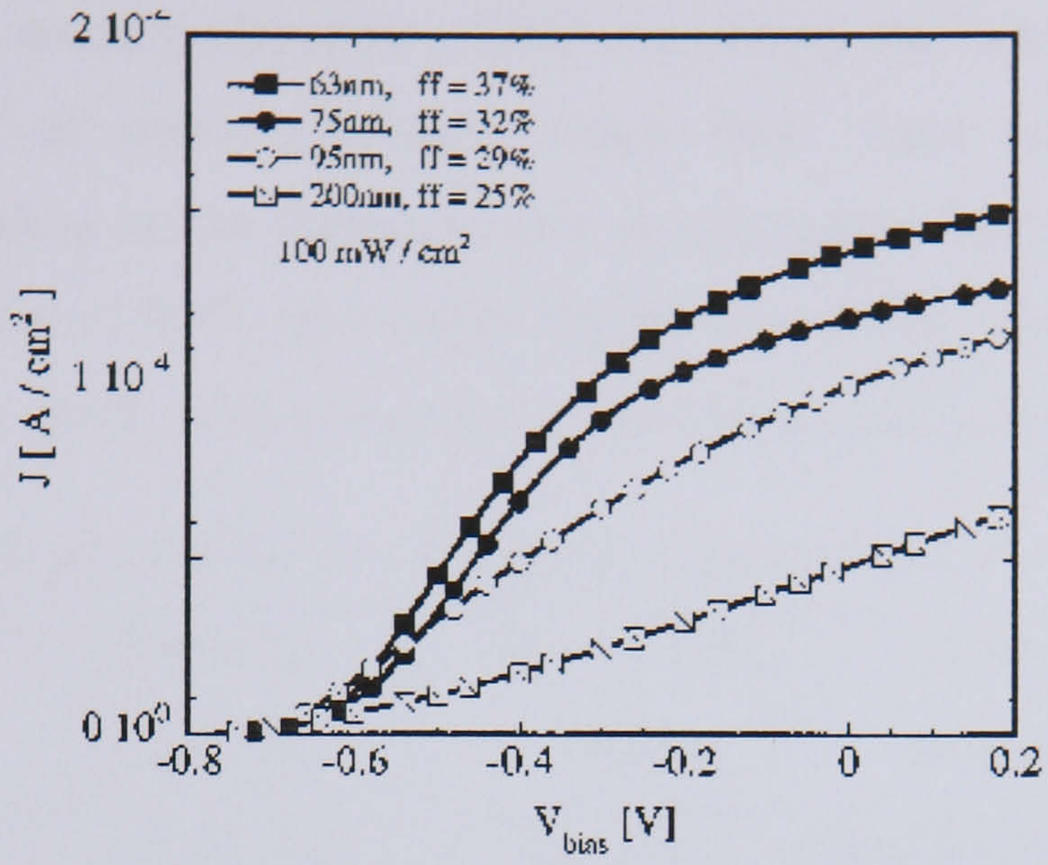


Figure 1.11 [16] *The photocurrent density versus the applied bias of the ITO / TiO2 / MEH-PPV / Au with different polymer thickness. We note that the photocurrent starts to fall off before open circuit voltage.*

Photocurrent measurements were also taken before and after annealing the devices at 100 ^{0}C in air. The annealed devices showed roughly twice the J_{SC} compared to non-annealed devices. The average mobility of the device was estimated from the J-V characteristics. The annealed devices were found to have an average hole-mobility of 1.1×10^{-7} cm^2/Vs, while for annealed devices the average mobility more than twice as high at 2.7×10^{-7} cm^2/Vs. Therefore the higher mobility could be responsible for the higher J_{SC} seen in the annealed device.

The optimal device showed a J_{SC} of about 0.4 mAcm^{-2}, a fill factor of 0.42 and an open circuit voltage of 1.1 V under simulated AM1.5 illumination (100 mWcm^{-2}, 1 sun). The corresponding power conversion efficiency of the device under 1 sun is 0.18 %. This is the highest efficiency value reported under AM 1.5 (100 mw/cm^{-2}) conditions for this class of photovoltaic device to date. However, the efficiency is much less than that of the best polymer / fullerene photovoltaic devices.

The authors observed an improvement of device with age, which may be due to improvement of interfacial contacts. It has also been reported[34,79] that the contact between polymer and gold can improves with aging and temperature.

1.8.7 Polymer / TiO_2 devices with high hole-mobility polymer

It is expected that the performance of polymer / TiO_2 photovoltaic devices can be improved by using higher hole-mobility materials with reasonable light-harvesting properties. Higher mobilities help the dissociated holes to move quickly, which reduces

current loss due to recombination. Table 1.2 shows the reported time of flight hole-mobility values of some polymers, which have been used for TiO_2 / polymer photovoltaic devices in the literature. We would expect better device performance for devices consisting of TiO_2 and either PA-PPV or P3HT polymer, as these have the higher mobilities. Both of these polymers have been studied in combination with TiO_2.

Table 1.2 *Mobility values of the hole-conducting polymers used in TiO_2/polymer combination.*

Material	Mobility @ electric field (cm^2/Vs) (V/cm)		Type of transport	Reference
MEH-PPV	1.0×10^{-6}	2.0×10^5	Dispersive	[80]
MDMO-PPV	2.0×10^{-6}	2.5×10^5	Dispersive	[81]
PPV	1.4×10^{-5}	6.0×10^4	Dispersive	[82]
Spiro-MeOTAD	2.6×10^{-4}	2.6×10^5	Non-dispersive	[83]
BFB	3.0×10^{-4}	2.5×10^5	Highly dispersive	[84]
P3HT	3.0×10^{-4}	2.5×10^5	Dispersive	[85,86]
P3BT	1.5×10^{-3}	6.0×10^4	Dispersive	[87]
PA-PPV	4.0×10^{-3}	4.0×10^4	Non-dispersive	[88]

Carter's group[22] prepared an efficient device consisting of TiO_2 and PA-PPV polymer (IP = 5.3 eV). Anatase dense TiO_2 films of thickness in the range 50 to 100 nm were prepared by spin coating a solution of $Ti(OCH_2CH_3)_4$ and ethyl alcohol, which also contains water and hydrochloric acid. The resultant films were sintered at 450 ^{0}C for 30 minutes to form thin films of anatase TiO_2. Polymer films of 80 -120 nm were deposited on top of the TiO_2 layer by spin coating the PA-PPV / p-xylene solution before depositing the top Au electrode. The device showed a peak quantum efficiency of 25 % and monochromatic power conversion efficiency of 3.9 % at a wavelength of 435 nm. This was the highest reported value for TiO_2 / polymer solar cells under monochromatic conditions. However, the power conversion efficiency of TiO_2 / PA-PPV device under solar simulator was less than TiO_2 / MEH-PPV device of 0.18 %[16]. This is probability due to the blue-shifted spectral absorbance of PA-PPV. The development of efficient TiO_2 / polymer device will require polymer absorption further into the visible. This results support the fact that good EQE and power conversion efficiency values under monochromatic condition, do not guarantee good photovoltaic energy conversion under AM 1.5 illumination[38]. It is essential to measure power

conversion efficiency of solar cells under standard conditions (AM1.5, 100 $mWcm^{-2}$) as well for comparison of different solar cells.

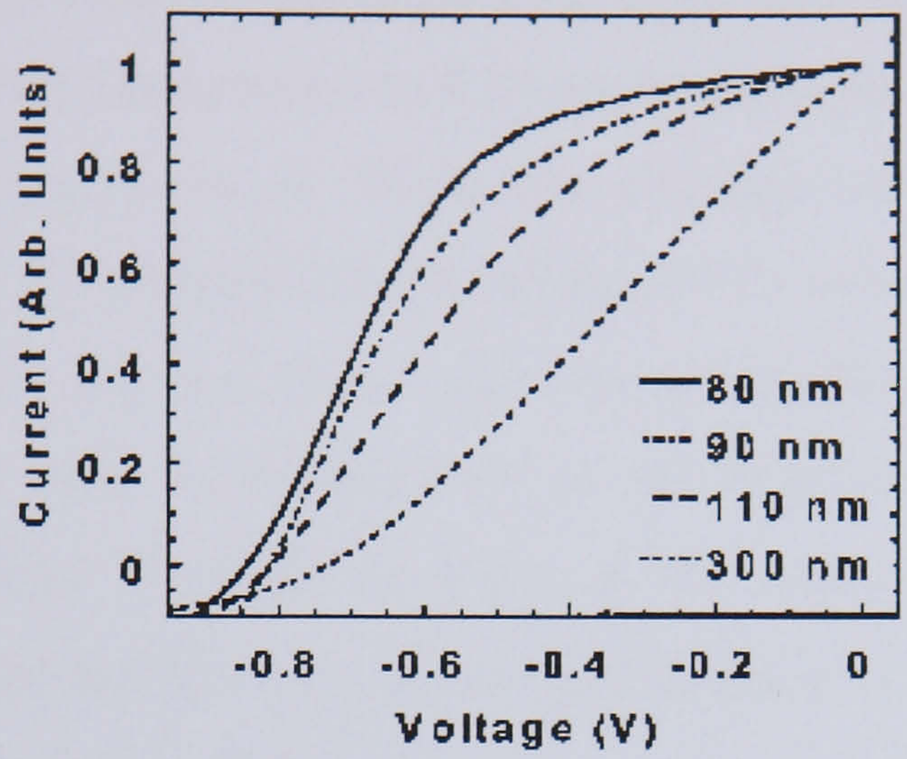


Figure 1.12 [22] N*ormalised photocurrent versus applied bias for the ITO / TiO2 /PA-PPV / Au device with different polymer thickness. We note that the photocurrent starts to fall off before the open circuit voltage.*

Figure 1.12 shows the normalised photocurrent versus the applied bias of the ITO / TiO_2 / PA-PPV / Au with different polymer layer thicknesses. We note that the photocurrent falls off around the open circuit voltage and the fill factor improves with decreasing polymer thickness, as noted in the Figure 1.11.

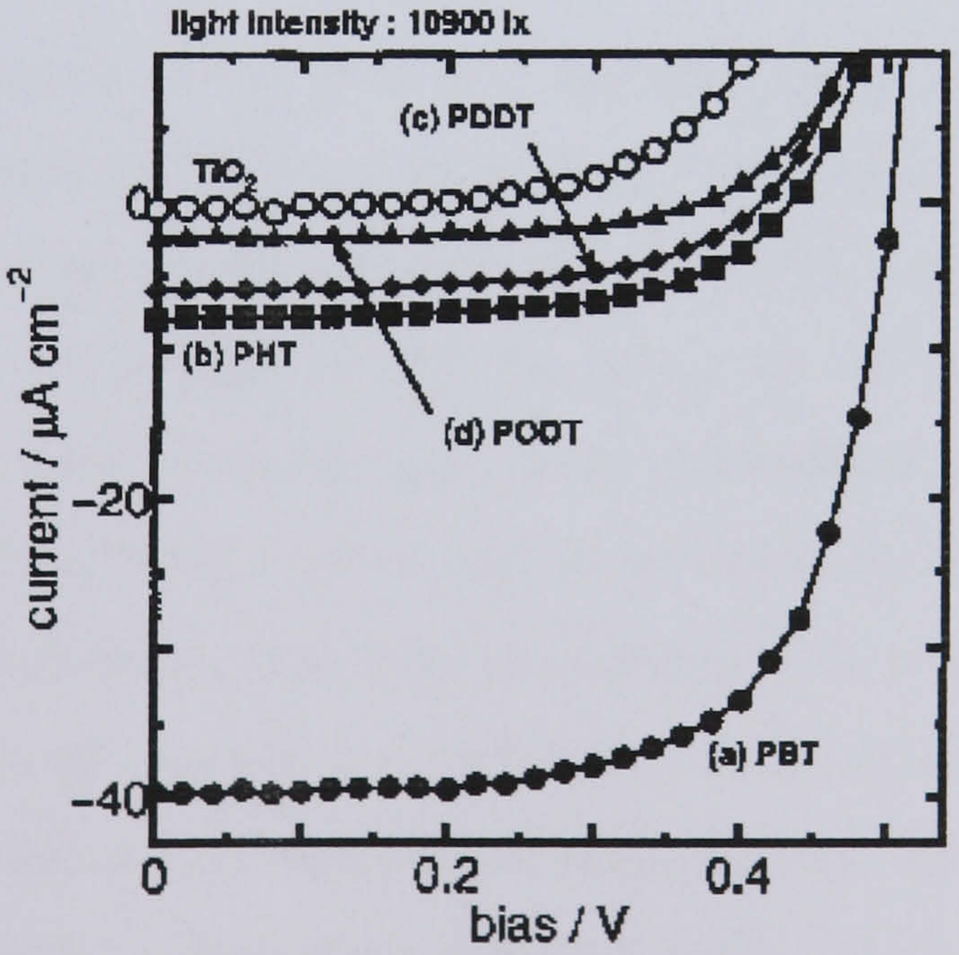


Figure 1.13 [17] *J-V characteristics of devices of poly(3-alkylthiophene) (PAT) polymer (PATs, alkyl= butyl, hexyl, dodecyl and octadecyl) and TiO_2under the light irradiation at 10900 lx (≈ 50 $mWcm^{-2}$).*

Pandey and co-workers[17] focussed on quasi-solid state cells based on high hole mobility polymers, poly(3-alkylthiophene)s, (PATs, alkyl= butyl, hexyl, dodecyl and

octadecyl) and TiO_2 using a polymer gel. TiO_2 layers of thickness 100-200nm were electrochemically deposited on FTO (F doped SnO_2) glass. Thereafter, TiO_2 colloids (P25) were pasted onto the deposited TiO_2 layer followed by sintering at 450 ^{0}C for 1hr. The substrates were immersed into 0.25 wt. % chloroform solution of HT-PAT and kept for 12 hr at room temperature. The device structure was FTO / TiO_2 / TiO_2 / HT-PAT / PGE / Pt, where the polymer gel electrolyte (PGE) contained I_2 and LiI. The EQE of the device is found to increase drastically with decreasing alkyl chain length. Figure 1.13 shows that the device containing poly (3-butylthiophene) offers the best short circuit current of 40 μAcm^{-2} and high fill factor of 0.68 under light radiation at 10900 lx *(≈ 50 $mWcm^{-2}$).* It is appeared that the device performance of P3HT was limited by poor pore filling due to longer side length.

In 2001, Sariciftci and co-workers[89] reported better performance of TiO_2 / P3OT device than obtained in Ref. [17] using a Au electrode. They prepared thicker (2 μm) TiO_2 porous layer by doctor blading a colloidal paste (particle size ~13 nm) from Solaronix Co on to an ITO substrate. The P3OT polymer layer (100-200 nm) was spin coated before depositing the Au top electrode. The device showed a showed a short-circuit current density of about 230 μAcm^{-2} at 80 $mWcm^{-2}$ However, the short circuit current density is rather small. This may be due to poor sensitisation of TiO_2 by P3OT polymer.

In 2003, Savenije and co-workers[90] reported charge separation studies in TiO_2 / P3HT structures with different polymer layer thicknesses using the flash-photolysis time-resolved microwave conductivity technique (FP-TRMC). For irradiation from the polymer side at a wavelength of 540 nm (close to the absorption maximum of the polymer), the efficiency of charge separation per incident photon (IPCSE) showed a maximum value of 0.8 % for a spin coated layer thickness of 10 nm and then decreased strongly with increasing polymer layer thicknesses. For irradiation from the TiO_2 side, the IPCSE is increased over the first 10 nm to a value close to the maximum found for polymer side irradiation, and decreased only slightly for further increase in layer thickness. This result is consistent with the value of the exciton diffusion length reported for polythiophene polymer (~ 5 nm)[26]. The authors further reported that the IPCSE decreased at high light intensities. This may be attributed to the occurrence of exciton-exciton annihilation within the polymer layer. Figure 1.14 shows the conductivity transient of TiO_2 / polymer compared to single layers of TiO_2 and polymer after photoexcitation at 540 nm from polymer side. The figure clearly shows that the

photoconductivity of the bi-layer is significantly larger than that of either of single layers alone, particularly at longer time. This provides direct evidence for the sensitisation of TiO_2 by the polymer and for long lived charge separation.

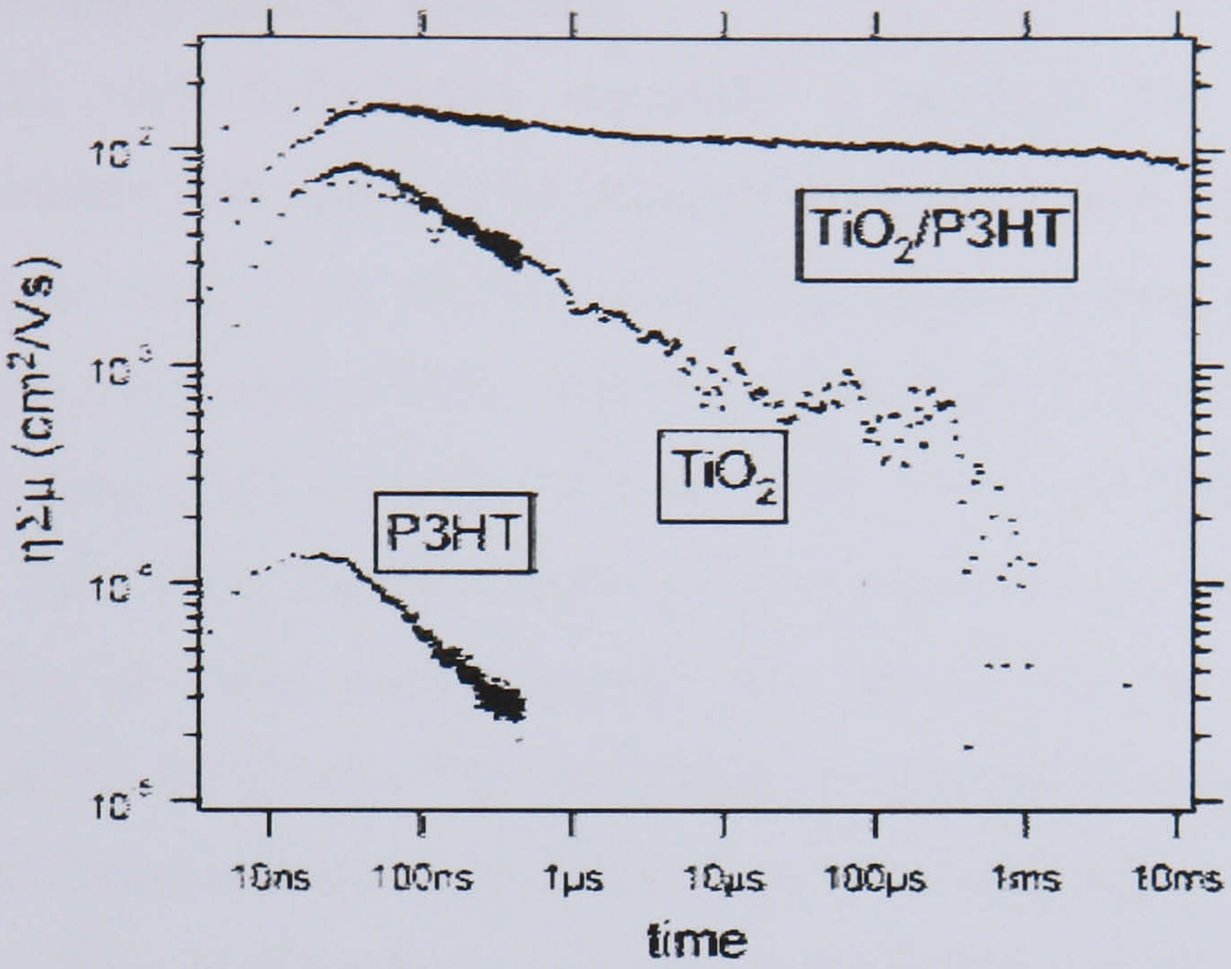


Figure 1.14 [90] *Transient changes in the conductivity on polymer-side flash-photolysis at 540 nm of a TiO_2 / P3HT bi-layer and layers of TiO_2 and P3HT alone.*

The advantage of this technique is that the intrinsic properties of the photoactive layer are measured in the absence of electrodes. The IPCSE values may be taken to be an upper limit for the IPCE. The mobility of the charge carriers in the active layer can also be estimated but the values are always greater than TOF values, because the method is sampling the most mobile charge carriers. Therefore, only an upper limit to the mobility in the active layer can be measured using this technique[91].

McGehee and co-workers[69] reported that poly(3-hexyl thiophene) (P3HT) appears to resist infiltration into mesoporous TiO_2 through the coiling of the polymer chains. However, infiltration of the polymer in to the mesoporous TiO_2 can be improved with increasing annealing temperature of the polymer film after deposition on to the TiO_2. The same authors recently reported[70] an efficient FTO / TiO_2 / P3HT / Ag photovoltaic cell which shows EQE of 10 % and 1.5 % power conversion efficiency under monochromatic 514 nm light. The TiO_2 films (pore size ~ 10 nm) made by dip coating a titanium ethoxide–block copolymer precursor mixture on a FTO substrate and followed by calcination. Photovoltaic cells were by infiltrating a 40-nm-P3HT layer into a 100-nm-mesoporous TiO_2 layer for 1 min at 200 °C. A spin coated P3HT overlayer and Ag top contact were applied on top of the TiO_2 film following infiltration. The results demonstrate that the P3HT chains are not infiltrated too deeply into the TiO_2 and

suggest that optimization of this type of photovoltaic device will require a change in polymer chain morphology to assist insertion into the pores of the TiO_2.

1.8.8 Polymer sensitisation with TiO_2

In 2002, Sariciftci's group reported[92] a spectroscopic (optical absorption, photoluminescence and steady state photo-induced absorption spectroscopy) study of composites made with a new polymer poly [bis(3-decyl-2-thienyl)-dithieno(3,2-b:2',3'-d) thiophene-4,4-dioxide], PTOX, and nanocrystalline TiO_2. For comparison, they studied other conjugated polymers such as P3OT, P3BT and MDMO-PPV with TiO_2. Nanoporous TiO_2 films were prepared on glass substrates by doctor blading a paste from Solaronix (colloidal anatase particle size approx. 13 nm) and the layers were sintered at 450 °C for 30 min. The composites were prepared by dipping the substrates into polymer solutions made with different solvents (0.2 mg/ml) for periods ranging from 5 h to 2 days, rinsing them in the solvent and then drying them under vacuum. Optical absorption spectra indicate that the PTOX polymer is well adsorbed into nanoporous TiO_2 films compared to other polymers. The remarkable compatibility with TiO_2 of PTOX, with respect to other conjugated polymers, makes this polymer a promising candidate for hybrid organic / inorganic photovoltaic cells. The authors propose that the reason for better adsorption of PTOX on TiO_2 may be due to lower molecular weight and/or better interaction more polar S,S-dioxide groups of the polymer. These features should allow the staining limitations (complete filling of the network, adhesion onto TiO_2) to be overcome.

1.8.9 Bulk heterojunction of TiO_2 / polymer using precursor method

In 2003, Janssen's group[20] reported a new and simple procedure for fabricating bulk heterojunction TiO_2 / polymer device. The active layer is prepared by in-situ conversion of a titanium isopropoxide precursor co-deposited from solution with a conjugated polymer. Thus, bulk-heterojunctions of MDMO-PPV and TiO_2 were made by spin casting a solution of MDMO-PPV and $Ti(OC_3H_7)_4$ followed by conversion at room temperature in the dark, in air overnight. The active layer, a MDMO-PPV:TiO_2 mixture, is sandwiched between ITO / PEDOT:PSS and LiF / Al an electrodes like polymer / fullerene system. Photoluminescence decreases with increasing amount of TiO_2 and is quenched by a factor of 19 in the 50 (v/v) % blend. Upon decreasing the fraction of TiO_2 to 20 (v/v) %, the peak quantum efficiency increases to 11 %. The

device shows J_{SC} = 0.6 $mAcm^{-2}$, V_{OC} = 0.52 V and FF = 0.42 under illumination with a simple halogen lamp, set at roughly 0.7 sun intensity. The corresponding overall efficiency of this device is 0.19 % under 0.7 sun (70 $mWcm^{-2}$). This alternative approach for preparing bulk heterojunction hybrid polymer / TiO_2 device, *in situ* growth of the TiO_2 network from an organic precursor, is promising but appears to be limited by poor electron transport in the amorphous TiO_2.

Although TiO_2 / polymer combinations have been widely investigated for solar cell application, there are very few studies on combinations of polymers with different metal oxides in the literature[77,93,94].

Recently, however, Janssen's group[95] reported an efficient ITO / PEDOT:PSS / MDMO-PPV:ZnO / Al device, which showed external quantum efficiency of 40 % at the absorption maximum of the MDMO-PPV polymer. The group was successfully able to blend ZnO particles (~5 nm) and MDMO-PPV polymer in polar solvent mixture. The efficient performance is attributed to increased interfacial area due to very small size of ZnO nanoparticles (~ 5 nm) compared TiO_2 colloidals (~15-30 nm).

Anderson and co-workers[93] showed that photoinduced electron transfer from MEH-PPV polymer to SnO_2 nanoporous thin film occurs on an 800 fs time scale. However, the injection rate for SnO_2 is slower than TiO_2 (<100 fs) despite a lower-lying conduction band. Nevertheless, Savenije and co-workers[94] more recently demonstrated that the charge separation efficiency per incident photon in SnO_2 / low band gap oligomer combinations more than a factor of 30 higher than in TiO_2 / oligomer combinations using TRMC. The SnO_2 / low band gap oligomer combination is also another promising candidate for the application in photovoltaic devices.

1.9 Summary

Despite the effective combination of polymer and TiO_2 components, the highest external quantum efficiency (25 % at 435 nm) and power conversion efficiencies (< 0.2 % under 1 sun) are still low compared to the best values for other polymer-based solar cells. The difference is largely in the value of the short circuit current density, J_{SC} (see Table 1.3), whilst the values of open circuit voltage, V_{OC}, are similar to the best published data for organic solar cells. The reduced J_{SC} may be due to a number of factors: small optical depth, poor sensitization of the oxide film, large pore size / nanostructure scale compared to the exciton diffusion length, poor charge transport, fast recombination, or imperfect interfaces.

Table 1.3 *Performance of best reported PCBM / polymer devices compare with reported hybrid TiO_2/polymer devices under AM 1.5 conditions.*

TiO_2/Polymer	J_{SC} ($mAcm^{-2}$)	V_{OC} (V)	FF	**η (%)**	Reference
MEH-PPV	0.40	1.10	0.42	**0.18**	[16]
MDMO-PPV	0.60	0.51	0.42	**0.19***	[20]
P3HT	0.31	0.49	0.40	**0.06**	[73]
PCBM/polymer					
MEH-PPV	8.40	0.87	0.40	**2.9**	[96]
MDMO-PPV	5.25	0.83	0.62	**3.3***	[61]
P3HT	8.50	0.55	0.60	**3.5***	[97]

* Performance under 70-80 $mWcm^{-2}$, while others under 100 $mWcm^{-2}$.

In this thesis, we first report the optimisation of device design using a fluorene bi-thiophene polymer in contact with TiO_2 and then optimise the device performance by using wide range of polymers with different optoelectronic properties and porous metal oxides with different microstructures.

Chapter 2

Materials and Experimental Techniques

This chapter describes the details of the materials and experimental techniques, including electrical characterisation, UV-VIS optical absorption spectroscopy, transient absorption spectroscopy, cyclic-voltammetry, Kelvin probe, time of flight and electroabsorption spectroscopy, that have been used in this work.

2.1 Materials

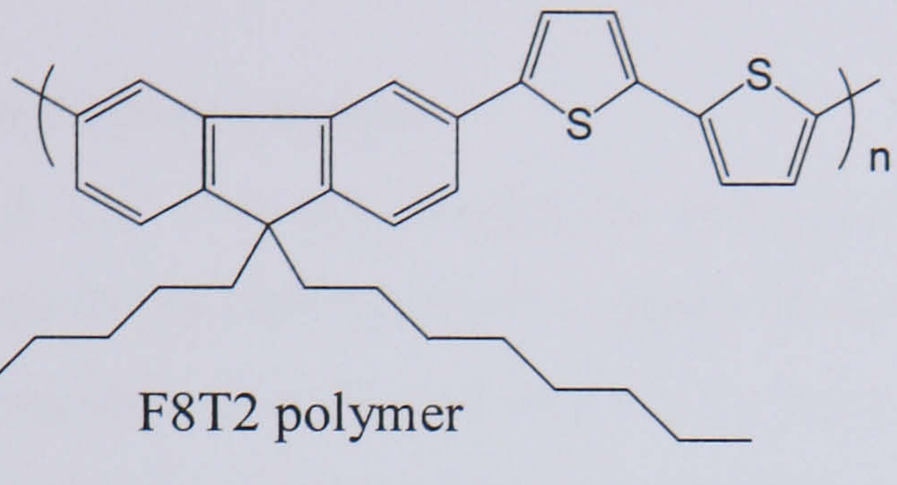
Several nanocrystalline metal oxides (ZnO, SnO_2, TiO_2), polymers and co-polymers based on conjugated triaylamine, thiophene and phenylene vinylene units have been used in this work.

2.1.1 Thiophene polymers

Two thiophene polymers, were used as hole transporting materials, Poly(9,9-dioctylfluorene-co-bithiophene) F8T2 and regioregular Poly(3-hexyl thiophene) P3HT polymers. The chemical structures of both polymers are shown in Figure 2.1. Field effect transistors (FETs) have been made with these polymers[98,99]. The hole mobility of spin coated F8T2 film using FET structure is 1.5×10^{-3} cm^2/Vs[100] and it can be enhanced to 0.01 - 0.02 cm^2/Vs by aligning the F8T2 polymer chain parallel to the direction of the transport[98]. This polymer has a high ionization potential of 5.5 eV[101] and possesses a liquid crystalline phase above 265 ^0C[98]. This polymer was synthesized by the Dow Chemical Company, while the other thiophene polymer, regioregular P3HT, was

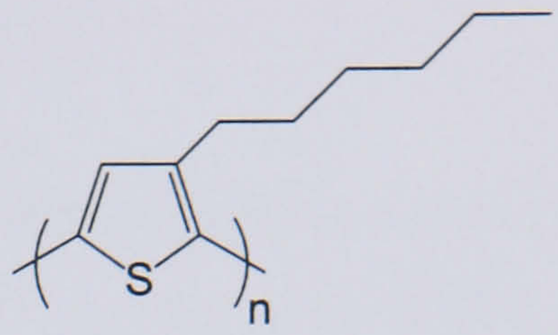
synthesized by Merck NBSC Ltd. Both polymers had been carefully purified to remove catalyst residues and other inorganic contaminants.

(a)



F8T2 polymer

(b)

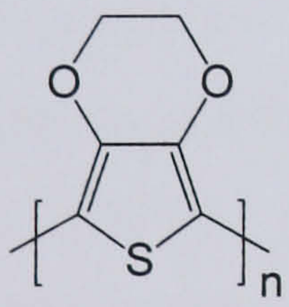


P3HT polymer

Figure 2.1 *Chemical structures of (a) poly(9,9-dioctylfluorene-co-bithiophene) (F8T2) polymer and (b) poly(3-hexylthiophene) (P3HT) polymer.*

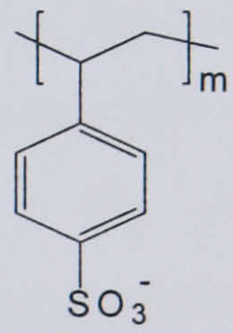
The regioregularity, defined as the percentage of stereoregular head-to-tail (HT) attachment of hexyl chains to the 3-position of the thiophene rings[102], of the P3HT polymer used in this work is greater than 96 %. P3HT absorbs further into the red compared to F8T2 and the optical absorption feature of these polymers will be discussed in the next chapters. The highest FET hole-mobilities, of 0.05 -0.1 cm^2/Vs, have been reported for a P3HT sample with 96 % regioregularity[102]. However, the TOF mobility value of the P3HT polymer (96 % regioregularity) is lower, at ~ 10^{-4} cm^2/Vs[85]. More recently, our group[86] found balanced ambipolar transport in P3HT with a comparable electron mobility of ~ 10^{-4} cm^2 V^{-1} s^{-1} at electric fields ≥ 10^5 V/cm.

(a)



PEDOT

(b)



PSS^-

Figure 2.2 *Chemical structures of (a) poly(3,4-ethylenedioxythiophene) (PEDOT) polymer and (b) poly(sterenesulfonate) (PSS) polymer*

In some cases, a highly conductive thiophene based polymer, poly (sterenesulfonate) (PSS) doped poly (3,4-ethylenedioxythiophene) (PEDOT), was used as hole-collecting electrode. The chemical structures of PEDOT and PSS are shown in Figure 2.2 (a) & (b). The doped polymer was purchased from BAYTRON-BAYER AG, Business Group Basic & Fine Chemicals Company and is optically transparent in

visible and has high electrical conductivity and work function ($\Phi \sim 5.2$ eV[37,60]) when deposited on ITO.

2.1.2 Triarylamine polymer

A high hole mobility triaylamine polymer, poly(9,9-dioctylfluorene-*co*-bis-*N,N'*-(4-butyl phenyl)-bis-*N,N'*-phenyl-1,4-phenylenediamine) (PFB), was also used in this study. This material was also synthesized by the Dow Chemical Company and carefully purified to remove catalyst residues and other inorganic contaminants. However the PFB polymer absorbs less strongly in the visible than F8T2. It has a lower ionization potential I_P (5.1 eV) compared to 5.5 eV for F8T2. The chemical structure of PFB polymer is shown in Figure 2.3.

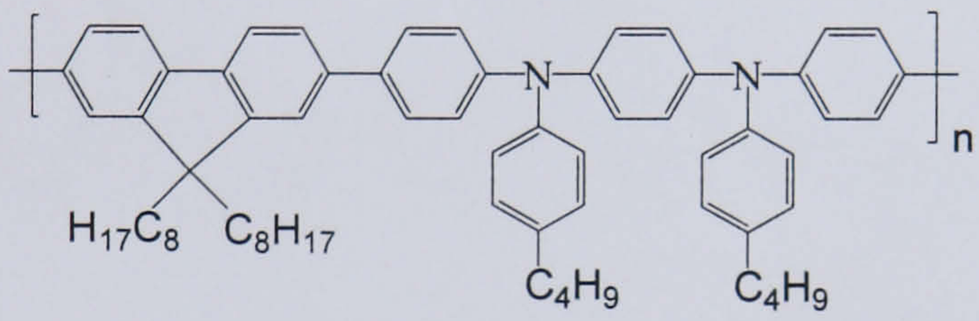


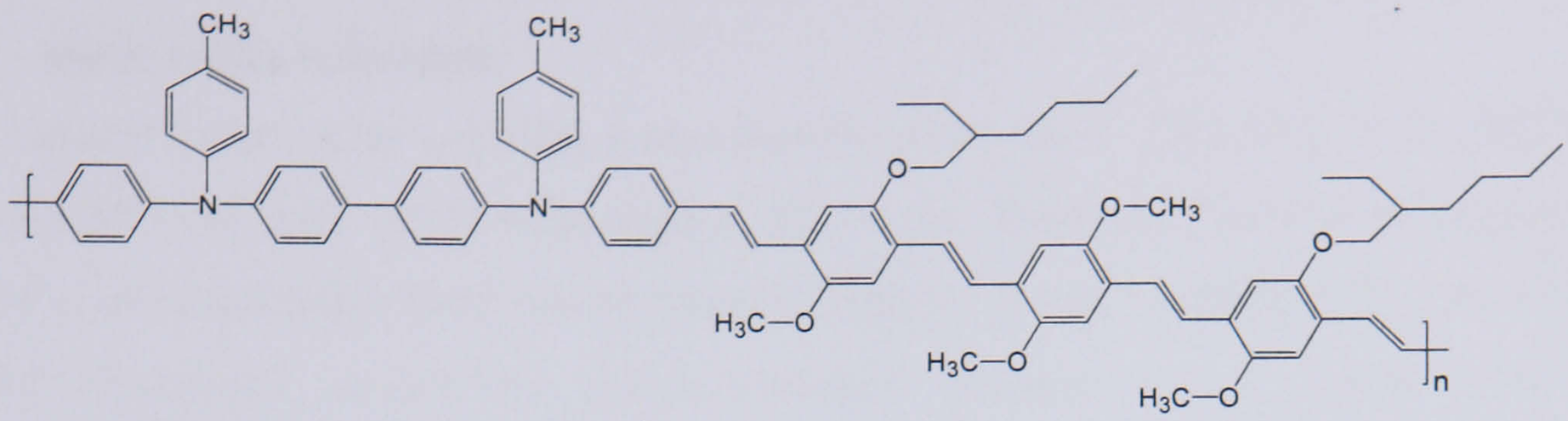
Figure 2.3 *Chemical structure of poly (9,9-dioctylfluorene-co-bis-N,N'-(4-butyl phenyl)-bis-N,N'-phenyl-1,4-phenylenediamine) (PFB).*

2.1.3 PPV polymers

Three PPV polymers were also used as hole-transporters in this work and the names and the structures[103-105] of the polymers are shown in Figure 2.4 (a), (b), and (c). All the polymers have MEH-PPV subunits and the first two contain TPD groups. TPD (4M)-MEH-M3EH-PPV polymer is a statistical co-polymer, while the others are alternating copolymers. Average molar mass of TPD (4M)-MEH-M3EH-PPV, TPD(4M)-MEH-PPV and MEH-DOO-PPV polymer are 35700 g/mol (29 repeated units), 53100 g/mol (66 repeated units) and 34300 g/mol (55 repeated units) respectively[105].

These polymers were synthesized by the group of Prof. H. H. Horhold at the University of Friedrich Schiller, Germany using HORNER– type polycondensation. The MEH-DOO-PPV copolymer has broad optical absorption in the visible spectrum peaking at about 502 nm, while TPD containing polymers absorb less strongly in the visible but have better hole-transport properties than MEH-DOO-PPV. The optical absorption properties of these polymers will be discussed in detailed in the chapter 4.

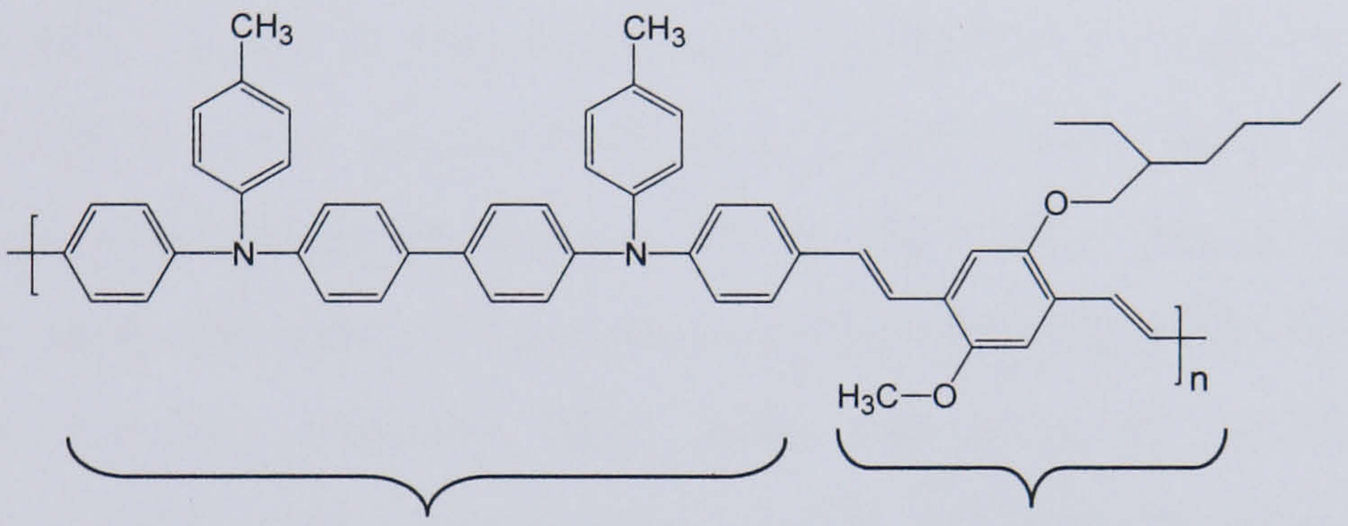
(a)



TPD MEH-PPV M3EH-PPV

TPD(4M)-MEH-M3EH-PPV

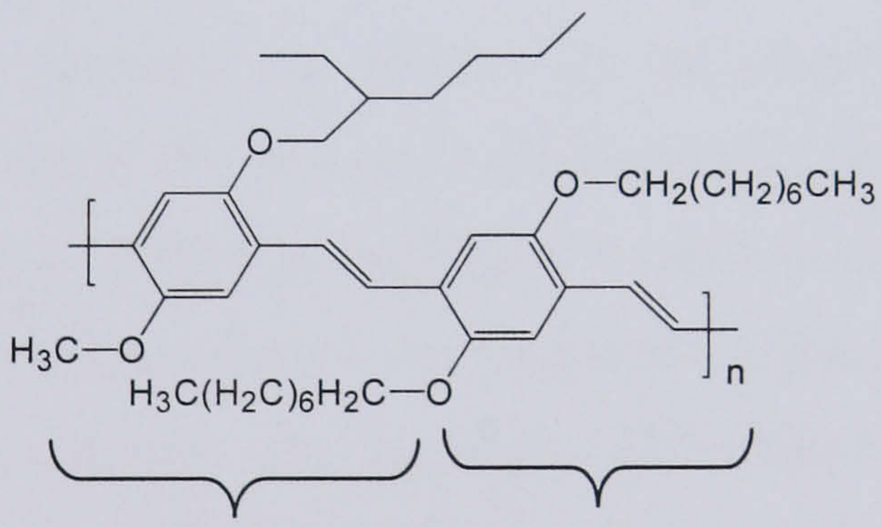
(b)



TPD MEH-PPV

TPD(4M)-MEH-PPV

(c)



MEH-PPV DOO

MEH-DOO-PPV

Figure 2.4 *Chemical structures*[103-105] *of (a) poly[(1,4-phenylene-(4-methyl phenyl)amino-4,4'-diphenylene-(4-methylphenyl)amino-1,4-phenylene-ethenylene-2-methoxy-5-(2-ethylexyloxy)-1,4-phenylene-ethenylene)-co-(2,5-dimethoxy-1,4-phenylene-ethenylene-2-methoxy-5-(2-ethyl hexyloxy)-1,4-phenylene-ethenylene)] TPD(4M)-MEH-M3EH-PPV terpolymer (b) poly[(4-methylphenyl) amino-4,4'-diphenylene-(4-methylphenyl)amino-1,4-phenylene-ethenylene-2-methoxy-5-(2-ethylhexyloxy)-1,4-phenylene-ethenylene-1,4-phenylene] TPD(4M)-MEH-PPV copolymer (c) poly[2-methoxy-5-(2-ethylhexyloxy)-1,4-phenylene-ethenylene-2,5-dioctyloxy-1,4-phenylene-ethenylene] MEH-DOO-PPV copolymer*

2.1.4 Metal oxide colloidals

Several metal oxide colloidal pastes namely ZnO, SnO_2, TiO_2 (IC), TiO_2 (ECN), TiO_2 (ECN*) and TiO_2 (P25) were used in this thesis. Scanning Electron Microscopic images of all metal oxide films can be found in Figure 5.1 and 5.8 (chapter 5). The ECN and ECN*(scattered paste) TiO_2 pastes, colloidals dispersed in an organic mixture (terpineol/ethylcellulose), were synthesised at the Energy Centre for Netherlands (ECN) as described in the Ref. [106], while other pastes, colloidals dispersed in aqueous solution, were synthesised here, Imperial College (IC). The aqueous TiO_2 (IC) paste was prepared as described in Ref. [56] with an assistance of Mr. Alex Green, using chemicals purchased from Sigma-Aldrich. The paste was then mixed with polyethylene glycol (PEG) MW 20,000 so that the amount of PEG in the titanium dioxide paste corresponds to 50 % of the weight of titanium dioxide in the paste. (This addition of PEG increases the porosity of the titanium dioxide film). The mixture was slowly stirred for 5 hours at room temperature to ensure complete blending of the PEG and titanium dioxide paste. Similarly, aqueous SnO_2 paste was prepared by Mr. Alex Green. Aqueous ZnO and P25 pastes were prepared by Dr. Ana Peiro as described in the Ref. [107] and Ref. [108] respectively.

2.2 Sample fabrication

Samples were prepared on Indium Tin Oxide (ITO) coated glass substrates, Fluorine doped Tin Oxide (FTO) coated glass substrate or spectrosil B substrate which were first cleaned by ultrasonic agitation in acetone and isopropanol. For cyclic voltammetry and optical absorption measurements, polymer samples were prepared by spin coating on FTO substrate and spectrosil / ITO respectively. Single layer (polymer) and bi-layer (polymer and dense TiO_2) samples with different layer thicknesses prepared on ITO for exciton diffusion length measurements. Samples for time-of-flight measurements were also prepared on ITO and the top contact was aluminum (~50 nm). The thickness of the polymer film for TOF measurement was typically between 1 and 1.5 μm.

For transient absorption spectroscopy measurements, four layers were prepared on top of the ITO substrate (~1 cm^2, 10-15 Ω / square), namely a dense TiO_2 'Hole Blocking' layer (HBL), a porous metal oxide layer, a dip-coated polymer layer and a spin-coated polymer layer.

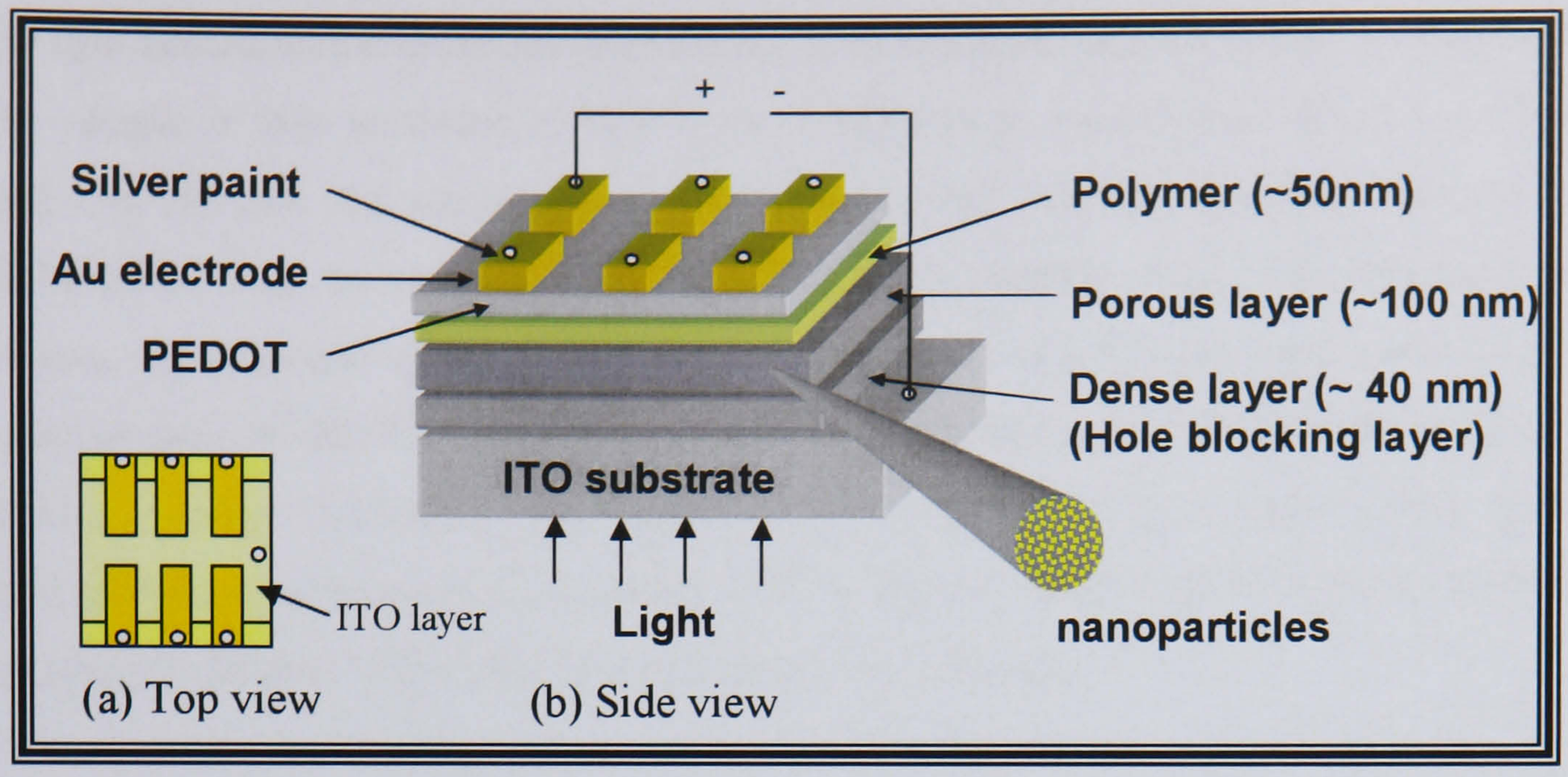


Figure 2.5 *A schematic representation of multilayer device structure view from the (a) top and (b) side.*

For electrical measurements, Au top contact was deposited on the polymer. In some devices, a PEDOT:PSS layer was deposited on top of the polymer layer before depositing the metal contact. Figure 2.5 shows a schematic representation of multilayer device structure view from the top and side. There were six devices per substrate to check reproducibility and the area each active device was about 4.2 mm^2.

The porous metal oxide layer is required to increase the interfacial area for charge separation[109]. The dip coating step is necessary to improve pore filling. The final, spin coated polymer layer is required to fill the pores, thus increasing optical density and improving film uniformity[109,110]. The ITO substrate was first covered with a thin dense TiO_2 layer using a spray pyrolysis technique[111]. A thin porous metal oxide layer (100 nm-200 nm) was deposited by spin-coating the diluted aqueous metal oxide paste or organic TiO_2 paste (dissolved in tetrahydrofuran, THF) onto the dense TiO_2 layer. The films were then sintered at 450 ^{0}C for 30 minutes in air. The dip-coated layer was prepared on the porous metal oxide layer by immersing the metal oxide electrode in a solution of polymer in C_6H_5Cl (~2 mg/ml) at 60-120 ^{0}C overnight. The dip-coated film was then "wiped" by a quick blow with dry nitrogen gas (oxygen free) and heated at about 50 ^{0}C in air. A 50 nm polymer layer was then deposited on the substrate by spin coating from a polymer solution in C_6H_5Cl (10 mg/ml) at 2000 rpm.

The deposition of PEDOT:PSS on top of the polymer is somewhat tricky as we normally observe less adherence of PEDOT:PSS with polymer if we do not adopt the following procedures: The PEDOT:PSS solution is first untrasonicated for 10 minutes and then heated for 5 minutes at 90 ^{0}C. The solution is then filtered with a 0.45 μm filter

and spin coated on the dried semiconducting polymer layer in a water free environment. The sample is then annealed at 100 ^{0}C for 5 minutes in a glove box which was filled with dry N_2 gas. Au electrodes are deposited either onto the polymer film or the PEDOT:PSS film by thermal evaporation though a shadow mask. The Au contacted devices are annealed again at 100 ^{0}C for 5 minutes in a N_2 gas environment. It is essential that the PEDOT:PSS layer should be annealed for not more than 15 minutes because a longer annealing time degrades the layer[112]. The thicknesses of the layers were as follows unless stated otherwise: HBL (~40 nm) / porous metal oxide (~100 nm) / polymer (~50 nm) / PEDOT:PSS (~50 nm) / Au (~60 nm).

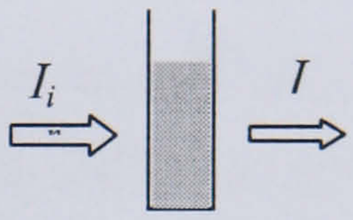
2.3 Ultraviolet and Visible (UV-VIS) Optical Absorption Spectroscopy

Ultraviolet and visible (UV-VIS) optical absorption spectroscopy was used to study the absorption of the polymers, active layers and other materials. UV-VIS absorption spectroscopy is the measurement of the attenuation of a beam of light after it passes through a sample.

Experimental measurements are usually made in terms of transmittance (T), which is defined as:

$$T = \frac{I}{I_{in}} \tag{2.1}$$

where I is the light intensity after it passes through the sample and I_{in} is the initial light intensity



The Beer-Lambert law relates the absorption of light to the properties of the material the light is travelling through assuming interference can be neglected. The absorbance of a solution, Optical Density (OD), can be written as

$$OD = \varepsilon\, c\, l \tag{2.2}$$

where ε (litres/mole-cm) is called the molar extinction coefficient of the solute at the wavelength of measurement, c (moles/litre) is the concentration of the solute, and l (cm) is the optical path length. The relation between OD and T is:

$$OD = -\log_{10} T = -\log_{10}\left(\frac{I}{I_{in}}\right) \tag{2.3}$$

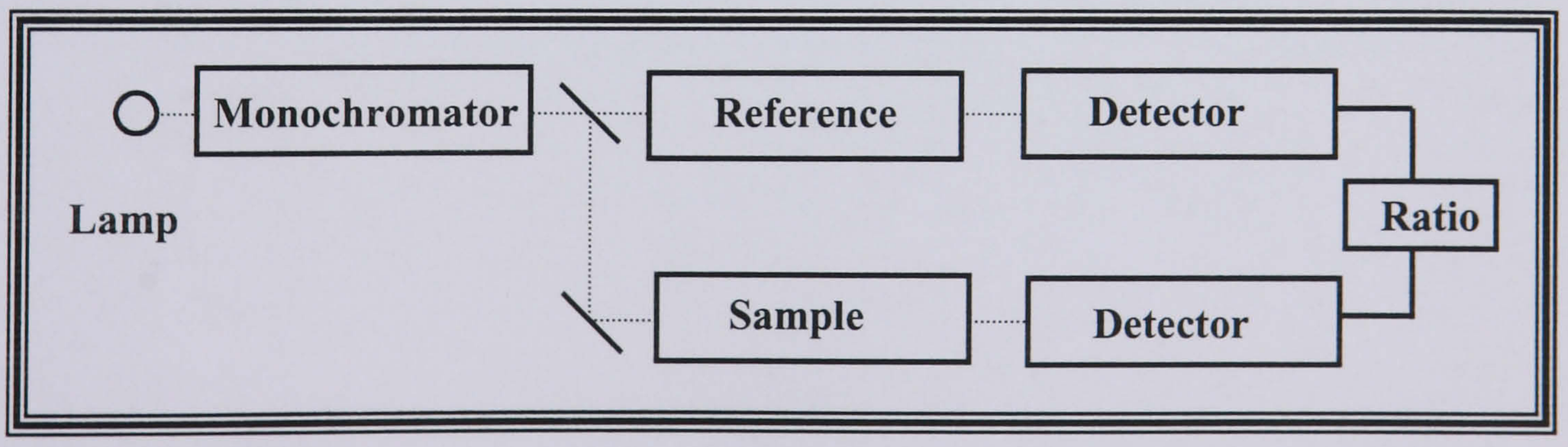


Figure 2.6 *Schematic diagram of a UV-VIS Optical absorption spectrophotometer*

The UV-VIS spectrometer is shown schematically in Figure 2.6. The double-beam design greatly simplifies finding absorbance of the solute by measuring the transmittance of the sample and reference (empty cuvette, bare ITO substrate or

BIBL. LONDIN.

spectrosil) simultaneously. Most spectrometers use a mirrored rotating chopper wheel to alternately direct the light beam through the sample and reference. The detection electronics or software program can then manipulate the measurements to give the absorbance as the wavelength scans to produce the spectrum of absorbance as a function of wavelength.

If the reflection and scattering of the sample is negligible, then absorption coefficient α can be related to T as follows:

$$T = \exp(-\alpha l) \qquad (2.4)$$

To find the absorption coefficient, α, which is clearly directly proportional to the concentration and the molar extinction coefficient from the definition of OD above[113].

$$\alpha = \left(\frac{OD}{l}\right) \ln(10) = \varepsilon c \ln 10 = 2.303\, \varepsilon c \qquad (2.5)$$

It is not possible to measure ODs greater than around 3.0 with the UV-VIS spectrometer.

Optical absorption spectra of both polymer film on spectrosil or ITO and of chemically doped polymer solution were obtained using a 'UNICAM' UV-VIS absorption spectrometer with 2 nm resolution. The concentration of the polymer in solvent and the size of the cuvette were ~ 10^{-5} mol/l and 4.5cm × 1cm × 1cm.

2.4 Transient absorption spectroscopy

Transient absorption spectroscopy is a technique used to gain information about the time-evolution of excited species created in a sample by photoexcitation. This technique has been extensively used with dye-sensitised electrodes to study the charge recombination kinetics. The experimental details will be presented after discussing the principle of the technique.

2.4.1 Principle

The experiment involves irradiation of a sample with a short intense pulse of light known as a "pump" pulse, and observing the resultant changes in the sample's optical density. The change in optical density may be determined by monitoring the transmission of a second, weaker, light pulse known as the "probe" pulse, which is delayed by a fixed time relative to the pump pulse[114] or may be continuous. Thus the experiment involves pumping the sample with a very short pulse of laser light and then, probing the excited states using a second pulse or continuous beam.

Measuring the transmitted intensity of the probe pulses tells us about the number of photo-induced states present. This number changes with time as photoinduced species decay to lower energy states.

The change in light intensity can be converted into an optical density (OD) change. According to the Beer-Lambert law, we can write the optical density as follows:

$$OD(\lambda, t) = \varepsilon(\lambda)\, c\, l = \log_{10}\left[\frac{I_{in}(\lambda)}{I(\lambda)}\right] \qquad (2.6)$$

where $I_{in}(\lambda)$ and $I(\lambda)$ are intensity of the incident and transmitted light of wavelength of λ, $\varepsilon(\lambda)$ is the extinction coefficient of the absorbing species at the probe wavelength λ, c is the concentration of absorbing species, and l is the path length of the sample.

The change in optical density (ΔOD) at a delay time t after excitation is

$$\Delta OD(\lambda, t) = OD_t(\lambda, t) - OD_0(\lambda, 0)$$

$$= \log_{10}\left[\frac{I_{in}(\lambda)}{I_t(\lambda,t)}\right] - \log_{10}\left[\frac{I_{in}(\lambda)}{I_0(\lambda,0)}\right]$$

$$\Delta OD(\lambda, t) = \log_{10}\left[\frac{I_0(\lambda,0)}{I_t(\lambda,t)}\right] \qquad (2.7)$$

where $OD_t(\lambda, t)$ and $I_t(\lambda,t)$ are the optical density and transmitted light intensity respectively at a delay time t after excitation, $OD_0(\lambda, t)$ and $I_0(\lambda,0)$ are the initial optical density and transmitted light without excitation of the sample.

The data collected by the oscilloscope was converted to units of ΔOD (λ, t). The change in optical density can be calculated by using the equation

$$\Delta OD\ (\lambda, t) = k \times \frac{V(t)}{V_0} \qquad (2.8)$$

where V(t) is the transient signal size which is proportional to the change in light intensity. V_0 is the dc voltage level, which is proportional to the intensity of the probe light. Equation 2.8 is obtained using a binomial expansion in the limit where the change in light intensity, and the resulting V(t), are small. The constant, k is independent of photodiode or probe wavelength and contains two factors[114]: a factor of (1/2.303) which comes from the logarithmic conversion and a second, amplifier specific factor. The amplifier specific factor of the apparatus we used is set to 1 and the factor k is therefore equal to1/2.303.

There may be different photo induced species present simultaneously in the photoexcited sample. Singlet excitons, triplet excitons, polarons, bi-polarons are all possible. Each one of these has own absorption spectrum. Thus, probe photons of different energies will be absorbed by the different species present. Transient absorption experiments generally consist of pumping with pulses in the blue part of the spectrum to photo excite the polymer. Probing at wavelength corresponding to maximum polaron absorption, this is normally near IR. It is therefore essential to know the absorption spectrum of the polymer and polaron absorption spectrum so that one can select suitable pump and probe wavelengths to observe the polaron.

2.4.2 Chemical doping

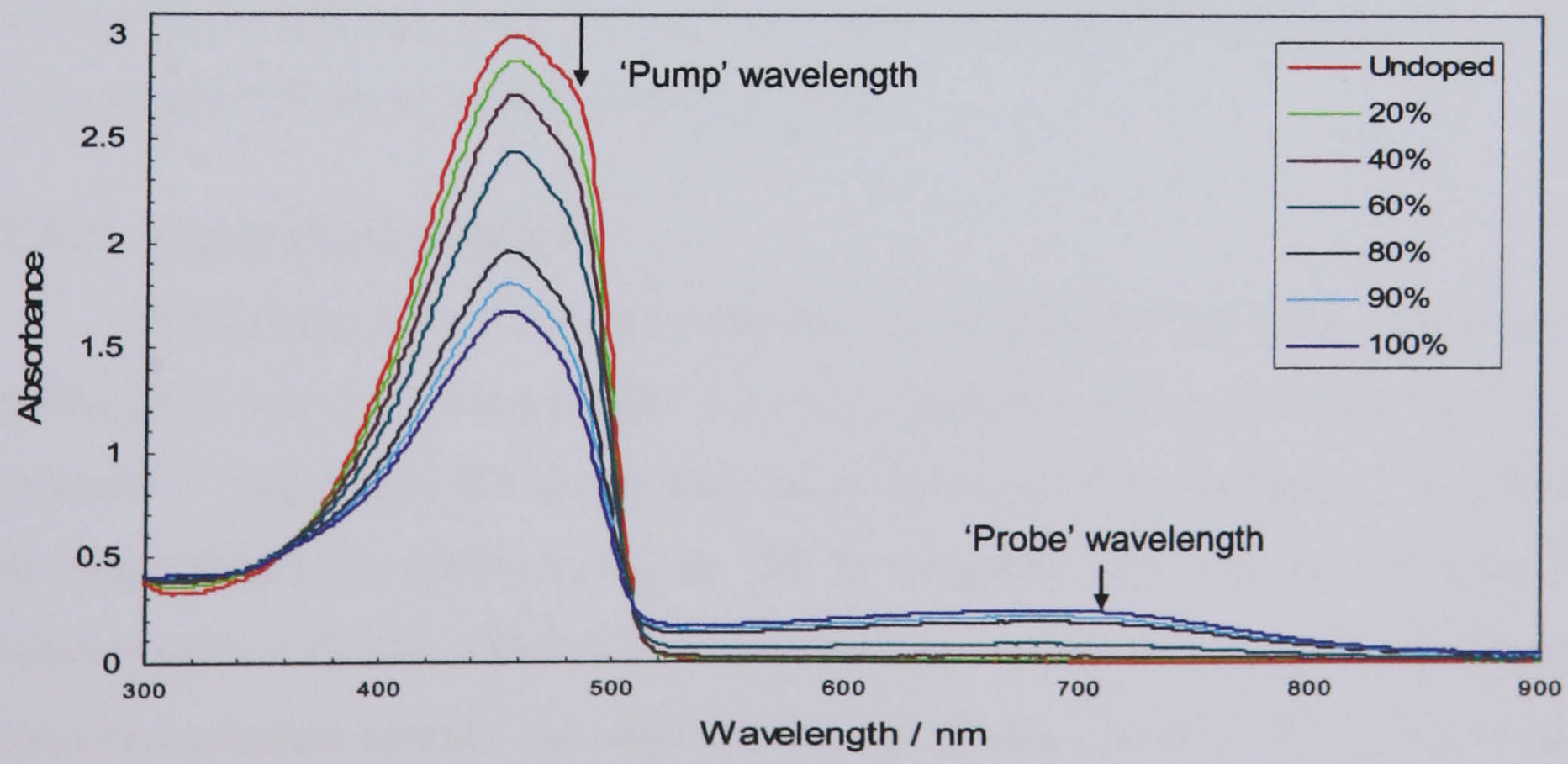


Figure 2.6 *The UV-VIS Optical absorption spectrum of Fe^{3+} doped F8T2 at different concentration of dopant relative to monomers of F8T2. The concentration of the F8T2 polymer in toluene and the size of the cuvette were 5×10^{-5} mol/l and 4.5 cm ×1 cm ×1 cm.*

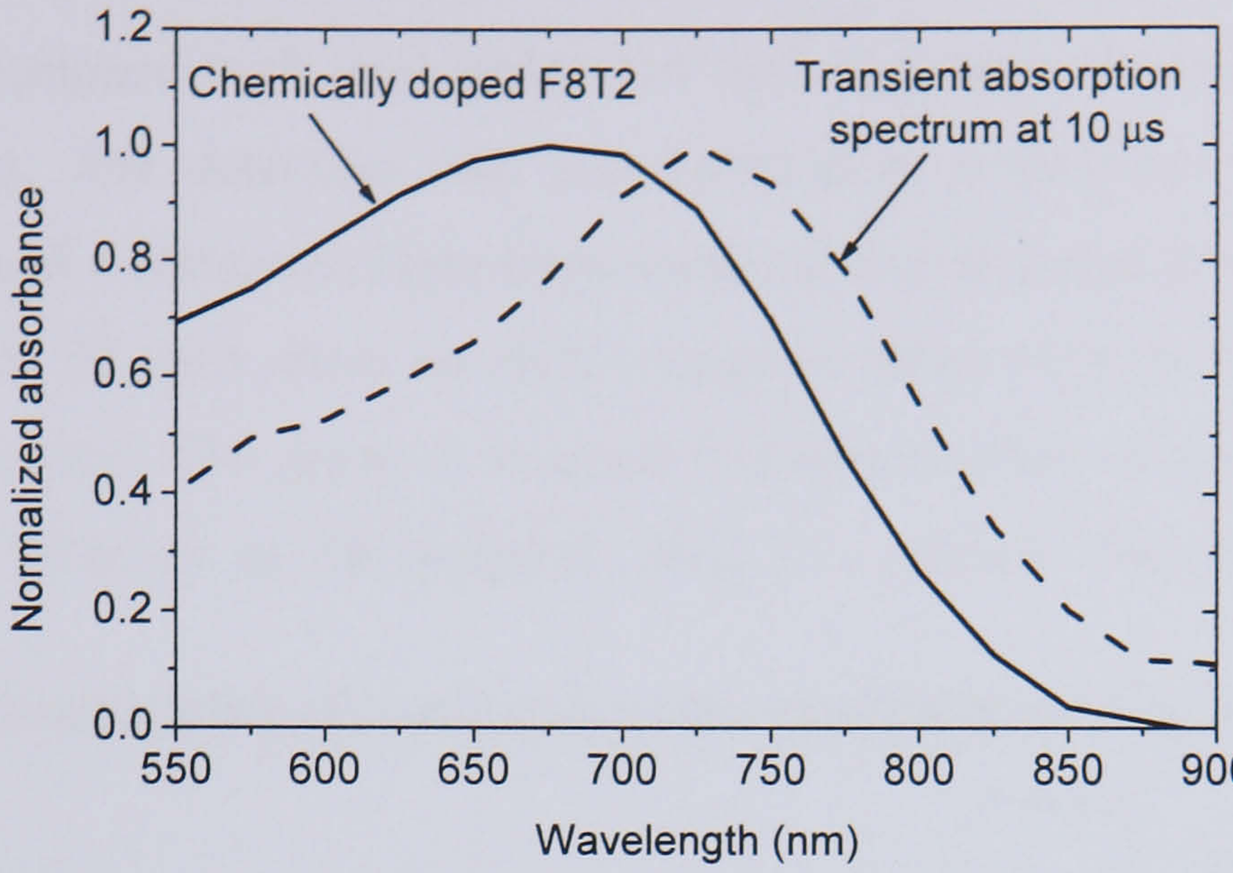


Figure 2.7 *F8T2 cation absorption spectrum recorded following chemical oxidation with $FeCl_3$ (solid line) (from Fig. 2.10) and following photoinduced charge separation (dashed line). The former was measured in solution (toluene) and in the presence of $FeCl_4^-$ counterions.*

The absorption spectra of chemically doped polymer solutions and the transient absorption spectra of photoexcited polymer / TiO_2 structures were obtained to find the 'pump wavelength' and 'probe wavelength'. Here, we discuss the experimental details of absorption spectroscopic measurement of, for example, F8T2 / TiO_2 structure. Figure 2.6 shows the absorption spectrum of Fe^{3+} chemically doped F8T2, where one can find the maximum absorption of the polymer around 500nm and the polaron absorption around 700. A polaron transient absorption spectrum similar to the polaron spectrum in the chemically doped solution was obtained for a TiO_2 / F8T2 sample structure between the wavelengths 500 nm 900 nm as shown on Figure 2.7. The pump wavelength was chosen to be 500 nm, close to maximum absorption of F8T2 polymer, and the probe wavelength 720 nm to detect positive polaron.

2.4.3 Experimental details

All transient absorption measurements were performed by using a microsecond to millisecond transient spectrometer that was designed and constructed by Dr. James Durrant[114]. The Figure 2.8 shows the optical layout of the microsecond to millisecond transient absorption spectrometer. A 150 W tungsten lamp was used as 'probe' light source, while a PL201, PTI dye laser 'pumped' by a LN1000 Megaplus nitrogen laser is used as excitation source. An optical pipe was used to transmit the ~ 30 μJ excitation pulses to the sample. The probe wavelength was selected by two monochromators before and after the sample, which minimize the amount of probe light incident on the sample and the amount of scatter/emission reaching the photo detector[115]. A high gain

photodiode equipped with appropriate low and high pass filtering was employed as detection unit. The detection unit was coupled to a GOULD 475 digital storage oscilloscope and a computer. Data were collected on timescales from 300 ns to 100 ms, averaging over 50 laser shots on each timescale. Data were plotted as the change in absorbance vs time. The decay is assigned to recombination between electrons in TiO_2 and positive polarons in the polymer, once the polaron absorption band has been identified.

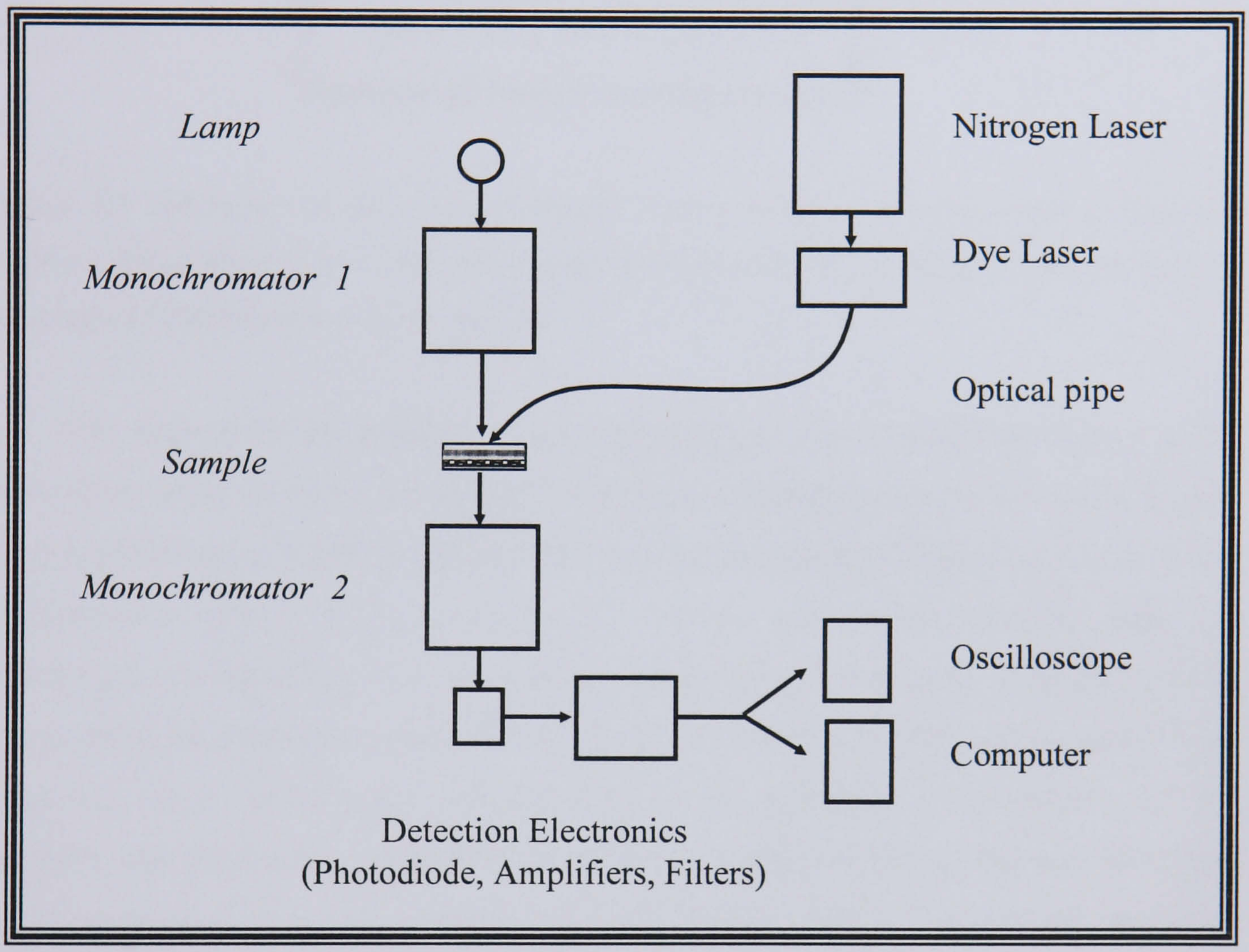


Figure 2.8 *The optical layout of a microsecond to millisecond transient absorption spectrometer; a tungsten lamp is used as 'probe' source, while a dye laser 'pumped' by a nitrogen laser is used as excitation source. An optical pipe transmits the excitation pulse to the sample.*

To confirm that the transient absorption is due to the polaron, detailed transient absorption studies are also performed on pristine polymer films as control experiments. If these studies reveal no evidence of any absorption feature, which could be assigned to the triplet, for instance, on time scale of charge recombination dynamics (0.1 μs - 100 ms), then the decay in absorbance as a function of time after the excitation can be attributed to recombination of polarons with electrons to the TiO_2 by photoinduced charge transfer.

2.5 Exciton diffusion length measurements

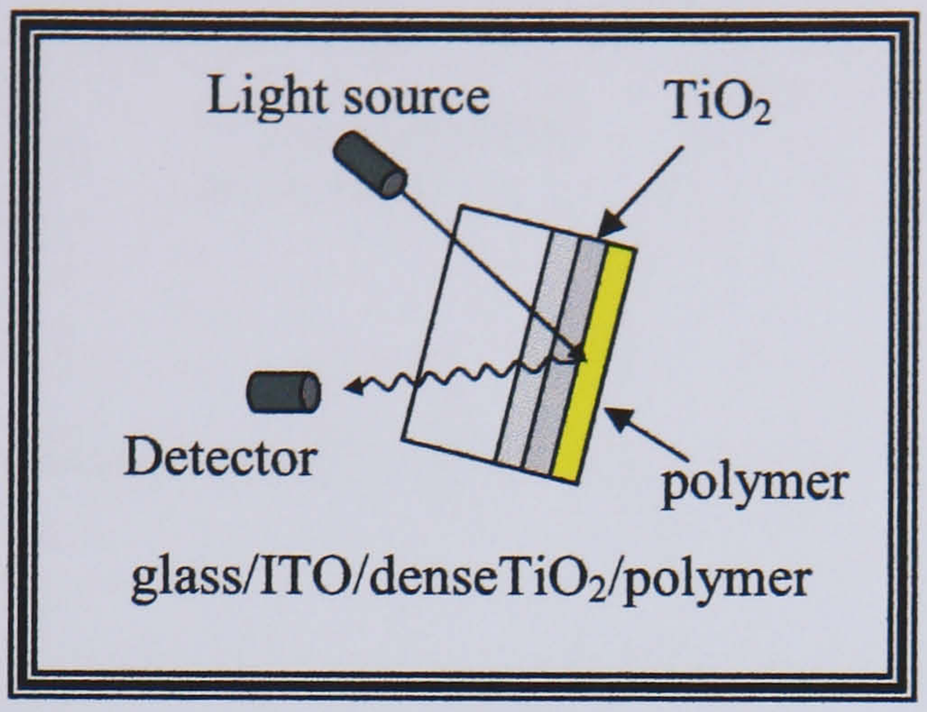


Figure 2.9 *Schematic of the arrangement for measurement of exciton diffusion length of polymer. The polymer was excited with monochromatic light, of wavelength corresponding to absorption of the polymer, through the ITO.*

The exciton diffusion length of several polymers was estimated by following the method described in Ref. [19]. Figure 2.9 shows the arrangements for the measurement of exciton diffusion length of polymer which was done inside a FlouroMax fluorescence measurement system. The polymer was excited with monochromatic light, of wavelength corresponding to the maximum absorption of the polymer, through the ITO. The relative photoluminescence (PL) of the polymer layers on ITO and on dense TiO_2 substrates, at a wavelength corresponding to the maximum luminescence of the polymer, was obtained as a function of the polymer layer thickness. The polymer layer thickness on the dense TiO_2 layer was estimated from the UV-VIS optical absorption of the layer and the known absorption coefficient of the polymer. The relative luminescence was found to vary linearly with polymer layer thickness both on ITO and dense TiO_2 but for ITO the curve passes through zero, while for TiO_2 the linear trend indicates that the PL will vanish at a finite thickness. We therefore interpret this quenching thickness as the approximate exciton diffusion length of the polymer.

2.6 Cyclic voltammetry

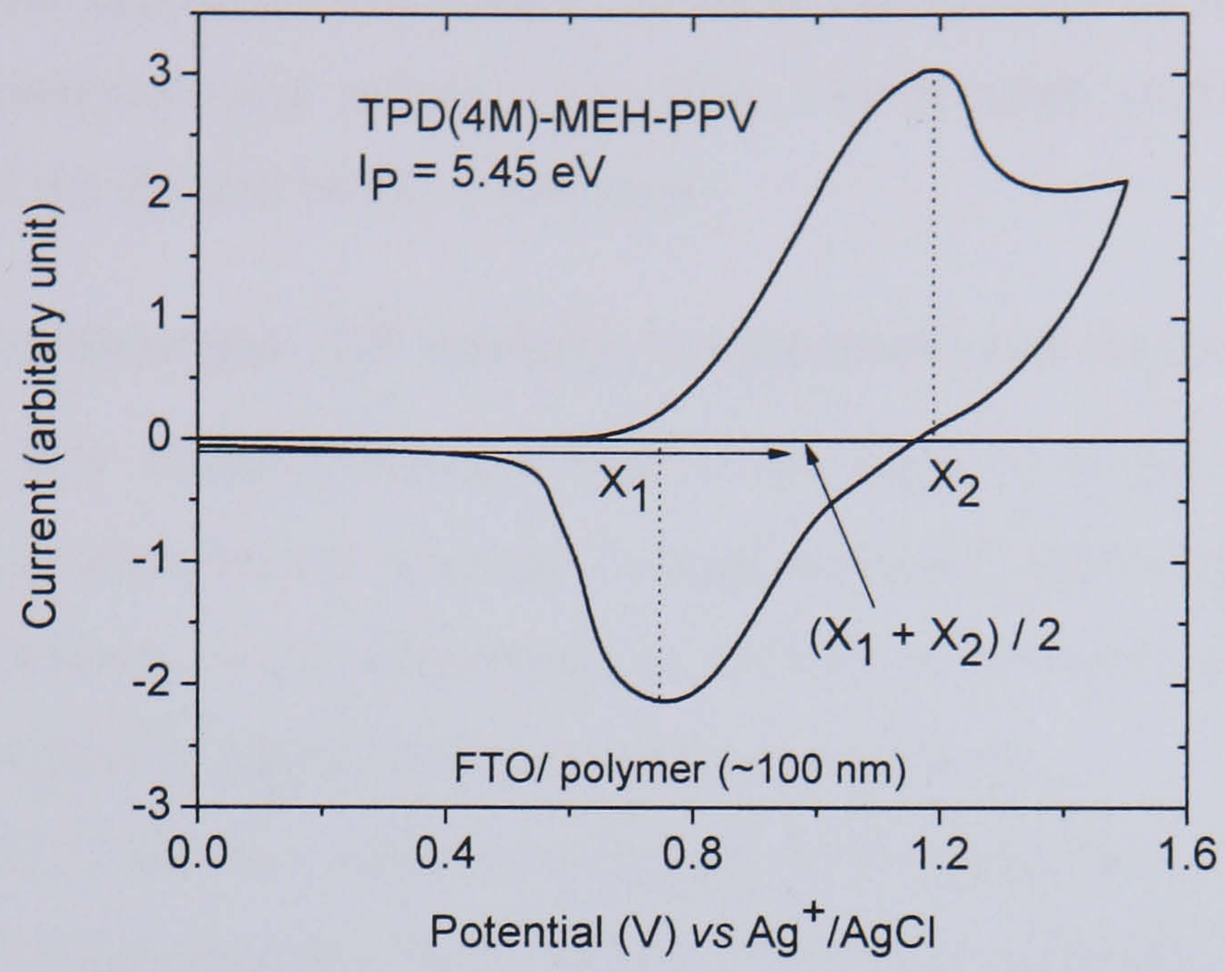


Figure 2.10 *Typical cyclic voltammograms of spin coated TPD (4M)-MEH-PPV polymer films on FTO substrates.*

The cyclic voltammetry technique was applied to determine the ionization potential of the polymers we studied. In this experiment, a simple standard three electrode cell was used and it consisted of a platinum wire as a counter electrode, polymer film of thickness 100 nm spin coated on to FTO (Hartford glass, TEC 15) conducting glass as a working electrode and an Ag/AgCl as a reference electrode. A redox inactive background electrolyte (0.1 M tetrabutylammonium tetrafluoroborate) was used to minimize the effect of transport of analyte through migration to the working electrode[116]. The solution was prepared in a glove box which was filled with dry nitrogen gas. All the components of the three electrode cell were cleaned and the cell was degassed with dry nitrogen gas before each experiment was conducted. Typical cyclic voltammograms of spin coated TPD (4M)-MEH-PPV polymer films on FTO substrates is shown in Figure 2.10.

2.7 Time of flight (TOF) technique

The TOF technique was used to measure the mobility of charge carriers in some conjugated polymers and porous TiO_2 films. The principle of this technique and the experimental details will be discussed here.

2.7.1 Principle of the TOF mobility measurement technique

In the TOF mobility measurement, a thin sheet of carriers is generated near the surface of a sample, which is usually a high resistivity semiconductor with negligible thermal equilibrium carrier concentration, sandwiched between two electrodes, at least one of which must be semi-transparent and non-injecting.

Figure 2.11 shows a schematic diagram of the measurement set up. The sample, of thickness d, is subjected to a large electric field due to a voltage V applied between the electrodes. Depending on the polarity of the applied voltage, either positive or negative carriers may be drawn across the sample. Since both TiO_2 and the conjugated polymers studied here, have large energy gaps (usually more than 2 eV), few carriers should be present at equilibrium and negligible current flows through the sample in the dark. A short laser pulse is flashed at the sample through the transparent electrode. The photon energy is chosen so that it exceeds the energy gap of the sample materials. A sheet of electron-hole pairs is created near the transparent electrodes, if the absorption coefficient at that wavelength is high enough.

The carriers of sign opposite to that being studied are rapidly pulled towards the transparent electrode, while the remaining carriers drift across the samples towards the counter electrode under the influence of the electric field.

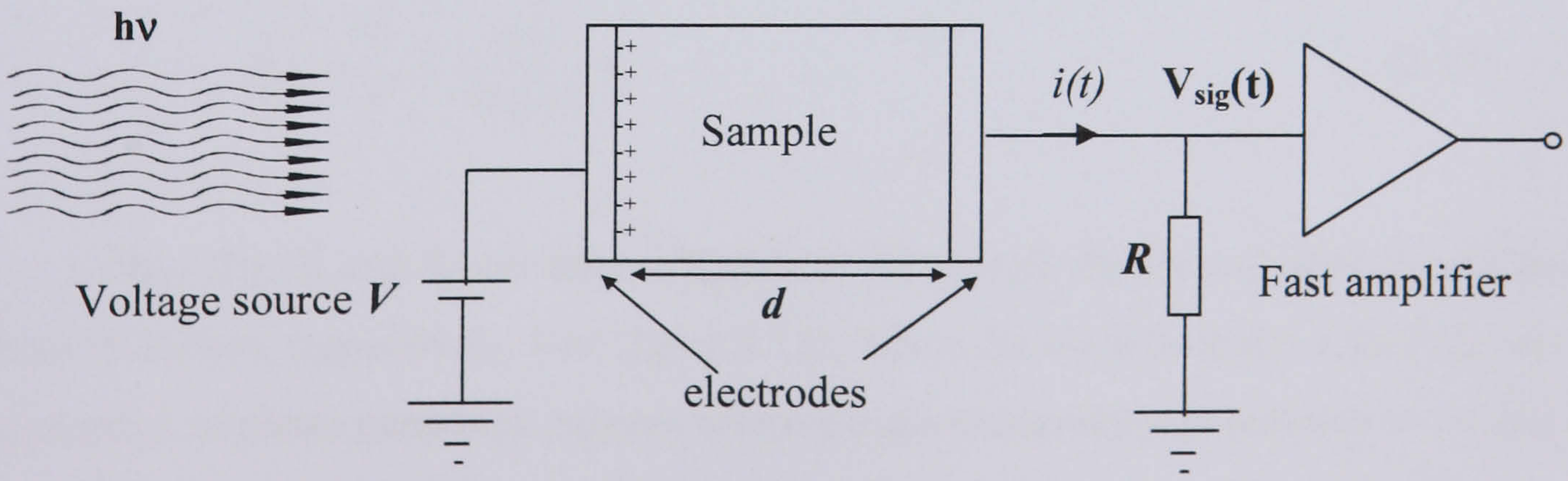


Figure 2.11 *Schematic diagram of a TOF mobility measurement set up*

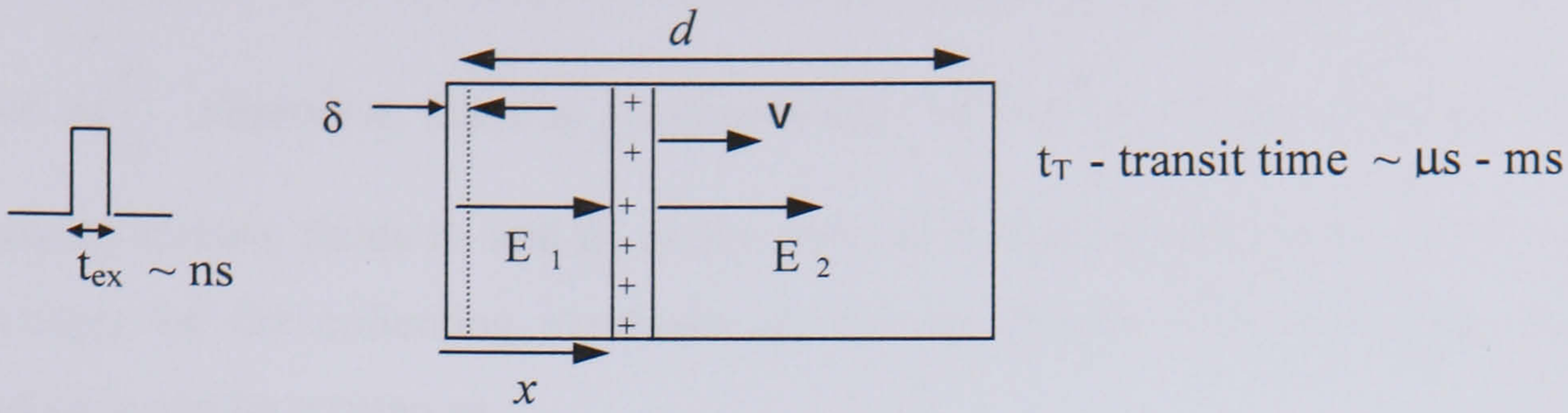


Figure 2.12 *Illustration of the principle underlying the mobility measurement in a sample. E_1 and E_2 are defined in the text.*

If the following conditions (a) to (d) are satisfied[117],

(a) The thickness of the sample d is large compared to the optical absorption depth δ in the sample.

$$\delta << d. \tag{2.9}$$

(b) The excitation laser pulse width, t_{ex}, is very small compared to the transit time, t_T, of the photogenerated carriers across the sample, at a given electric field.

$$t_{ex} << t_T \tag{2.10}$$

(c) The photo-generated charge, Q must be less than the charge stored across the sample CV, where C is the capacitance of the sample and V is the applied bias.

$$Q << CV \tag{2.11}$$

(d) The dielectric relaxation time, τ_{rel}, is very much longer than the transit time t_T.

$$\tau_{rel} >> t_T \tag{2.12}$$

then the drifting sheet of carriers at position x will modify the applied field $\frac{V}{d}$ so that:

$$E_1 = \frac{V}{d} - \frac{qN}{\varepsilon\varepsilon_0 Ad}(d-x) \tag{2.13}$$

$$E_2 = \frac{V}{d} + \frac{qN}{\varepsilon\varepsilon_0 Ad}x \tag{2.14}$$

Here the E_1 and E_2 are electric fields in the sample before and after the drifting sheet of carriers, respectively, (see figure 2.12), q is -e for electron and + e for hole, N is the number of photo generated carriers which escape recombination between $x = 0$ and $x = \delta$, A is the illuminated area and ε is the dielectric constant of the sample material.

This shows that the drifting sheet of carriers perturbs the field within sample. If the number of generated carriers is kept sufficiently small, then the internal field can be

taken as $\frac{V}{d}$, otherwise, there is a redistribution of charges on the electrode due to the changing electric fields E_1 and E_2 as the sheet of charge carriers progresses. The change in charge on the collecting electrode due to the drifting sheet of charge carriers at position x can be written as

$$\Delta Q(x) = eN\frac{x}{d} \qquad (2.15)$$

There are two different measurement modes of TOF technique, current mode and current integration mode. The current mode is applying when the RC time constant is less than the transit time, $RC << t_T$ and the current integration mode when $RC >> t_T$. The current mode is the more traditional mode. The choice between these two modes depends largely on the sample capacity and the order of magnitude of the transit time t_T for the sample involved. In general, the current integration technique is more sensitive particularly if t_T lies in the range below about 10^{-6} sec[117]. In the case of the conjugated polymers and porous TiO_2 we studied, t_T is greater than 10^{-6} sec and so current mode TOF mobility measurement technique is sufficient and more practical.

In the current mode, the voltage across the resistance R (see figure 2.11) is proportional to the current flowing through the sample.

$$V_{sig}(t) \propto i(t) \qquad (2.16)$$

In the ideal case, the current $i(t)$ induced in the external circuit due to the drifting sheet of carriers is given by

$$i(t) = \frac{eN}{d}\,\mathsf{v}, \qquad 0 < t < t_T \qquad (2.17)$$

$$i(t) = 0, \qquad t \geq t_T \qquad (2.18)$$

where v is the drift velocity of the sheet of carriers. Thus, when the carriers exit the sample at the collecting electrode, a sharp decrease in the current occurs. Sketches of an ideal and more realistic transient TOF current $i(t)$ following the light flash are shown in Figure 2.13. In practice an unavoidable broadening occurs, due to the diffusion of charge carriers during the field-induced drift so that the sheet of charge progressively spreads out about its mean position during its motion. The TOF trace thus shows a **rounded fall-off** around $t = t_T$ as shown by the solid line in the Figure 2.13.

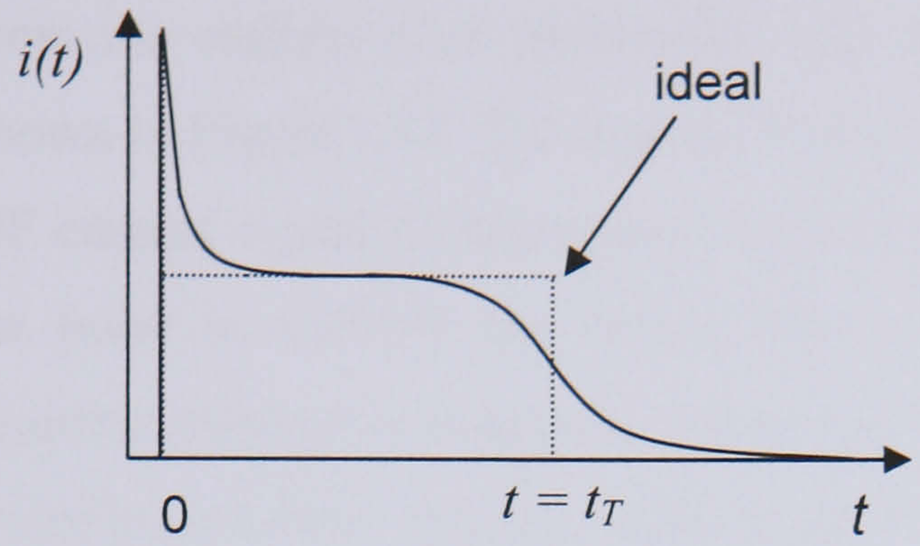


Figure 2.13 *Typical TOF profile (solid curves) compare with idealized TOF sketch (dash line).*

Apart from diffusion, in real measurements, the TOF profile can be further influenced by the following effects: (a) long RC response time (b) loss of carriers due to deep trapping (c) variation in drift velocity as a function of x due to sample inhomogeneity (d) local electric field variation due to trapped space charge, and (e) spreading of the photogenerated sheet of charge to a width comparable to d, if the absorption coefficient is small.

There are different conventions for determining the carrier transit time. It could be determined from either the point where the current has decayed to half of its value in the plateau region t_T, or from the point of intersection of the asymptotes to $i(t)$ when plotted in a double logarithmic plot (t_0). It has been reported that the transit time t_T provides a more accurate value of the TOF mobility than t_0[118].

The ratio of the thickness to the transit time gives the drift velocity of the photogenerated carriers. The ratio of the velocity to the field then gives the mobility.

$$\mu = \frac{d^2}{V\, t_T} \tag{2.19}$$

Selection of the sign of the bias voltage allows electron and hole -transients to be independently studied.

The safest procedure is to determine the mobility of the carriers over a wide range of applied field. A Poole-Frenkel[119] like dependence of mobility on electric field, $\ln \mu \propto E^{1/2}$, has been observed experimentally for a wide range of low mobility materials and also expected through simulation.

2.7.2 Continuous-time random walk (CTRW) model for Dispersive Transport

For many low mobility semiconductors, charge trapping is important and the quite different behaviour indicated in Figure 2.13 is observed. The current decreases

continuously from the earliest time observable, and the current flow extends to very long times as shown in Figure 2.14. This type of transport is called *dispersive transport.*

The TOF current signal of this type of materials on a linear *i* - *t* scale does not show a distinct point to identify the transit time. There have been many models proposed to describe dispersive transport. Scher and Montroll[120] introduced a model known as the continuous-time random walk (CTRW) where the transport lattice is energetically or spatially disordered so that charges hop with a wide range of hopping rates[120], resulting in dispersive kinetics, and the formalism of CTRW has been the most widely used. Nelson[55] also applied a version of the CTRW model nanocrystalline TiO_2 in order to simulate experimental measurements of charge recombination kinetics in dye sensitised TiO_2 electrodes under lower bias. The simulation considered that the medium contains an exponential tail of traps states, that only one electron is allowed per trap with the results that the current decays faster with time when more electrons are used. This is the first simulation charge transport study, which takes into account trap filling effects.

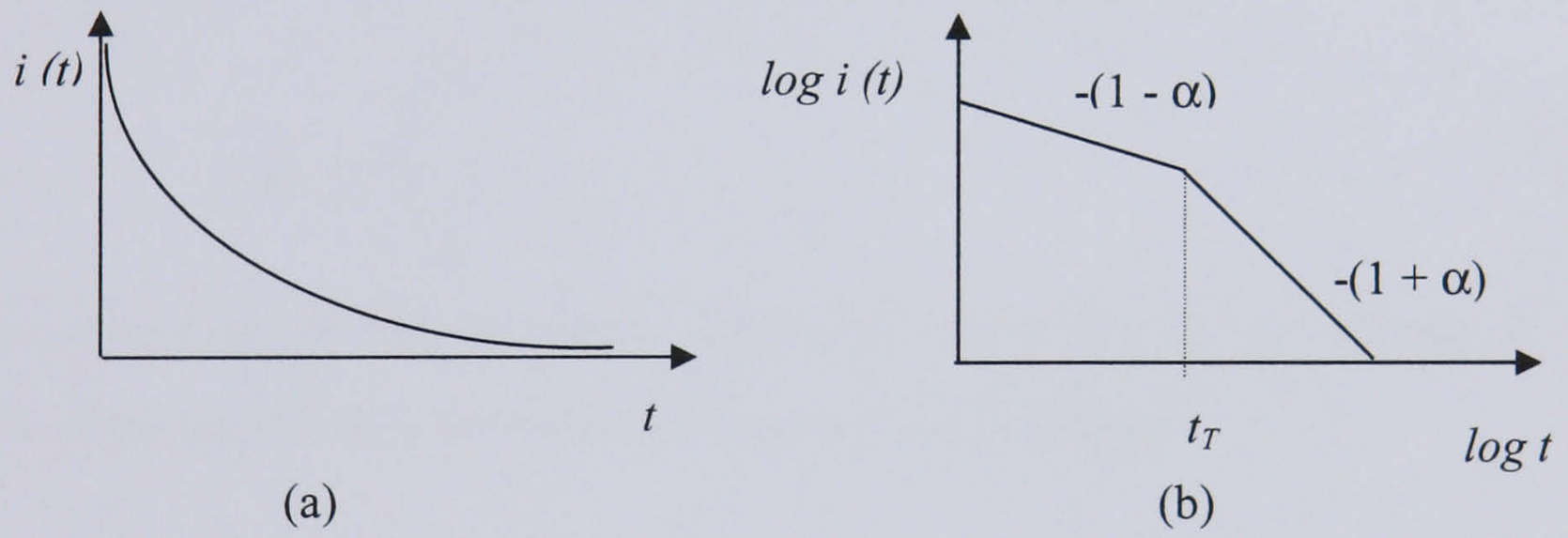


Figure 2.14 *A typical* (a) *dispersive photocurrent transient and (b) the corresponding double logarithmic plot*

A key prediction of the CTRW model is that the photocurrent transient decays as follows, when the density of trap states has the form, $N(\varepsilon) = N_0 \exp\left(-\frac{\varepsilon}{\varepsilon_0}\right)$,

$$i(t) \sim t^{-(1-\alpha)}, \quad t < t_T \tag{2.20}$$

$$i(t) \sim t^{-(1+\alpha)}, \quad t > t_T \tag{2.21}$$

where $\alpha = \frac{kT}{\varepsilon_0}$ is a disorder parameter that has a value between 0 and 1. The more disordered the material, the smaller the value of α and the more dispersive the transport.

The model predicts that the current decreases even before the carriers reach the counter electrode. When a reasonable fraction of carriers reach the electrode, the current

begins to decrease at a faster rate due to the carrier removal. In the case of such dispersive transport double logarithmic (log i – log t) representation is employed. Before applying this scheme, one has to make certain that the dispersive signal is not due to accumulation of bulk space charge. The double logarithmic plot of the current $i(t)$, corresponding to equation, tends towards two lines with slopes – (1 - α) and – (1 + α) as shown in Figure 2.14, in the limit $t \rightarrow 0$ and $t \rightarrow \infty$, respectively. The gradient of TOF profile should equal -1 close to the change in slope of the asymptotes.

The double logarithmic plots of $i(t)$ are routinely used to analyse the transient photocurrents observed in time of flight experiments on organic semiconductors. Moreover, the Scher-Montroll[120] theory predicts, the sum of the slope of two linear portions is – 2.0 in the double logarithmic plot, in the case of an exponential density of states, just as anticipated from the power law exponent expressions. However, this prediction has seldom been observed in the low mobility organic semiconductors.

A modified multiple trapping model assigns different power law dependencies of the photocurrent transient i(t) before and after the transit time t_T:

$$i(t) \propto \begin{cases} t^{-(1-\alpha_i)} & , t < t_T \\ t^{-(1+\alpha_f)} & , t > t_T \end{cases} \qquad (2.22)$$

where α_i and α_f are the dispersion parameters and have values between 0 and 1. The values of the parameters decrease with increasing dispersion.

2.7.3 Experimental details

The TOF experimental setup was arranged as shown in Figure 2.11. The sample was mounted inside a helium-exchange-gas Oxford Instruments Optistat[DN] cryostat. The carriers were generated with a frequency-trebled Nd:YAG laser (spectral wavelength 355 nm, pulse width less than 6 ns, energy per pulse ~ 7 mJ, repetition rate 1 Hz, and nominal beam diameter 2-8 mm), illuminating through the ITO. The laser intensities were controlled by an optical filter between the laser source and the sample. Care was taken to keep the generated charge less than 5 % of the capacitor charge stored on the sample to avoid space-charge effects. The photocurrent transients were monitored with a TDS 3052 digital oscilloscope.

2.8 Electrical characterization

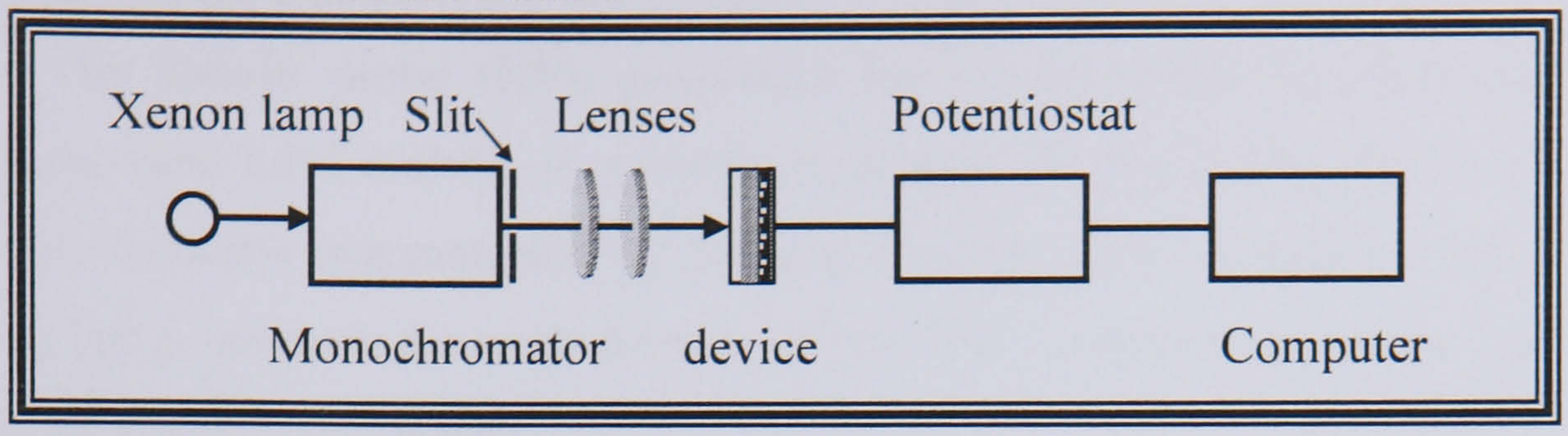


Figure 2.15 *Schematic diagram of the experimental set up for quantum efficiency and J-V measurements*

The photovoltaic performance of the devices was studied by measuring photocurrent quantum efficiency spectra and current density-voltage (J-V) characteristics under light illumination. A schematic of the experimental setup used for external quantum efficiency (EQE) and J-V measurements of devices is shown in Figure 2.15. The devices were housed in a home built sample holder with a quartz window. The light source was a 100 W Xenon lamp, which was driven by a Bentham 505 stabilized power supply. The light from the lamp was dispersed by a CM110, 1/8 m monochromator, which was controlled by computer. Current and voltage measurements were taken using a computer controlled Keithley 237 high voltage SMU (source measure unit). For EQE measurements, the photocurrent density of the sample, $J_{SC}(\lambda)$, and the photocurrent density of the calibrated silicon photodiode, $J_{SC}^{Si}(\lambda)$, were obtained at a particular position for different wavelengths. The intensity of the light, $P(\lambda) = \frac{J_{SC}^{Si}(\lambda)}{SR_{Si}(\lambda)}$ was calculated as function of wavelength using the known spectral response of the photodiode, $SR_{Si}(\lambda)$ and photocurrent spectrum of the silicon photodiode at the same position where the sample was. The EQEs were calculated by using the equation $EQE(\lambda) = \frac{J_{SC}(\lambda)}{P(\lambda)} \frac{hc}{e\lambda}$ as function of wavelength, λ. Monochromatic J-V measurements were taken at the wavelength that gave the highest photocurrent. Reverse and forward bias measurements were carried out separately with a voltage step size of 0.02 V. Forward bias corresponds here to ITO biased negatively with respect to the counter electrode. J-V characteristics in the dark were measured both before and after the measurements of the illuminated J-V characteristics in order to confirm that the device behaviour was not changed by illumination. J-V characteristics were also taken under simulated sunlight using a home-built computer-controlled potentiostat measurement unit and a halogen lamp calibrated to air mass (AM) 1.5 equivalent intensity (100 mW cm^{-2}).

2.9 The Kelvin Probe (KP) technique

The Kelvin probe (KP), postulated by the renowned Scottish scientist W. Tompson, later Lord Kelvin, is a useful technique for measuring the work function difference between two materials by forming a parallel plate capacitor. This technique was applied to estimate the work function of the ITO substrates and of the PEDOT:PSS coated ITO used in this work.

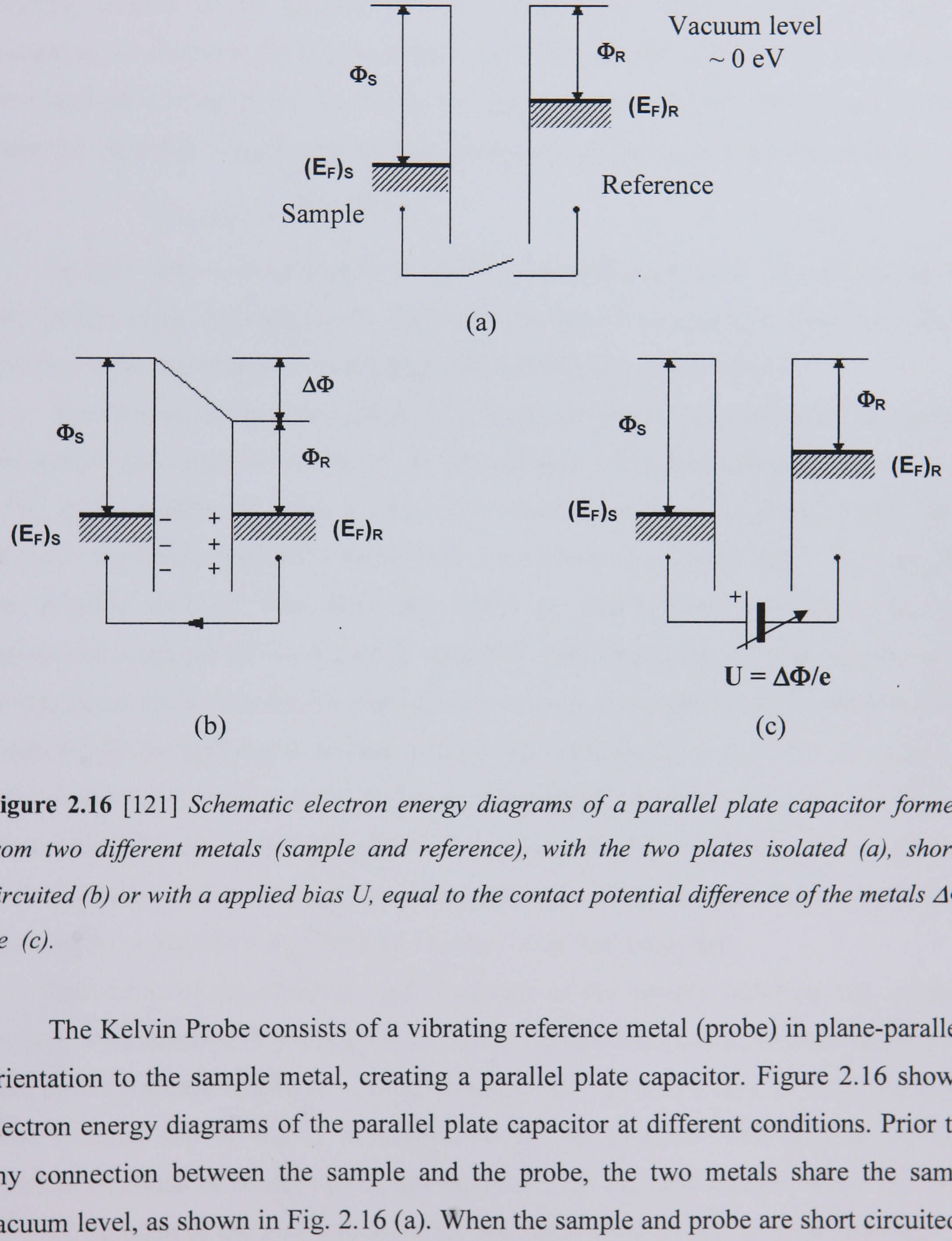


Figure 2.16 [121] *Schematic electron energy diagrams of a parallel plate capacitor formed from two different metals (sample and reference), with the two plates isolated (a), short-circuited (b) or with a applied bias U, equal to the contact potential difference of the metals $\Delta\Phi$ / e (c).*

The Kelvin Probe consists of a vibrating reference metal (probe) in plane-parallel orientation to the sample metal, creating a parallel plate capacitor. Figure 2.16 shows electron energy diagrams of the parallel plate capacitor at different conditions. Prior to any connection between the sample and the probe, the two metals share the same vacuum level, as shown in Fig. 2.16 (a). When the sample and probe are short circuited, charge must flow from the metal with smaller work function to the metal with large work function until equilibration of the Fermi level is achieved as shown in Figure 2.16

(b). This charge transfer results in an electric field in the gap between the two plates and a drop is equal to the difference in the work functions of the metals and is known as the contact potential difference (CPD).

Lord Kelvin suggested that the CPD can be measured by applying an external compensating voltage, U, equal and opposite to the CPD (Figure 2.16 (c)) so that no charge exchange between the plates take place and the capacitor is discharged. In practice, modern Kelvin probes rely on a periodically vibrating plate (the probe) brought in proximity to the sample surface, such that an alternating current i(t) flows in the circuit as a result of the time-varying capacitance C(t). This current can be zero, when the capacitor is discharged through an applied external compensating voltage, U.

$$U = \Delta\Phi/e = \frac{\Phi_S - \Phi_R}{e} \qquad (2.25)$$

In this work, a commercially available probe has been used. The KP apparatus used in this work was built by Dr. Dmitry Poplavskyy[37] using a probe and measuring electronics purchased from Besocke Delta Phi GmbH (Jülich, Germany).

The measurements were carried out with Dr. Poplavskyy's assistance. The probe was a small gold mesh circle which was vibrated above the sample surface, about 1 mm away, with amplitude of about 0.5 mm and vibration frequency of about 170 Hz. The vibration amplitude could be continuously varied between 0 and 2 mm[37]. The sample was mounted on a 3D translation stage where the probe-sample separation could be varied with a μm precision. A lock-in amplifier with a high gain I/V preamplifier was used to detect the ac current at a resonance frequency. The signal could be compensated automatically by applying a dc bias voltage that corresponds to the CPD. In order to reduce undesirable EM noise, the probe and the sample were housed inside a metal box, the so called Faraday cage arrangement. The typical accuracy of a single reading of the CPD was about 10 mV. The CPD measurements were always taken from three different places on the measured sample and an average value was calculated.

Estimation of the absolute work functions of the sample materials rely on the absolute work function of probe material (gold). Cacialli and co-workers reported[122] that work function measurements of ITO substrates by KP method using gold as a reference probe material can be highly dependent on the environment. This may be due to chemical reactions or adsorption of gas molecules on the gold surface, which modify the work function of the gold and therefore the value deduced for the work function of the sample materials. For this reason, all KP measurements were performed inside the nitrogen-filled dry glove box in order to remove any possible effects of oxygen or water

on studied samples. However, effects due to nitrogen adsorption on the surface cannot be ruled out. It has previously been reported that the work function of gold is significantly reduced from its nominal value of 5.1 eV[33] when it is placed in air or nitrogen[123,124]. Nevertheless, the work function of gold is relatively stable provided that the ambient conditions do not change reference and for this reason, gold is preferable to other low work function metals, such as Al, Ca.

Freshly cleaved highly oriented pyrolitic graphite (HOPG) has been used by Dr. Dmitry Poplavskyy[37] as a reference sample to estimate absolute work function of the sample. The work function of freshly cleaved HOPG has been shown to be reasonably independent of ambient atmosphere and equal to ~ 4.5 eV[123]. Based on the work function of HOPG, the probe work function was estimated to be around 4.5 eV in the N_2 gas ambient. This is considerably lower than the nominal value of ~ 5.1 eV.

2.10 Electro-absorption spectroscopic technique

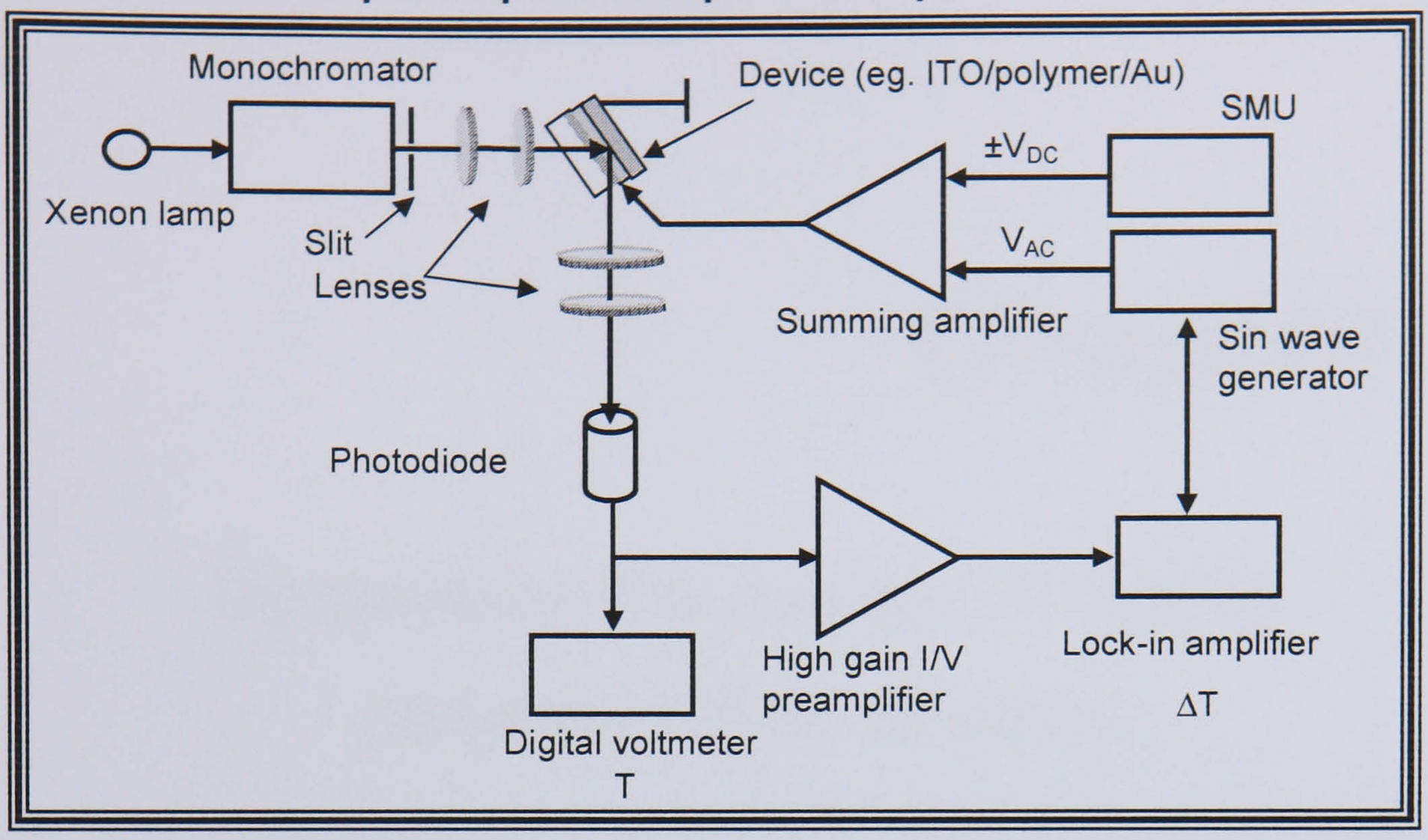


Figure 2.17 *Schematic diagram of the experimental set up for electroabsorption measurements*

The electroabsorption spectroscopic technique was used to find the built-in voltage V_{BI} of the single polymer layer sandwiched between ITO or dense TiO_2 layer and metal electrodes. The value of V_{BI} could be combined with the measured work function of the ITO (or dense TiO_2) substrate to estimate the work function of the evaporated top contact on the polymer.

Figure 2.17 shows a schematic of the experimental set up for electroabsorption measurements. A Xenon lamp with a CM110 monochromator was used as the light source. The light was incident on the device through the ITO side, reflected back from the top contact of the device, and detected by a Si photodiode. The modulation frequency was 5 kHz, and V_{AC} was varied in the range 0.2 – 1 V. The DC response from the photodetector, the transmittance T, was measured by a BlackStar 4503 digital voltmeter while the modulated change in transmittance ΔT was measured by a EG & G 5210 lock-in amplifier, equipped with a high gain I/V pre-amplifier (EG & G model 5182). The absorption of the device is modulated by an externally applied AC voltage, V_{AC}, and the relative change in its transmittance, $\Delta T/T$, which is proportional to the change in absorption, is measured as a function of the wavelength λ of the incident light and DC bias voltage V_{DC}. The electroabsorption signal at the resonance wavelength at the frequency of modulating AC voltage is proportional to the product $V_{AC} \times (V_{DC} - V_{BI})$[37]. This allows to determine the built-in voltage, V_{BI} by measuring $\Delta T/T$ as a function of V_{DC} at a fixed value of V_{AC} [80].

Chapter 3

Optimising the design of hybrid polymer / TiO_2 Devices

This chapter addresses several issues that determine the performance of photovoltaic devices consisting of TiO_2 and poly (9,9-dioctylfluorene-co-bithiophene) (F8T2) and presents a novel, multi-layer design for hybrid TiO_2 / polymer devices

3.1 Abstract

Here we study the charge recombination kinetics and photovoltaic performance of composites of poly (9,9-dioctylfluorene-co-bithiophene) (F8T2) polymer with nanocrystalline TiO_2. Efficient photoinduced charge transfer is observed in this system, whilst charge recombination is relatively slow (~100 μs-10 ms). Polymer infiltration into thick porous TiO_2 layers is improved by melt-processing and treatment of the TiO_2 surface. We study the effects of different layer thickness, top contact, and interfacial area on device performance under monochromatic conditions. The External Quantum Efficiency (EQE) of a device with a Au top contact is increased by reducing the TiO_2 and polymer layer thicknesses. Inserting thin porous TiO_2 layer into a thin bi-layer device increases the EQE by a factor of five. Photovoltaic performance under AM1.5 equivalent illumination was also studied as a function of the TiO_2 / polymer device design. The fill factor is increased from 0.24 to 0.41 by dip coating the TiO_2 electrode into the polymer solution before spin coating a second polymer layer and the corresponding overall power conversion efficiency is increased by 50 %. We find that both short-circuit current density and the open circuit voltage increase with decreasing

spin coated polymer layer thickness. The improved device produced an open circuit voltage of 0.94 V, short circuit current density of about 0.4 $mAcm^{-2}$ and a fill factor of 0.44 under simulated air mass 1.5 illuminations. However, the device produced poor quality current density-voltage (J-V) characteristics. We investigated this by varying the energy barrier at the polymer/metal interface using alternative polymers and different hole-collecting electrode materials. We find that the energy barrier at the polymer / metal is responsible for the degraded current-voltage characteristics. We reduce the energy step by introducing a PEDOT:PSS layer between the polymer and the top Au electrode as a hole-collector. The introduction of PEDOT:PSS layer improved both the J-V characteristics and the short circuit current density by over 50 %. An optimised multilayer device produced J_{SC} of 0.61 $mAcm^{-2}$, fill factor of 0.45 and V_{OC} of 0.76 V under AM1.5 illumination. The power conversion efficiency of this improved multilayer device is, 0.21 %, three times greater than the device without either the dip coated polymer layer or PEDOT:PSS.

3.2 Charge generation in single layer and bi-layer devices

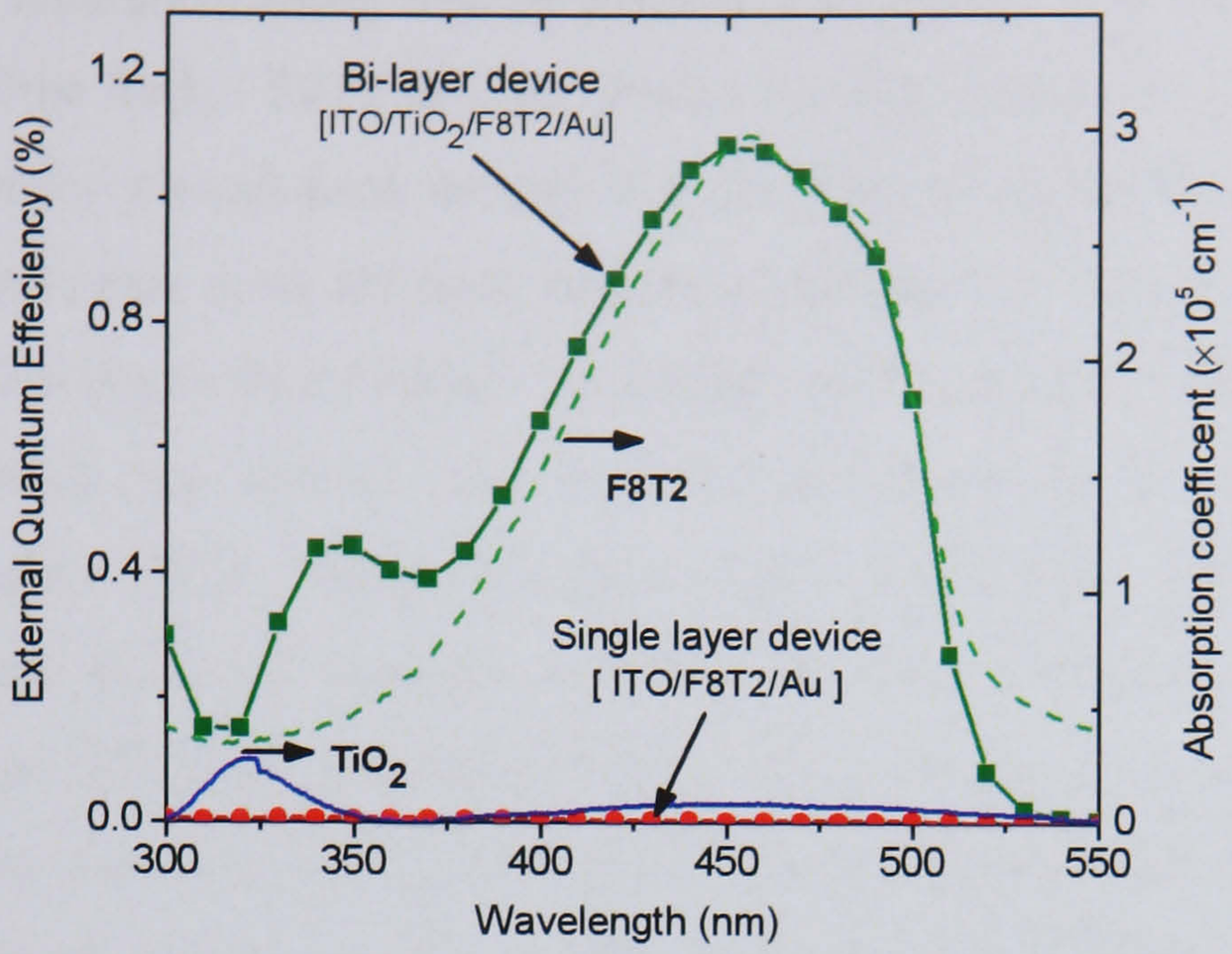


Figure 3.1 *Quantum efficiency spectra of single layer [ITO / F8T2 (100 nm) / Au] and double layer [ITO / dense TiO_2 (100 nm) / F8T2 (100 nm) / Au] devices. Absorbance spectra of F8T2 polymer on ITO (dashed line) and dense TiO_2 on ITO (solid line) are also shown for comparison.*

Figure 3.1 shows a comparison of external quantum efficiency (EQE) spectra for single layer [ITO / F8T2 (100 nm) / Au] and bi-layer [ITO / dense TiO_2(100 nm) / F8T2(100 nm) / Au] devices. The conjugated polymer layer (F8T2) has a broad optical absorption in the visible spectrum and has a peak absorption coefficient of 2.9×10^5 cm^{-1} at 460 nm, while TiO_2 has negligible absorption in the visible region of the spectrum and absorbs significantly only below 350 nm. The apparent absorption beyond 375 nm in the TiO_2 films may be due to scattering by the nanocrystalline TiO_2 particles. The peak photocurrent observed in the single layer device is 0.042 μAcm^{-2} under monochromatic light intensity of 2.7 $mWcm^{-2}$ at 460 nm, corresponding to peak quantum efficiency of only about 0.01% at the maximum absorption of the polymer. The poor quantum efficiency of the single layer device is probably due to inefficient exciton dissociation resulting in poor charge separation in the polymer.

To overcome the inefficient exciton dissociation or charge separation in a single polymer, we introduced a TiO_2 layer between ITO and the F8T2 polymer. The peak photocurrent observed in the TiO_2 / F8T2 bi-layer is well over 200 times greater than the peak photocurrent observed in the single layer device. Photocurrent generation in F8T2 is therefore greatly improved with addition of the TiO_2 layer. Efficient charge separation and extremely slow recombination between the positive polaron in the

polymer and electron in the TiO_2 are observed in the TiO_2/F8T2 structure. The details of this charge separation study will be discussed in section 3.4. The quantum efficiency spectrum of the TiO_2 / F8T2 bi-layer device broadly follows the absorption features of F8T2 except for a small peak around 350 nm. The device shows *symbatic* response[125], which suggests that most efficient exciton dissociation is observed at the TiO_2 / F8T2 interface rather than F8T2 / metal[125] provided that the sample is illuminated through the ITO. The small peak around 350 nm in the device cannot be attributed solely to the absorption of the F8T2. This peak must be due to absorption in the TiO_2, producing free charge carriers above the band gap or influenced by interference. Although introduction of TiO_2 layer into single polymer layer device increases the quantum efficiency more than factor of two, only 1.1 % of incident photons of wavelength 440 nm contributed to the photocurrent in the external circuit. Thus the peak External Quantum Efficiency (EQE) of the bi-layer is only 1.1 % at 460 nm.

The poor EQE may be attributed to limited charge separation due to the limited interfacial area, short exciton diffusion length of the polymer (exciton diffusion length of the F8T2 polymer is 5 nm, please see section 4.3.4 for more details) and / or poor charge collection. Since excitons formed in a polymer diffuse only a few nm before they dissociate (or recombine), a short exciton diffusion length limits the charge generation. Efficient photocurrent generation in this system requires that the TiO_2 be structured on the scale of the exciton diffusion length of the polymer to increase number of dissociate sites. Poor charge collection results when photo generated charge carriers, both negative and positive charges recombine and do not contribute to the photocurrent. We will first discuss the improvement of charge collection using different top contacts and then address the influence of interfacial area on charge separation.

3.3 Charge collection with different top electrodes

3.3.1 Quantum efficiency

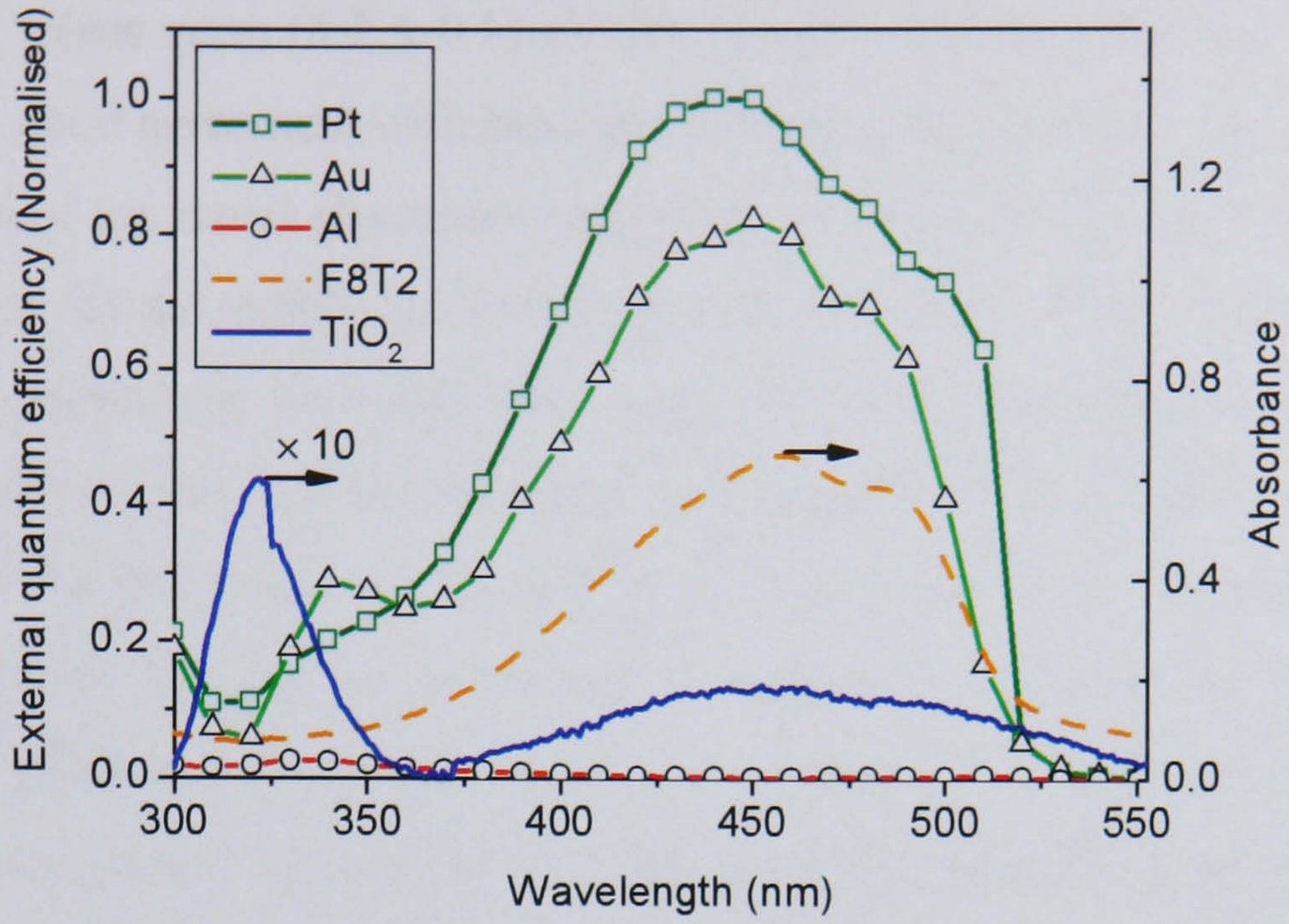


Figure 3.2 *Quantum efficiency spectra of TiO_2 / F8T2 bi-layer devices with different top contacts (at zero bias). Absorbance spectra of F8T2 polymer film of thickness 50 nm on ITO (dashed line) and dense TiO_2 of thickness 50 nm on ITO (solid line) are also shown for comparison. The absorption spectrum of TiO_2 has been scaled by a factor of ten so that it can be more readily seen.*

Figure 3.2 shows a comparison of EQE spectra for TiO_2 / F8T2 bi-layer devices with different top contacts. Comparison with the optical absorption spectra of the dense TiO_2 layer (blue solid line) and polymer layer (orange dashed line) on their own shows that the photocurrent is predominantly due to absorption in the polymer for the case of high work function electrodes (Au or Pt) device and due to absorption in TiO_2 in the case of the Al electrode. The peak external quantum efficiencies at wavelengths near the absorption maximum of the polymer (470 nm) for devices with both Au and Pt contacts are about two-orders of magnitude greater than for the Al contacted device. We note that the direction of the short circuit current flow in the Al contacted device is opposite to that in the Au and Pt devices: electrons travel to the ITO in the Pt and Au devices, while holes travel to the ITO in the Al device. This result can be understood by considering the appearance of the built-in voltage inside the polymer film due to the difference in work functions Φ between the ITO and the top metal electrode.

3.3.2 Fermi levels of the top electrodes

The work functions of ITO and PEDOT:PSS, were measured by the Kelvin probe method. The values were (5.2 ± 0.1) eV for PEDOT:PSS and (4.5 ± 0.1) eV for ITO electrodes, in good agreement with previous reports in the literature. The question of the work function of top metal electrodes requires a more careful approach. While the work function values for the metals can be found in the literature[33] those values are measured on carefully cleaned (or atomically flat) surfaces in high vacuum. It is clear that the interface between a polymer and an evaporated metal film is far from ideal, as chemical reactions [24,126] or formation of a damage layer[34]can occur. It has been shown that, for example, the work function of Au on top of conjugated polymers may be smaller than the expected value of 5.1 eV by as much as 0.2-0.3 eV[36,37,127]. For this reason we have performed electroabsorption studies on single-layer devices with the aim of determining the work functions of evaporated Al, Au and Pt electrodes at the contact with F8T2. The bottom electrodes were either ITO ($\Phi \sim 4.5$ eV) or ITO / PEDOT:PSS ($\Phi \sim 5.2$ eV[60]).

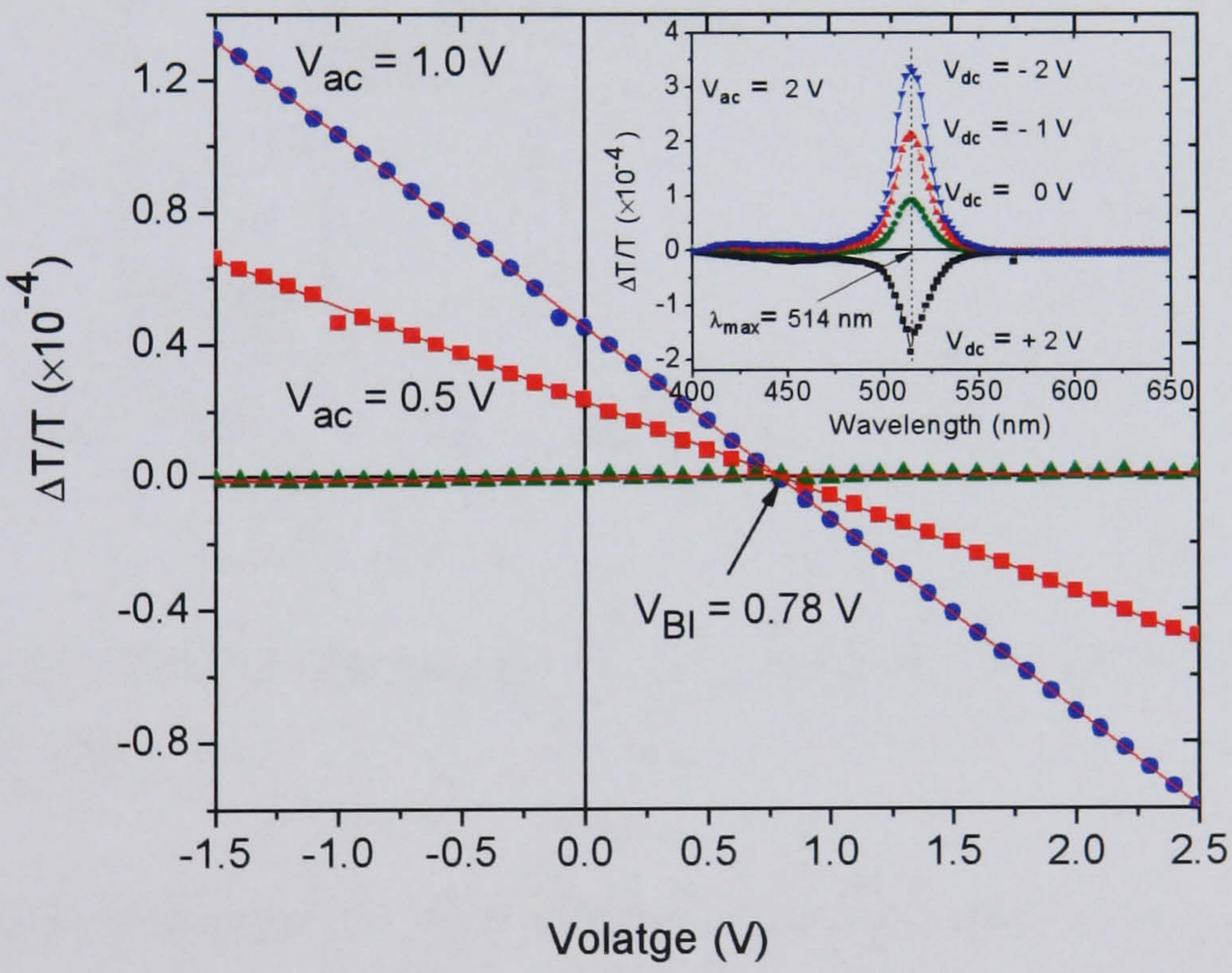
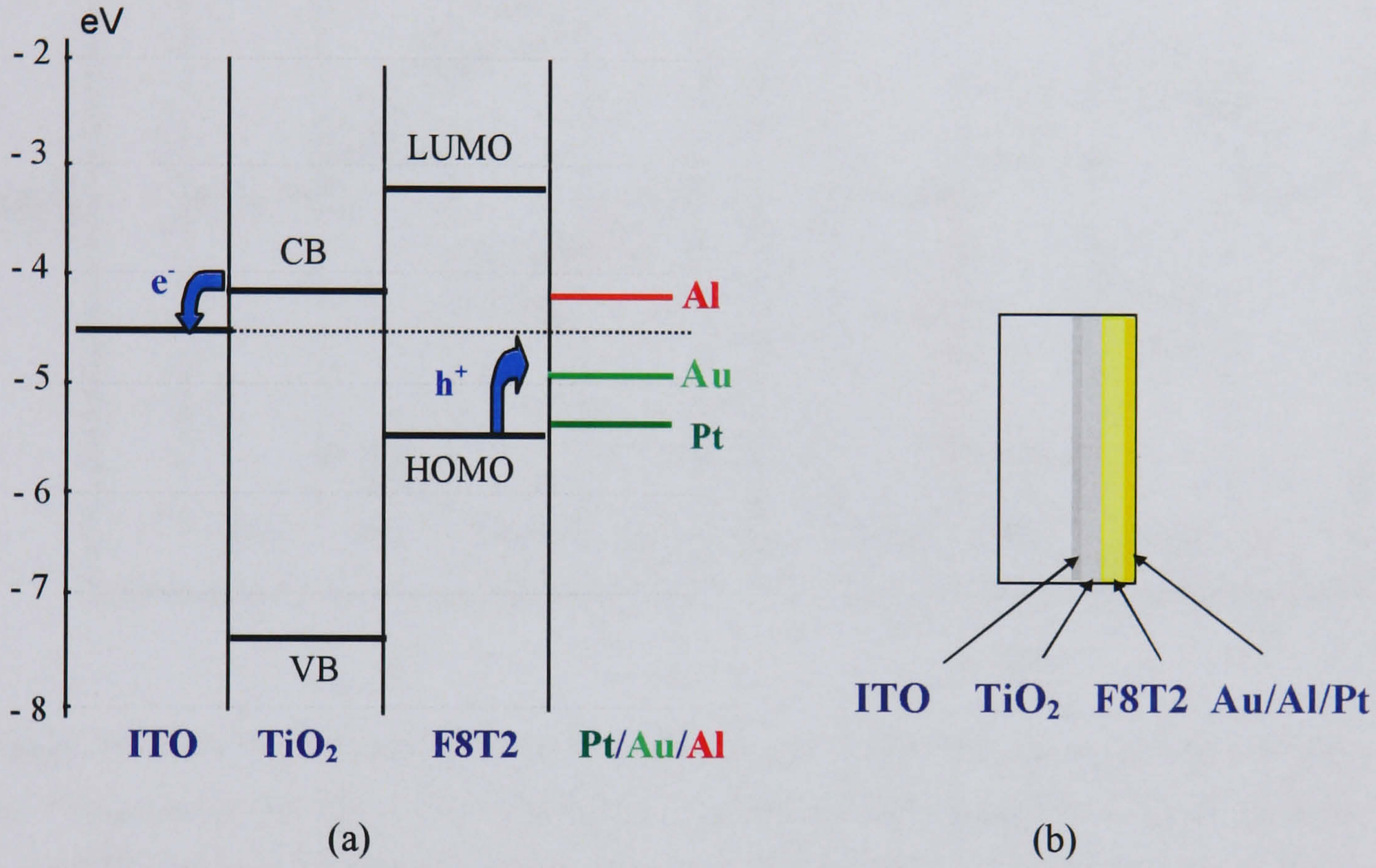


Figure 3.3 *Bias voltage dependence of the electroabsorption signal at a photon energy of hc/λ_{max} for ITO / PEDOT:PSS / F8T2 (100 nm) / Al device. Inset shows 1st harmonics electroabsorption spectra of the device. The dashed vertical line indicates the photon energy of hc/λ_{max} = 2.4 eV that yields a maximum signal.*

The inset of Figure 3.3 shows the first harmonic electroabsorption spectrum for ITO / PEDOT:PSS / F8T2 (100 nm) / Al sample for a fixed value of the AC voltage. The spectra of the device exhibited a single strong peak with a maximum at the photon energy hc/λ_{max} = 2.4 eV (λ_{max} = 514 nm) that scaled linearly with the DC bias voltage as

indicated by the vertical dashed line in the inset of the figure. Figures 3.3 show the dependence of $\Delta T/T$ at the photon energy hc/λ_{max} with DC bias voltage in ITO / PEDOT:PSS / F8T2 (100 nm) / Al. These implied that the sample was free of traps and the signal was due to the bulk of the polymer film. The built-in voltage ($V_{BI} = \Phi_{anode} - \Phi_{cathode}$, if interface dipoles are negligible) is given by the magnitude of the DC voltage at which $\Delta T/T$ falls to zero. For the ITO / PEDOT:PSS / F8T2 (100 nm) / Al, V_{BI} is 0.8 V. The work function of the Al electrode on the F8T2 polymer is calculated to be about 4.4 eV which is close to the value for clean Al of 4.3 eV[33].



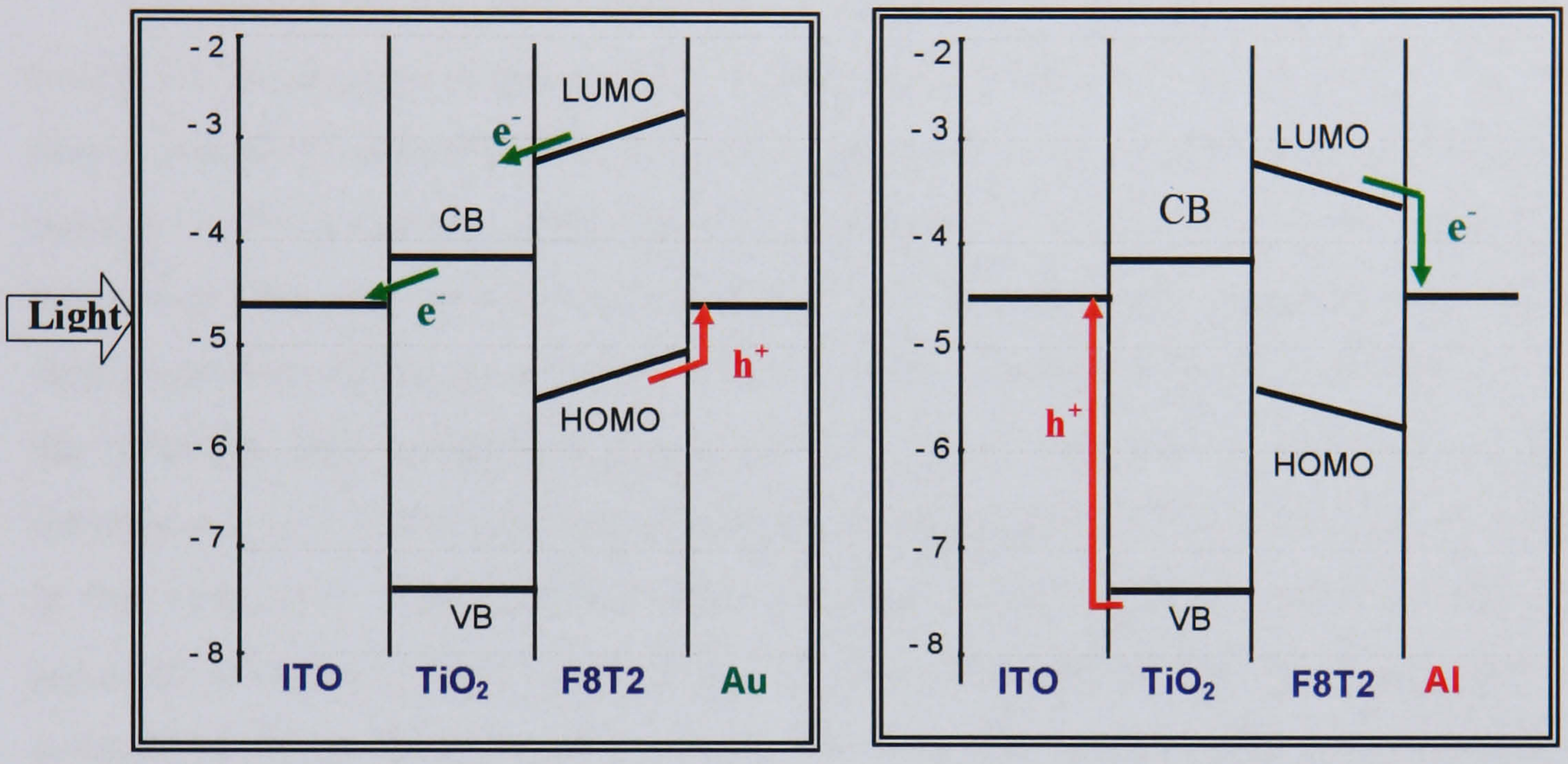
(a) (b)

Figure 3.4 *(a) Proposed electronic energy-level diagram and (b) Schematic diagram for ITO / TiO_2 / F8T2 / metal*

Similar measurements were performed on devices with Au and Pt electrodes. Unlike Al contacted devices, these devices exhibited additional electroabsorption peaks, the number and shape of which varied from sample to sample. Moreover, the amplitudes of these peaks did not always scale linearly with the DC bias voltage. In this case a reliable measurement of the built-in voltage, and correspondingly the work function of the top electrode, is not possible as there is apparently a strong contribution to the measured signal from interfacial regions in addition to that from the bulk. The origin of this additional interfacial contribution to the signal is not clear but could be due to several reasons such as morphological changes in the polymer during the evaporation process, or chemical reaction between the polymer and the metal due to a

strong affinity between noble metals and sulfur, present in the polymer. Therefore we tentatively assumed that the work function of Au on F8T2 was $\Phi_{Au} \sim 4.9$ eV, similar to other polymer systems[36], while the work function of Pt on F8T2 should be about 0.4 eV (according to the differences in literature values of Φ_{Pt} and Φ_{Au}[33]), i.e. $\Phi_{Pt} \sim 5.3$ eV (Figure 3.3).

3.3.3 Field inside the device



(a) (b)

Figure 3.5 *Short circuit conditions under illumination for both Au and Al devices (a) electrons are transported to the ITO and holes to the Au, (b) electrons are transported to the Al and holes to the ITO. Since the field to be dropped within the TiO_2 by its native n-type doping, the bands do not bend in the TiO_2. As the TiO_2 is moderately n-type, due to native defects, while the polymer is undoped, most of the potential will be dropped across the polymer layer, as illustrated, and band bending in the TiO_2 should be negligible. For typical doping levels (< 10^{16} cm^{-3})[128] the quasi-Fermi level of the TiO_2 is expected to lie within a few hundred meV of the conduction band of TiO_2.*

Based on the proposed work functions for the top contact metals, there is a positive built-in voltage, $V_{BI} = \Phi_{metal} - \Phi_{ITO}$, inside the polymer film in Au and Pt devices, and a negative built-in voltage in devices with Al top contact. Under illumination at short circuit, excitons generated in the polymer layer near the TiO_2 / polymer interface transfer negative charge to the TiO_2 and positive polarons form within the polymer. The electrons flow through the TiO_2 to the ITO electrode and positive polarons through the polymer to the Au or Pt electrode, assisted by the field due to

built-in voltage in the device. Note that, because TiO_2 is deposited on top of ITO in these structures, the polarity is reversed compared to most other organic photovoltaic devices, where holes flow towards the ITO. In the case of the Al electrode, the sign of the short circuit current (i.e., the polarity of the device) was reversed, as would be expected from the opposite sign of V_{BI}. In this case positive charges will be attracted to the ITO and electrons to the Al contact, reversing the direction of the current (see Figure 3.5)

The shape of the EQE spectrum of both the Pt and Au contacted devices resembles the absorption spectra of both polymer and TiO_2, while the EQE of the Al device resembles only the TiO_2 absorption spectrum. This suggests that the electron transport in the polymer is better than hole-transport in the TiO_2. (The hole-mobility in the porous TiO_2 was too low to be measured[129]). TiO_2 is known to trap holes at surface states, and this will be an important effect in nanocrystalline TiO_2. A second factor is the relatively high background doping of the weakly n-type TiO_2 compared to the intrinsic polymer, which will tend to reduce the magnitude of the built-in electric field in the TiO_2 layer. Therefore the built-in voltage in the Al device helps the photo-generated electrons in TiO_2 travel through the polymer to the Al electrode, while photo-generated holes in F8T2 do not reach the ITO electrode through TiO_2 due to the very poor hole-transport in the TiO_2. Therefore the EQE of the Al device only resembles the absorption of the TiO_2. On the other hand, in the Au contacted device, the built-in voltage, hole mobility of polymer and electron mobility of TiO_2 all favour hole transport through polymer and electron transport through TiO_2, with the result that the EQE spectrum resembles the absorption spectrum of both materials. The much lower external quantum efficiency observed for Al compared to Au or Pt device implies that hole transport in TiO_2 and electron transport in F8T2 is poor compared to hole transport in F8T2 and electron transport in TiO_2.

For efficient charge collection in TiO_2 / polymer devices, high work function materials must be used for the hole collecting contact.

3.4 Charge separation and recombination kinetics

The present and the next two sections address the influence of interfacial area and layer thickness on charge separation and photocurrent generation in TiO_2/F8T2 structures. To increase the interfacial area and so the number of charge dissociation sites, we modified the bi-layer structure by incorporating an additional porous TiO_2 layer between the dense TiO_2 layer and F8T2 polymer film to create a tri-layer. We studied polymer penetration into the porous film using transient optical spectroscopy.

Figure 3.6 shows the absorption spectrum of chemically oxidized F8T2 polymer and the transient absorption spectrum of a structure consisting of porous TiO_2 and F8T2 polymer at 10 μs after excitation by a pulse of wavelength 500 nm, intensity 50 μJ/pulse/cm^2. The transient optical spectrum, which peaks at 720 nm, is assigned to the positive polaron in F8T2. Detailed transient absorption studies were performed on pristine F8T2 films as control experiments (excitation at 500 nm and probe at 720 nm). These studies reveal no evidence of any absorption feature, which could be assigned to the triplet, for instance, on the time scale of the charge recombination dynamics (0.1 μs - 100 ms). Therefore, the decay in absorbance as a function of time after the excitation is attributed to recombination of F8T2 polarons with electrons to the TiO_2 by photoinduced charge transfer.

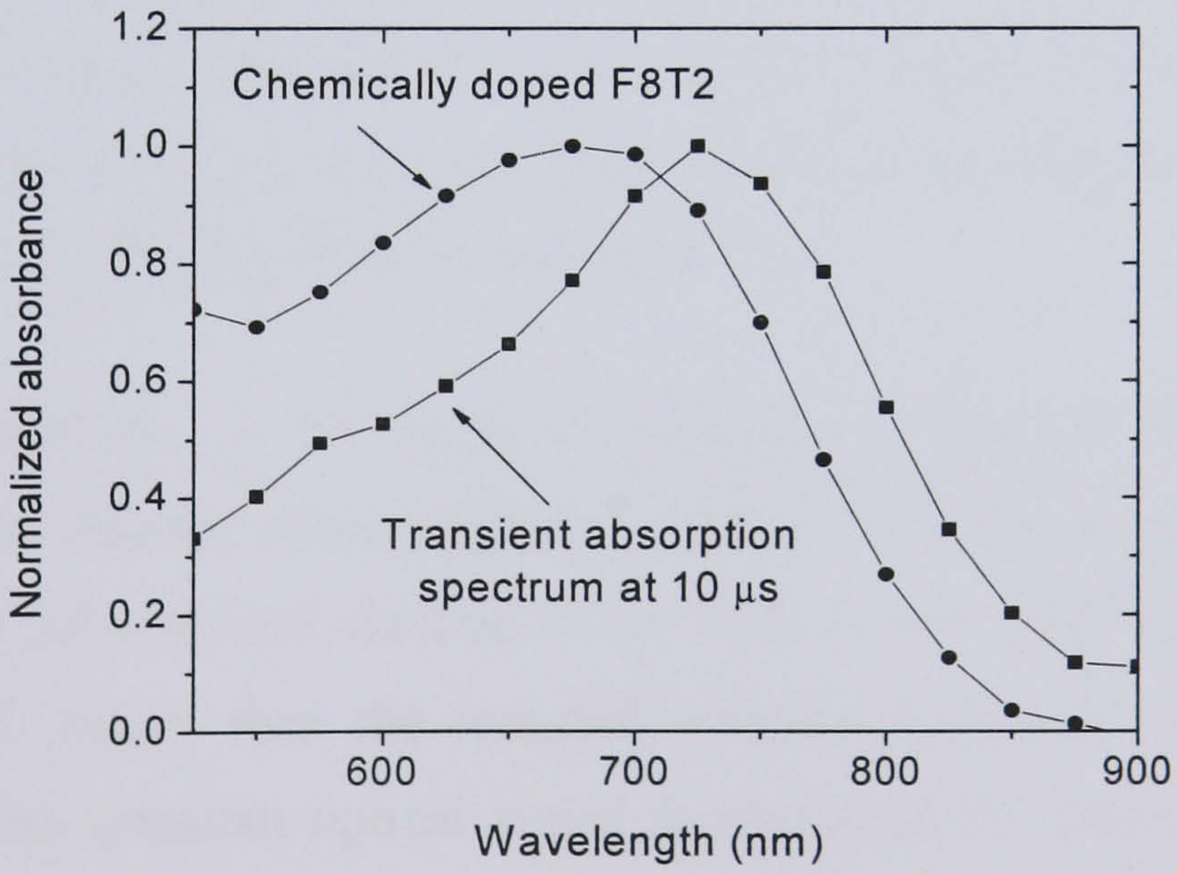


Figure 3.6 *F8T2 cation absorption spectra recorded following chemical oxidation with $FeCl_3$ (circles) and following photoinduced charge separation (squares). The former was measured in solution (toluene) and in the presence of $FeCl_4^-$ counter ions.*

In the first studies of recombination kinetics, two different thicknesses, 100 nm and 600 nm, of additional porous TiO_2 layers were used. We first discuss the charge separation and photocurrent generation studies in the thick tri-layer structure. The transient absorption kinetics for the thick TiO_2 / F8T2 structure on a logarithmic time

scale under excitation pulse intensity of about 50 μJ/pulse/cm^{-2} (corresponding to 1.26 x 10^{14} incident photons /pulse/cm^2) is shown Figure 3.7. The samples were excited at 500 nm, the wavelength corresponding to maximum absorption of the polymer, and the decay of the transient signal, corresponding to the decay of F8T2 polarons, was measured at 720 nm. The inset of Figure 3.7 shows the sample structure for the transient absorption measurement.

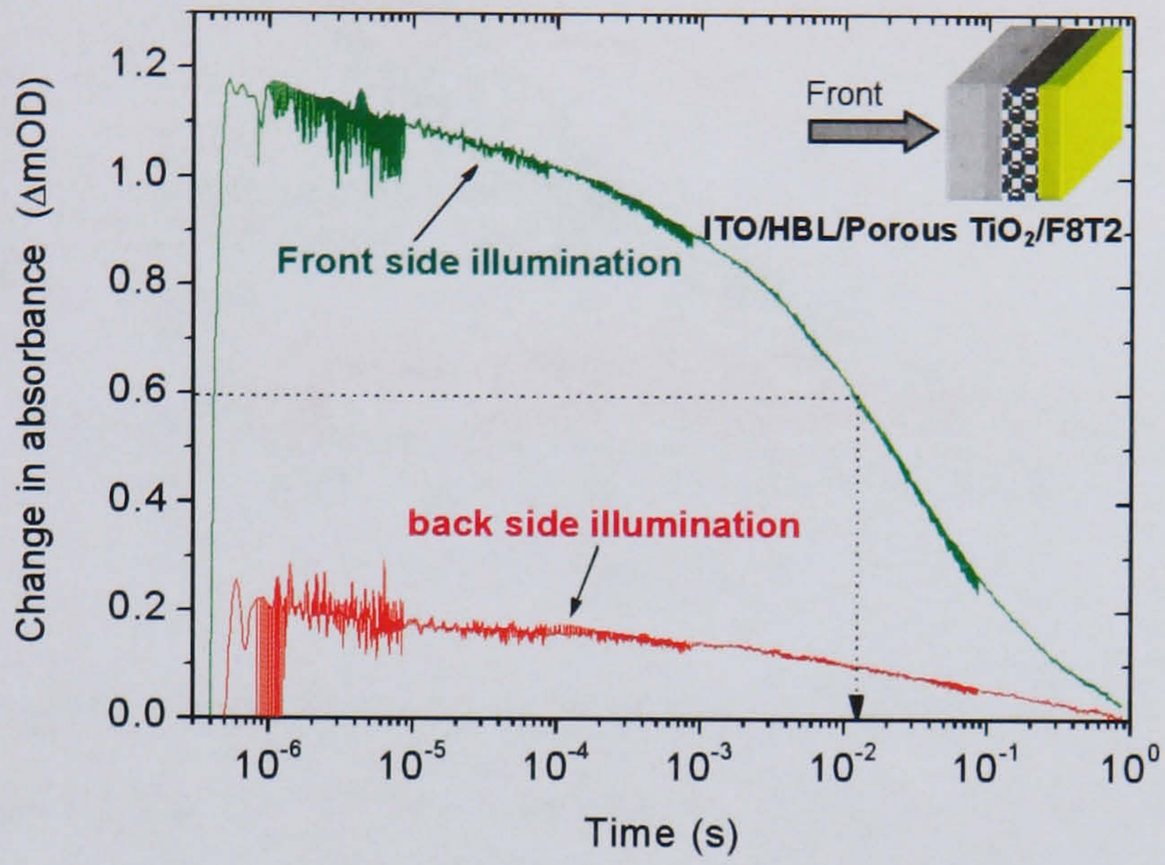


Figure 3.7 *Transient absorption kinetics following the positive polaron state of F8T2 on a TiO_2 nanocrystalline layer. The insert shows the sample structure for this measurement. The excitation density is about 50 μJ / pulse / cm^2 at 500 nm and the decay is assigned to recombination between electrons in TiO_2 and F8T2$^+$ polarons. Data were collected using a probe wavelength of 720 nm, corresponding to the absorption maximum of F8T2$^+$ polarons, at room temperature. HBL stands for hole blocking layer.*

The magnitude of the transient absorption signal of the structure, indicates efficient charge transfer from polymer to TiO_2. Recombination between the positive polaron in the polymer and electron in the TiO_2 is extremely slow with a half time of around 10 ms, longer than the reported recombination time in dye sensitized solar cells[48,52,130]. The transient optical signal is measured for illumination from the back (polymer side) and front sides. Comparison of these signals reveals the extent of polymer penetration into the film. The lower signal for back side than front side illumination indicates that less light reaches the charge separating interface for back side illumination. This is attributed to poor polymer penetration into the porous film, leaving a layer of polymer on the back side of the film which attenuates the light reaching the TiO_2 / polymer interface. To improve the pore penetration, the sample was annealed. The transient absorption kinetics and the corresponding device performance will be discussed in the next section.

3.5 Polymer penetration into porous TiO_2 by melt processing

3.5.1 Charge separation

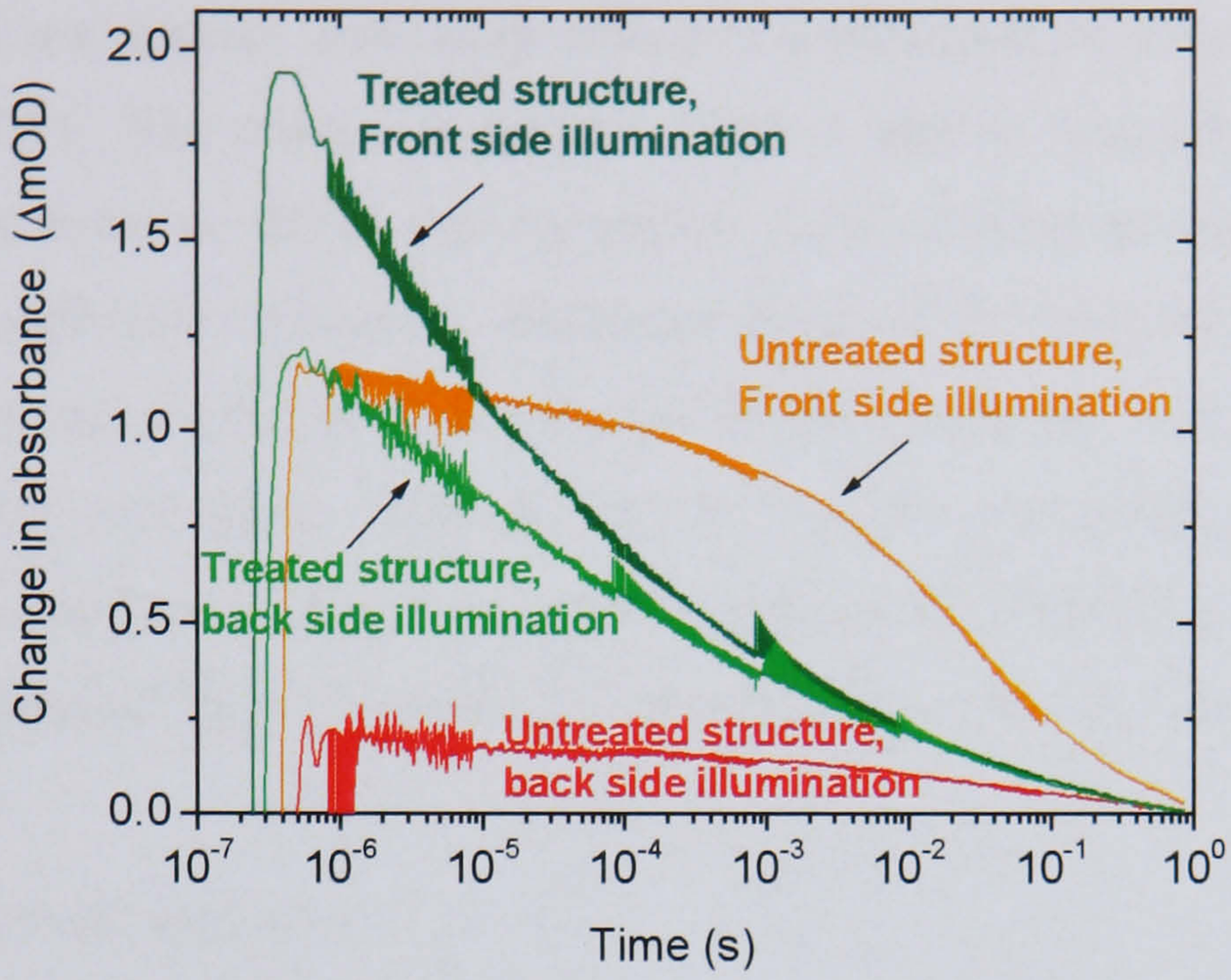


Figure 3.8 *Transient absorption due to the positive polaron state of the F8T2 polymer at 720 nm following laser pulse excitation at 500 nm, at an excitation density of 50 μJ / pulse / cm^2. The decay is assigned to recombination between electrons in TiO_2 and F8T2$^+$ polarons. Green colour curves represent transient absorption kinetics for an ITO / dense TiO_2 (100 nm) / porous TiO_2 (600 nm) / F8T2 (200 nm) structure which has been surface treated (porous TiO_2) and annealed (polymer on porous TiO_2). Red and orange curves are for an untreated structure. The difference between the response for front (TiO_2) and back (polymer) side illumination in the latter case shows that without additional treatments, the spin coated polymer does not penetrate into the thick (600 nm) porous TiO_2 layer.*

Figure 3.8 shows the transient absorption signal for two thick tri-layer samples with 100 nm hole blocking layer, 600 nm porous TiO_2 and 200 nm F8T2 polymer, under laser light intensity of about 50 μJ / pulse / cm^2. One sample was treated with titanium isopropoxide [$Ti(iPr)_4$] solution before spin-coating the polymer and was annealed at 300 °C to melt the spin-coated polymer into the pores. The polymer possesses a liquid crystal phase at 260 ^{0}C. The $Ti(iPr)_4$ surface treatment is intended to increase the OH- population on the surface of TiO_2 substrate in order to improve adhesion between TiO_2 surface and the polymer. The second sample (discussed in the previous section) was neither surface-treated nor annealed. In both cases the transient optical signal is measured for illumination from the back (polymer side) and front sides. Comparison of these signals reveals the extent of polymer penetration into the film. In the case of the untreated sample, the lower signal for back side than front side

illumination indicates that less light reaches the charge separating interface for back side illumination. For the treated and annealed sample, the signals for back and front side illumination are similar, indicating effective penetration of polymer into the highly structured TiO_2. The charge separation yield is higher, suggesting better interfacial contact. (We estimate the charge separation yield as close to unity from the polaron extinction coefficient). However, the faster decay of the signal for the treated sample indicates that recombination is accelerated by the treatments, with the polaron half life reducing from ~10 ms to ~100 μs. This is consistent with more intimate interfacial contact. Nevertheless the lower value still compares favourably with values reported for polymer-fullerene blends (1-100μs)[76,131] and solid dye sensitised solar cells[48,49,53,130].

3.5.2 Quantum efficiency

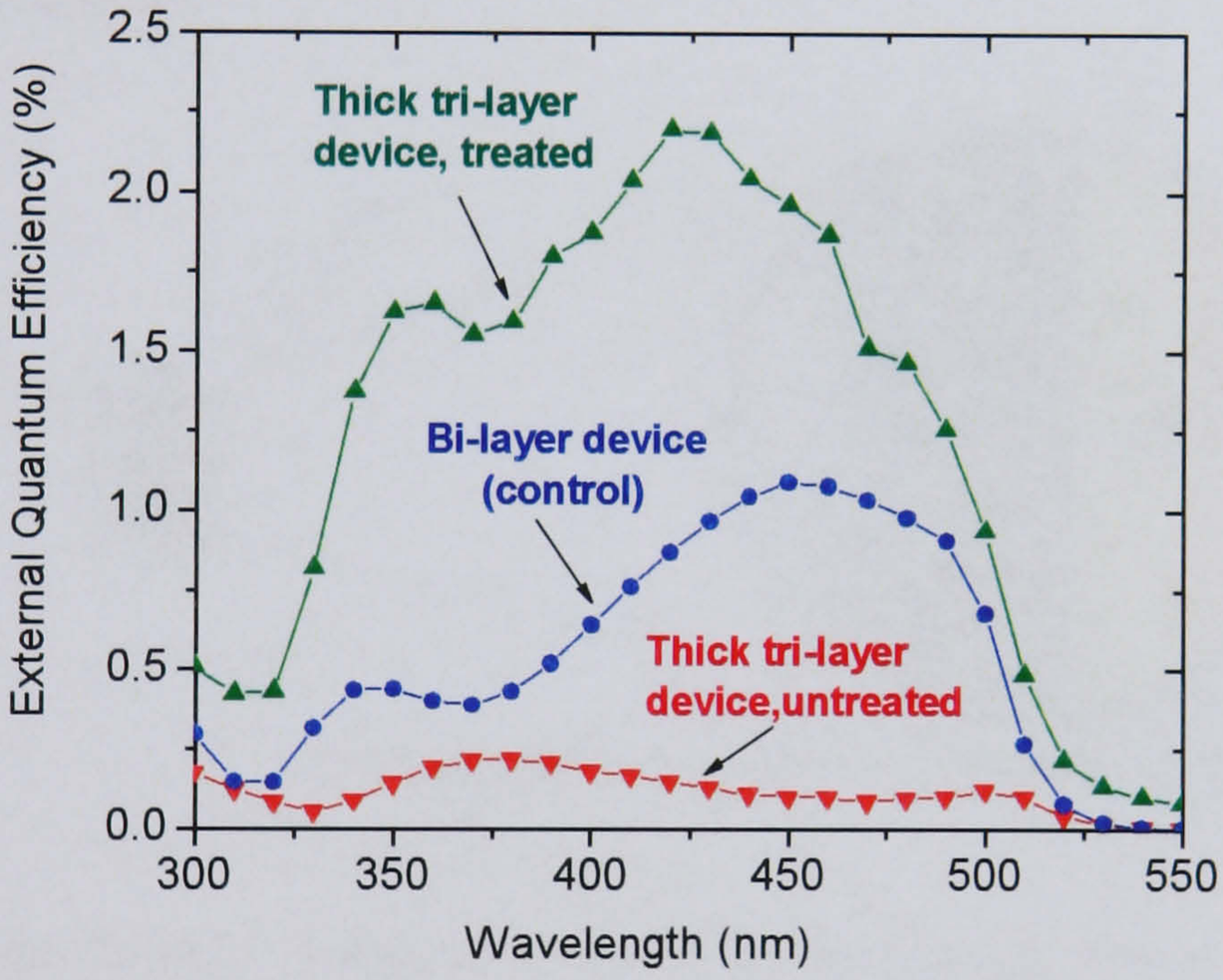


Figure 3.9 *External quantum efficiency spectra of bi-layer (control) treated and untreated tri-layer devices, showing the effect of treatment. Details of the structures and layer thickness of the corresponding devices are given in Table 3.1.*

EQE spectra of the corresponding treated and untreated tri-layer devices are compared with a control bi-layer device in Figure 3.9. All devices were contacted with Au contacts and illuminated through the ITO. Improved EQE upon introducing the porous layer is only achieved after the surface treatment and annealing steps. This is consistent with the evidence that such treatments are needed for polymer penetration into the pores of the TiO_2 in thick layer device (last section). Without these process steps, the EQE for the thick tri-layer device is worse than for the control (bi-layer deice)

probably due to the lower charge separation yield and the increased series resistance of the additional TiO_2 layer of thickness 600 nm.

Green photoluminescence from these thick tri-layer device is observed, when the device is illuminated with a blue monochromatic light of wavelength 470 nm. This is due to excitons, produced within the non-infiltrated polymer layer on top, recombining before they reach the interface. Figure 3.10 illustrates the recombination of an exciton produced near to the electrode and emission of a photon. Generally only excitons, which are generated within a few nm from the interface, are able to contribute to the current[132]. The others recombine before they reach an interface. Decreasing polymer layer thickness may reduce the recombination deep within polymer layer. Although decreasing thickness of the photoactive polymer leads to reduced absorption and exciton generation, it improves light harvesting because the extra absorption did not lead to charge separation.

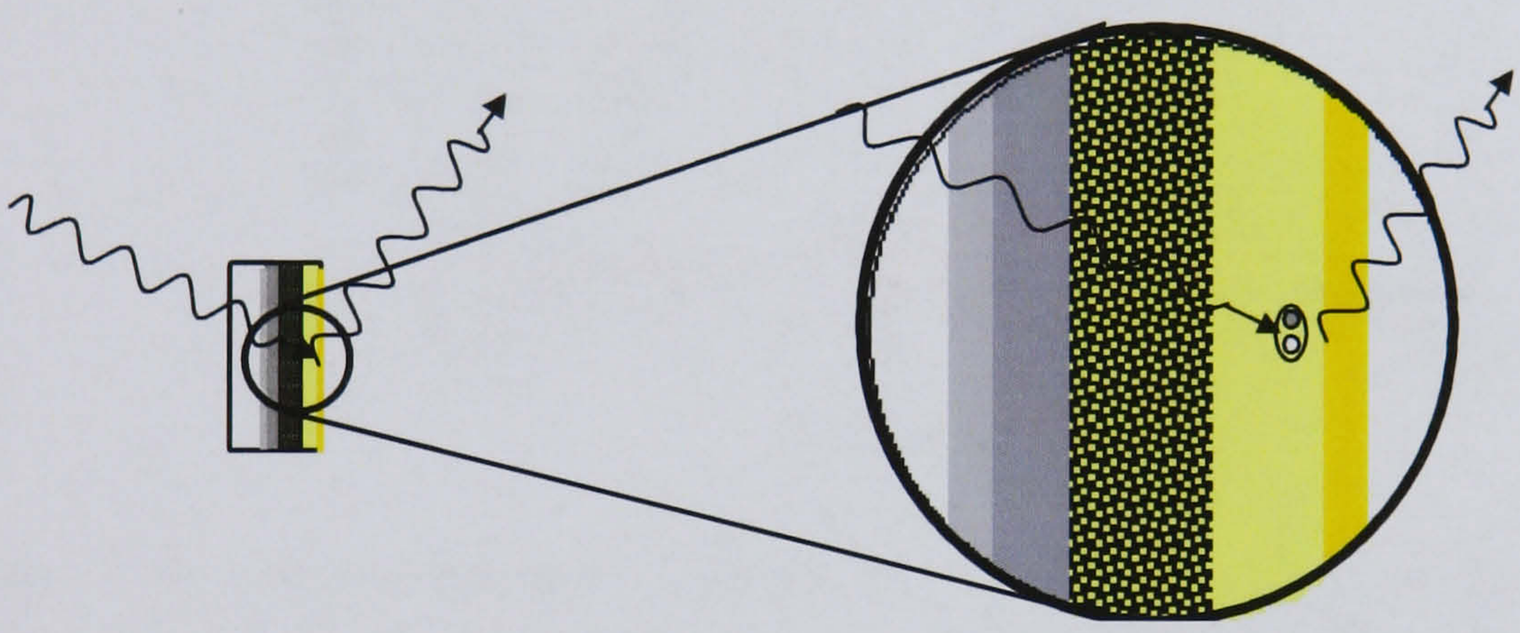


Figure 3.10 *Excitons produced deep within the polymer recombine before they exit the electrode and are responsible for photoluminescence in the sample.*

In the next section, we will discuss the photovoltaic performance of the thin tri-layer devices with reduced thickness of about 100 nm and show the melt processing step is not necessary for polymer infiltration in thin tri-layer devices.

3.6 Influence of device thickness and interfacial area

Here we look at the effect of the thicknesses of each of the layers in the tri-layer device on the EQE. We compare the following devices with the devices discussed in the previous section: a thin bi-layer device with 50 nm dense layer and a thin tri-layer device with 50 nm dense layer and 100 nm porous layer. EQE spectra of these devices are shown in Figure 3.9 & 3.11. The table summarises the layer thicknesses and peak EQE of theses devices. All devices were contacted with Au contacts and illuminated through the ITO.

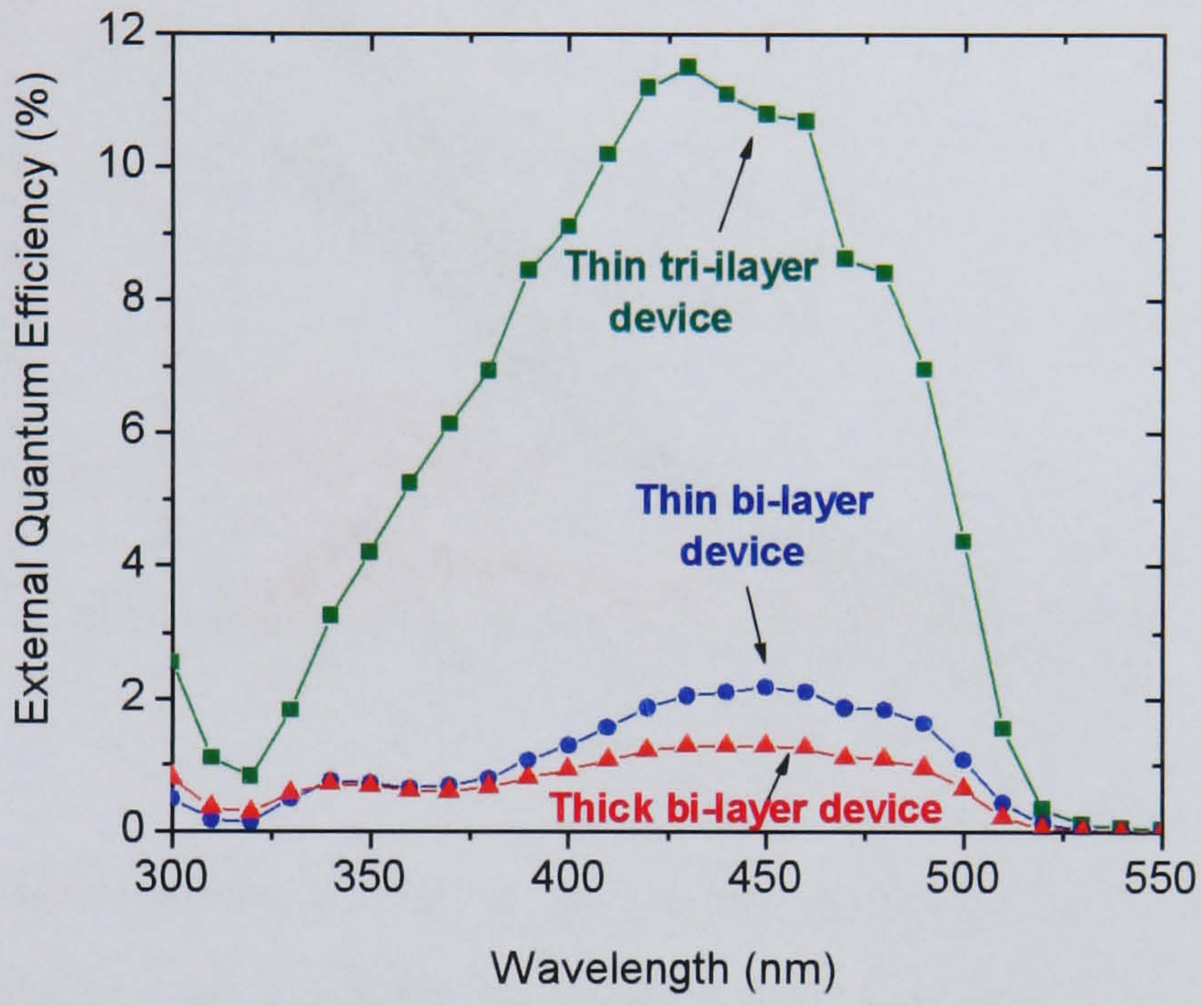


Figure 3.11 *External quantum efficiency spectra of ITO / TiO_2 / F8T2 / Au devices with different TiO_2 and polymer layer thickness and interfacial area. Details of the structures and layer thickness of the corresponding devices are given in Table 3.1.*

Table 3.1 Layer thicknesses and peak EQE of devices presented in Figures 3.9 & 3.13.

Devices	Dense TiO_2 Layer (nm)	Porous TiO_2 Layer (nm)	Polymer Layer(nm)	Peak EQE (%)
Thick bi-layer	100	-	100	**1.3**
Thin bi-layer	50	-	50	**2.2**
Thin tri-layer	50	100	75	**11.5**
Thick tri-layer, untreated	100	600	200	**0.2**
Thick tri-layer, treated	100	600	200	**2.2**

Comparing thin and thick bi-layer devices, the higher EQE of the thin bi-layer device can be attributed to reduced series resistance by the thinner TiO_2 and polymer layer. The thin bi-layer device shows peak quantum efficiency about 2.2 %, which is comparable to the treated sample discussed in the previous section, while the bi-layer

device with thick TiO_2 shows peak quantum efficiency 1.1 %. The majority of the charge dissociation occurs at the TiO_2 / polymer interface and the electrons must traverse the thickness of the TiO_2 film to reach the ITO. The electrons meet less resistance on their way to the electrode in thin TiO_2 layer device than thick TiO_2 device. The higher quantum efficiency of the thin bi-layer device may therefore be due to reduction of serial resistance of the thick dense layer.

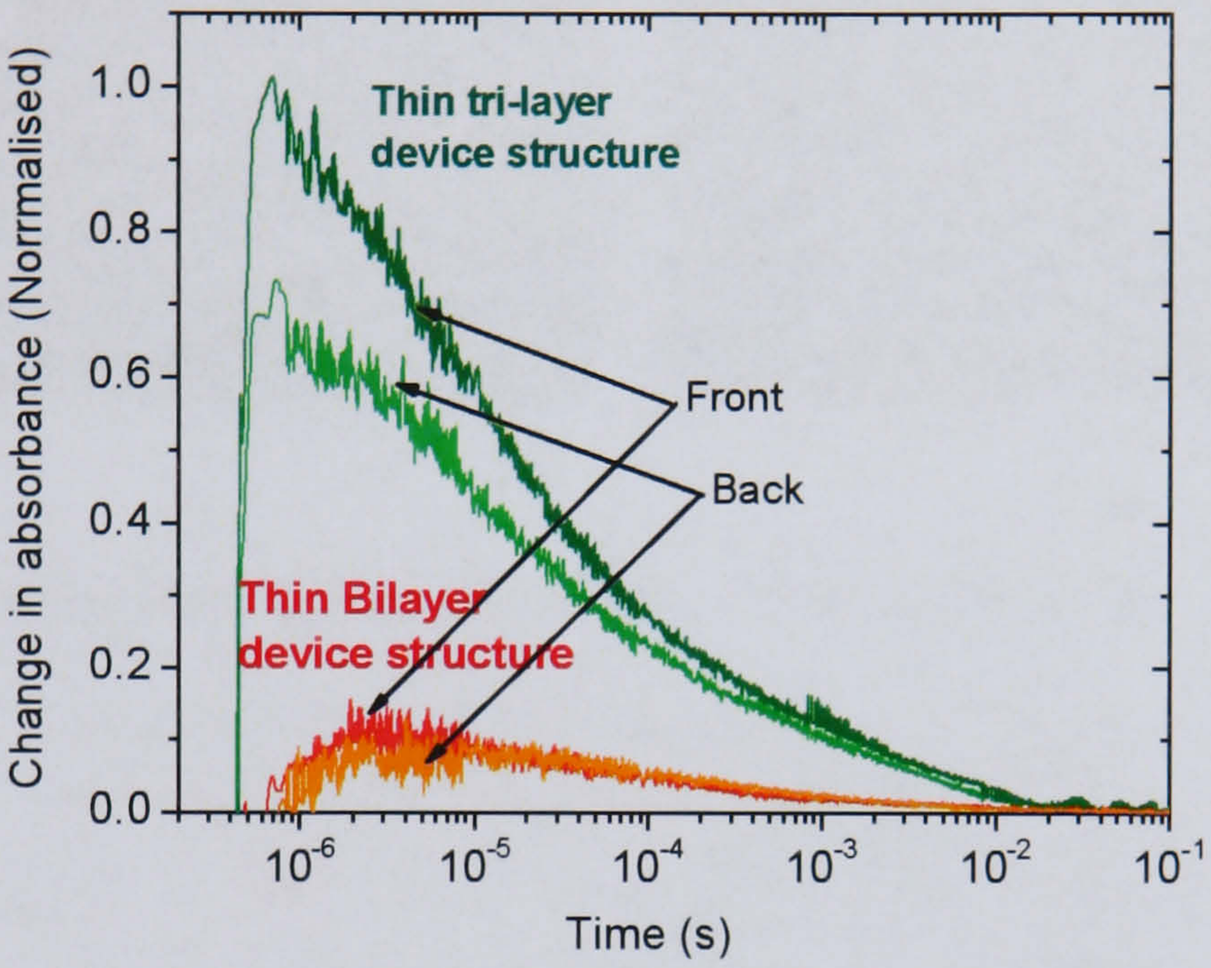
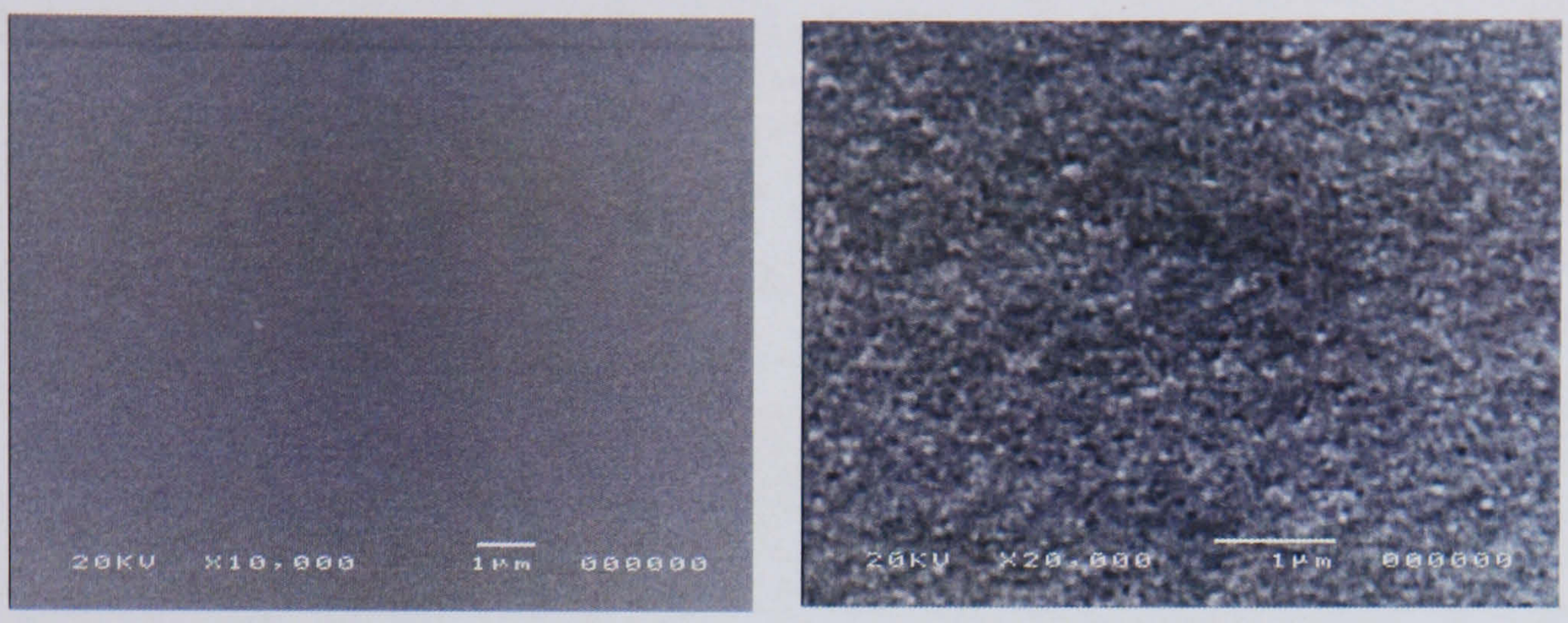


Figure 3.12 *Transient absorption due to the positive polaron state of the F8T2 polymer at 720nm following laser pulse excitation at 500nm, at an excitation density of 30 μJ/pulse/cm^2. The decay is assigned to recombination between electrons in TiO_2 and F8T2$^+$ polarons. Red (front) and orange (back) curves represent transient absorption kinetics for an ITO / dense TiO_2 (50 nm) / F8T2 (50 nm) bi-layer structure. Green curves are for ITO / dense TiO_2 (50 nm) / porous TiO_2 (100 nm) / F8T2 (50 nm) tri-layer.*

Next a thin porous layer (100 nm) is introduced into the thin bi-layer device. Figure 3.11 shows how this increases the EQE by a factor of five, to reach a peak EQE of 11.5 % at 440 nm. The improved quantum efficiency of the tri-layer devices may be attributed to increased interfacial area due to the presence of the porous TiO_2 layer. The increased interfacial area increases the charge separation yield. Figure 3.12 shows that the magnitude of the transient absorption signal increases by a factor of 5-7 on insertion of the porous TiO_2 layer in the bi-layer structure. The similar kinetics obtained in the tri-layer device for both front and back-side illumination confirms that the polymer infiltration is effective in the thin tri-layer device structure and suggests that the additional melt processing step is not necessary in thin tri-layer devices. In fact, the thin tri-layer device with melt processing step shows worse device performance. High-

resolution SEM images of dense and porous layers shown in figure 3.13 confirmed that the surface roughness is increased by adding the porous TiO_2 layer. This effect enhances the area available for exciton dissociation.



(a) (b)

Figure 3.13 *SEM images of (a) dense TiO_2 layer (b) porous TiO_2 layer*

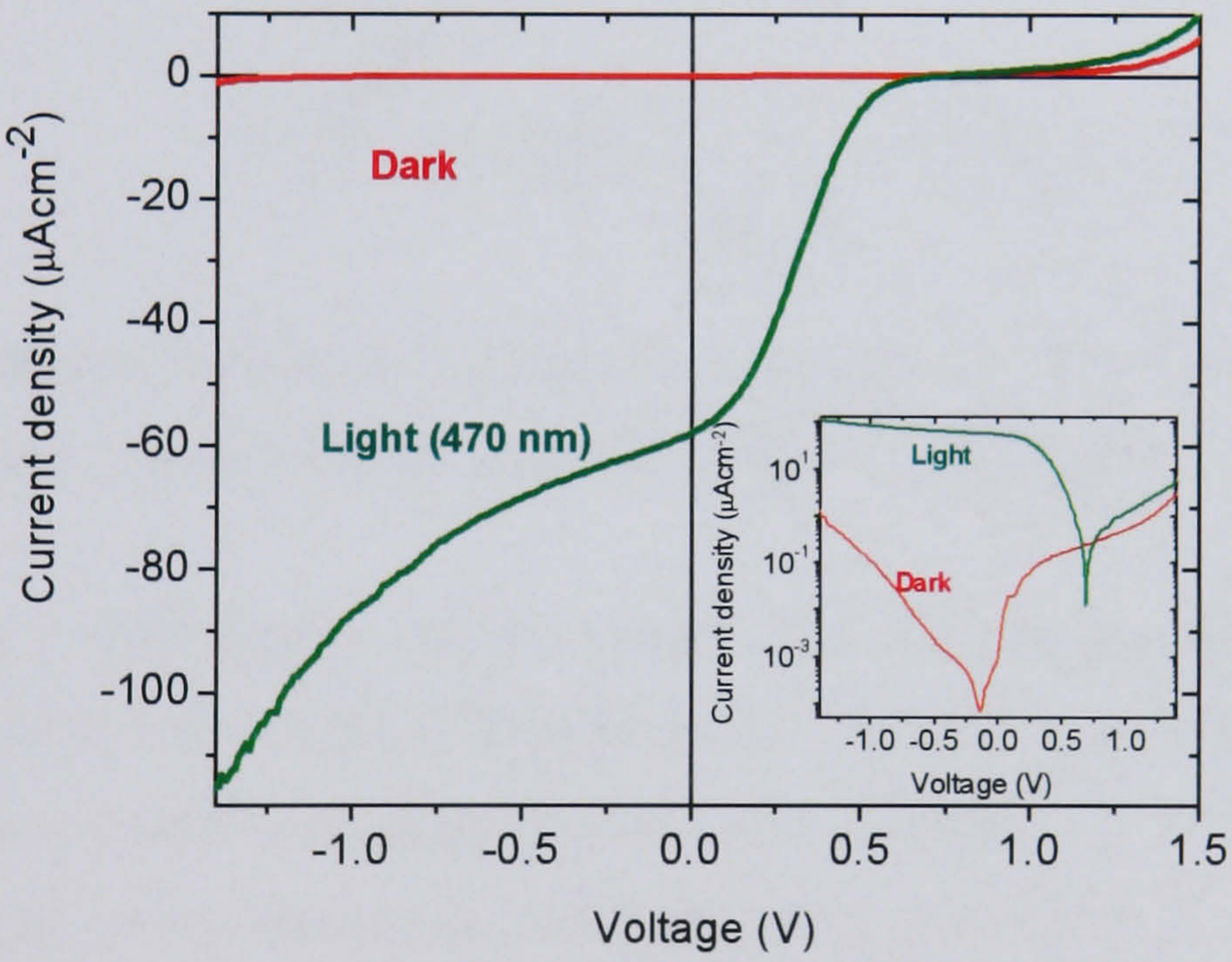


Figure 3.14 *Current density – voltage (J-V) characteristics of the thin tri-layer device, ITO / HBL / porous TiO_2 (100 nm) / F8T2 (75 nm) / Au in dark (red) and under illumination of wavelength of 470 nm and an intensity 1 $mWcm^{-2}$. Inset shows semi-logarithmic J-V characteristics of the device in dark (red) and under illumination of wavelength of 470 nm and intensity 1 $mWcm^{-2}$.*

Figure 3.14 shows the photovoltaic properties of the thin tri-layer device (ITO / HBL (50 nm) / porous TiO_2 (100 nm) / F8T2 (75 nm) / Au). The device produced an open circuit voltage, V_{OC} of 0.65 V, fill factor, FF of 0.30 and a short circuit current density 58 μAcm^{-2} under illumination by monochromatic wavelength of 470 nm and an intensity of 1 $mWcm^{-2}$. The corresponding power conversion efficiency of the device is

over 1 % under monochromatic light of wavelength 470 nm and intensity about 1 $mWcm^{-2}$. The photocurrent density increased by a factor of 2 at –1.4 V compared to the short circuit photocurrent density under the same conditions. The effect of the bias indicates an improvement in the efficiency of collecting separated charges in the device or may indicate injection under reverse polarity. However, photocurrent starts to fall off before the open circuit voltage. In the dark, the device shows weakly rectifying behaviour, with a forward bias turn on at around 1.0 V.

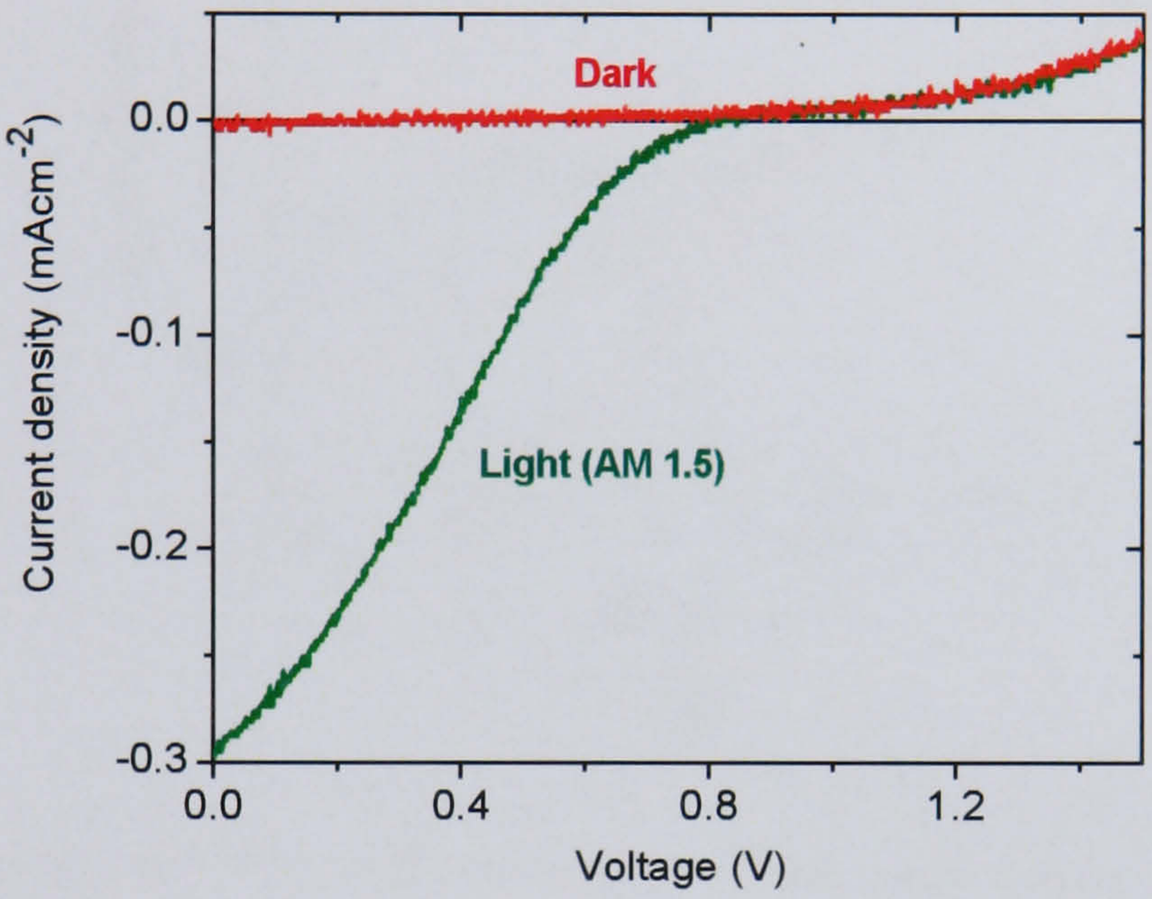
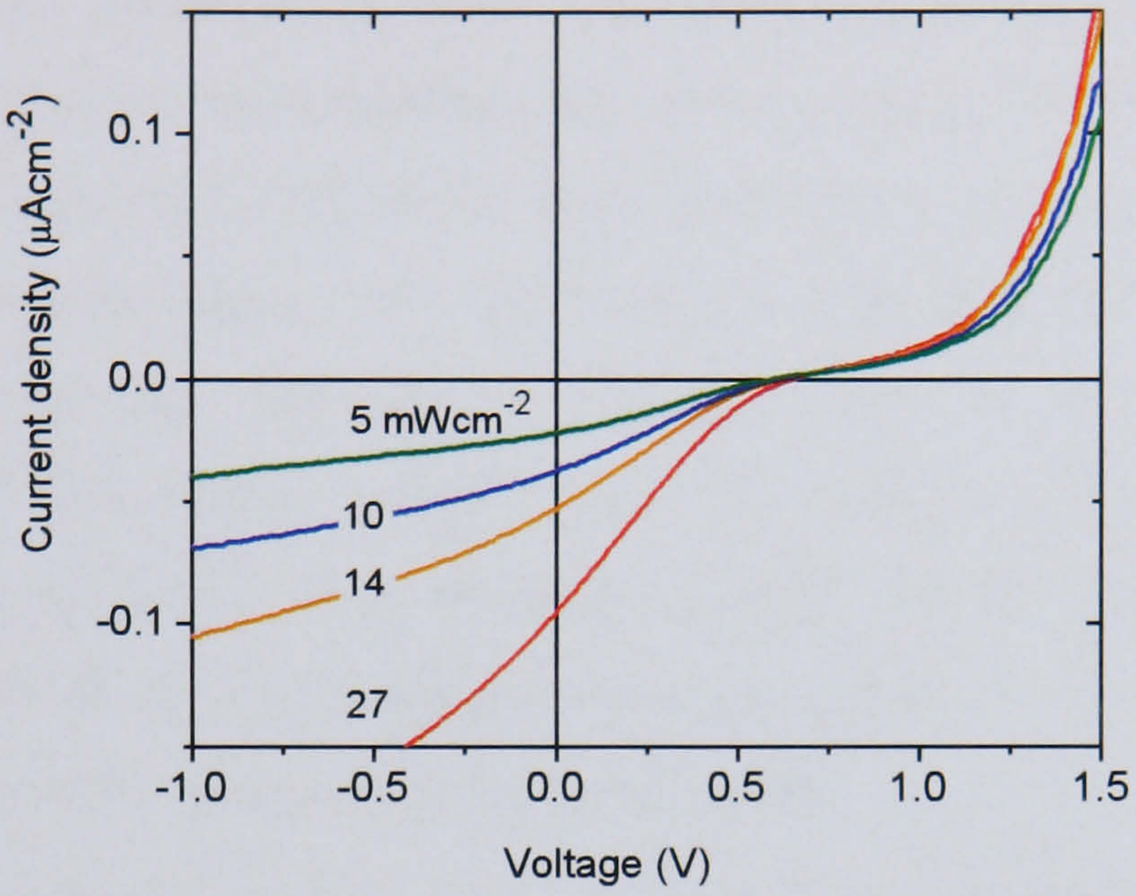


Figure 3.15 *J-V characteristics of the thin tri-layer device, ITO / HBL / porous TiO_2(100 nm) / F8T2(75 nm) / Au, under air mass (AM) 1.5 conditions (100 $mWcm^{-2}$, 1 sun) and in dark.*

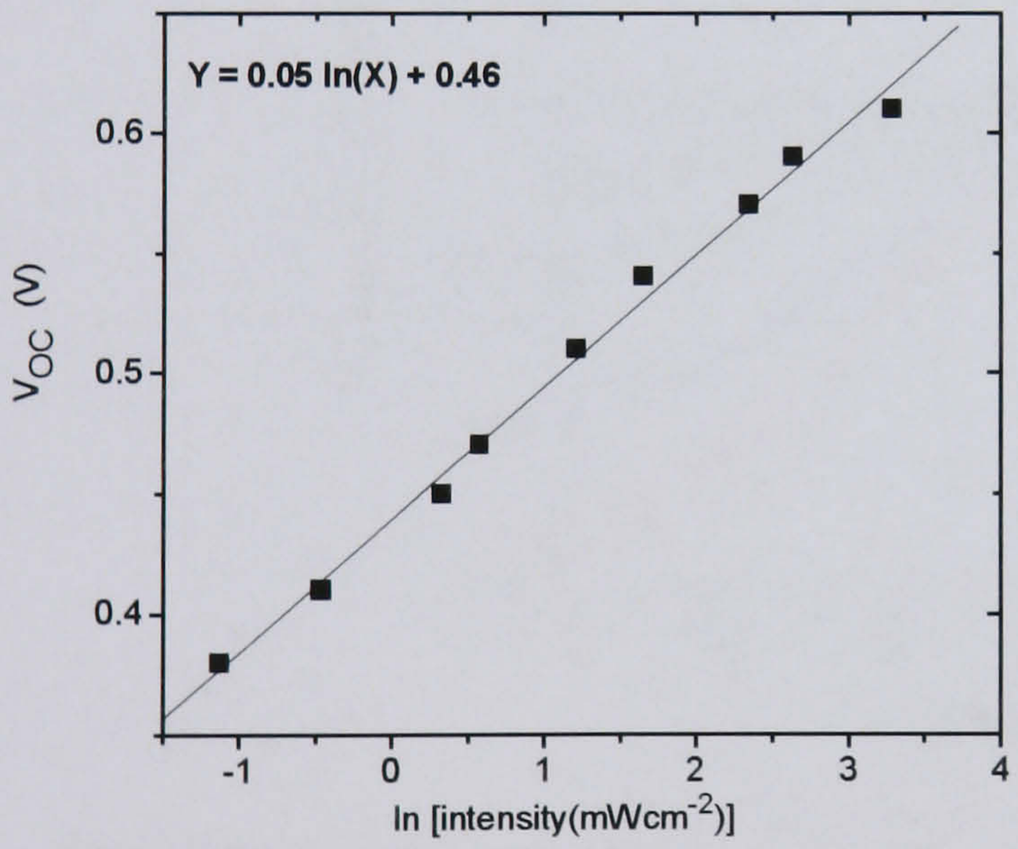
The current density-voltage characteristics of the thin tri-layer device under air mass (AM) 1.5 conditions (100 $mWcm^{-2}$, 1 sun) and in the dark are shown in Figure 3.15. The device produced good open circuit voltage V_{OC} of 0.8 V and a reasonable short circuit current density J_{SC} of 0.3 mA cm^{-2} under AM 1.5 conditions. However, the current falls off before reaching V_{OC}, leading to a point of inflection or 'kink' in the J-V characteristics and low fill factor FF (0.24) as we observed under monochromatic conditions and a low η of 0.06 %. This 'kink' in the J-V characteristics is also observed in bi-layer devices with Au as a top contact (see, Figure 3.16). Similar shapes of J-V characteristics have been observed elsewhere for polymer / TiO_2 structures[16,21,133] (see, Figure 1.11 and 1.12) and molecular film solar cells[59] (see, Figure 1.8). We will investigate the origin of this effect by varying light intensity, wavelength, alternative polymer and different metal contact in the next sections.

3.7 Effect of light intensity

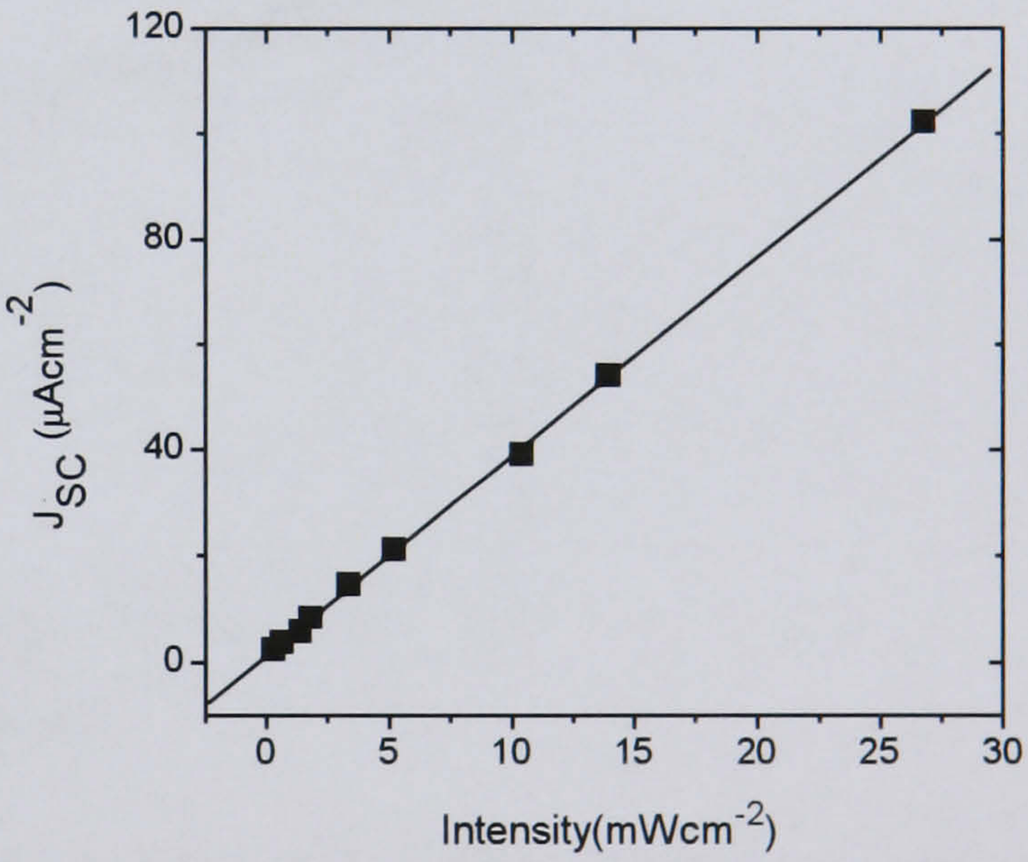
In this section we examine the kink in the J-V characteristic of the bi-layer device (ITO / dense TiO_2 (50nm) / F8T2 (50 nm) / Au) by varying the light intensity (both monochromatic and solar light) and wavelengths with the same photocurrent generation rate.



(a)



(b)



(c)

Figure 3.16 *(a) J-V characteristics as a function light intensity under monochromatic laser illumination of wavelength 404 nm for a bi-layer device (ITO / dense TiO_2 (50nm) / F8T2 (50 nm) / Au). (b) and (c) show open circuit voltage (V_{OC}) and short circuit current density (J_{SC}) as a function of the monochromatic laser light intensity for the bi-layer device respectively.*

Figure 3.16 (a) shows the J-V characteristics of a bi-layer device (ITO / dense TiO_2 (50nm) / F8T2 (50 nm) / Au) with different laser intensities, I_{in} of wavelength 404 nm). The bi-layer device was chosen to simplify the analysis. Since the kink in J-V

characteristic is present even in bi-layer device, the effect is not due to porous layer. Figure 3.16 (b) & (c) show open circuit (V_{OC}) and short circuit current density (J_{SC}) of the bi-layer device as a function of the monochromatic laser light intensity respectively. The power law ($J_{SC} \propto I_{in}^{\alpha}$) fit to the data and shows a nearly linear ($\alpha \approx 0.87$) intensity dependence of the photocurrent. The near-linear dependence of the photocurrent indicates that bimolecular recombination is minimal compare to charge collection.

The Figure 3.16 (a) further shows that the fill factor of the device is poor at high intensity under monochromatic light. The kink in J-V becomes more pronounced under increasing monochromatic light intensity. Similar behaviour is observed in the J-V characteristics of thin tri-layer device under the solar simulator at different light intensities (see, Figure 3.17). These observations show that the kink in the J-V curves is not due to an effect of charge trapping in the system, since such effects would become less important, not more, at higher illumination levels.

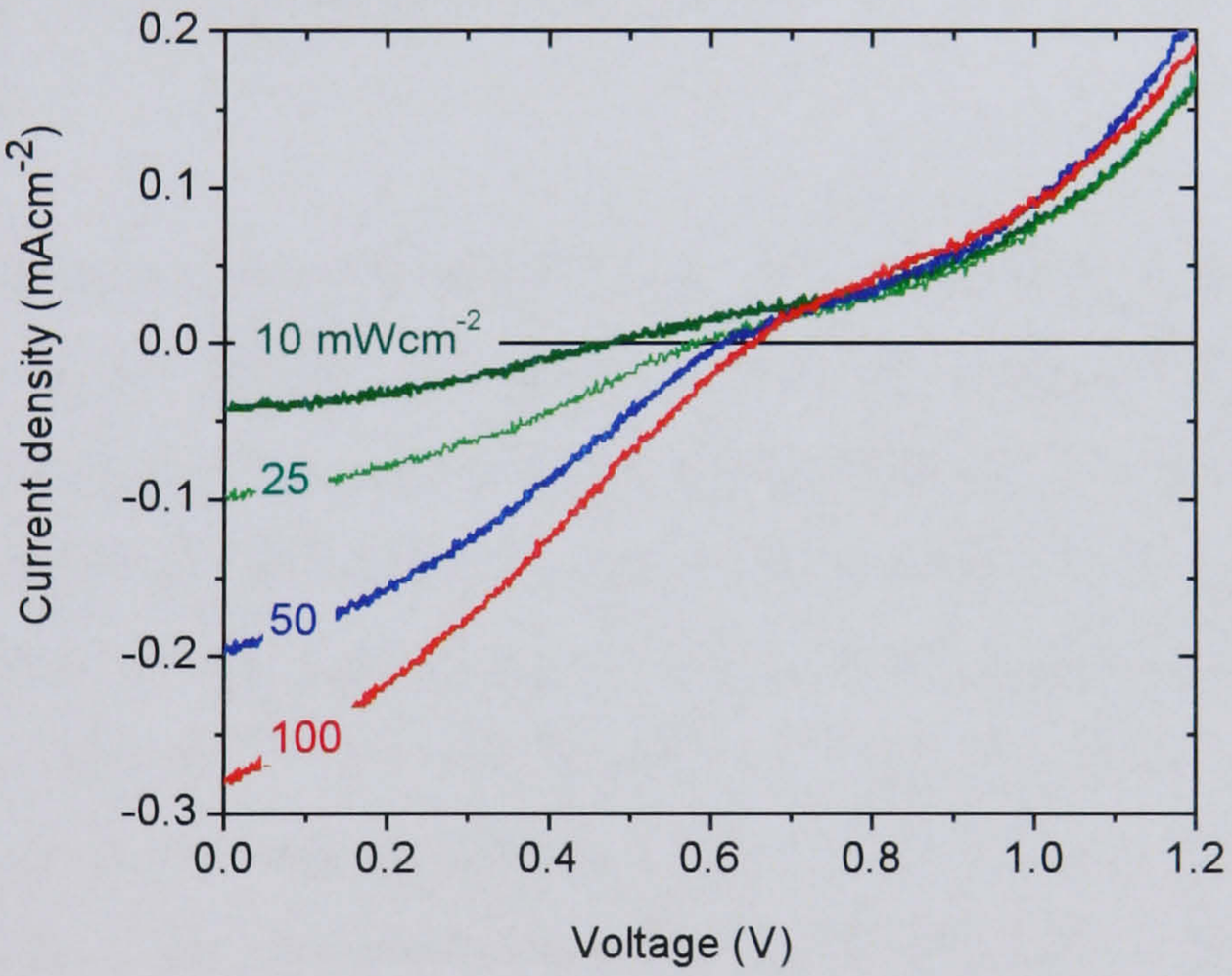


Figure 3.17 *J-V characteristic of the thin tri-layer device (ITO / dense TiO_2 (50 nm) / porous TiO_2 (100 nm) / F8T2 (75 nm) / Au) under simulated sun light of different intensities.*

In order to study whether the effect is related to a diffusive driving force for photocurrent generation, J-V curve (see Figure 3.18) was measured under different monochromatic wavelengths while keeping the same photocurrent density. At 470 nm, most light is absorbed near to the front of the device and the diffusive force driving electrons and holes to the counter electrode is strongest, while at 420 nm and 510 nm the absorption coefficient, and hence driving force is much weaker. However, Figure 3.18 shows that varying the wavelength from 470 nm to 510 nm, which changes the

absorption depth from 2.9×10^5 to 1×10^5 cm^{-1}, had no observable effect on the shape of the curve.

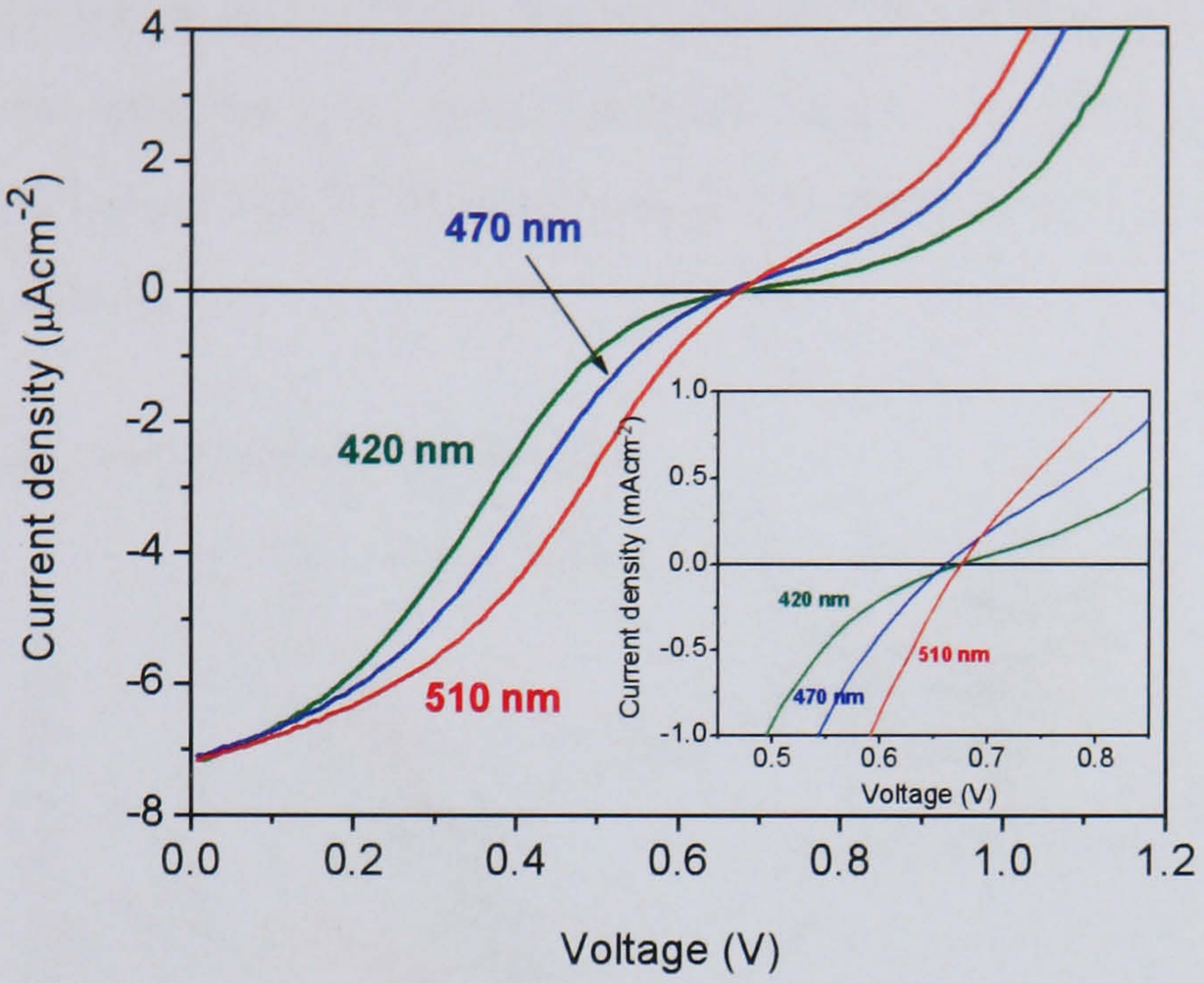


Figure 3.18 J-V *characteristics of ITO / dense TiO_2 / F8T2 / Au under monochromatic illuminations.*

In summary, we have investigated the kink in the J-V curve of ITO / TiO_2 / F8T2 / Au devices under different wavelengths, and light intensity. The feature persists at different wavelength indicating that the kink is not a result of the spatial distribution of photogeneration rate, and under increasing light intensity, indicating that it is not due to charge trapping. The kink may however be due to the energy barrier at the polymer-gold interface. In section 3.9, we will discuss J-V measurement on bi-layer devices made using polymers with different ionization potential compared to the work function of the gold electrode. In the next section, we will discuss the effect of dip treatment on device performance.

3.8 Improvement of fill factor by dip treatment

The effect of dip-coating the TiO_2 with polymer before spin coating the polymer will be discussed in this section. To introduce a dip coated layer between the porous TiO_2 electrode and the spin coated polymer layer, the porous TiO_2 electrodes were immersed in a solution of F8T2 in toluene (~1 mg/ml) at 50 ^{0}C for 18 hours prior to spin coating the polymer.

3.8.1 Charge recombination kinetics

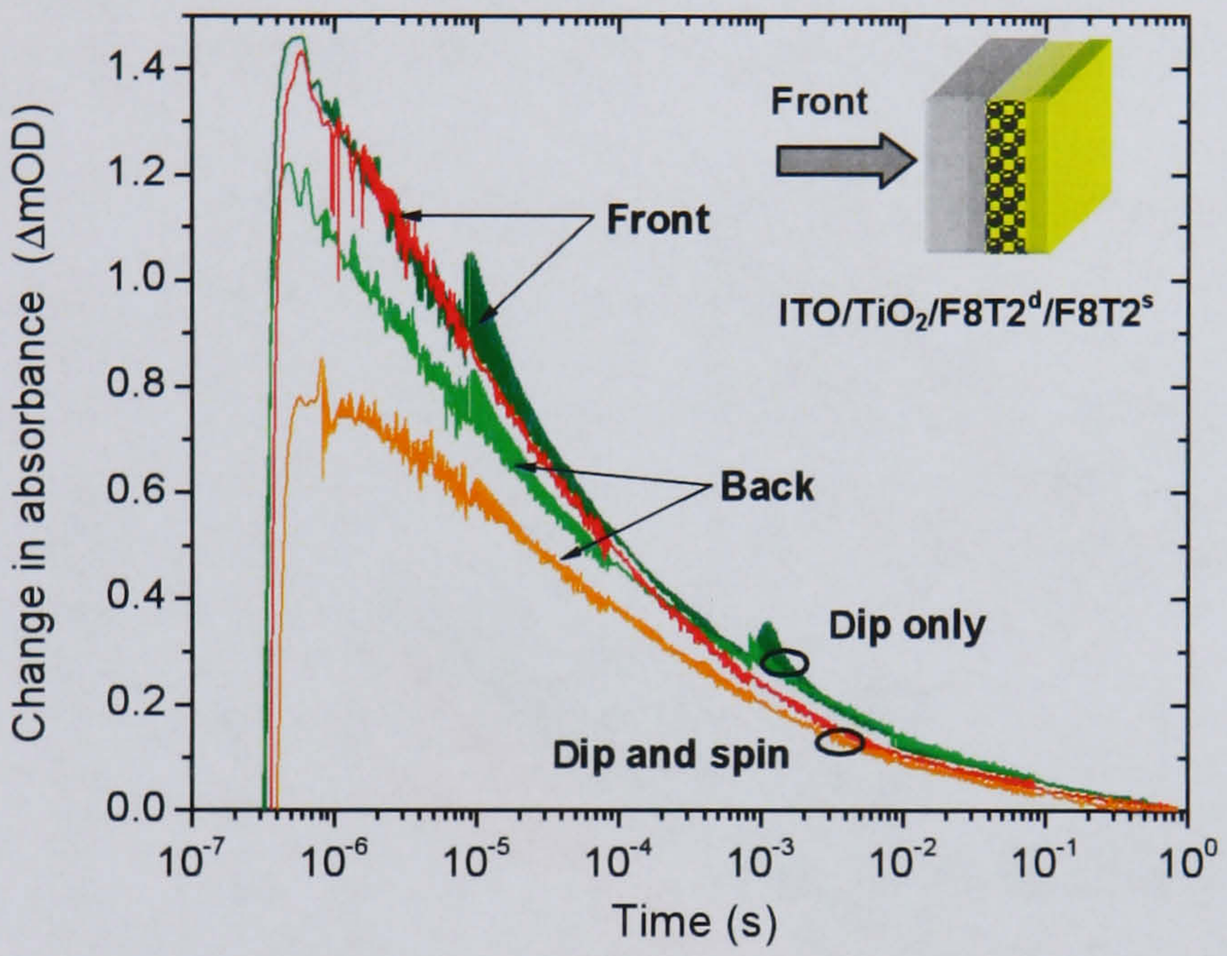


Figure 3.19 *Transient absorption signals for ITO / HBL / porous TiO_2 (100 nm) / F8T2^d and ITO / HBL / porous TiO_2 (~100 nm) / F8T2^d / F8T2^s (75 nm), where superscript d indicates 'dip coated' and s, is 'spin coated'. The inset shows the sample structure. The transient absorption due to the positive polaron state of the F8T2 polymer at 720nm following laser pulse excitation at 500nm, at an excitation density of 30 μJ/pulse/cm^2. The decay is assigned to recombination between electrons in TiO_2 and F8T2$^+$ polarons. Green (front) and light green (back) colour curves represent transient absorption kinetics for dip coated structure, while red (front) and orange (back) colour curves represent transient absorption kinetics for dip- and spin-coated structure.*

Figure 3.19 compares the recombination kinetics of samples consisting of ITO / HBL / Porous TiO_2 (100 nm) / F8T2^d and ITO / HBL / porous TiO_2 (100 nm) / F8T2^d / F8T2^s (75 nm), where the superscript d indicates 'dip coated' and s, is 'spin coated'. The absorbance of dip-coated structure was similar to the structure with both dip- and spin coated polymer. This is probably due to spin coating of polymer on dip-coated electrode removes some of the dip coated polymer layer. Since the size of transient absorption signal for the structure, which is dipped only is similar to the signal for

structure which is both dip- and spin coated; we infer that the charge separation occurs very close to the TiO_2 nanocrystal-polymer interface. We estimate the charge separation yield as close to unity from the extinction coefficient of the polymer. The similar shape of the recombination kinetics for back and front side illumination in the dip-coated sample indicates that effective polymer penetration is achieved by dip coating. Since excess polymer would leave a layer of polymer on the back-side of the film, a lower signal is observed due to in dip and spin coated structure. The lower signal for back side illumination of the dip and spin coated structure is attributed to the filtering of pulse light by the excess polymer, which may be deposited on top of the film by spin coating.

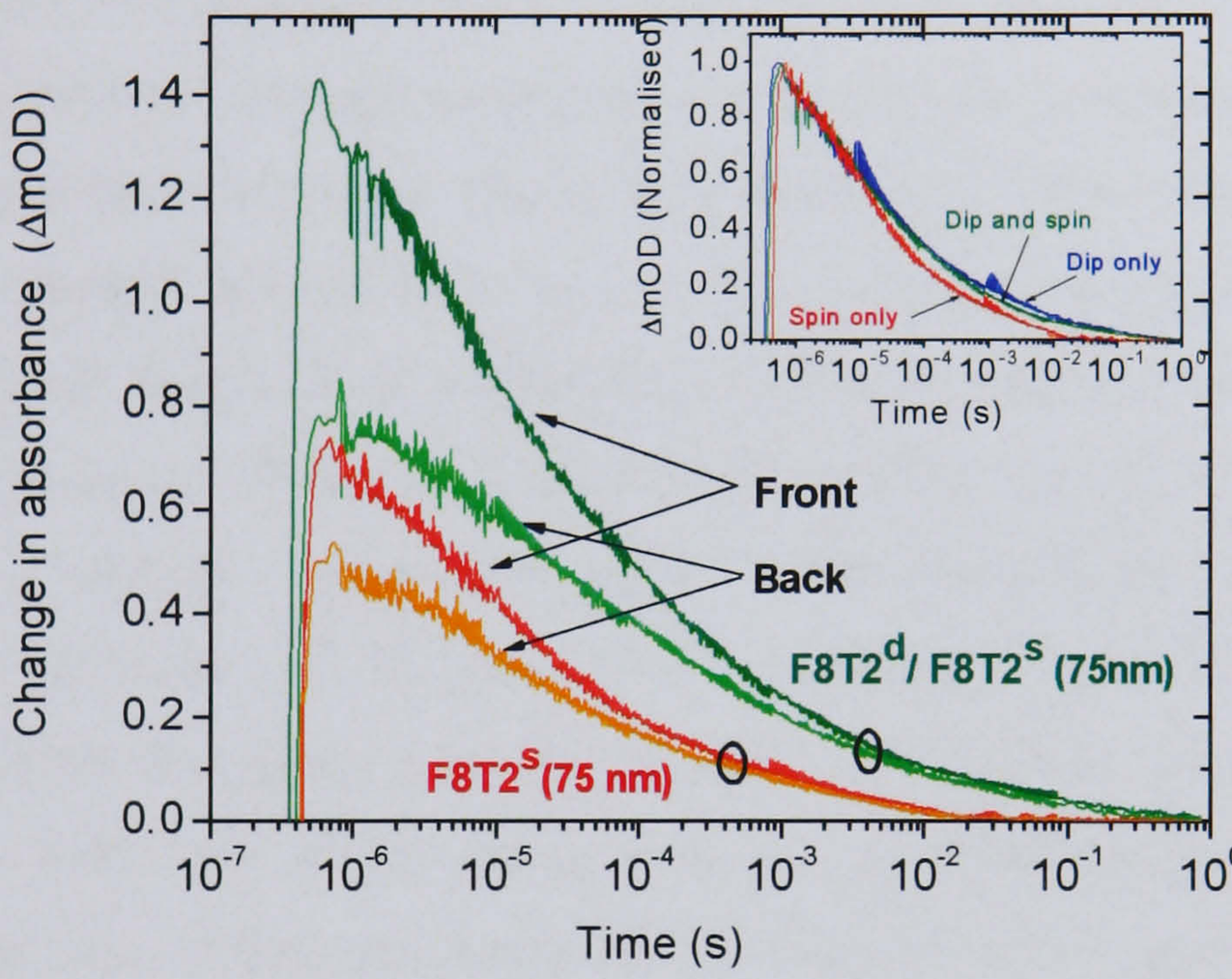


Figure 3.20 *Transient absorption signals for ITO / HBL / porous TiO_2 (~100 nm) / $F8T2^d$ [red(front) and orange(back) colour curves] and ITO / HBL / porous TiO_2 (~100 nm) / $F8T2^s$ (75 nm) [green(front) and light green (back) colour curves], when the structures illuminated from both TiO_2 side (front) and polymer side (back), where superscript d indicates 'dip coated' and s, is 'spin coated'. Inset shows the normalised transient absorption signals for ITO / HBL / porous TiO_2 (~100 nm) / $F8T2^d$ / $F8T2^s$ (75 nm) structures: dip-coated F8T2 (blue curve), spin-coated F8T2 (red curve) layers and both (green curve), when the structures illuminated from TiO_2 side. The transient absorption due to the positive polaron state of the F8T2 polymer at 720nm following laser pulse excitation at 500nm, at an excitation density of 30 μJ/pulse/cm^2. The decay is assigned to recombination between electrons in TiO_2 and $F8T2^+$ polarons.*

Figure 3.20 shows the recombination kinetics of structures ITO / HBL (50 nm) / porous TiO_2 (100 nm) / $F8T2^s$ (75 nm) and ITO / HBL (50 nm) / porous TiO_2 (100 nm) / $F8T2^d$ / $F8T2^s$ (75 nm). The figures 3.19 & 3.20 clearly indicate that the charge separation yield is significantly increased, when the dip-coated layer is introduced. This

is probably due to increasing contact surface area between polymer and TiO_2 by the dip treatment process, which improves polymer infiltration. The inset of Figure 3.20 compares normalised transient absorption signals for ITO / HBL / porous TiO_2 (100 nm) / $F8T2^d$ / $F8T2^s$ (75 nm) structures: dip-coated F8T2, spin-coated F8T2 layers and both, when the structures are illuminated from TiO_2 side. The dip-coated layer appears to increase the recombination time.

3.8.2 Photovoltaic performance

The effect of the dip coated layer on photovoltaic performance is examined using devices based on similar structures (ITO / HBL / porous TiO_2 (~100 nm) / F8T2 / Au) discussed above. J-V characteristics of the devices under solar simulator illumination of intensity 100 $mWcm^{-2}$ are shown in Figure 3.21 and the corresponding photovoltaic parameters of these devices are tabulated in Table 3.2. The device with spin coated polymer only showed V_{OC} of 0.8V, J_{SC} of 0.3 mA cm^{-2} and a low FF of 0.24. The fill factor is increased from 0.24 to 0.40 by introducing an additional dip-coated layer and the power conversion efficiency is increased by 50 %. The device with only a dip-coated layer produced a better short circuit current density than the others of 0.33 $mAcm^{-2}$ and a fill factor of 0.50, but a reduced open circuit voltage of 0.61 V. Although it is surprising that dip coating alone should lead to the higher J_{SC}, this is consistent with the amplitude of the TAS signal. The poor J_{SC} of spin-coated samples can be explained by the optical filter effect, and improved by reducing spin-coated layer thickness as discussed next.

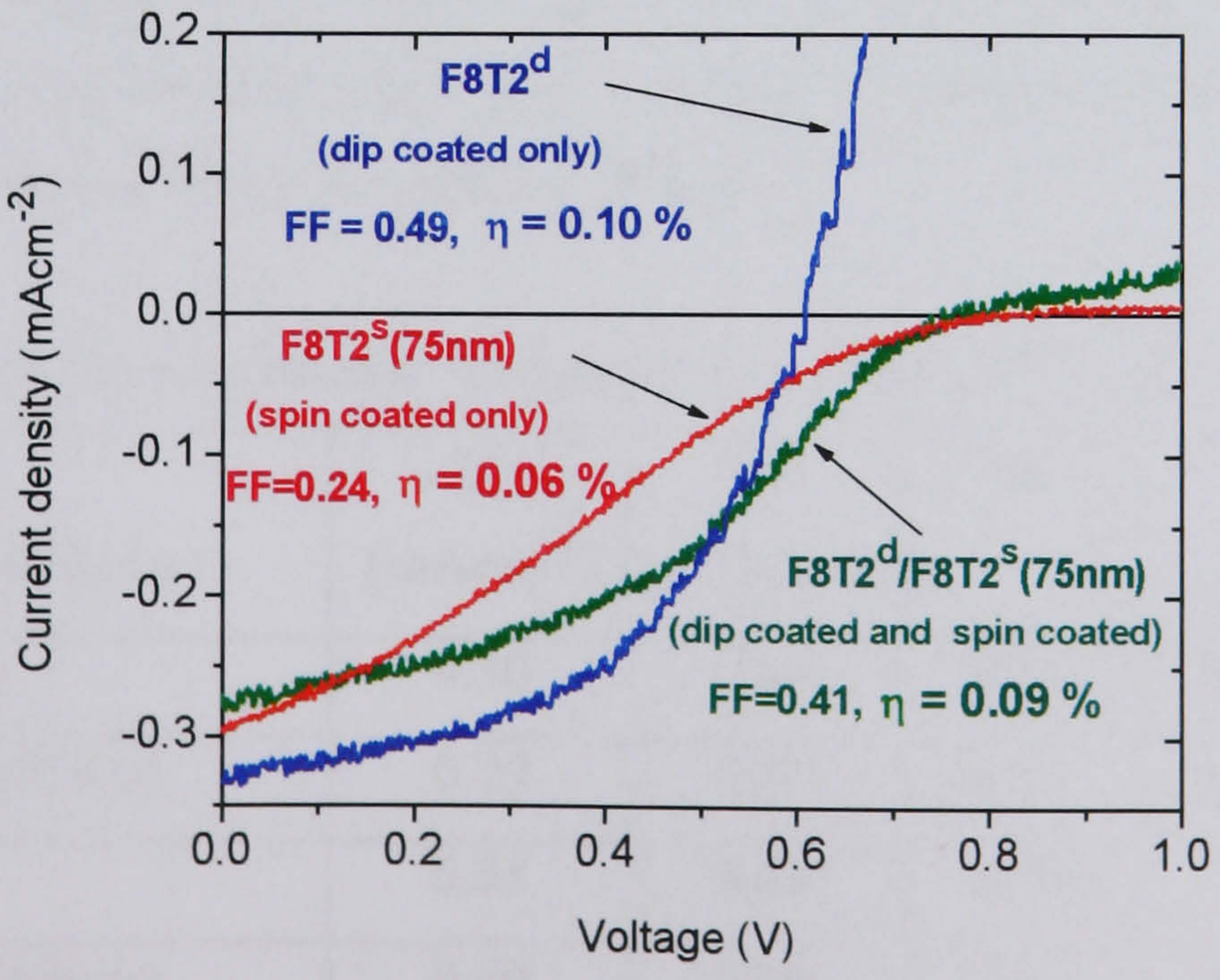


Figure 3.21 *J-V characteristic of ITO / HBL / porous TiO_2 (~100 nm) / F8T2 / Au devices with different F8T2 layer thickness under AM 1.5 condition (100 $mWcm^{-2}$). The corresponding photovoltaic parameters of each device are given in Table 3.2.*

J-V characteristics of ITO / HBL(50 nm) / porous TiO_2 (~100 nm) / F8T2 / Au devices with varying effective polymer thickness from 50 to 105 nm under simulated solar illumination of ~100 $mWcm^{-2}$ intensity are shown in Figure 3.22. We estimated the effective polymer thickness on porous TiO_2 by comparing the optical absorption of the polymer coated TiO_2 electrode with the known absorption coefficient of the polymer on spectrosil, assuming the TiO_2 is ~ 50 % porosity. Short circuit current densities J_{SC} are highly dependent on the polymer thickness, increasing from 0.19 $mAcm^{-2}$ to 0.40 $mAcm^{-2}$ when the polymer thickness is decreased from 105 nm to 50 nm, while V_{OC} increases slightly from 0.80 V to 0.94 V. The fill factor also increases from 0.38 to 0.50 with decreasing polymer thickness

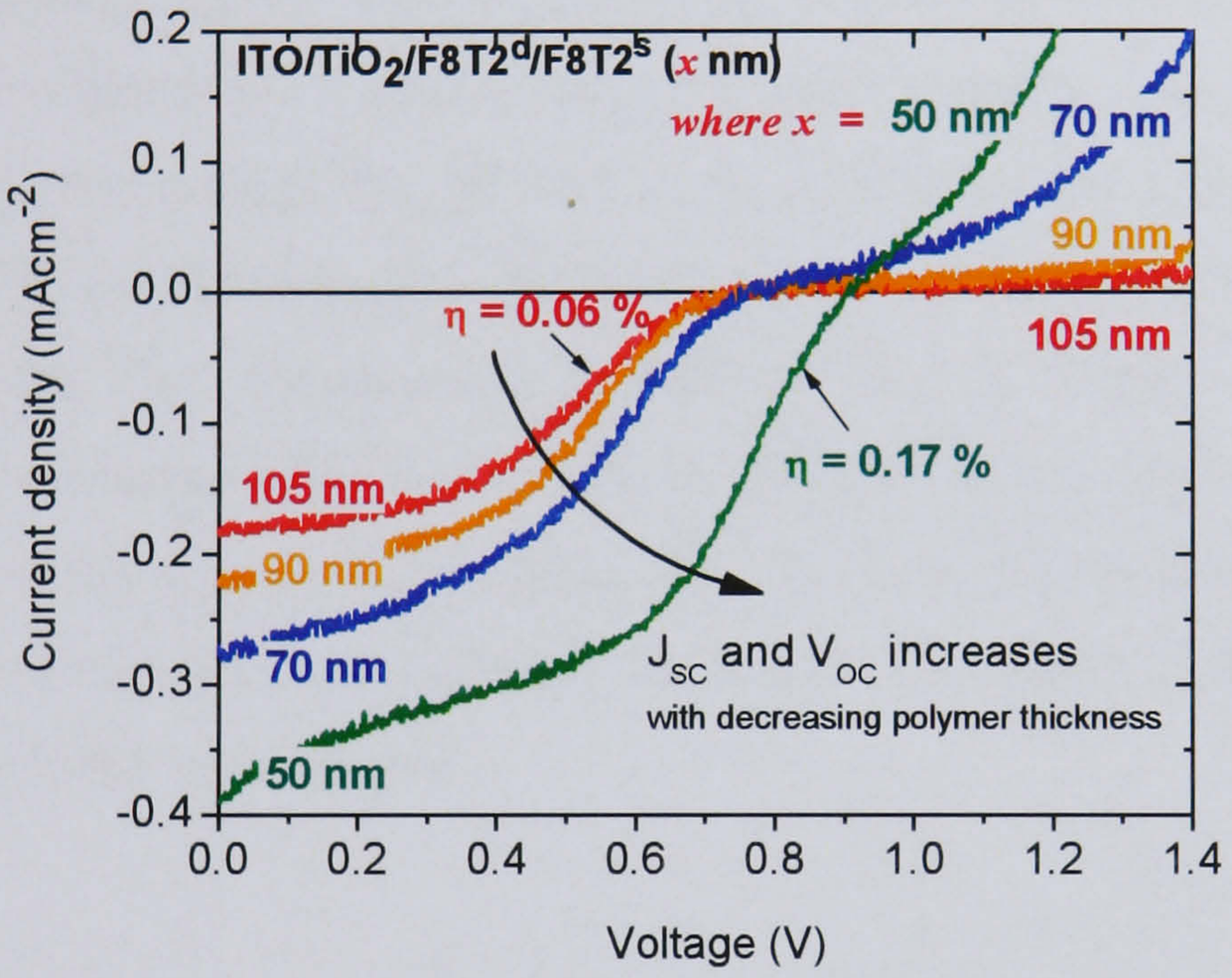


Figure 3.24 *J-V characteristics of ITO / HBL / porous TiO_2 (~100 nm) / F8T2 / Au devices with different spin-coated F8T2 layer thickness under AM 1.5 condition (100 $mWcm^{-2}$). Photovoltaic parameters of the best device are given in Table 3.2.*

Table 3.2 *Photovoltaic parameters of the devices presented in Fig. 3.21 & 3.22.*

Devices (ITO/TiO_2/F8T2/Au)	**Jsc ($mAcm^{-2}$)**	**V_{OC} (V)**	**FF**	**η (%)**
$F8T2^s$(75 nm)	0.30	0.80	**0.24**	**0.06**
$F8T2^d$/$F8T2^s$(75nm)	0.29	0.78	**0.41**	**0.09**
$F8T2^d$	**0.33**	**0.61**	0.50	0.10
$F8T2^d$/$F8T2^s$**(50nm)**	**0.40**	**0.94**	0.44	**0.17**

Comparison of these device performances and transient absorption measurements suggests that part of the spin coated layer acts as an optical filter, due to the small

exciton diffusion length of the F8T2 polymer. Generally only excitons which are generated within a diffusion length of the interface are able to contribute to the current[132]. The others recombine before they reach an interface. Decreasing polymer layer thickness may increase the probability of excitons diffusing to the interface and reduce losses to recombination. Although decreasing thickness of the photoactive polymer leads to reduced absorption and exciton generation, for sufficiently thick layers (> 50 nm) the savings through exciton harvesting out weight loss in absorption.

In summary, dip-coating improves polymer infiltration, although device with dip-coating layer alone offers reasonable photocurrent, a spin-coating layer is essential for better device performance. The second spin-coated layer is required to fill the pores, thus increasing optical density and improving film uniformity. The layer thickness should be optimised to minimise losses to optical filtering. The improved device yielded an open circuit voltage V_{OC} of 0.94 V, short circuit current density J_{SC} of 0.4 $mAcm^{-2}$ and a fill factor of 0.44 under simulated sunlight of intensity 100 $mWcm^{-2}$ (1 sun) (see Figure 3.22). The overall device performance is 0.17 % and is comparable to the best previously reported efficiency for a TiO_2 / polymer device under 1 sun

Here we note that increasing the thickness of the polymer layer leads to an enhanced kink effect and reduced fill factor. The origin of this kink feature will be discussed in the next sections.

3.9 Effect of interfacial barrier at polymer / metal interface

A 'kink' in the J-V curve similar to that seen in our devices has been seen before in other TiO_2 / polymer / Au systems (ITO / TiO_2 / MEH-PPV / Au[16] ITO / TiO_2 / PA-PPV / Au[22] and ITO / TiO_2 / BFB / Au[133]) where the polymer has ionization potential of at least 5.3 eV, producing a significant energy step ($\geq$0.4 eV) at the polymer / Au interface. The feature has also been observed in molecular thin film solar cells (e.g. ITO / CuPc / C60 / Al), where there is an energy step to hole-injection from ITO to CuPc but disappears when PEDOT:PSS (Φ_{work} = 5.3 eV) is inserted between ITO and CuPc[59].

To study whether the energy step at the polymer-metal interface might be responsible for the kink in the J-V characteristics, we varied the energy step by using alternative polymers and different top contact metals. The energy step at the polymer/metal is reduced either by replacing F8T2 polymer with PFB polymer (IP = 5.1 eV) (which has a HOMO level closer to their Fermi level of Au) or by replacing Au with Pt (which have Fermi level closer to HOMO of F8T2). We therefore study J-V characteristics of ITO / TiO_2 / F8T2 / Au, ITO / TiO_2 / PFB / Au and ITO / TiO_2 / F8T2 / Pt. Figure 3.23 shows the proposed energy electronic energy-level diagram for ITO/TiO_2/polymer/metal solar cell.

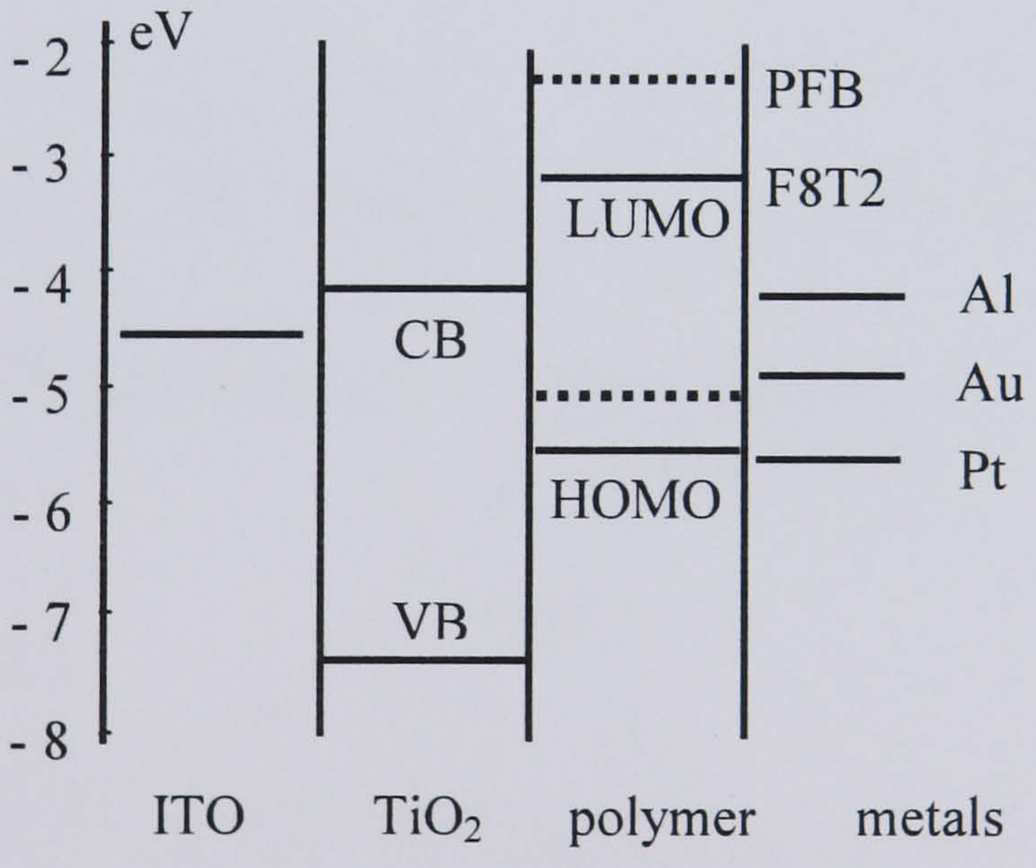


Figure 3.23 *Proposed electronic energy-level diagram for ITO / TiO_2 / polymer / metal solar cell. HOMO and LUMO levels of F8T2 and PFB are shown by solid lines and dotted lines, respectively.*

Figure 3.24 compares dark J-V characteristics of ITO / TiO_2 / F8T2 / Au, ITO / TiO_2 / PFB / Au and ITO /TiO_2 / F8T2 / Pt. The very small dark current values in the ITO / TiO_2 / F8T2 / Au device compared to the other two devices can be attributed to a

larger energy barrier for hole injection at the polymer / metal interface, illustrated by the energy level diagrams in Figure 3.23. Since the open circuit voltage of a solar cell is limited by, amongst other factors, currents injected from the electrodes opposing the photocurrent, we would expect a higher open circuit voltage in the ITO / TiO_2 / F8T2 / Au device compared to the other two devices

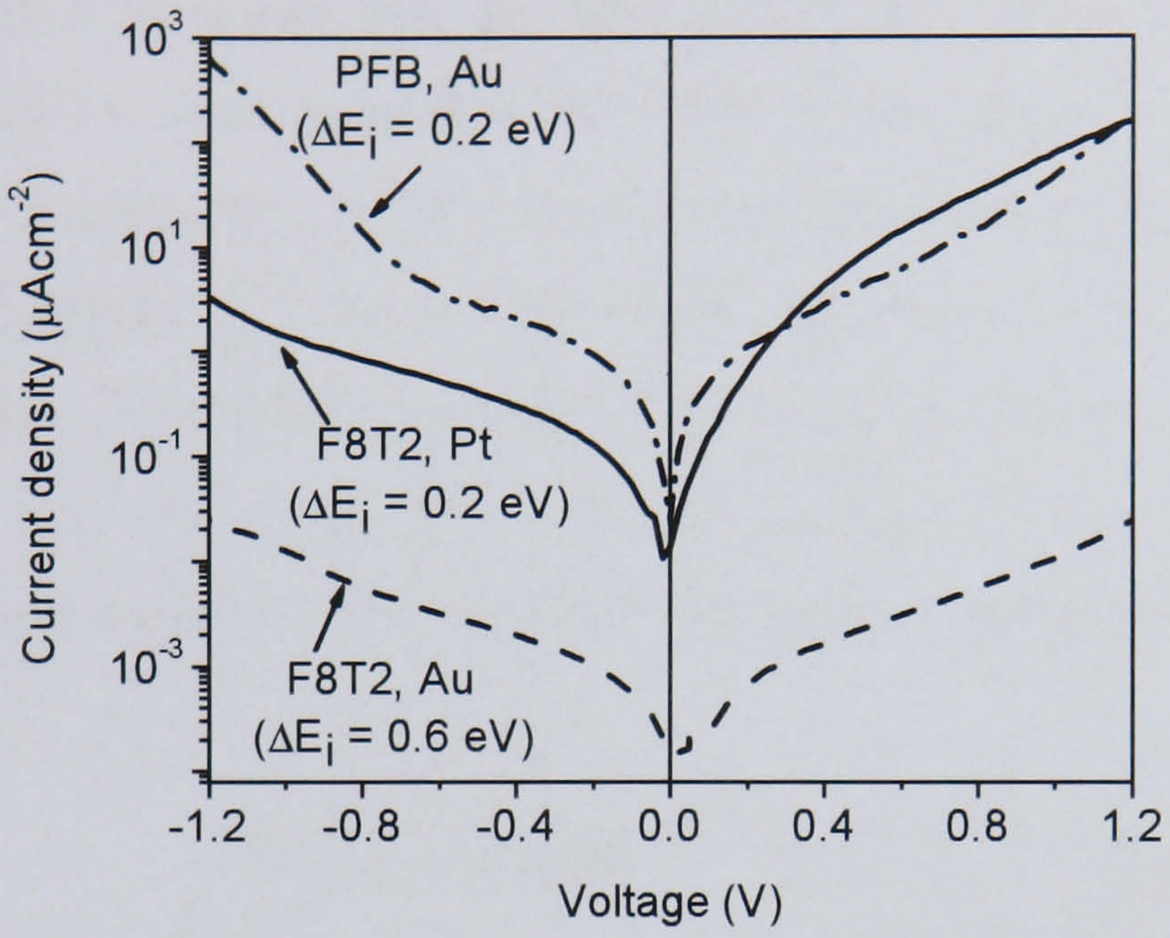


Figure 3.24 *J-V characteristics of ITO / TiO_2 / polymer / metal devices in the dark. Data are shown for PFB / Au, F8T2 / Pt and F8T2 / Au polymer/metal combinations.*

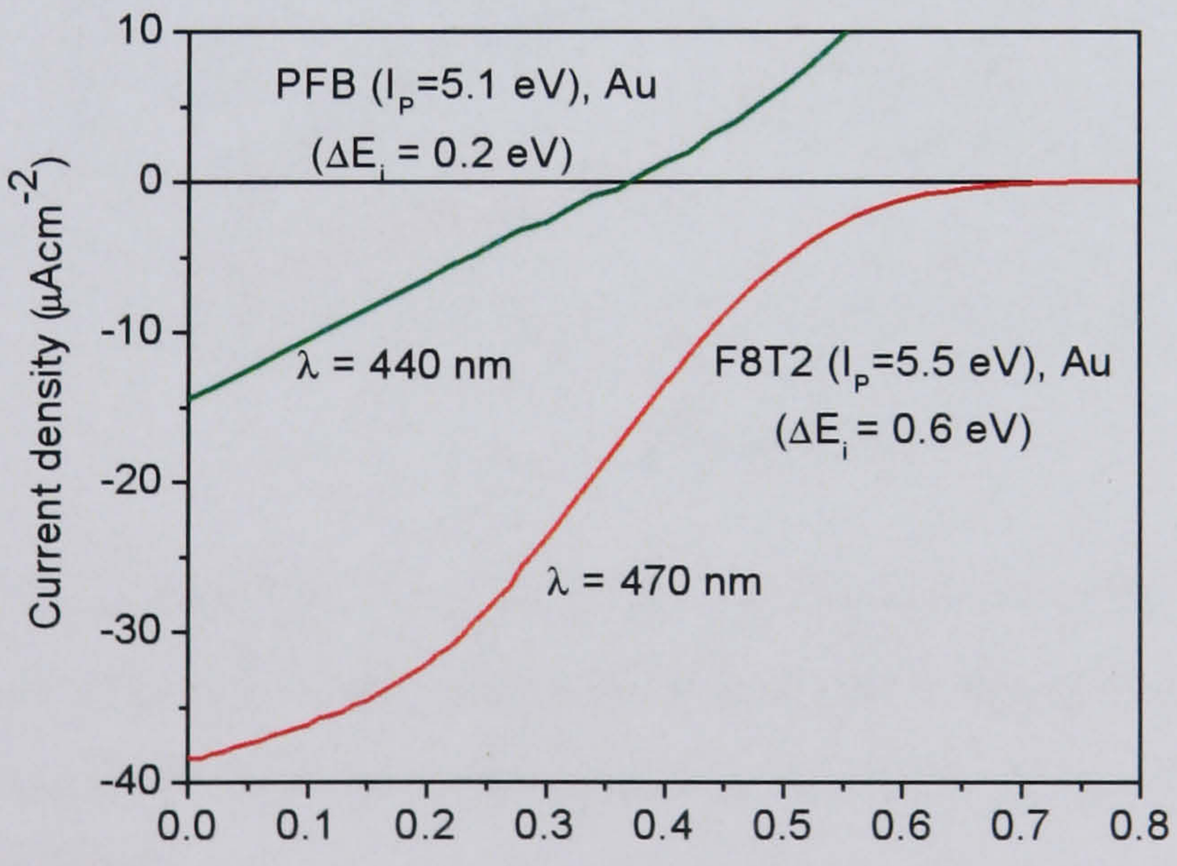


Figure 3.25 J-*V characteristics of ITO / TiO_2 / F8T2 / Au and ITO / TiO_2 / PFB / Au bi-layer devices, under monochromatic illumination and in the dark.*

Figure 3.25 compares the J-V characteristic of ITO / TiO_2 / F8T2 /Au and ITO / TiO_2 / PFB / Au bi-layer devices under monochromatic illumination at wavelengths corresponding to the maximum short circuit currents of the corresponding devices. The

PFB device shows no kink in the photocurrent-voltage curve around open circuit voltage, and the fill factor is better than for the F8T2 device, although the overall efficiency is lower. The lower V_{OC} for the PFB than the F8T2 device is consistent with easier hole injection at the Au-polymer contact. (The lower J_{SC} for PFB is mainly due to the lower photon flux at the wavelength used).

Figure 3.26 shows that the kink is not also visible when the Au electrode is replaced with Pt, confirming that the 'kink' is not due to the bulk properties of the polymer or the polymer / TiO_2 interface or the photogeneration profile but due to physical properties of the polymer/metal interface. Thus, the 'kink' in the J-V characteristics of the F8T2 / Au device may be due to the energy step, $\Delta E_i = I_P - \Phi$ at the F8T2 (I_P = 5.5 eV) / Au (Φ = 4.9 eV) interface. These experimental results are explained by a model developed with J. Nelson & J. Kirkpatrick, which is discussed in Ref. [134].

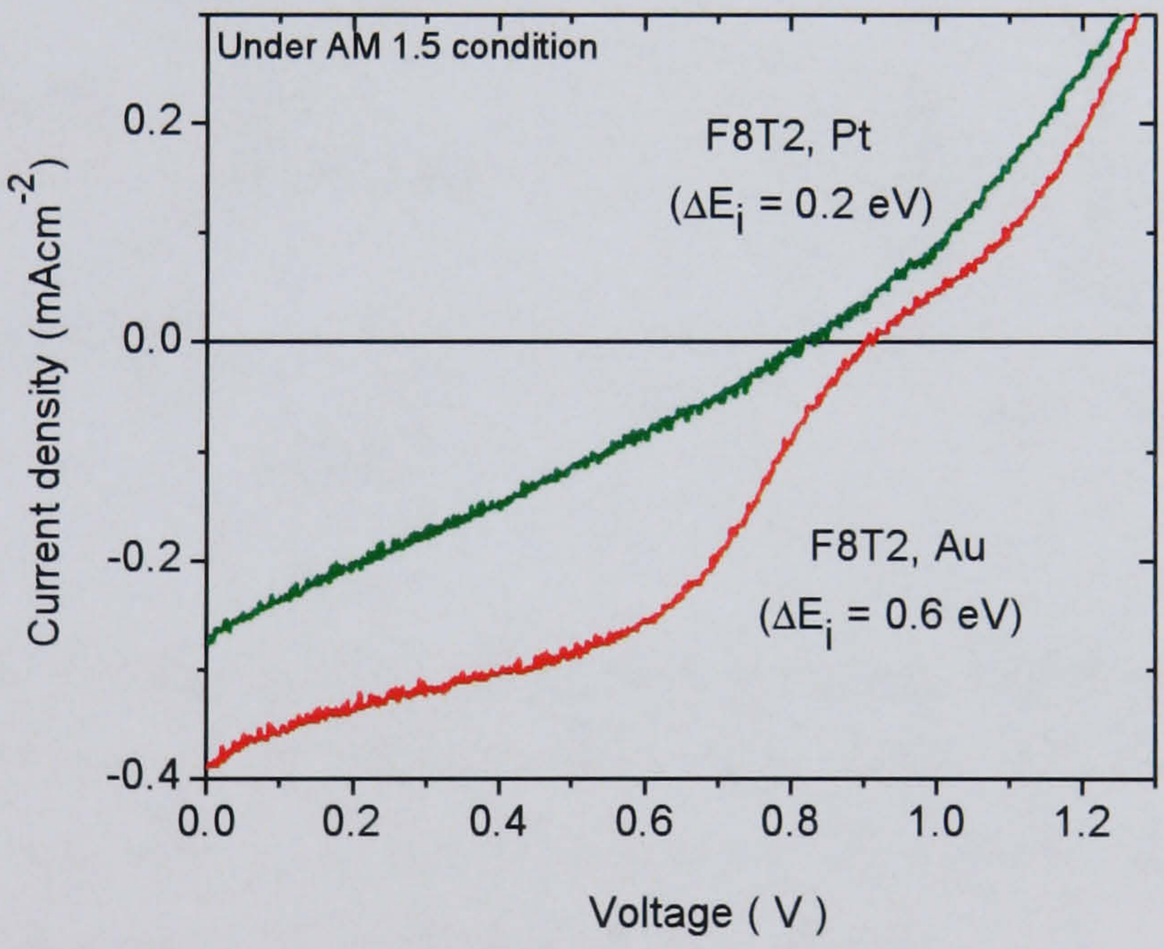
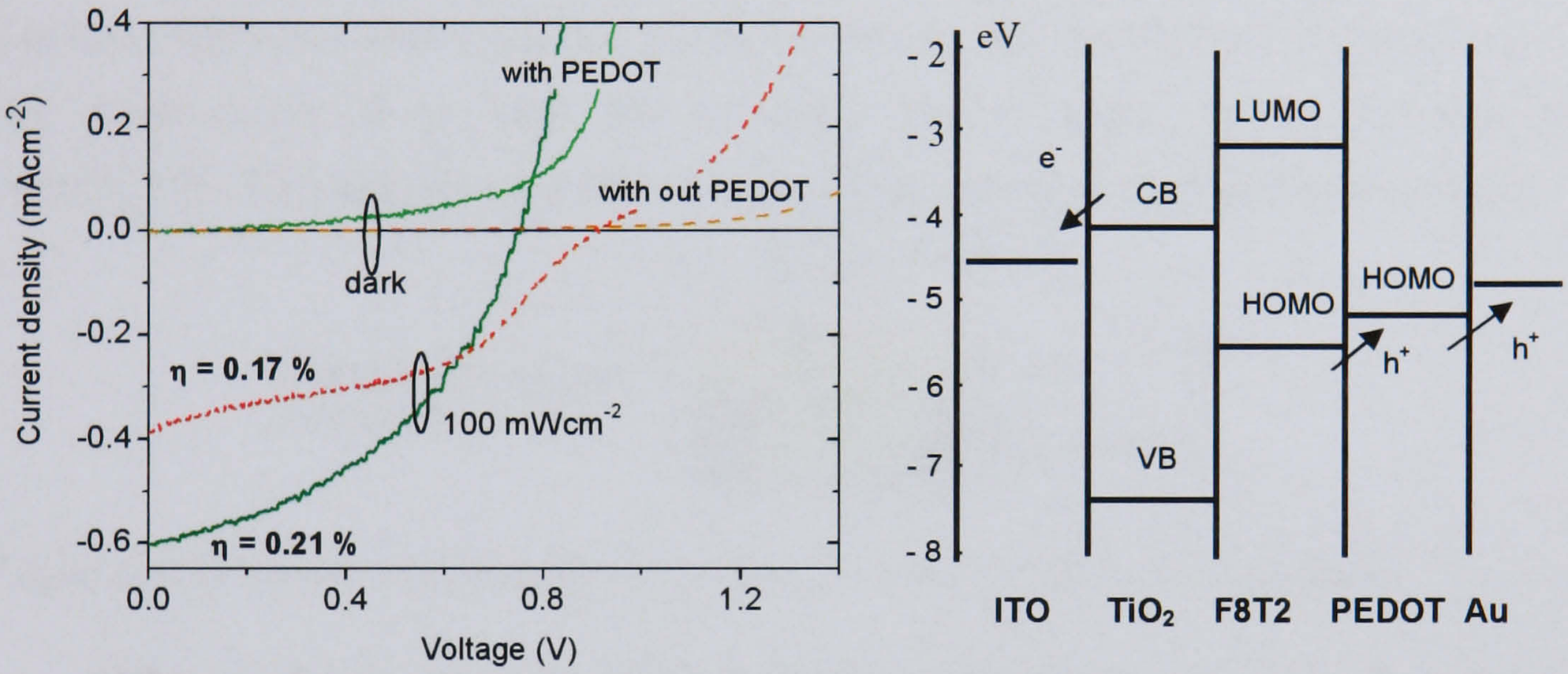


Figure 3.26 *J-V characteristics of ITO / HBL (50 nm) / porous TiO_2 (100 nm) / F8T2^d / F8T2^s (50 nm) / metal solar cells under illumination by a solar simulator (100 mWcm^{-2}, air mass 1.5). Data are shown for Pt and Au metal electrodes. ΔE_i refers to the estimated energy step at the polymer-metal interface.*

3.10 PEDOT:PSS as hole collector

The Au top contact in our devices may limit photocurrent collection in several ways. First, the low effective work function of Au (4.9 eV) when evaporated on top of polymer films[34-36] leads to a relatively small electric field to assist charge collection at short circuit. The low Au work function may also lead to an energy barrier at the interface with a high I_P polymer, which, as we discussed in the previous section, may reduce the rate of hole-collection. Finally, potential damage to the polymer surface from evaporated gold may enhance the probability of exciton quenching near that interface. Therefore, we have studied the effect of introducing a PEDOT:PSS layer between polymer and top Au contact on the photovoltaic performance of TiO_2 / F8T2 devices.



(a) (b)

Figure 3.27 *(a) J–V characteristics in the dark and under simulated AM 1.5 solar irradiation (100 mW cm^{-2}, 1 sun), of F8T2 devices (ITO / HBL / porous TiO_2 (100 nm) / F8T2 (50 nm) / PEDOT:PSS / Au) with (solid lines) and without (dash lines) the PEDOT:PSS layer. (b) Proposed electronic energy-level diagram for the solar cell.*

Figure 3.27 (a) shows J-V characteristics of two devices, (ITO / HBL/Porous TiO_2 (~100nm) / F8T2 (50nm) / Au) one with and the other without a PEDOT:PSS layer between the F8T2 and Au, under AM1.5 condition and in dark. The insertion of the PEDOT:PSS layer increases the J_{SC} from 0.40 mAcm^{-2} to 0.61 mAcm^{-2}. Similar observations were also found in several MEH-PPV based polymer bi-layer and multilayer devices, we studied. The details of the study will be discussed in the next chapter. The V_{OC} of the TiO_2 / F8T2 device, however, slightly decreases from 0.93 to 0.75 V. Nevertheless, the overall efficiency is increased from 0.17 % to 0.21 %. The optimised performance of TiO_2 / F8T2 device is slightly higher than the previous best reported values (0.18 %) for TiO_2 / polymer device.

Dark J-V characteristics of the devices (see Figure 3.27(a)) clearly show that the forward-bias dark current for the device with PEDOT:PSS is much higher (110 times at + 1.0 V) than for the device without PEDOT:PSS, confirming that the energy barrier for hole injection at the polymer / metal interface is reduced by introduction of the PEDOT:PSS layer which has a work function of 5.3 eV, similar to ionisation potential of the F8T2 polymer of 5.5 eV (see Figure 3.27(b)). The short circuit current density and fill factor of a TiO_2 / polymer bi-layer device can increase when the energy step at the polymer / metal interface is reduced (see section 3.3). Thus, the increase in J_{SC} may be due to improved charge transfer between polymer and top contact, resulting from the lower energy step. The decrease in V_{OC} upon introduction of the PEDOT:PSS layer is also quite consistent with a reduced interfacial energy step and increased hole-injection. The improvement of J_{SC} may also be partly due to doping of the polymer by PEDOT:PSS. This and other possible reasons are discussed in detail in the next chapter.

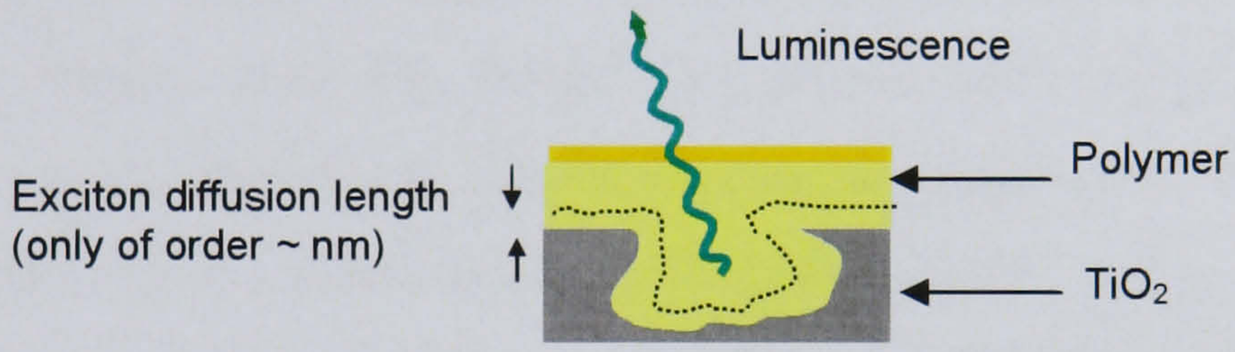


Figure 3.30 *Schematic representation of the interface between TiO_2 pore and polymer.*

Although the device with F8T2 polymer shows better performance than any previously reported TiO_2 / polymer solar cell, green photoluminescence from the device is still observed when it is illuminated with blue monochromatic light of wavelength 470 nm. This is probably due to the short exciton diffusion length of F8T2 polymer (~5 nm, see section 4.3.4). SEM images of the porous TiO_2 film (see, Figure 5.8 (a)) show that there are some large pores of more than 20 nm in the spin coated porous TiO_2 films. Figure 3.30 illustrates how the exciton diffusion length of a polymer, compared to the pore size, may influence the charge separation. Since the exciton diffusion length of the F8T2 polymer is around a few nm, only excitons produced near to the interface contribute to the photocurrent and the rest of them recombine and emit luminescence. A longer exciton diffusion length of polymer should enable more excitons to diffuse to the TiO_2 / polymer interface without recombining and then dissociate at the interface. Thus, polymer with a longer exciton diffusion length such as MEH-PPV based polymers, are expected to reduce the losses by exciton recombination and offer higher photocurrent density in TiO_2 / polymer devices. We will therefore focus on the performance of device using polymers with longer exciton diffusion length in the next chapter.

3.11 Summary

We have studied the charge separation and photovoltaic properties of hybrid TiO_2 / polymer structures. Efficient photo-induced charge transfer is observed from a fluorene-thiophene copolymer, F8T2, to the TiO_2 film, while interfacial recombination is relatively slow (10 ms -100 μs). Device performance is improved by reducing thickness of both TiO_2 and polymer layers, which is explained by reduced series resistance and reduced optical filtering. Inserting a thin (~100 nm) porous layer of TiO_2 into a planar TiO_2 / polymer structure increases EQE by a factor of five. A dip coating step improves polymer infiltration into the porous film and increases the fill factor of the device and η by 50 %. Although devices with only a dip coated layer offer reasonable photovoltaic performance, a spin coated layer is essential for better device performance. This second spin-coated layer is required to fill the pores, thus increasing optical density and improving film uniformity. The polymer layer thickness should be optimised to minimise losses to optical filtering. Devices with F8T2 polymer and Au contacts suffer from a poor fill factor. Comparison with other polymer-interface combinations suggests that this is due to an energy mismatch at the hole collecting interface, and that contacts which allow good hole-injection tend to lead to higher fill factors in this system. The introduction of a PEDOT:PSS layer between the polymer and the metal contact improves both the device efficiency and J_{SC} by over 50 %.

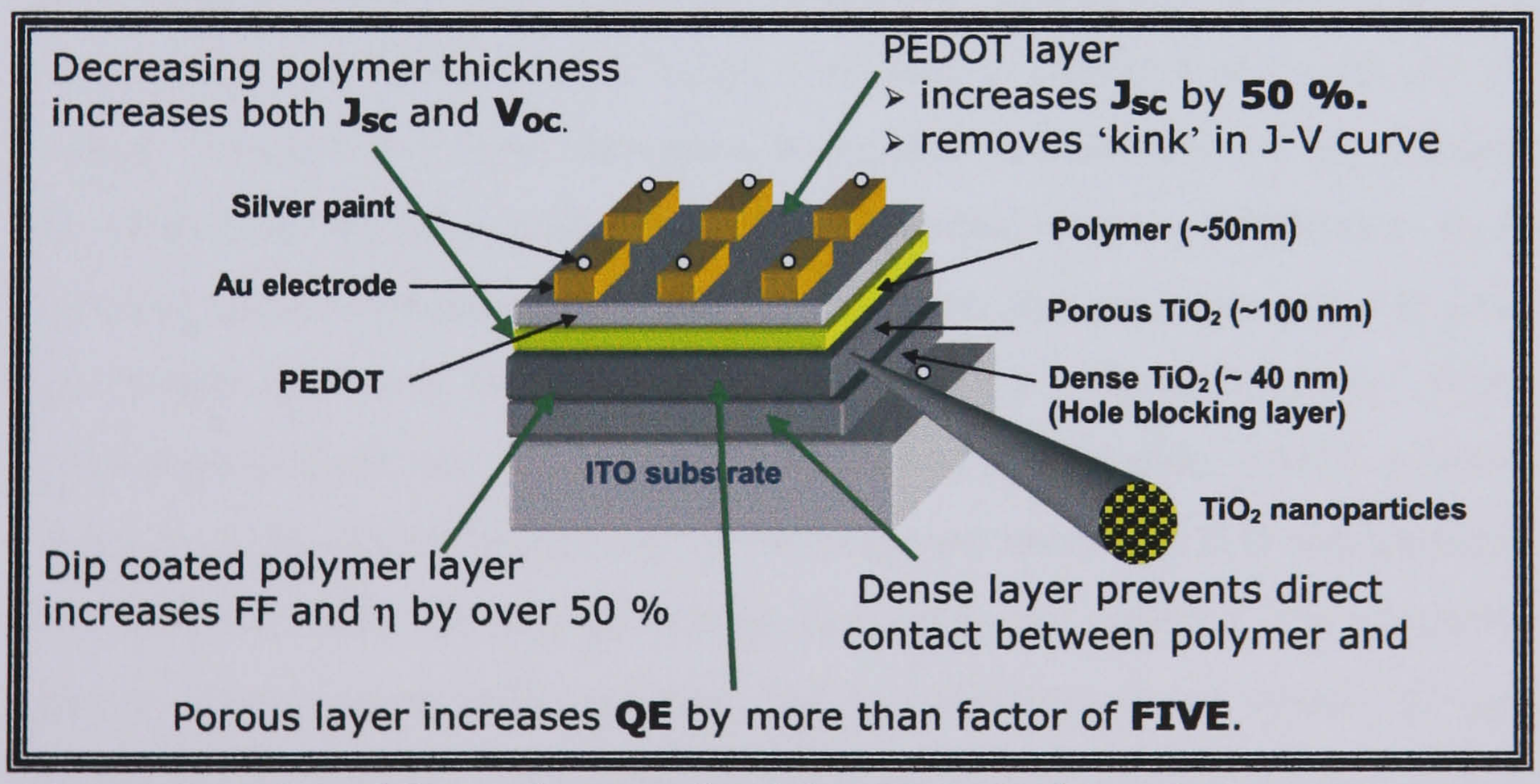


Figure 3.29 *Role each layer of optimised multilayer TiO_2 / polymer device.*

An optimised multilayer (see, Figure 3.29) device produced J_{SC} of 0.61 $mAcm^{-2}$, fill factor of 0.45 and V_{OC} of 0.76 V under AM1.5 illumination. The power conversion efficiency of this improved multilayer device is 0.21 %, three times greater than a similar device without either the dip coated polymer layer or PEDOT:PSS layer.

Chapter 4

Influence of optoelectronic properties of polymers

This chapter explores the influence of optoelectronic properties of polymers on the device performance and the effect of PEDOT:PSS on charge collection.

4.1 Abstract

We focus on a series of high hole-mobility PPV based polymers in contact with nanocrystalline TiO_2 films. Photoluminescence quenching, time-of-flight mobility measurements and optical spectroscopy were used to characterize the exciton transport, charge transport and light harvesting properties, respectively, of the polymers, and correlate these material properties with photovoltaic device performance. In addition, transient optical measurements were used to show that excellent polymer penetration into highly structured TiO_2 networks is achieved by a dip coating step. Photovoltaic performance of polymer / TiO_2 hybrid devices was studied under AM1.5 conditions as a function of the device design and of the polymers used. We find that photocurrent is primarily limited by the photogeneration rate and by the quality of the interfaces, rather than by hole-transport in the polymer. Device performances are significantly improved by introducing a PEDOT:PSS layer between the polymer and the top Au electrode in all combinations of devices, we studied. Optimized devices incorporating both dip-coated polymer and PEDOT:PSS layers produced a short circuit current density of about 1 $mAcm^{-2}$, a fill factor of 0.49 and an open circuit voltage of 0.86 V under simulated AM1.5 illumination (100 $mWcm^{-2}$, 1 sun). The corresponding power conversion efficiency under 1 sun was ≥ 0.40 %.

4.2 Introduction

In the previous chapter, we studied the photovoltaic performance of TiO_2 / F8T2 devices as a function of the fabrication route and device design. We improved polymer penetration into the porous film through a range of strategies such as melt-processing of the F8T2 polymer (which possesses a liquid-crystalline phase[98]) into the porous TiO_2 electrodes, reducing the nanoporous TiO_2 film thickness, and dip-coating porous TiO_2 electrode in a dilute polymer solution before spin coating a second polymer layer. We have also improved charge collection by introducing a PEDOT:PSS layer under the top contact. The power conversion efficiency, η of our optimised TiO_2 / F8T2 multilayer device was three times greater than that of the device without either dip coated polymer layer or PEDOT:PSS. The performance was better than any previously published hybrid TiO_2 / polymer device.

Despite the successful hybrid polymer / TiO_2 device design, the power conversion efficiency of these devices was an order of magnitude smaller than the best power conversion efficiency achieved using similar polymers with fullerenes rather than TiO_2 as the electron acceptor. The difference is largely in the value of the short circuit current density, J_{SC}. The values of open circuit voltage, V_{OC}, and fill factor, FF, for the hybrid cell are similar to the best published values for polymer / fullerene solar cells. The reduced J_{SC} may be due to a number of factors: small optical depth, poor sensitization of the oxide film, large pore size / nanostructure scale compared to the exciton diffusion length, poor charge transport, fast recombination, or imperfect interfaces. However, it is difficult to analyze these losses on the basis of previous studies in the literature, on account of wide variations in materials and fabrication techniques.

This chapter attempts to identify the mechanisms limiting the J_{SC}, through a systematic study of the effect of the optoelectronic properties of the polymer on the performance of a model polymer-TiO_2 hybrid system. We focus on a series of MEH-PPV based polymers characterized by long exciton diffusion length, some of which have high hole-mobility and good red absorbance. These polymers are compared with the F8T2 polymer studied in chapter 3. Through complementary studies of device performance and the charge transport and light harvesting properties of these materials, we show that photocurrent is limited primarily by the photogeneration rate and by the quality of the interfaces, rather than by hole-transport in the polymer. Optimized devices incorporating the additional dip-coated and PEDOT:PSS layers produced a J_{SC} about 1 mA cm^{-2} and a η of 0.41 % under 1 sun, approximately double the best previously reported value for a TiO_2 / polymer hybrid device[16] under the same conditions.

4.3 Optoelectronic properties of the polymers

Here we first study the optoelectronic properties of three MEH-PPV based polymers, namely MEH-DOO-PPV, TPD (4M)-MEH-PPV and TPD (4M)-MEH-M3EH-PPV and a fluorene-bithiophene co-polymer, F8T2. The chemical name and the structures of the polymers can be found in chapter 2 (section 2.1).

4.3.1 Polymer absorption and adsorption on to TiO_2

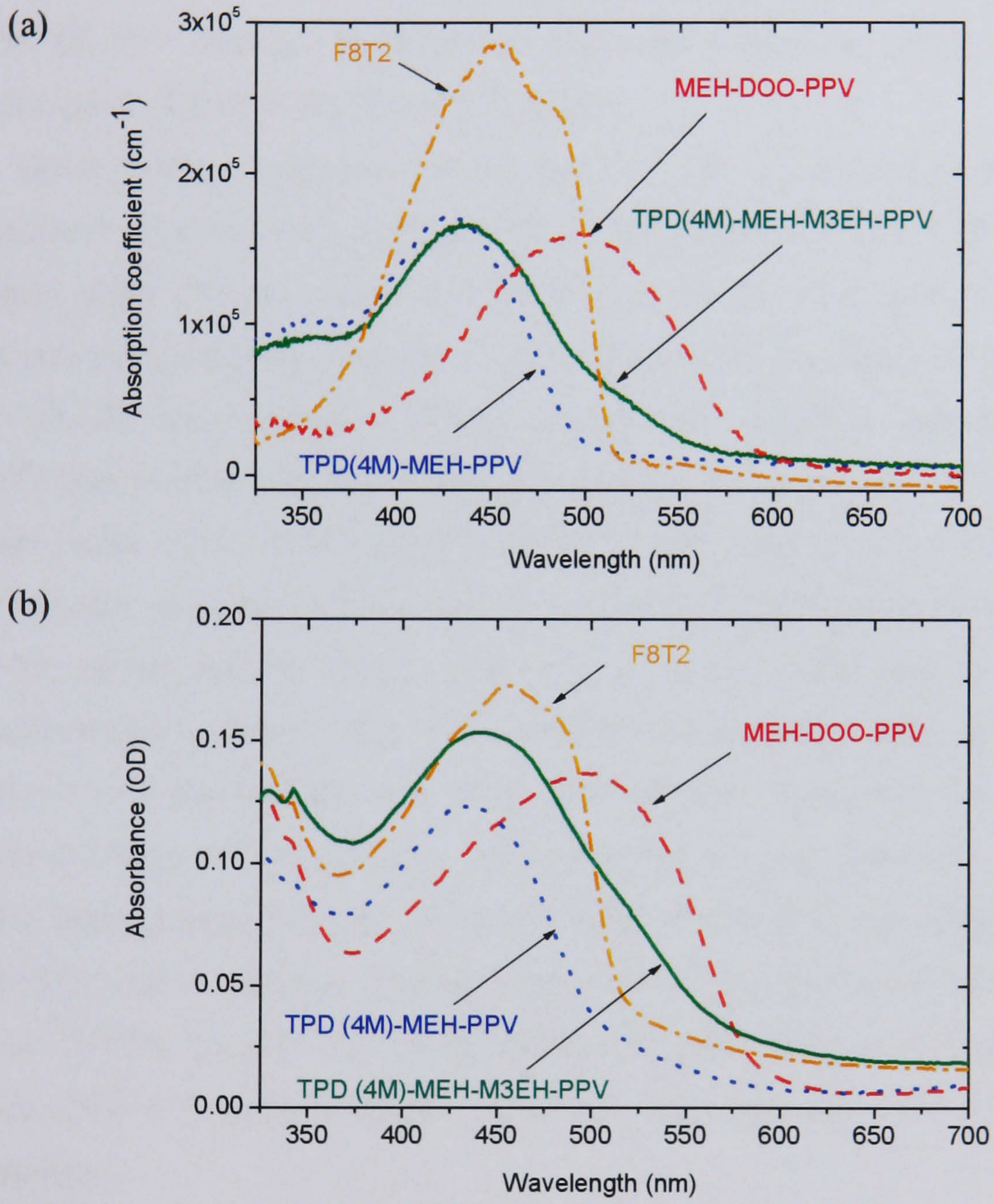


Figure 4.1 *(a) Absorption spectra of the polymers, deduced from UV-VIS optical absorption spectra of thin polymer films on spectrosil B substrates (b) UV-VIS optical absorption spectra of TiO_2 nanoporous films of thickness about 100 nm, after dipping in the respective polymer / C_6H_5Cl (1 mg/ml) solutions for 18 hrs at 60 ^0C.*

Optical absorption spectra for thin films of each of the three MEH-PPV polymers and F8T2 polymer spin-coated on spectrosil B substrates are shown in Figure 4.1 (a). The magnitude of the absorption coefficient is similar for all MEH-PPV based polymers, while F8T2 polymer has a higher absorption coefficient than any of these MEH-PPV polymers in the wavelength range from 375 nm to 500 nm. F8T2 has a

broad optical absorption in the visible spectrum peaking at about 460 nm, while MEH-DOO-PPV polymer absorbs further into the red, with peak absorption at 502 nm.

The absorption spectrum of the TPD (4M) MEH-M3EH-PPV polymer is red shifted slightly compared to that of TPD (4M) MEH-PPV. Whilst TPD (4M) MEH-PPV and MEH-DOO-PPV are strictly alternating copolymers, the TPD (4M) MEH-M3EH-PPV polymer is a statistical condensation copolymer consisting of TPD (4M) MEH-PPV $(AB)_x$ repeat units and M3EH-PPV $(CB)_y$ repeat units in the ratio x:y = 50:50[105]. The M3EH-PPV units are therefore believed to be responsible for the red shoulder in the absorption of TPD (4M) MEH-M3EH-PPV.

Good uptake of polymer by the porous TiO_2 is essential for efficient device performance. Figure 4.1 (b) compares the optical density of porous TiO_2 electrodes of thickness about 100 nm following dip-coating in solutions of each of the MEH-PPV based polymers and F8T2 polymer. F8T2 polymer sensitises the TiO_2 better than any of the MEH-PPV based polymers. This is expected from the higher absorption coefficient of F8T2 compared to MEH-PPV based polymers and may also be assisted by the lower average molar mass (26,800 g/mol)[135] of F8T2 (see table 4.1). The MEH-PPV based polymers also sensitise the TiO_2 well. This may be assisted by an interaction between the TiO_2 surface and the oxygen atoms of the alkoxy substituents on the MEH-PPV subunits of each polymer[92]. The TPD (4M)-MEH-M3EH-PPV polymer shows a better uptake by TiO_2 than the other two MEH-PPV polymers. This may be due to the higher number of alkoxy substituents in the polymer repeat unit (see chapter 2). Another reason for the better sensitisation by TPD(4M)-MEH-M3EH-PPV compared to TPD(4M)-MEH-PPV may be the lower average molar mass of the TPD (4M)-MEH-M3EH-PPV polymer (35,700 g/mol)[105] or the TPD(4M)-MEH-PPV polymer (53,100 g/mol)[105]. It was observed that polymer uptake by porous TiO_2 increases with dipping time and temperature.

4.3.2 Hole mobility of the polymers

The polymer hole-mobilities were studied by the time-of-flight (TOF) method. Figure 4.2 (a) shows a typical room temperature hole transient for the TPD (4M)-MEH-PPV polymer, in an ITO / polymer (1.2 μm) / Al device structure, at two different electric fields. The inset of Figure 4.2 (a) shows the corresponding transients on a double logarithmic scale. The transient shows an initial spike followed by a distinctive plateau and then by a broad tail. The constant current plateau in the hole-transient of TPD (4M)-MEH-PPV polymer indicates non-dispersive transport. Figures 4.2 (b) and (c) show typical hole transients for MEH-DOO-PPV and TPD (4M)-MEH-M3EH-PPV

polymers, in ITO / polymer / Al device structures with polymer thicknesses of 1.5 μm and 1.2 μm respectively. The transients are more dispersive, but still show clear transit times. The comparison of Figures 4.2 (b) and (c) shows that hole-transport in MEH-DOO-PPV polymer is less dispersive than in TPD (4M)-MEH-M3EH-PPV polymer.

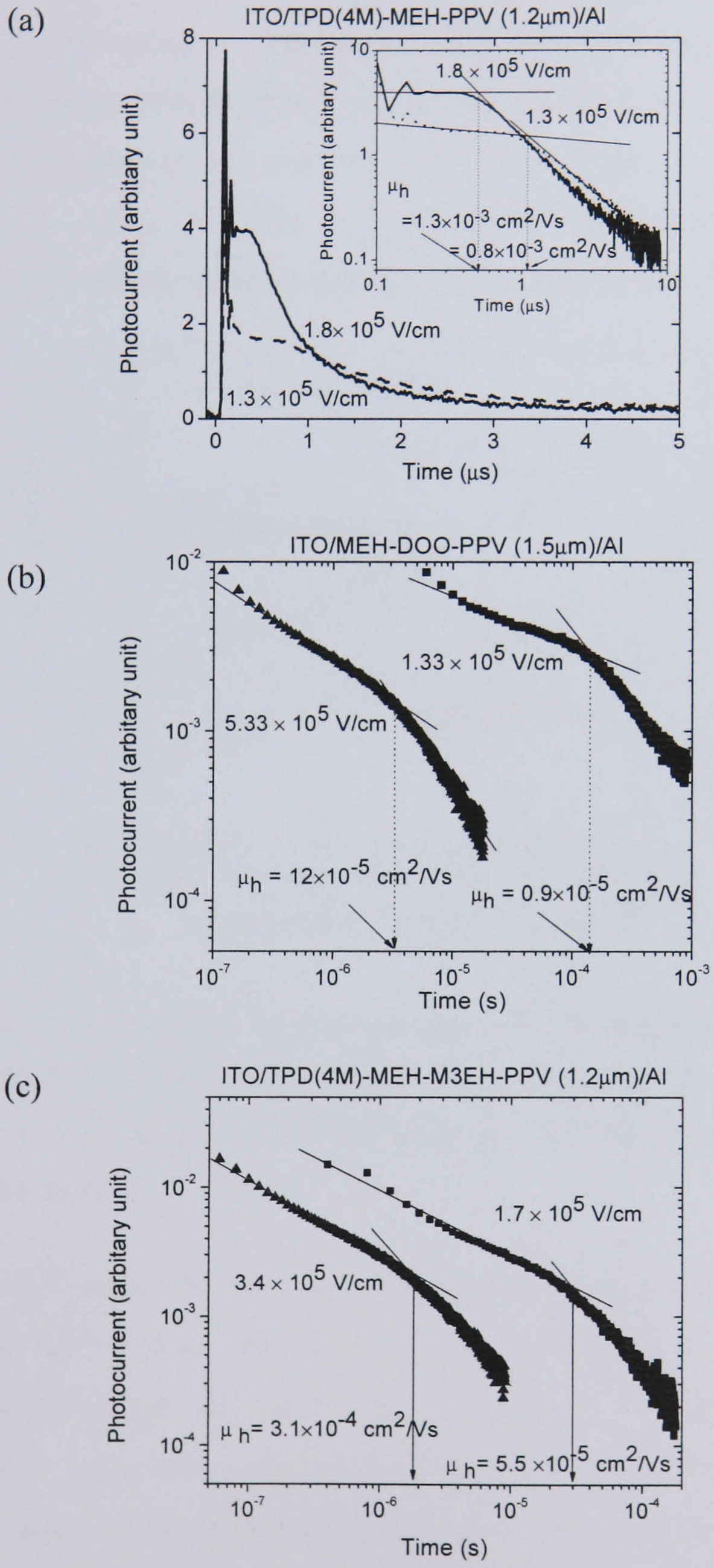


Figure 4.2 *Typical TOF hole transients in (a) ITO / TPD (4M)-MEH-PPV (1.2 μm) / Al (b) ITO / MEH-DOO-PPV (1.5 μm) / Al, (c) ITO / TPD (4M)-MEH-M3EH-PPV (1.2 μm) / Al at two different fields. The built in voltage for the ITO / polymer /Al structure is assumed to be 0.3 V.*

The drift mobility at an applied electric field E was calculated from the expression $\mu = \frac{d}{t_T E}$, where d is the polymer thickness and t_T is the transit time. Here, we note that the collected charge was less than 5 % of the sample capacitor charge in all cases. The electric field across the samples can therefore be assumed constant and we can apply this expression in confidence to calculate the mobility of the polymers. The electric field was calculated taking into account a built-in voltage of 0.3 V, namely the work function difference between the ITO (4.6 eV) and Al (4.3 eV) electrodes. The work function values of ITO and Al were estimated by Kelvin probe and electroabsorption spectroscopy measurements (as described in section 3.3.2).

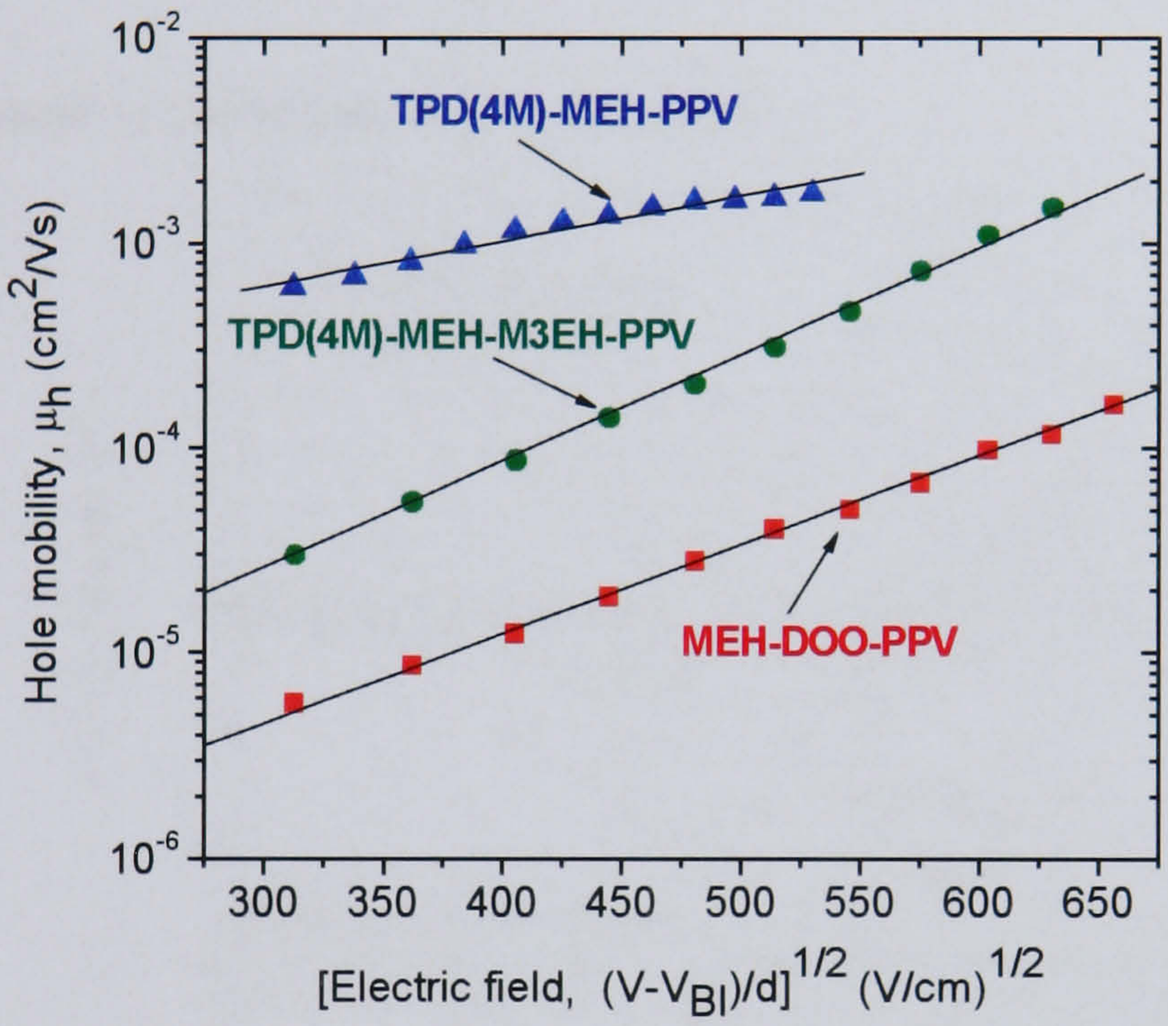


Figure 4.3 *The variation of the room temperature TOF hole-mobility μ_h with electric field for these three MEH-PPV based polymers: TPD (4M)-MEH-PPV (triangles), TPD (4M)-MEH-M3EH-PPV (circles) and MEH-DOO-PPV (squares). The built in voltage for the ITO / polymer /Al structure is assumed to be 0.3 V.*

Figure 4.3 shows the electric field dependent variation of the room-temperature hole-mobility for all three MEH-PPV polymers. The hole mobilities of all polymers follow a Poole-Frenkel dependence $\mu_h \propto \exp(\beta E^{1/2})$[119]. The two TPD containing polymers show higher hole-mobility than the MEH-DOO-PPV polymer. This may be due to the positive influence of the TPD group on hole-transport. The TPD (4M)-MEH-PPV polymer shows higher hole mobility than the other two polymers in the range of electric fields from 0.9×10^5 V/cm to 5×10^5 V/cm. The TPD (4M)-MEH-PPV polymer also shows weaker field dependence, while both TPD (4M)-MEH-M3EH-PPV and MEH-DOO-PPV polymers show strong field dependence. Estimating an electric field of

1×10^5 V/cm within an efficient TiO_2/polymer photovoltaic device (polymer thickness ~ 50-100 nm) at short circuit, the TPD (4M)-MEH-PPV polymer would be expected to give the best hole transport in devices. However, hole-transport in both TPD (4M)-MEH-M3EH-PPV and MEH-DOO-PPV polymers should improve in thinner devices. According to measurements by Ruth Rawcliffe, F8T2 polymer shows highly dispersive hole-transport and strongly field dependent TOF hole-mobility in the range of 10^{-5} - 10^{-4} cm^2/Vs over the electric field range $1 \times 10^4 - 6 \times 10^4$ V/cm[136]. F8T2 performs rather better as an aligned thin film in field effect transistor structures and FET hole mobility of F8T2 polymer is 0.01 - 0.02 cm^2/Vs in aligned F8T2 polymer[102], but such alignment cannot be achieved in the present devices.

4.3.3 Ionisation potential of the polymers

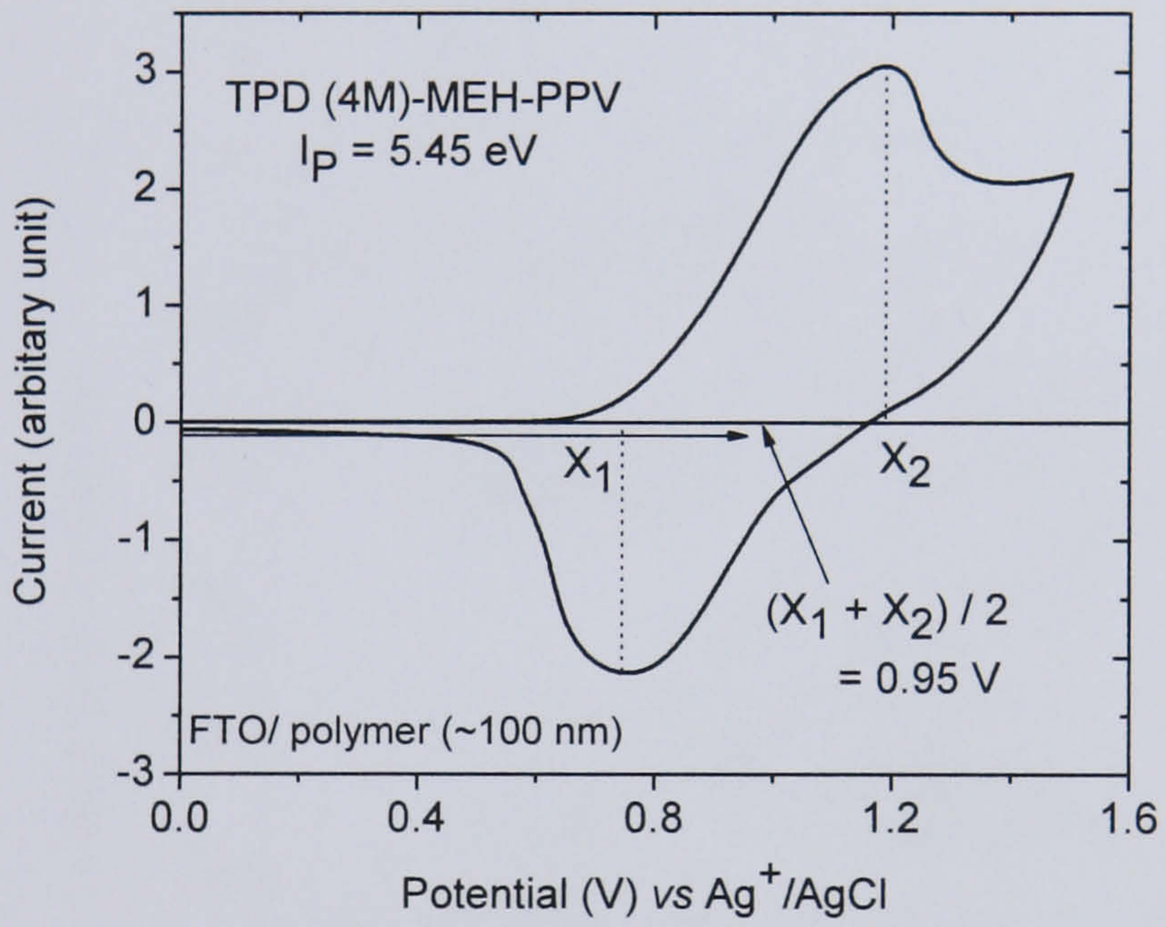


Figure 4.4 (a) *Cyclic voltammograms of spin coated TPD (4M)-MEH-PPV (solid line) polymer films on FTO substrates in repetitive cycle, scan rate 50 mV/s, Ag^+/AgCl as a reference electrode, FTO as working electrode and Pt as a counter electrode.*

Cyclic voltammograms of the these MEH-PPV polymers and the F8T2 polymer were measured in thin films (~100 nm) of the polymer on FTO substrates immersed in acetonitile containing 0.1 M tetrabutylammonium tetrafluoroborate as a supporting electrolyte. A moderate scan rate of 50 mV/s was chosen for the cyclic voltammetric characterisation of these polymer films to reduce "IR loss". With a faster scan rate, newly oxidised species could be generated and saturate before the earlier generated oxidised species reach the counter electrode, resulting in the "IR drop"[137]. Figure 4.4 shows the cyclic voltammograms of TPD (4M)-MEH-PPV polymer film on FTO substrate. The oxidation potential of each polymer was estimated with respect to a reference Ag^+ / AgCl electrode. The ionisation potential of the polymers is calculated

from the reference potentials and lies between 5.25 eV and 5.55 eV for all four polymers. The values are compared in the third column of table 4.1.

4.3.4 Exciton diffusion length of the polymers

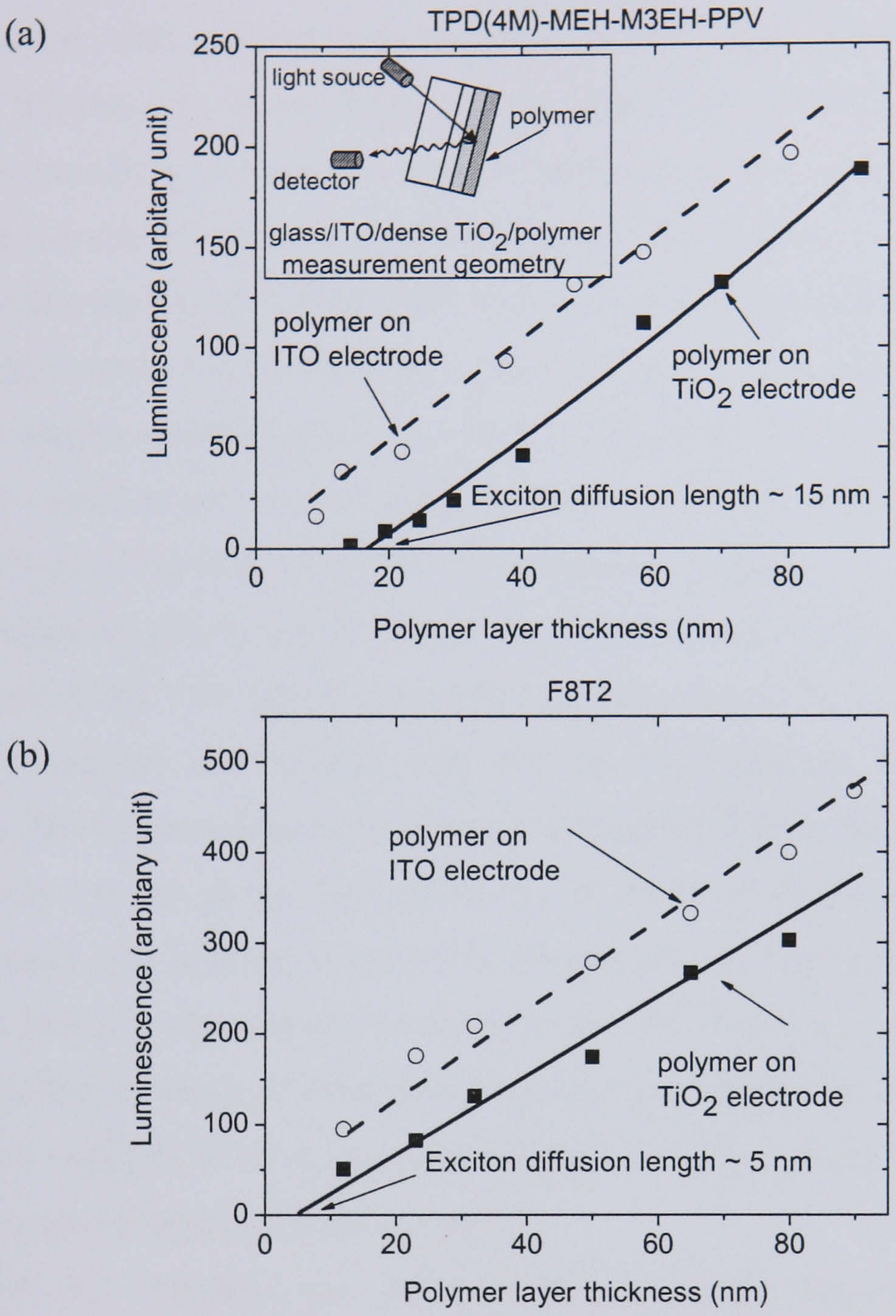


Figure 4.5 *Photoluminescence at 600 nm from a spin-coated polymer layer [(a) TPD (4M)-MEH-M3EH-PPV and (b) F8T2] on ITO (circles, dashed line) and on ITO / dense TiO_2 (squares, solid line) substrates, as a function of polymer layer thickness. The polymers were excited with 400 nm light through the ITO. The inset of the figure 4.5 (a) shows the measurement geometry in the spectrofluorimeter.*

The exciton diffusion length in TPD (4M)-MEH-M3EH-PPV and F8T2 polymer was estimated using the method described in Ref. [19]. Figure 4.5 (a) shows the relative photoluminescence of the TPD (4M)-MEH-M3EH-PPV polymer layers on ITO and dense TiO_2 substrates 600 nm, as a function of polymer layer thickness when the polymer was excited with 400 nm light through the ITO coated glass substrate. The

photoluminescence measurements were taken using a FlouroMax 3.0 spectrofluorimeter and the inset of Figure 4.5 (a) shows the measurement geometry. The polymer layer thickness on the dense TiO_2 layer was estimated from the UV-VIS optical absorption of the layer using the known absorption coefficient of the polymer. The luminescence varies linearly with polymer layer thickness on ITO, and approximately linearly with polymer thickness on dense TiO_2. For the dense TiO_2 substrate, the trend predicts complete quenching of luminescence at a layer thickness of about 15 nm, and we can therefore estimate the exciton diffusion length in the polymer as (15 ± 4) nm. This is similar to that determined in MEH-PPV (20 nm) by a similar technique[19]. The other two PPV polymers also contain MEH-PPV sub-units and we may expect that their exciton diffusion lengths would be similar to those of TPD (4M)-MEH-M3EH-PPV and MEH-PPV. We could therefore reasonably assume the exciton diffusion length of MEH-DOO-PPV and TPD (4M)-MEH-PPV polymers are ~15 nm.

Figure 4.5 (b) shows the relative photoluminescence of the F8T2 polymer layers on ITO and dense TiO_2 substrates at 600 nm, as a function of polymer layer thickness when the polymer was excited with 400 nm light through the ITO coated glass substrate. The luminescence varies linearly with polymer layer thickness on ITO, and on dense TiO_2. For the dense TiO_2 substrate, the trend predicts complete quenching of luminescence at a layer thickness of 5 nm, and we can therefore assume the exciton diffusion length in the polymer as about 5 nm. This value is in good agreement with exciton diffusion length of other polythiophene polymers. Note that exciton diffusion lengths are expected to be shorter in thiophene polymers than in PPV polymer, because of faster singlet-triplet intersystem crossing.

Table 4.1 compares the exciton diffusion length, ionisation potential, hole-transport, and absorption properties of these three MEH-PPV polymers and the F8T2 polymer. The ionization potential of each polymer lies between 5.20 eV and 5.55 eV. The last two columns of Table 4.1 compare the hole-mobility at a given electric field and the nature of hole transport. The hole mobility of the TPD (4M)-MEH-PPV polymer is higher than the other polymer studied here. However, the spectral absorbance properties are better in MEH-DOO-PPV polymer. Overall, the TPD (4M)-MEH-M3EH-PPV polymer shows the most promising combination of hole-transport and absorption properties for solar cell application. The influence of the optoelectronic properties of these polymers on the performance of TiO_2 / polymer devices will be discussed in section 4.6, after discussing the charge recombination kinetics and device optimisation.

Table 4.1 *Summary of optoelectronic parameters for the polymers studied. Where M_{wt} represents the average molecular mass, α the peak absorption coefficient, λ_{max} is the wavelength corresponding to peak absorption, I_P the ionization potential, L_d the exciton diffusion length and μ_h the hole mobility at a fixed electric field.*

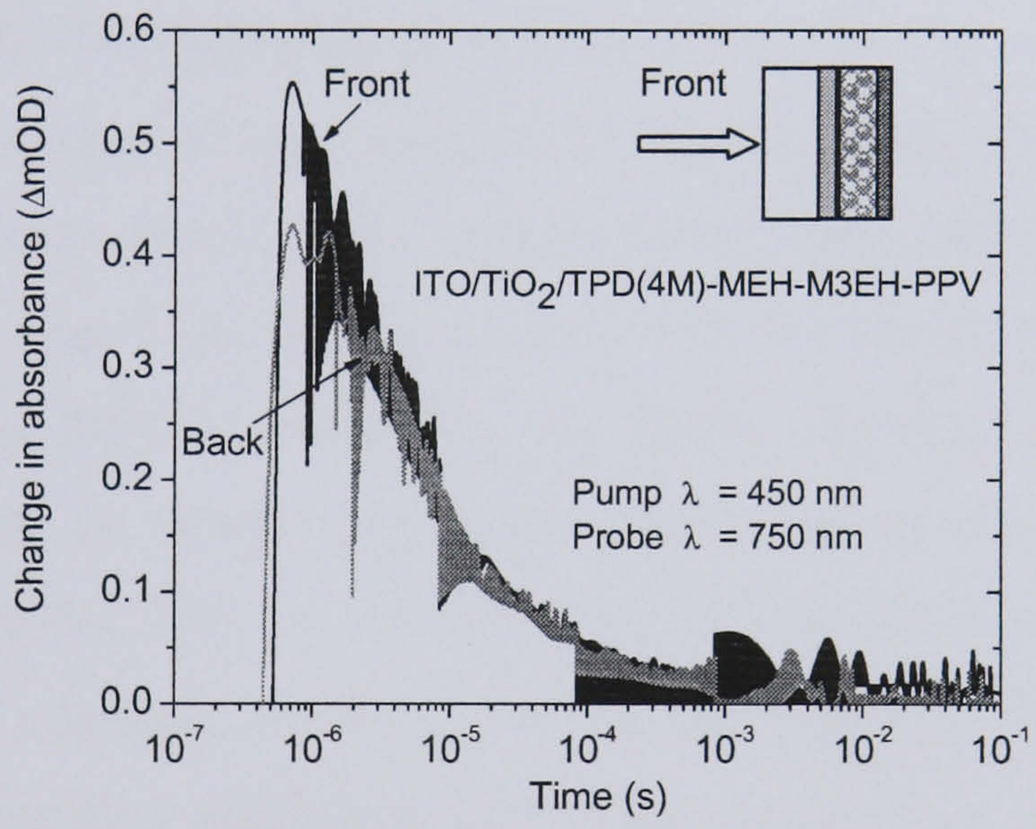
Polymers	M_{wt} (g/mol)	Peak α ($\times 10^5 cm^{-1}$)	λ_{max} (nm)	I_P (eV)	L_d (nm)	μ_h * (cm^2/Vs)	Type of transport
MEH-DOO-PPV	34,300[103]	1.60	502	5.25	15	3.3×10^{-5}	Dispersive
TPD (4M)-MEH-M3EH-PPV	35,700[105]	1.67	439	5.30	15	2.8×10^{-4}	Dispersive
TPD (4M)-MEH-MPPV	53,100[105]	1.74	428	5.45	15	2.0×10^{-3}	Non-dispersive
F8T2	26,800[135]	3.10	460	5.55	5	10^{-5}-10^{-4}	Highly dispersive[136]

* at 2.5×10^5 V/cm,

4.4 Charge recombination kinetics and polymer infiltration

In the previous chapter, we showed that infiltration of the fluorene-bithiophene polymer into the porous TiO_2 film can be achieved either by heat or dip-treatment. Here we show that the infiltration of the MEH-PPV polymers into porous TiO_2 is improved by dip-coating. Nanosecond-microsecond spectroscopy technique was again used to estimate the extent of polymer penetration into porous TiO_2 in a TiO_2 / polymer structure. Comparison of the magnitude of the photoinduced absorption signal for illumination from the polymer side and from the substrate side indicates the extent of polymer penetration into the porous TiO_2. Provided that the pore volume exceeds the volume of polymer applied, complete polymer penetration results in identical photoinduced absorption signals for illumination from either side, while incomplete penetration leads to a smaller signal for illumination from the polymer side, due to the optical filtering of the pump light by the layer of polymer not incorporated into the porous film.

(a)



(b)

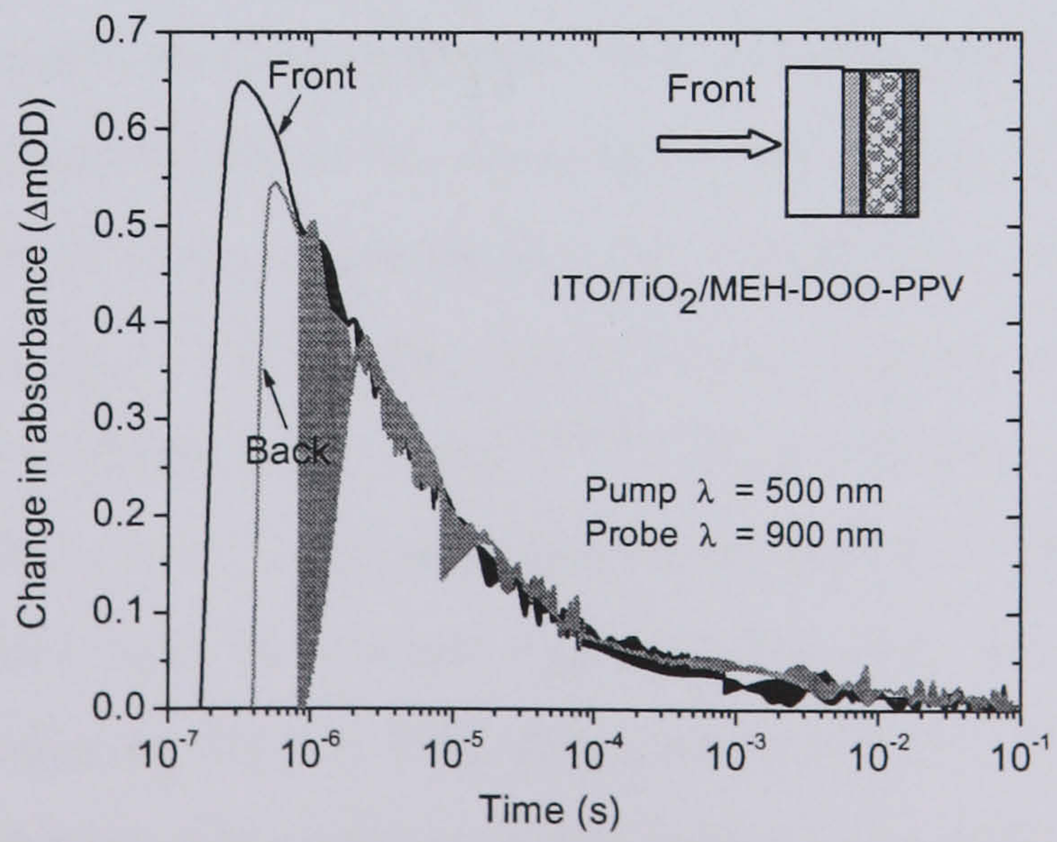


Figure 4.6 *Transient absorption kinetics following photoexcitation of ITO / HBL / porous TiO_2 / polymer using (a) TiO_2 / TPD(4M)-MEH-M3EH-PPV polymer and (b) MEH-DOO-PPV polymer. The inset shows the sample structure: ITO / HBL / porous TiO_2 / polymer. The*

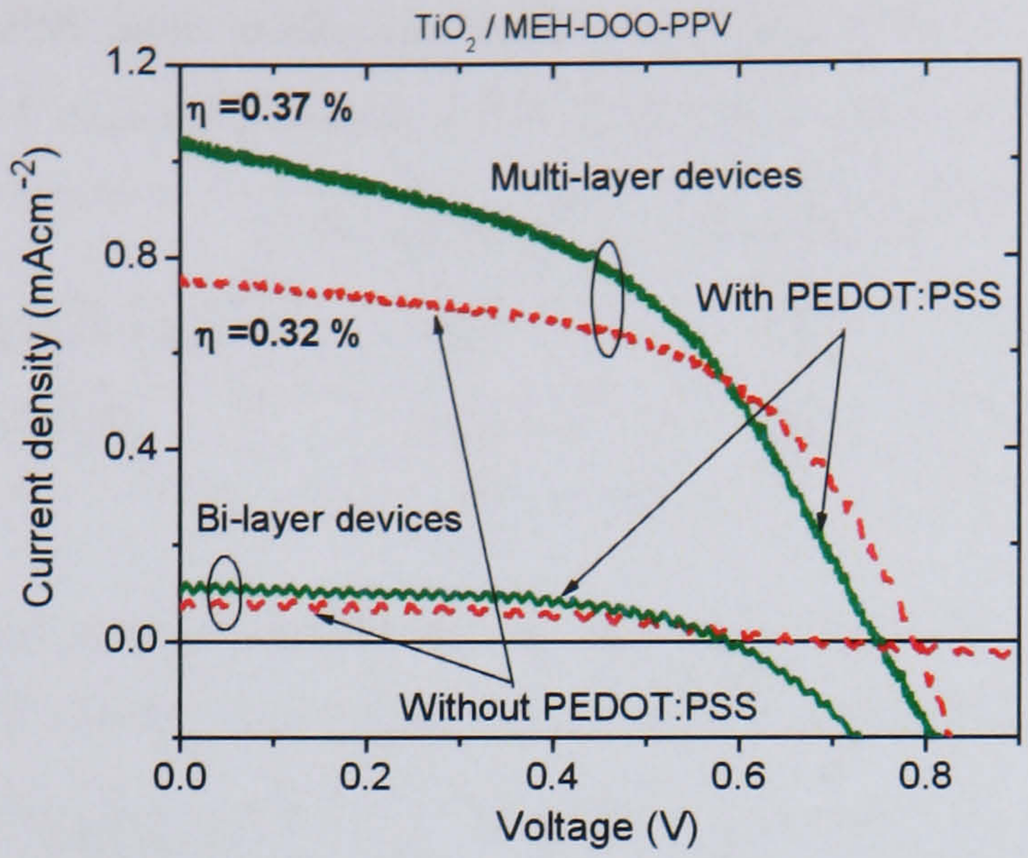
excitation density was about 30 μJ / pulse / cm² (corresponding to 1.3 × 10¹⁴ incident photons / pulse / cm²). The transient absorption is assigned to hole-polarons in the polymer and the decay to interfacial recombination between electrons in the TiO_2 and hole-polarons in the polymer. Black lines indicate illumination from the substrate ('front') side and grey lines correspond to illumination from the polymer ('back') side.

Figure 4.6 (a) shows the transient absorption kinetics for porous TiO_2 / TPD (4M)-MEH-M3EH-PPV at a probe wavelength of 750 nm and porous TiO_2 / MEH-DOO-PPV at a probe wavelength of 900 nm under excitation by pulses of intensity ~ 30 μJ / pulse / cm^2. In each case, the probe wavelength was chosen as the maximum of the photoinduced absorption spectrum recorded after 10 μs. No photoinduced absorption signal was observed at the probe wavelength for pristine films of either polymer, therefore the observed signal for the composite films on the (0.1 μs -100 ms) timescale can safely be assigned to hole-polarons rather than to triplet states. The inset shows the sample structure. Each sample was excited at the peak absorption wavelength of the polymer (450 nm for TPD (4M)-MEH-M3EH-PPV and 500 nm for MEH-DOO-PPV).

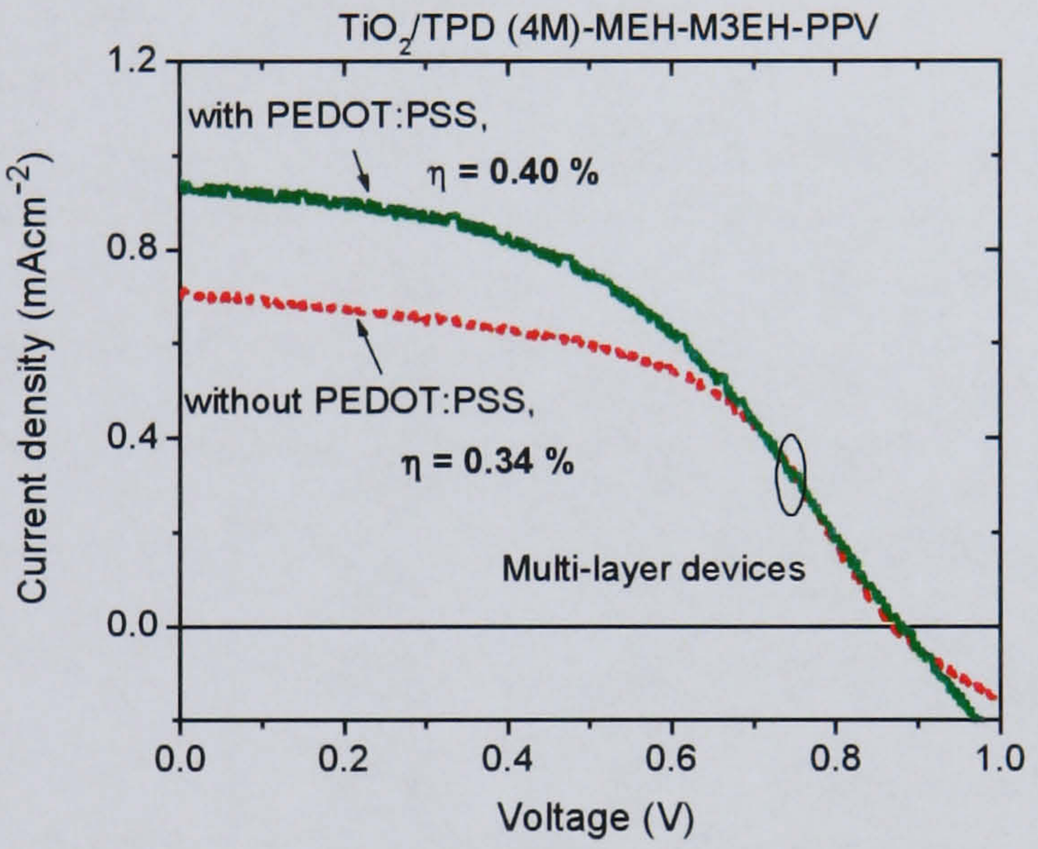
The layer structures of each sample are identical with layer thicknesses of about 50 nm HBL, 100 nm porous TiO_2 and about 50 nm effective polymer thickness, including both dip coated and spin coated layers. We estimated the effective polymer thickness on porous TiO_2 by comparing the optical absorption of the polymer coated TiO_2 electrode with the known absorption coefficient of the respective polymer on spectrosil, assuming the TiO_2 is ~ 50 % porous. The optical density of the active layers after dip and spin coating is about 0.3-0.4 at the pump wavelength. The shape and magnitude of the transient absorption signals are almost identical for illumination from the back (polymer side) and front (substrate side), indicating that polymer penetration is excellent in both structures. However, the decay of the signal in each case is relatively fast, with a half time of 5-10 μs, compared to the slower recombination times of 100 μs – 10 ms observed in TiO_2 / F8T2 solar cells in the last chapter. Although faster than the values for dye sensitised solar cells[46,48,49], these recombination times compare reasonably well with values (1-100 μs) reported for polymer-fullerene blends[76], which are used as the active layer in efficient organic solar cells. The slightly faster charge recombination kinetics in TiO_2 / TPD (4M)-MEH-M3EH-PPV compared to TiO_2 / MEH-DOO-PPV samples may be due to the higher hole-mobility in the TPD (4M)-MEH-M3EH-PPV polymer[138].

4.5 Effect of PEDOT:PSS layer

(a)



(b)



(c)

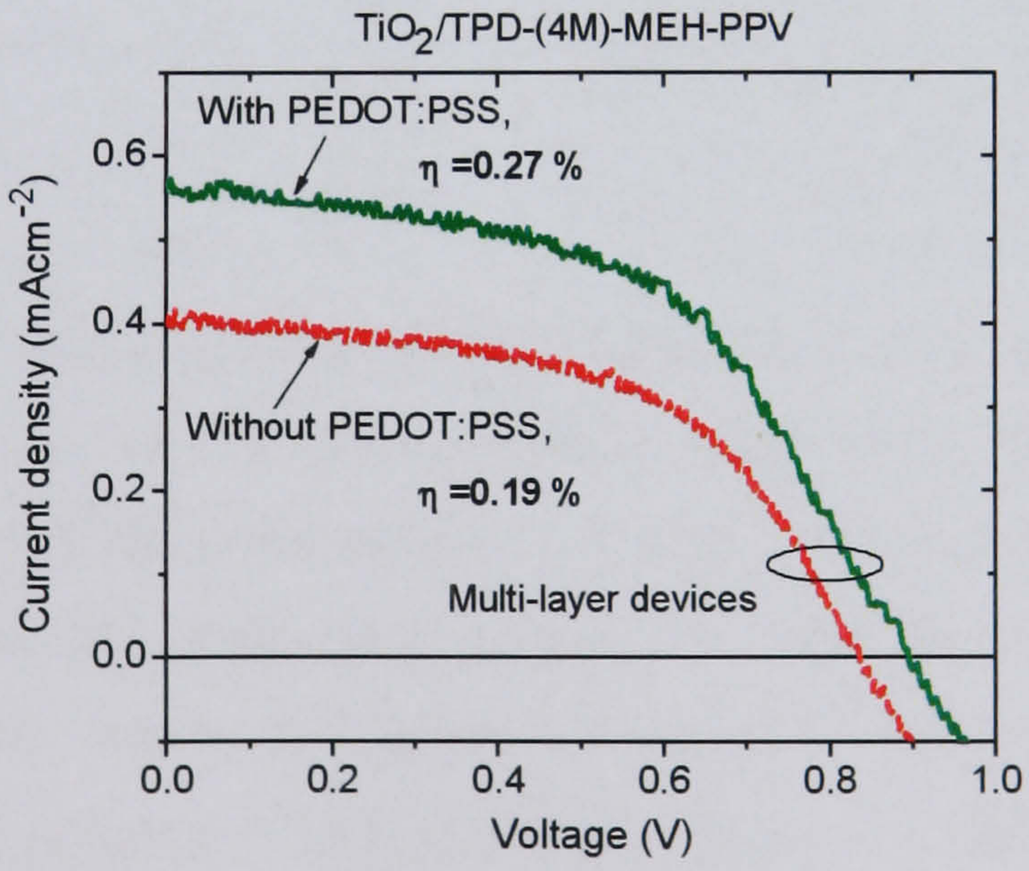


Figure 4.7 *J-V characteristics of multilayer [ITO / HBL (50 nm) / porous TiO_2 (100 nm) / polymer ^{d,s} (~50 nm) / Au] and bi-layer [ITO / HBL(50 nm) / polymer^{d,s} (~50 nm) / Au] with and without a PEDOT:PSS layer under the Au top contact. Measurements were performed under simulated (100 mWcm^{-2}, air mass 1.5) solar illumination. The polymers used were (a) MEH-DOO-PPV, (b) TPD (4M)-MEH-M3EH-PPV, and (c) TPD (4M)-MEH-PPV. In each case, the solid (dotted) lines represent the J-V characteristic of the device with (without) a PEDOT:PSS layer. The corresponding photovoltaic parameters are shown in Table 4.2 and 4.3.*

Table 4.2 *The photovoltaic parameters of MEH-DOO-PPV polymer bi-layer devices with and without a PEDOT:PSS layer under simulated irradiation AM 1.5 (100 $mWcm^{-2}$). The values correspond to the J-V characteristics of the bi-layer device shown in Figure 4.7 (a).*

Device	J_{SC} (μAcm^{-2})	V_{OC} (mV)	FF	η(%)
Without PEDOT:PSS	73	648	0.528	**0.025**
With PEDOT:PSS	123	583	0.549	**0.039**

Table 4.3 *The photovoltaic parameters of our multilayer TiO_2 / polymer devices under simulated AM 1.5 (100 $mWcm^{-2}$) in comparison with the best reported devices in the literature.*

Polymer	PEDOT :PSS	J_{SC} ($mAcm^{-2}$)	V_{OC} (V)	FF	η (%)	Reference
P3HT	×	0.31	0.49	0.40	**0.06**	[73]
MEH-PPV	×	0.40	1.1	0.42	**0.18**	[16]
F8T2	×	0.40	0.92	0.45	**0.17**	This work
	√	0.60	0.75	0.46	**0.21**	This work
TPD(4M)-MEH-PPV	×	0.41	0.83	0.56	**0.19**	This work
	√	0.57	0.90	0.53	**0.27**	This work
MEH-DOO-PPV	×	0.74	0.78	0.56	**0.32**	This work
	√	1.04	0.74	0.48	**0.37**	This work
TPD(4M)-MEH-PPV	×	0.70	0.89	0.55	**0.34**	This work
	√	0.96	0.86	0.49	**0.41**	This work

Figure 4.7 shows the effect of a PEDOT:PSS layer under the Au electrode on the J-V characteristics of TiO_2 / polymer devices under AM1.5 illumination. Table 4.2 compares the photovoltaic performance of a bi-layer device with PEDOT:PSS and without PEDOT:PSS. The photovoltaic parameters of the multilayer devices, with and without PEDOT:PSS, shown in Figures 4.7 and 3.27 are compared with the best previously reported polymer / TiO_2 devices in Table 4.3. The short circuit current densities of all devices increase by at least 30 % upon introduction of the PEDOT:PSS layer and the overall power conversion efficiencies are significantly increased. The efficiency values for all of our devices that contain a PEDOT:PSS layer in table 4.3 are higher than the previous best reported values.

There are several possible reasons for the improvement in J_{SC} resulting from insertion of the PEDOT:PSS layer. One explanation is that PEDOT:PSS may cause a

chemical doping of the polymer[24,126] that reduces the contact resistance between the polymer and metal contact. A second possibility is that the PEDOT:PSS layer may protect the polymer film from damage during evaporation of the Au electrode[34], which could lead to an increase in the series resistance of the device. A third possibility is that PEDOT:PSS improves collection by minimising the energy step between polymer and top contact. Our experimental results discussed in section 3.9 and our simulation studies[134] show that interfacial energy steps should be minimised for efficient charge transfer between active layers and electrodes. It has also been shown that the work function of Au on top of conjugated polymers may be smaller than the expected value of 5.1 eV by 0.2-0.3 eV[35,37,127]. Since the ionisation potential of all the polymers are more than 5.20 eV, the energy barrier at the polymer / Au interface is expected to be at least 0.3 eV in the device without the PEDOT:PSS layer. In contrast, for the device with the PEDOT:PSS layer there should be no / small interfacial energy step because the PEDOT:PSS work function of (5.2 ± 0.1) eV[60] is similar to the ionisation potential of the polymers. The forward-bias dark current for the devices with PEDOT:PSS are much higher than for the device without PEDOT:PSS, confirming that the energy barrier for hole injection at the polymer / metal interface is reduced by introduction of the PEDOT:PSS layer.

The open circuit voltage decreases upon introduction of a PEDOT:PSS layer in all devices except in case of the high hole-mobility TPD (4M)-MEH-PPV polymer device, where both J_{SC} and V_{OC} increase. The more general reduction in V_{OC} can be explained in terms of the reduced interfacial energy step at the polymer-top-contact interface upon replacing Au (effective work function 4.9 eV) with PEDOT:PSS (work function 5.3 eV). The reduced barrier for hole-injection tends to increase the injected current and reduce V_{OC}, since the open circuit voltage of a solar cell is limited by, amongst other factors, currents injected from the electrodes opposing the photocurrent. Increased charge injection is also evident in the dark currents of PEDOT:PSS containing devices in all cases.

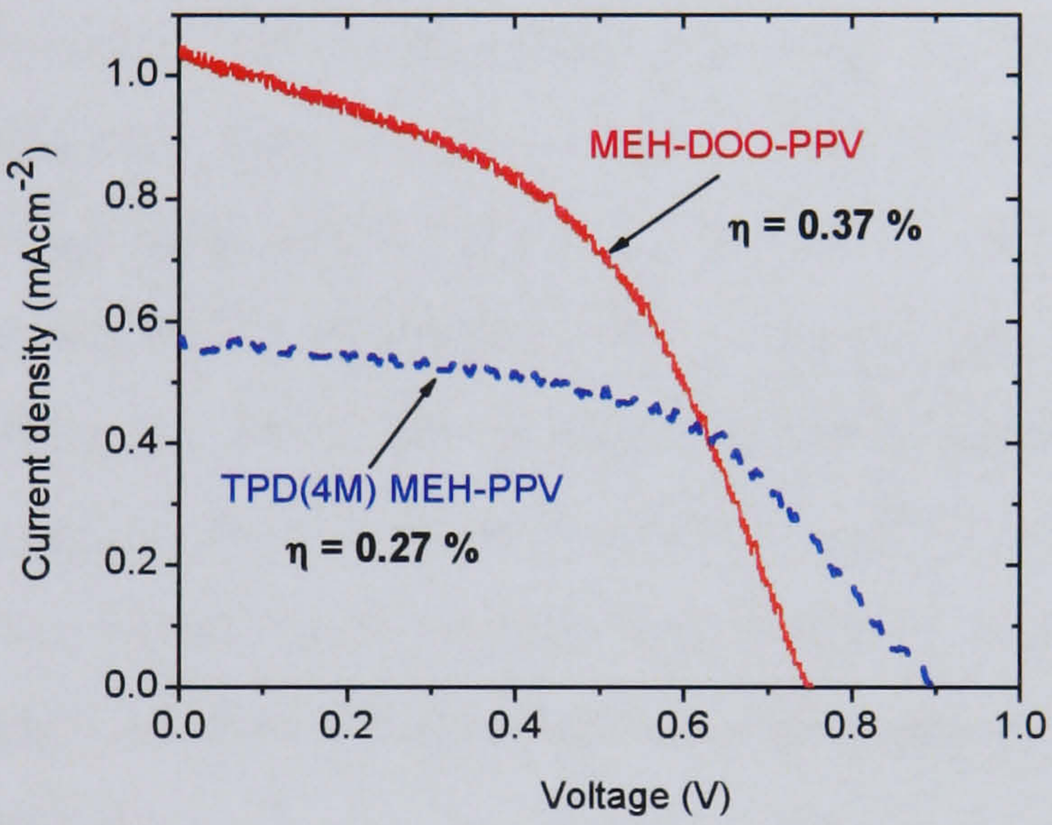
Note that the effect on V_{OC} is the reverse of that expected, if V_{OC} were controlled only by the difference in electrode work functions. Although the exact mechanism by which PEDOT:PSS increases J_{SC} is not clear, it appears to be related to the improved conductivity of the polymer / top contact interface.

4.6 Influence of polymer optoelectronic properties on device performance

We now consider the influence of the exciton diffusion length, hole transport and light havesting properties of the polymer on the performance of TiO_2 / polymer phtovoltaic devices. The short circuit current density of a TiO_2 / polymer photovoltaic device may depend upon the polymer through its light harvesting properties and exciton diffusion length as well as the uptake of the polymer by porous TiO_2 during dip-coating and spin coating. Good uptake of polymer by the porous TiO_2 is essential for efficient device performance. We found that all of these MEH-PPV polymers and F8T2 polymer sensitise the TiO_2 well.

4.6.1 Effect of spectral absorbance

(a)



(b)

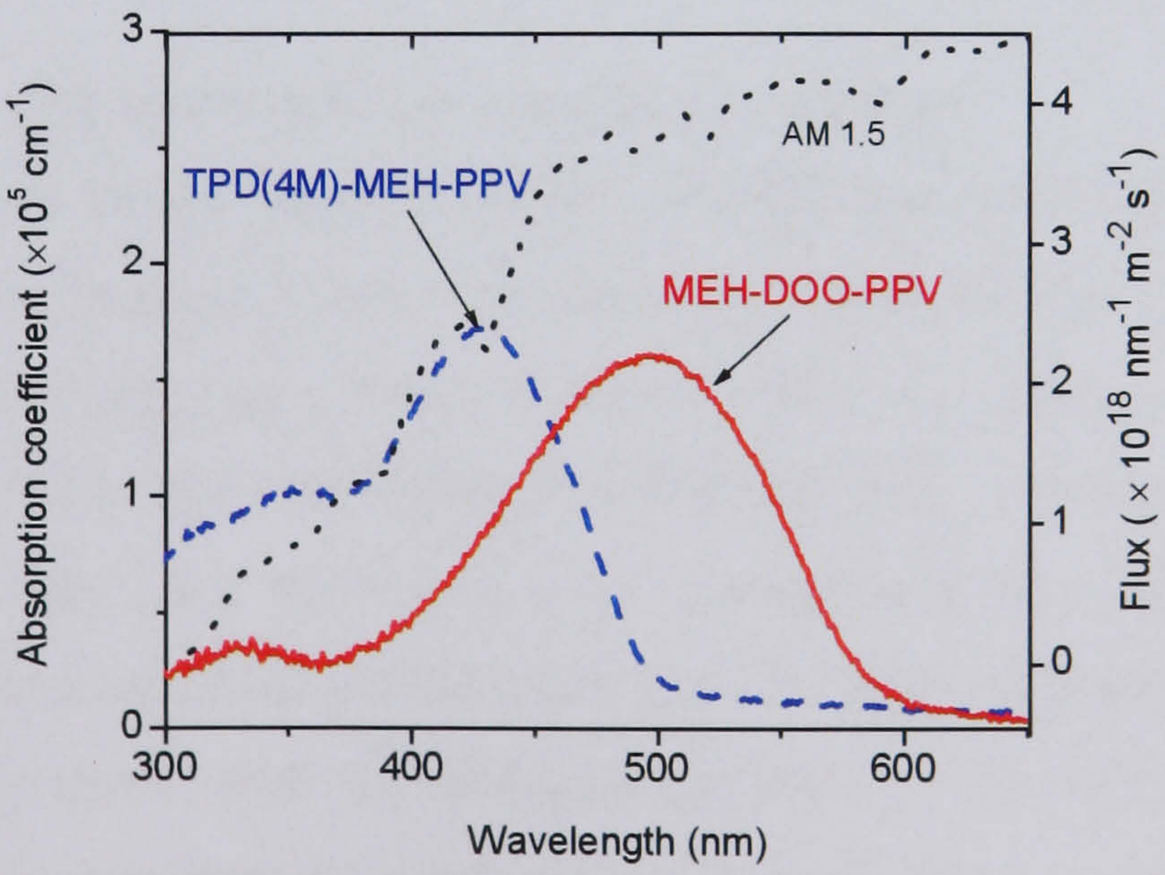


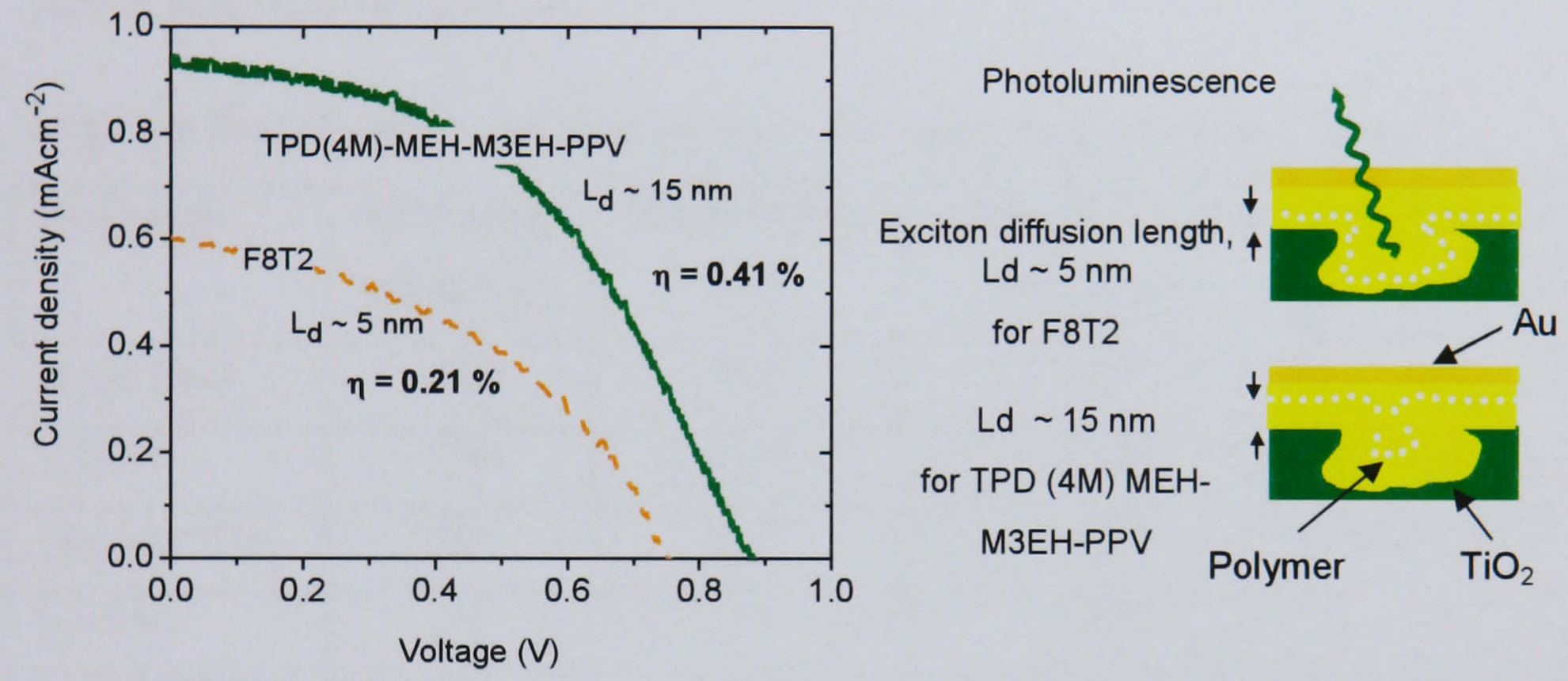
Figure 4.8 *(a) J-V characteristics of ITO / HBL (50 nm) / Porous TiO_2 (100 nm) / polymer (50 nm) / PEDOT:PSS / Au devices under simulated (100 mWcm^{-2}, air mass 1.5) solar illumination. The polymers used were MEH-DOO-PPV (solid lines) and TPD-(4M)-MEH-PPV (dashed lines). (b) Optical absorption spectra of the two polymers compared with the AM 1.5 solar photon flux spectrum (dotted lines).*

Figure 4.8 (a) shows the J-V characteristics of MEH-DOO-PPV and TPD (4M)-MEH-PPV polymer devices under simulated (100 $mWcm^{-2}$, air mass 1.5) solar illumination. The device structure was ITO / HBL (50 nm) / porous TiO_2 (100 nm) / polymer (50 nm) / PEDOT:PSS / Au in both cases. The optical absorption spectra of these polymers are compared with the solar photon flux spectrum in Figure 4.8 (b). The MEH-DOO-PPV polymer device produced the higher short circuit current density, J_{SC}, of more than 1 $mAcm^{-2}$, while the TPD (4M)-MEH-PPV polymer showed the higher V_{OC} of 0.92 V. The MEH-DOO-PPV device shows better overall device performance. The lower $J_{SC,}$ of 0.55 $mAcm^{-2}$ for TPD (4M)-MEH-PPV polymer compared to the MEH-DOO-PPV polymer can be attributed to the blue shifted absorption and lower spectral overlap with the solar photon flux spectrum (see Figure 4.8 (b)). Nevertheless, the power conversion efficiency of this TPD (4M)-MEH-PPV device, at 0.27 %, is 50 % higher than the best previously reported efficiency for a hybrid TiO_2/polymer solar cell[16]. The low J_{SC} observed for the TPD (4M)-MEH-PPV polymer, with mobility more than two orders of magnitude greater than MEH-DOO-PPV polymer, indicates that in these devices, light harvesting properties play a more important role than charge transport in determining $J_{SC.}$ The larger V_{OC} for TPD (4M)-MEH-PPV than for MEH-DOO-PPV polymer devices may result from either the higher hole-mobility, the larger separation between the HOMO level of the polymer and the conduction band of TiO_2, or both. The influence of the hole-mobility on overall device performance will be discussed in section 4.6.3.

4.6.2 Importance of exciton diffusion length of polymer

Here we focus on device performance of F8T2 and TPD (4M) MEH-M3EH-PPV polymers in an optimised device structure consisting of ITO / HBL (50 nm) / porous TiO_2 (100 nm) / polymer (50 nm) / PEDOT:PSS / Au. Figure 4.9 (a) shows J-V characteristics of F8T2 and TPD-(4M)-MEH-M3EH-PPV polymer devices under simulated (100 $mWcm^{-2}$, air mass 1.5) solar illumination. The device with F8T2 polymer shows power conversion efficiency of 0.21 %, while TPD-(4M)-MEH-M3EH-PPV polymer device shows 0.41 %. Although the device with F8T2 polymer shows better device performance than any previously reported TiO_2 / polymer solar cell[16], green photoluminescence from the device is still observed, when it is illuminated with a blue monochromatic light of wavelength 470 nm. This is probably due to the short exciton diffusion length of F8T2 polymer. The SEM images of the porous film show that there are some large pores of more than 20 nm in the spin coated porous TiO_2 films

(see Figure 3.15). Figure 4.9 (b) illustrates how the exciton diffusion length of a polymer, compared to the pore size, may influences the charge separation. Since the exciton diffusion length of the F8T2 polymer is around a few nm, only excitons produced near to the interface contribute to the photocurrent and the rest of them recombine and emit luminescence. On the other hand, the longer exciton diffusion length of TPD (4M) MEH-M3EH-PPV polymer should enable more excitons to diffuse to the TiO_2 / polymer interface without recombining and then dissociate at the interface. A longer exciton diffusion length polymer is expected to reduce the losses by exciton recombination and offer higher photocurrent density.



(a) (b)

Figure 4.9 *(a) J-V characteristics of ITO / HBL (50 nm) / porous TiO_2 (100 nm) / polymer (50 nm) / PEDOT:PSS/ Au devices under 1 sun. Polymers used were F8T2 (dashed line) and TPD (4M)-MEH-M3EH-PPV (solid line). (b) A schematic representation of the interface between TiO_2 pore and polymer, with different exciton diffusion lengths.*

Although the F8T2 polymer has comparable hole-mobility and a higher absorption coefficient over a similar spectral range to the TPD (4M) MEH-M3EH-PPV polymer, F8T2 based polymer devices show a lower short circuit current density. This is probably due to the shorter exciton diffusion length of the F8T2 polymer (~5 nm), stressing another key factor, apart from light harvesting, in photocurrent generation.

4.6.3 Influence of hole mobility of the polymer

Table 4.4 summarises the optoelectronic properties of the polymers studied and the performance of the corresponding devices. It has been reported[139] that open circuit voltage, V_{OC} in polymer / fullerene solar cells is strongly influenced by the energy separation between the HOMO level of the polymer and LUMO level of the fullerene,

and the differences in work function of the electrodes influence the V_{OC} in a minor way. We may therefore expect better V_{OC} in F8T2 device than the TPD (4M) MEH-PPV device due to larger energy separation between the HOMO level of the polymer and the conduction band of TiO_2. However, TPD (4M)-MEH-PPV polymer device offers the larger V_{OC} than higher I_P F8T2 polymer devices. This may result from the higher hole-mobility of TPD (4M)-MEH-PPV which may minimise interfacial recombination. The table further shows that the fill factor of the device also appears to be weakly correlated to the hole-mobility of the polymer. Higher hole-mobility polymer devices offer better fill factor and V_{OC}. The influence of the hole-mobility on overall device performance cannot, therefore, be ruled out.

Table 4.4 *The influence of optoelectronic properties of polymers on device performance*

Polymers	**TPD (4M)-MEH-PPV**	**MEH-DOO-PPV**	**TPD (4M)-MEH-M3EH-PPV**	**F8T2**
λmax (nm)	425	502	440	460
I_P (eV)	5.45	5.20	5.30	5.55
$*\mu_h$ (cm^2/Vs)	**10^{-3}**	**10^{-5}**	10^{-4}	10^{-5}- 10^{-4}
L (nm)	15	15	**15**	**5**
J_{SC} ($mAcm^{-2}$)	0.57	1.04	**0.96**	**0.60**
V_{OC}	**0.90**	**0.74**	0.86	0.75
FF	0.53	0.48	0.50	0.46
η (%)	**0.27**	**0.37**	**0.41**	**0.21**

* at 2.5×10^5 V/cm

In summary, the device made from TPD (4M)-MEH-M3EH-PPV showed the best performance. This is due to the best combination of optoelectronic properties for the TPD (4M)-MEH-M3EH-PPV polymer, such as high hole-mobility, good visible absorption, long exciton diffusion length (~15 nm) and moderate ionisation potential (5.30 eV) as well as its ability to sensitise TiO_2 (possibly assisted by the alkoxy side chain oxygen atoms). The fluorene thiophene copolymer device shows poorer performance than the MEH-PPV based polymer devices, despite having similar or better light absorption and charge transport properties. This is probably due to the shorter exciton diffusion length for this polymer.

4.7 Summary

We have studied the effects of conjugated polymer optoelectronic properties on the performance of a model polymer-TiO_2 hybrid system and the effect of PEDOT:PSS as hole collector. A comparison of the exciton transport, charge transport and light harvesting properties of three different MEH-PPV based polymers and a fluorene-bithiophene polymer was made. The performance of the corresponding photovoltaic devices was also assessed. Our results established that the short circuit current density is limited primarily by the photogeneration rate, and by the quality of the interfaces, rather than by the hole-transport properties of the polymer. Through a study of the sensitisation process and device design we found that excellent polymer infiltration into the porous TiO_2 could be achieved by dip coating, and that including a PEDOT:PSS layer beneath the top Au contact improves the short circuit photocurrent in all cases. An improved TiO_2 / polymer device incorporating both dip-coating and PEDOT:PSS layers produced a short circuit current density of about 1 $mAcm^{-2}$, a fill factor of 0.49 and an open circuit voltage of 0.86 V under 1 sun. The corresponding overall power conversion efficiencies of these devices were $\geq$ 0.40 % under 1 sun.

Although the reported efficiencies are a factor of two higher than the best previously reported value for a TiO_2 / polymer hybrid device, they are still lower than for polymer-fullerene solar cells, largely on account of relatively low J_{SC} values. Possible reasons may be the limited length scale of the nanostructure which may still allow exciton quenching despite the relatively long exciton diffusion length of MEH-PPV polymers or limited polymer up take. The next chapter will therefore focus on porous metal oxide of different microstructure with different polymers, in terms of polymer uptake, pore volume, particle diameter and morphology.

Chapter 5

The effect of TiO_2 microstructure and the type of metal oxide

This chapter examines the effect of modifying the properties of the porous metal oxide layer on the performance of metal oxide / polymer devices. We address the effect of the microstructure of the TiO_2 film, the film thickness, the type of metal oxide (TiO_2, ZnO and SnO_2), and of treatment of the TiO_2 surface with an alumina coating or a dye coating.

5.1 Abstract

Here we focus on several porous metal oxides with different microstructure combined with P3HT and TPD containing MEH-PPV polymers. Transient absorption spectroscopy, UV-VIS absorption spectroscopy, scanning electron microscopy and electrical measurements were used to study the influence of the microstructure of the metal oxide on the function and photovoltaic performance of metal oxide / polymer structures.

We prepared the first hybrid SnO_2 / polymer device using nanocrystalline SnO_2. The device produced a short circuit current density J_{SC} of 0.48 mA cm^{-2} and open circuit voltage V_{OC} of 0.75 V under AM 1.5 conditions. The corresponding overall power conversion efficiency was 0.17 %.

We studied the performance of TiO_2 / polymer devices as a function of device design, TiO_2 microstructure, exciton diffusion lengths of the polymer and active layer thicknesses. We found that a thin alumina coating on nanocrystalline TiO_2 increases both the open circuit voltage and fill factor of TiO_2 / polymer devices and hence overall

device performance over 25 %. This is attributed to the suppression of interfacial recombination by the thin alumina layer.

We observed that the performance of TiO_2 / polymer devices is highly dependent on the microstructure of the porous TiO_2, particularly on TiO_2 pore size relative to the exciton diffusion length of polymer, and on the active layer thickness. We achieved improved efficiency for hybrid TiO_2 / polymer solar cells based either TPD containing MEH-PPV polymer or P3HT polymer, using our novel multilayer device structure (described in chapter 3).

The best P3HT / TiO_2 multilayer device shows a short circuit current density of over 0.6 $mAcm^{-2}$, open circuit voltage of 0.58 V and a fill factor of 0.55 under AM 1.5 conditions (100 $mWcm^{-2}$, 1 sun). The corresponding AM 1.5 overall power conversion efficiency of the device is 0.2 %. This is more than a factor of three greater than the best reported value for P3HT / TiO_2 devices under AM1.5 conditions.

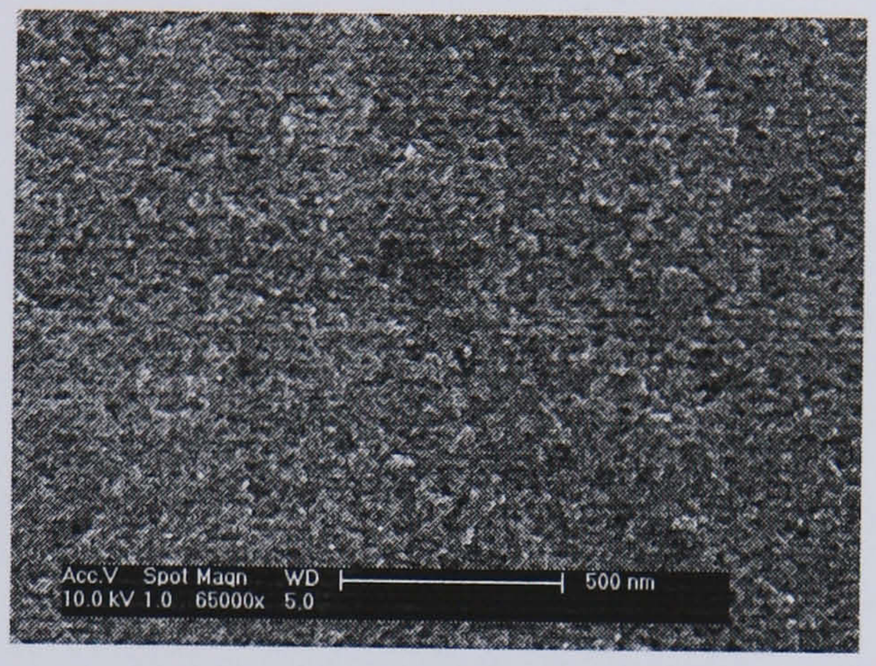
The highest efficiency was obtained for a hybrid TiO_2 / polymer solar cell based on TiO_2 and a TPD containing MEH-PPV polymer. The optimised device shows a peak external quantum efficiency of $\approx$ 40 % and short circuit current density $\geq$ 2 mA cm^{-2} for air mass (AM) 1.5 conditions (100 mW cm^{-2}, 1 sun). The AM 1.5 open circuit voltage reaches 0.64 V and the fill factor 0.43, resulting in an overall power conversion efficiency of 0.58 %.

5.2 The effect the type of metal oxide

Three types of porous metal oxide, namely porous ZnO, TiO_2 and SnO_2 films, were prepared to study the effect of the type of metal oxide. The ZnO colloidal film was milky in colour, while the TiO_2 and SnO_2 films were transparent. The milky colour of the ZnO film may be due to the large particle size, causing strong scattering of light, while the smaller particle size in TiO_2 and SnO_2 films causes negligible scattering.

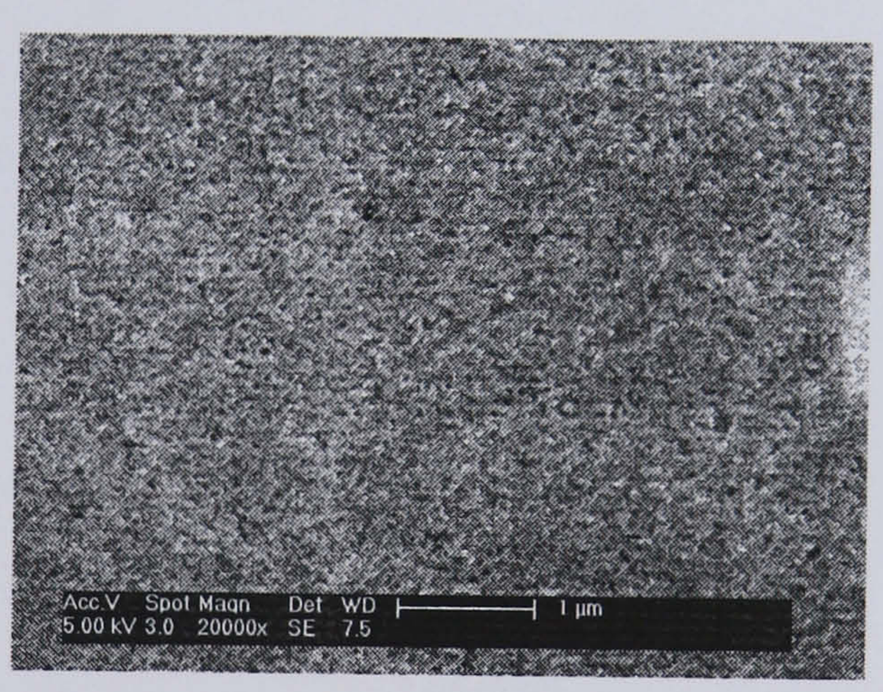
5.2.1 SEM Images

(a)



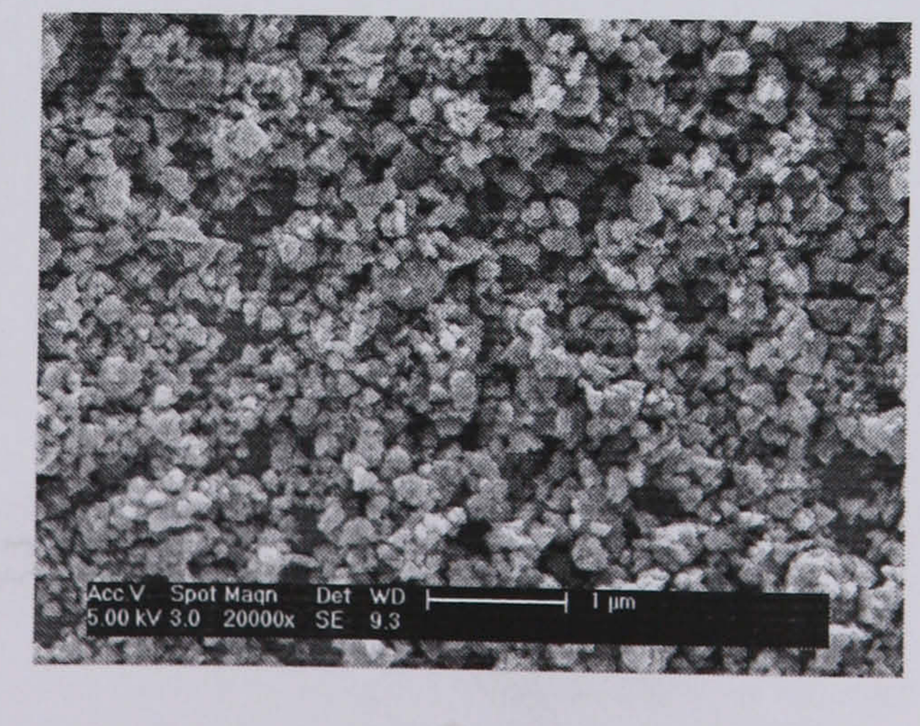
TiO_2 (IC)

(b)



SnO_2

(c)



ZnO

Figure 5.1 *SEM micrographs of the different metal oxide films (a) TiO_2, (b) SnO_2 and (c) ZnO.*

Figure 5.1 shows typical scanning electron micrographs of the TiO_2, SnO_2 and ZnO films. The micrographs of both the TiO_2 and SnO_2 films show that the films have a uniform distribution of particle sizes, ranging between 10 to 15 nm, small pore size and continuous interpenetrating network (A more detailed image can be found in Figure 5.8 (a)). However, the micrograph of the ZnO film shows that the film has larger particle sizes, in the range 40 to 80 nm, larger pore sizes (some of them over 100 nm) and form a discontinuous network due to some isolated particles. The ZnO film was much rougher than the other two films due to the larger particle size.

5.2.2 Photovoltaic performance

We made devices using these porous metal oxide films and TPD (4M)-MEH-M3EH-PPV polymer. This polymer has excellent optoelectronic properties as described in the last chapter. Dense TiO_2 was used as a hole-blocking layer (HBL) to prevent direct contact between the polymer and the ITO in all devices.

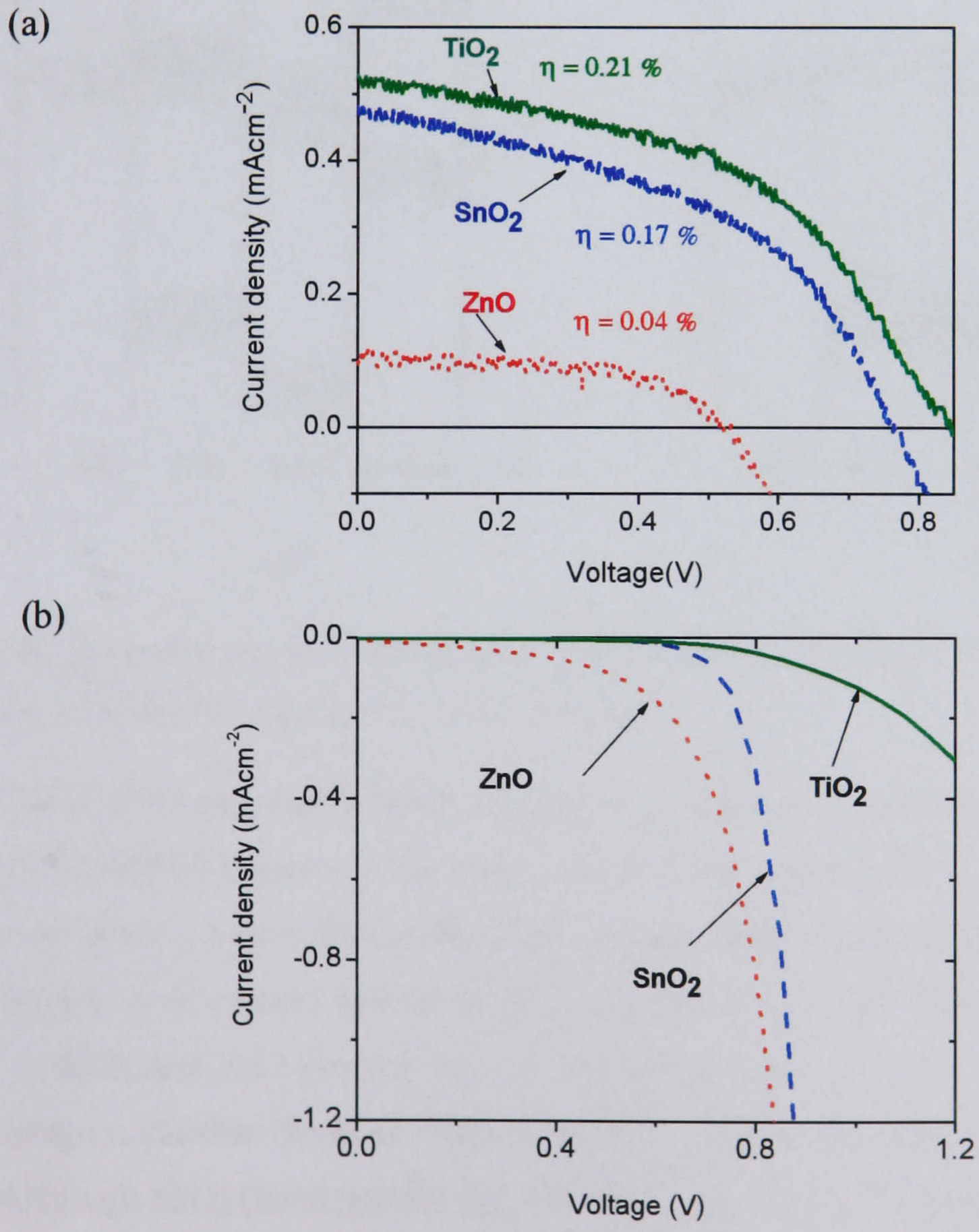


Figure 5.2 *J-V characteristic for ITO /HBL (50 nm) / porous metal oxide (~140 nm) / TPD (4M)-MEH-M3EH-PPV/Au (70 nm) / Au (a) under A.M. 1.5 illumination (1 sun) and (b) in the dark. The porous metal oxides are TiO_2 (solid line), SnO_2 (dashed line) and ZnO (dotted line).*

Figure 5.2 (a) and (b) show the current density-voltage characteristics for ITO / dense TiO_2 / porous metal oxide / TPD (4M)-MEH-M3EH-PPV / Au devices under air mass (AM) 1.5 conditions (100 $mWcm^{-2}$, 1 sun) and in the dark, respectively. The device made with porous SnO_2 produced a good short circuit current density J_{SC} of 0.48 mA cm^{-2} and open circuit voltage V_{OC} of 0.75 V under AM 1.5 conditions. The corresponding overall power conversion efficiency was 0.17 %. Although a few optical studies of SnO_2 / polymer hybrid structures and studies of efficient dye sensitised SnO_2 solar cells have been reported previously[93,94], there is as yet no report on SnO_2 / polymer hybrid devices. This is therefore the first working device to be reported. The performance of this SnO_2 / polymer device is comparable to several previously reported TiO_2 / polymer devices[16,17,19-21,68]. The SnO_2 / polymer system is therefore another promising material combination for low cost metal oxide / polymer solar cells.

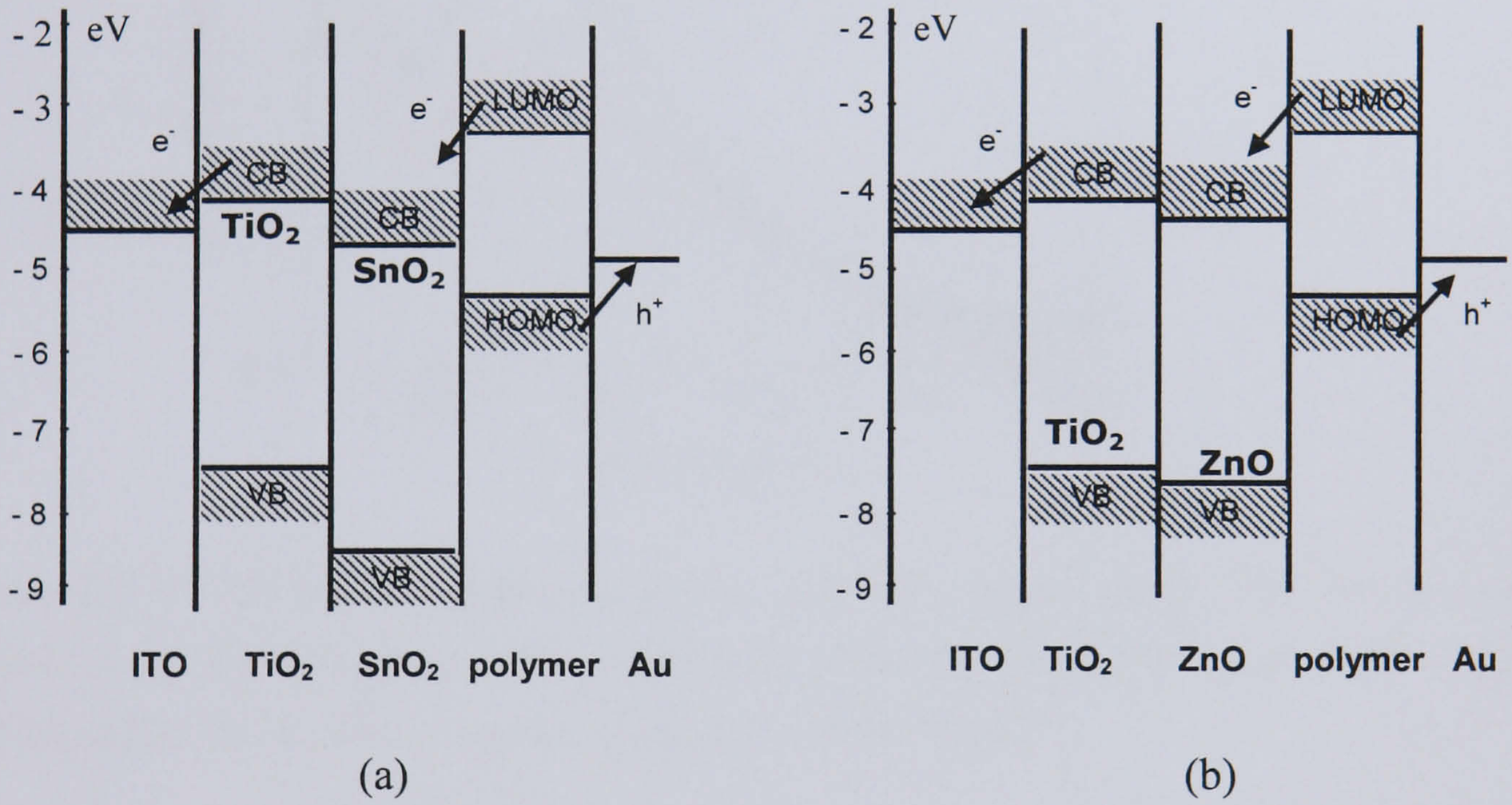


Figure 5.3 *Proposed electronic energy-level diagram for (a) ITO / dense TiO_2 / SnO_2 / polymer / Au device and (b) ITO / dense TiO_2 / ZnO / polymer.*

The ZnO device shows lower J_{SC} and V_{OC} than any of the TiO_2 or SnO_2 devices. This can be attributed partly to the lower interfacial area of the ZnO / polymer structure, due to the larger particle size of the ZnO colloids. Both ZnO and SnO_2 devices show much higher dark current and lower V_{OC} compared to TiO_2 device. The lower V_{OC} found in SnO_2 and ZnO devices may be due to the lower built in potential due to the lower lying conduction bands of ZnO and SnO_2[140] compared to TiO_2 (see, Figure 5.3).

Although SnO_2 (band gap 3.6 eV, CB band edge 4.6 eV[140]) is optically transparent and has a lower lying conduction band than ZnO (band gap 3.2 eV, CB band edge 4.4 eV[140]), the SnO_2 / polymer device showed better device performance. This is due to the better microstructure of SnO_2 with pores of size similar to the exciton diffusion length

in the polymer. Optimising the microstructure of the metal oxide is therefore crucial for the development of efficient polymer metal oxide / polymer devices.

The TiO_2 / polymer device show superior device performance to the other hybrid metal oxide / polymer devices that we studied. We will therefore focus on optimising the performance of TiO_2 / polymer device in the following section. Studies are in progress to improve both SnO_2 and ZnO devices.

5.2.3 Effect of metal oxide and dye coating treatments

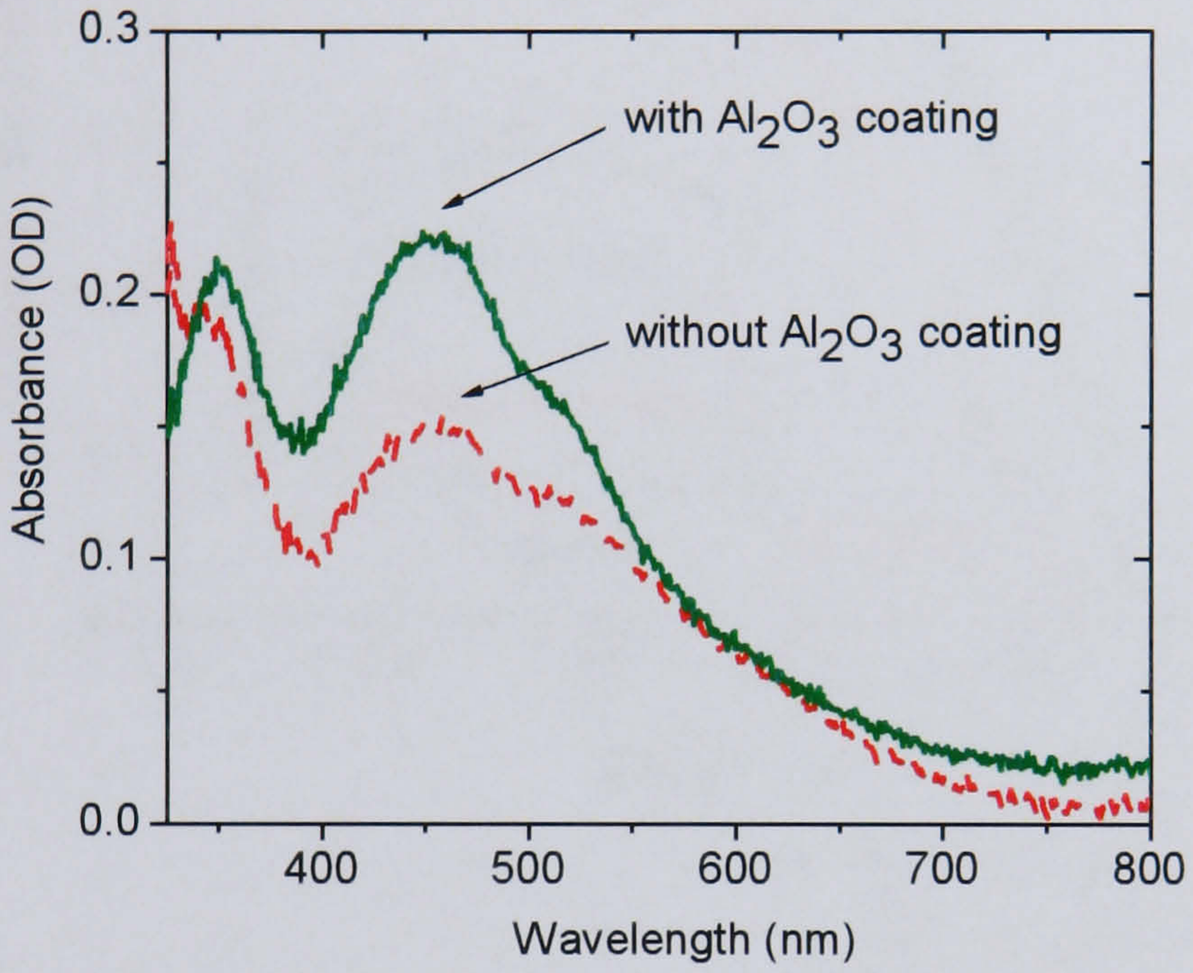


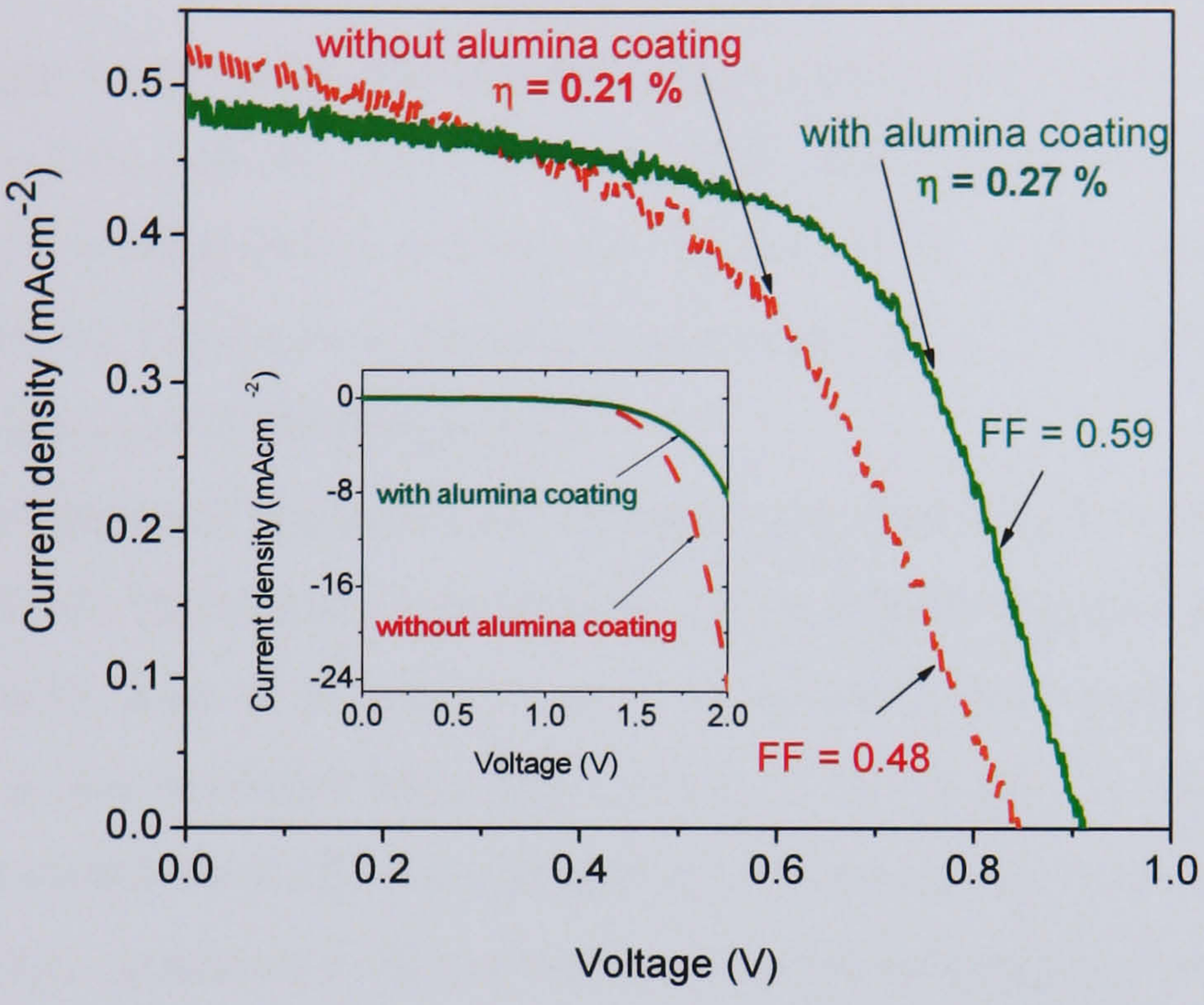
Figure 5.4 *UV-VIS optical absorption spectra of alumina coated (solid line) and uncoated (dashed line) TiO_2 nanoporous films of thickness about 140 nm, after dipping in TPD (4M)-MEH-M3EH-PPV / C_6H_5Cl (1 mg/ml) solutions for 18 hrs at 60 ^0C.*

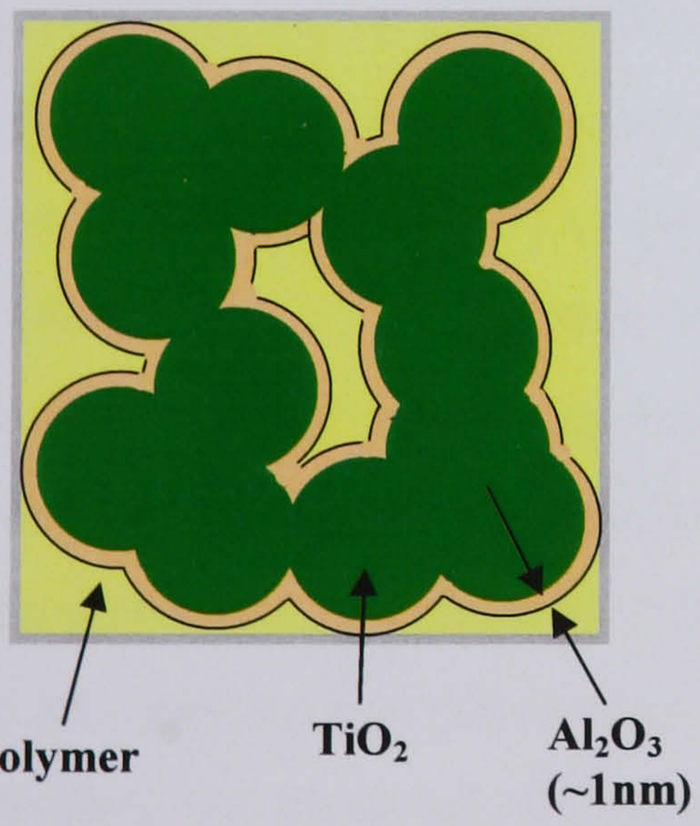
In an attempt to improve the performance of TiO_2 / polymer device, we treated the surface of the porous TiO_2 first by coating with a thin alumina (Al_2O_3) layer, and then by sensitising with a dye layer prior to spin-coating the polymer. We will first discuss the influence of the alumina coating on the performance of TiO_2 / polymer devices and then discuss the effect of the dye coating.

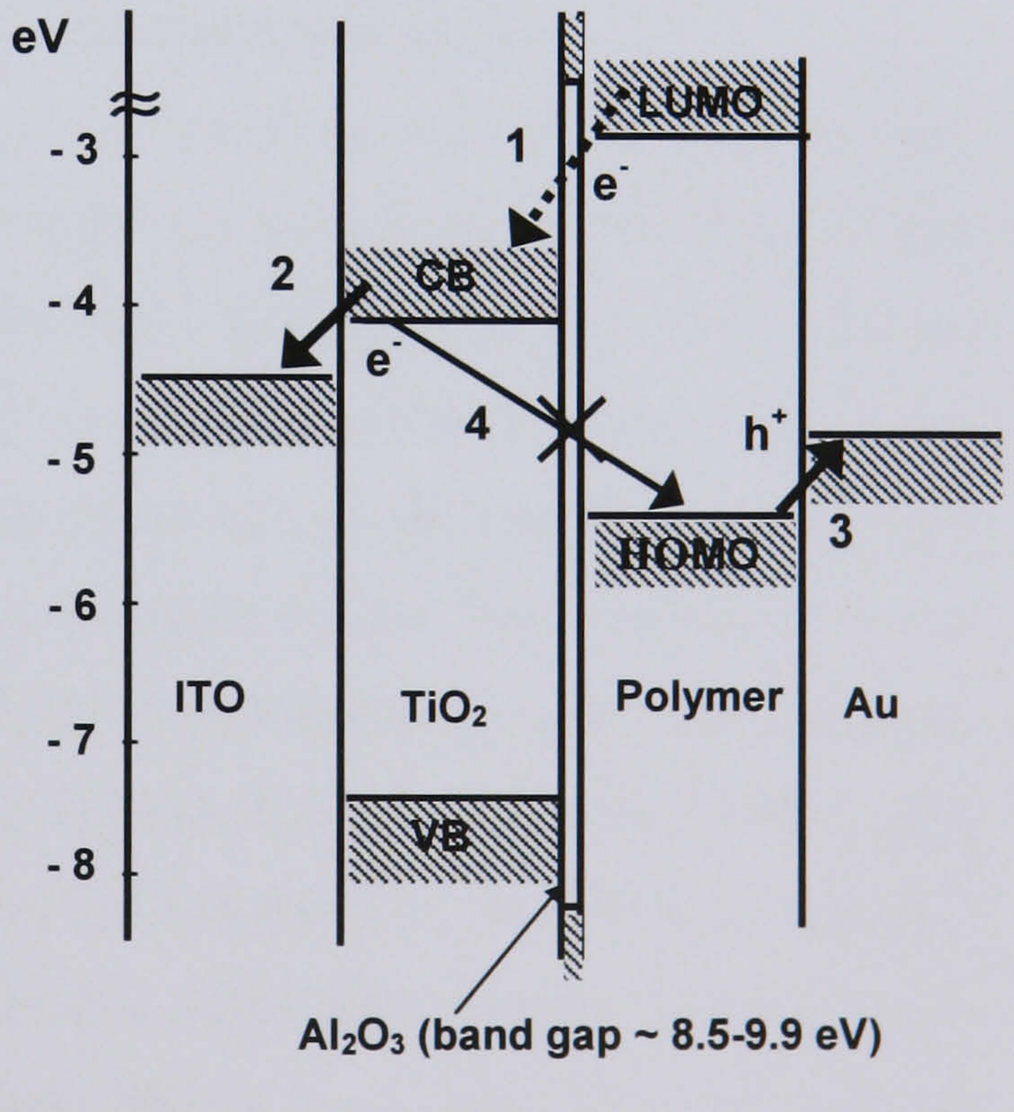
The surface of the porous TiO_2 was modified by dip-coating a thin alumina over layer on nanocrystalline TiO_2 as described in Refs.[52,116]. According to this cited references, separate high resolution transmission electron microscopy and XPS studies reveal that the thickness of the overlayer prepared in similar condition is between 0.7 and 1.0 nm. Figure 5.4 compares the absorbance of modified and unmodified porous TiO_2 electrodes following dip-coating in solutions of the polymer. The figure shows that surface modification of the porous TiO_2 film with the alumina coating improves the

polymer uptake. This is probably due to the more basic surface of the alumina coated porous TiO_2 film than the bare film, favouring polymer attachment. A similar observation was made in dye sensitised solar cells[43,140,141], where dye uptake was improved through surface modification of nanocrystalline SnO_2 and TiO_2 electrodes using overlayers of alumina as well as other basic oxides such as Y_2O_3 and MgO.

(a)







(b) (c)

Figure 5.5 *(a) Current density vs voltage characteristic under A.M. 1.5 conditions (1 sun) and in the dark (inset) for an ITO / dense TiO_2 (50 nm) / porous TiO_2 (140 nm) /Al_2O_3 (~1 nm) / TPD (4M)-MEH-M3EH-PPV/Au (70 nm) / Au devices (solid line) in comparison with a similar device without the alumina layer (dashed line), (b) Schematic representation of the nanocrystalline particles, coated alumina layer and infiltrated polymer (c) Proposed electronic energy-level diagram for the ITO / dense TiO_2 / porous TiO_2 /Al_2O_3 / TPD (4M)-*

MEH-M3EH-PPV / Au device, illustrating electron injection by tunnelling (1) from the LUMO level of the photo excited polymer through an ultra thin alumina layer. The transferred electrons are collected (2) by the ITO electrode (2), while photogenerated hole polarons are collected (3) by Au. The decrease in dark current and enhancement of V_{OC} in the presence of an alumina layer suggests that the wide band gap (8.5-9.9 eV[116]) alumina layer suppresses the back electron transfer from TiO_2 to the polymer (interfacial recombination) (4).

Figure 5.5 (a) shows the current-voltage characteristic for an ITO / dense TiO_2 (50 nm) / porous TiO_2 (140 nm) /Al_2O_3 (~1 nm) / TPD (4M)-MEH-M3EH-PPV/Au (60 nm) / Au device, and a similar device without the alumina layer, under A.M. 1.5 conditions (1 sun). Figure 5.5 (b) shows a schematic representation of the nanocrystalline particles, alumina coating and infiltrated polymer.

The insulating alumina layer increases the open circuit voltage from 0.84 V to 0.92 V and fill factor from 0.48 to 0.59, while slightly diminishing the short circuit current density from 0.52 $mAcm^{-2}$ to 0.49 $mAcm^{-2}$. The overall power conversion efficiency is thus increased from 0.21 % to 0.27 %. Despite the better polymer uptake by alumina coated electrode, the corresponding device shows slightly lower short circuit current density compared to devices with uncoated electrode. Nevertheless, the alumina coating improves the overall power conversion efficiency over 25 %.

The inset of the Figure 5.5 (a) shows that the alumina layer reduces the dark current and this is consistent with increased open circuit voltage upon alumina layer insertion. These observations suggest that the wide band gap (8.5-9.9 eV[52]) alumina layer suppresses back electron transfer from the conduction band of the TiO_2 to the HOMO level of the polymer (interfacial recombination) as illustrated by a proposed electronic energy-level diagram for the device in Figure 5.4 (c). The increase in V_{OC} is therefore attributed to suppression of interfacial recombination by the wide band gap alumina layer. The alumina layer may impede the electron injection from LUMO level of the photoexcited polymer to the conduction band of the TiO_2. However, it has been reported that photoinduced electron transfer from a MEH-PPV polymer to nanoporous TiO_2 occurs on a time scale of ~100 fs[77]. Since this is much faster than the time for radiative decay of the exciton, (~100s of ps) it is possible to slow down injection without significantly affecting the injection yield. Moreover, since we observe similar J_{SC} values for alumina coated and uncoated devices, the alumina layer appears to have negligible effect on the electron transfer yield from polymer to TiO_2.

Another possible mechanism by which the alumina coating may influence TiO_2 / polymer devices characteristics is modulation of the conduction band edge of the TiO_2

through deprotonation of the TiO_2[116] by more basic Al_2O_3. The resulting shift in the conduction band edge (and similar shift in the Fermi level) of TiO_2 may cause the V_{OC} to increase.

Table 5.1 *The influence of alumina coating on photovoltaic parameters of our hybrid TiO_2 / polymer devices and reported DSSC devices under AM 1.5 conditions (100 $mWcm^{-2}$, 1 sun).*

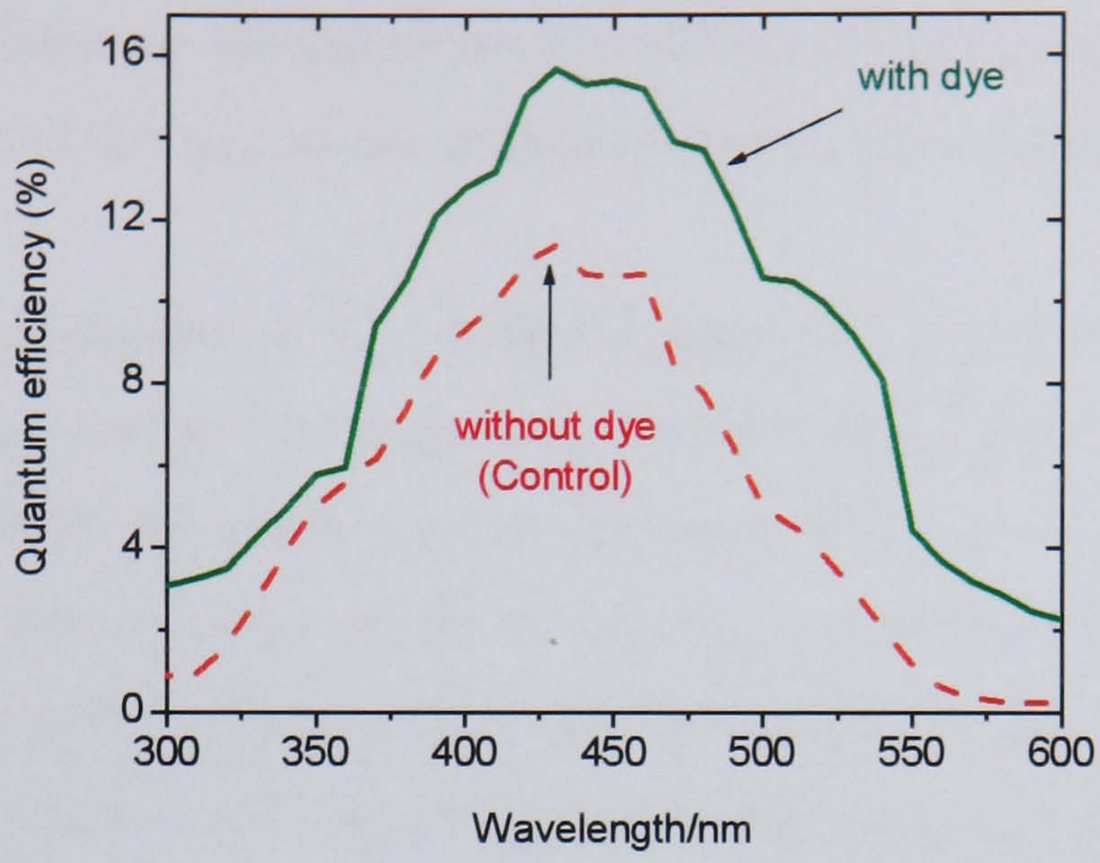
Device	Metal oxides	J_{SC} ($mAcm^{-2}$)	V_{OC} (V)	FF	η (%)	K (%)	Reference
Hybrid	TiO_2 (~140 nm)	**0.52**	**0.84**	**0.48**	0.21	**28**	This work
	$TiO_2 + Al_2O_3$	**0.49**	**0.92**	**0.59**	0.27		
Gratzel's DSSC*	TiO_2 (~ **8** μm)	**12.9**	0.70	0.66	5.9	**-12**	[140]
	$TiO_2 + Al_2O_3$	**10.0**	0.77	0.70	5.2		
Durrant's DSSC	TiO_2 (~ **8 μm**)	9.1	0.73	0.55	3.7	**50**	[52]
	$TiO_2 + Al_2O_3$	12.1	0.76	0.61	5.6		
Durrant's DSSC	TiO_2 (~ **4 μm**)	**5.0**	**0.71**	**0.54**	2.0	**25**	[52]
	$TiO_2 + Al_2O_3$	**5.0**	**0.76**	**0.58**	2.5		

**contained non sintered TiO_2 film (prepared by hydrolysis of titanium isopropoxide, peptization with HNO_3, and autoclavation at 230 ^0C. K is the percentage of efficiency improvement upon alumina coating.*

Similar effects of alumina coatings have also been observed in several dye sensitised liquid electrolyte solar cells (DSSC)[51,52,116,140,141]. Table 5.1 compares the influence of the alumina layer on our hybrid polymer / TiO_2 device with alumina treatment of several DSSCs of different porous layer thicknesses (8 μm and 4 μm) and made with different sintering conditions on cell performance. In all cases, the alumina layer increases FF and V_{OC}. The effect of the alumina coating on the V_{OC}, J_{SC} and fill factor, FF of the DSSC prepared by Gratzel's group is quite similar to the effect we observed for our hybrid device. However, the overall power conversion efficiency of their cell was decreased upon alumina layer insertion due to a larger decrease in J_{SC}, attributed to poor electrical contact between the (unsintered) particles caused by their insulating shell. A DSSC with 8 μm thickness porous layer prepared by Durrant's group shows a large increase in J_{SC}, while a cell with 4 μm thickness porous layer show no

increment in J_{SC}. Our device performance is most similar to Durrant's cell made with 4 μm porous TiO_2.

(a)



(b)

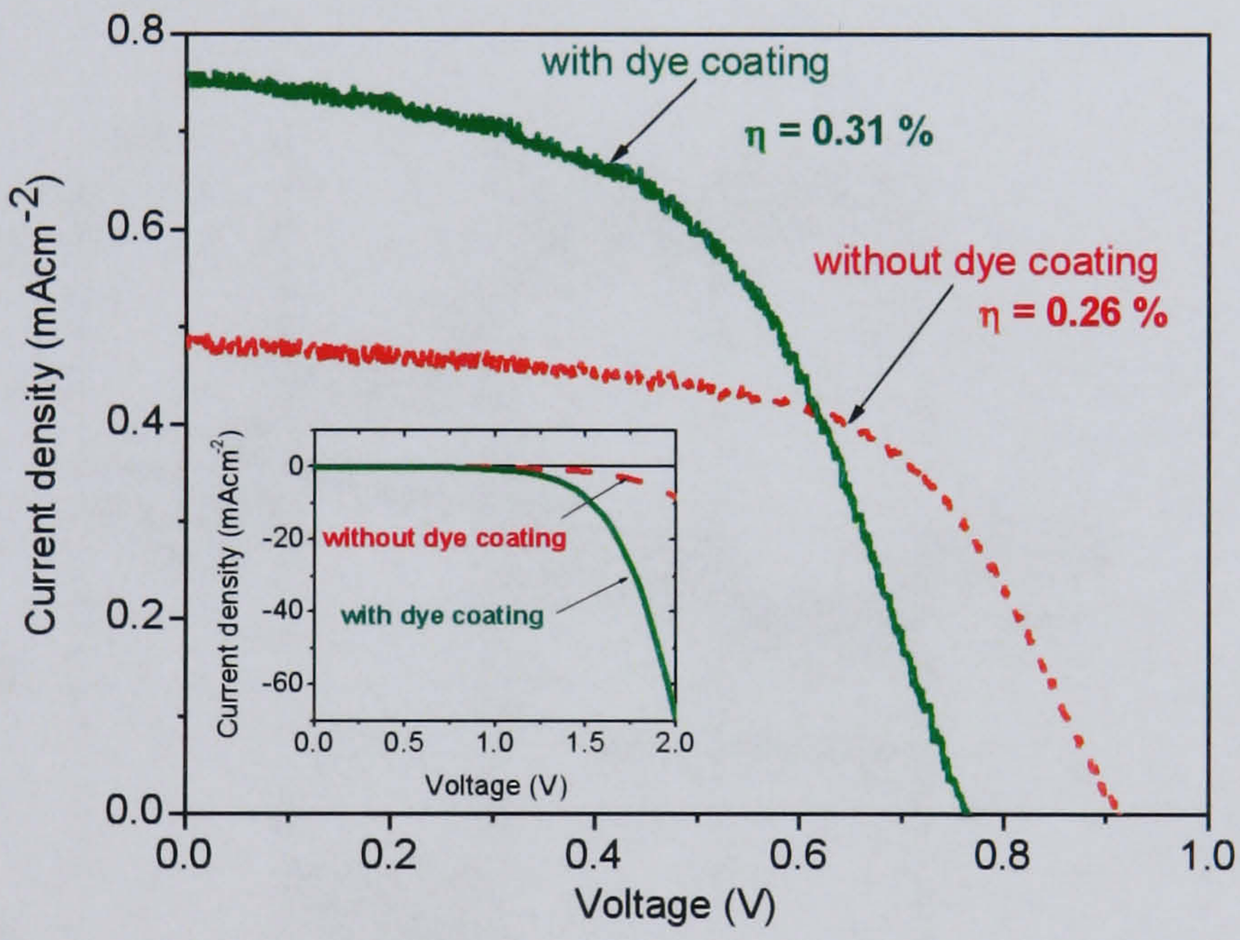


Figure 5.6 *(a) External quantum efficiency spectra and (b) J-V characteristics under A.M. 1.5 conditions (1 sun) and in the dark (inset) for an ITO / dense TiO_2 (50 nm) / porous metal oxide (140 nm) / Al_2O_3 / **dye** / TPD (4M)-MEH-M3EH-PPV (70 nm) /Au device (solid line) in comparison with a similar devices but without dye (dashed line).*

In order to study the effect of dye treatment on the performance of TiO_2 / polymer devices, we dip-coated a layer of dye (N719) onto an alumina coated TiO_2 electrode prior to spin coating the polymer. Figure 5.6 (a) and (b) show the external quantum efficiency (EQE) spectra and current-voltage characteristic under A.M. 1.5 conditions (1 sun) for the alumina coated devices with and without a dye layer. The EQE spectra clearly show that the light harvesting efficiency of the device is increased and extended to longer wavelengths by incorporation of the dye layer. The device performance under AM 1.5 conditions shows that J_{SC} is increased more than 50 % compared to the control

device. The dye layer, however, decreases the V_{OC} significantly, by about 0.15 V compared to the control. The inset to Figure 5.6 shows that the dark current of the dye coated device is increased by an order of magnitude compared to the control. This suggests a possible increase of back electron transfer from the conduction band of TiO_2 to the HOMO level of the dye or the polymer, even in the presence of the insulating alumina layer.

An additional influence on V_{OC} is the position of the HOMO level of the dye, which lies at a higher energy than that of the polymer (see Figure 5.7). In this system both dye and polymer are photo-excited. Because the V_{OC} is determined by the difference in quasi Fermi energy levels of the electron and hole in the photoexcited materials, and the hole Fermi energy level is limited by the HOMO level, the V_{OC} will tend to be reduced when a material of higher HOMO level (in this case the dye) is excited as well as the polymer.

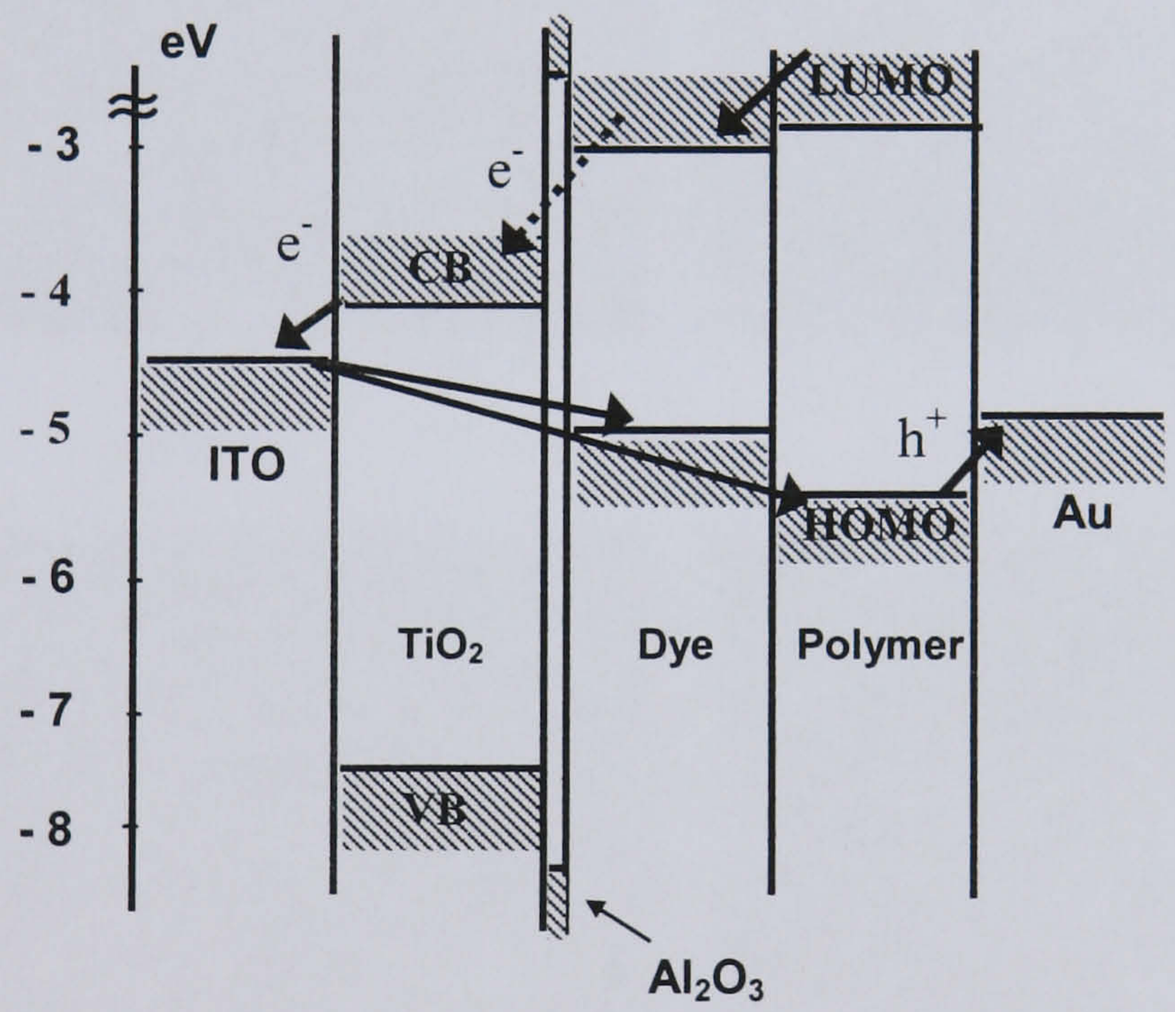


Figure 5.7 *proposed electronic energy-level diagram for ITO / TiO_2 /Al_2O_3 / Dye / TPD (4M)-MEH-M3EH-PPV / Au device.*

In the next section, we will discuss the effect of the TiO_2 microstructure on the performance of hybrid polymer / TiO_2 devices.

5.3 Effect of TiO_2 microstructure

Four different types of porous TiO_2 colloidal films called ECN, ECN* (scattered film), IC and P25, were chosen to study the effect of microstructure on recombination kinetics in TiO_2 / polymer structures and the performance of TiO_2 / polymer devices. The first two films, ECN and ECN*, was prepared by using the TiO_2 pastes received from Energy Centre for the Netherlands (ECN), while other IC and P25 pastes were prepared here at Imperial College (IC) with help of Mr. Alex Green an Dr. Ana Peiro respectively.

5.3.1 SEM Images of the TiO_2 films

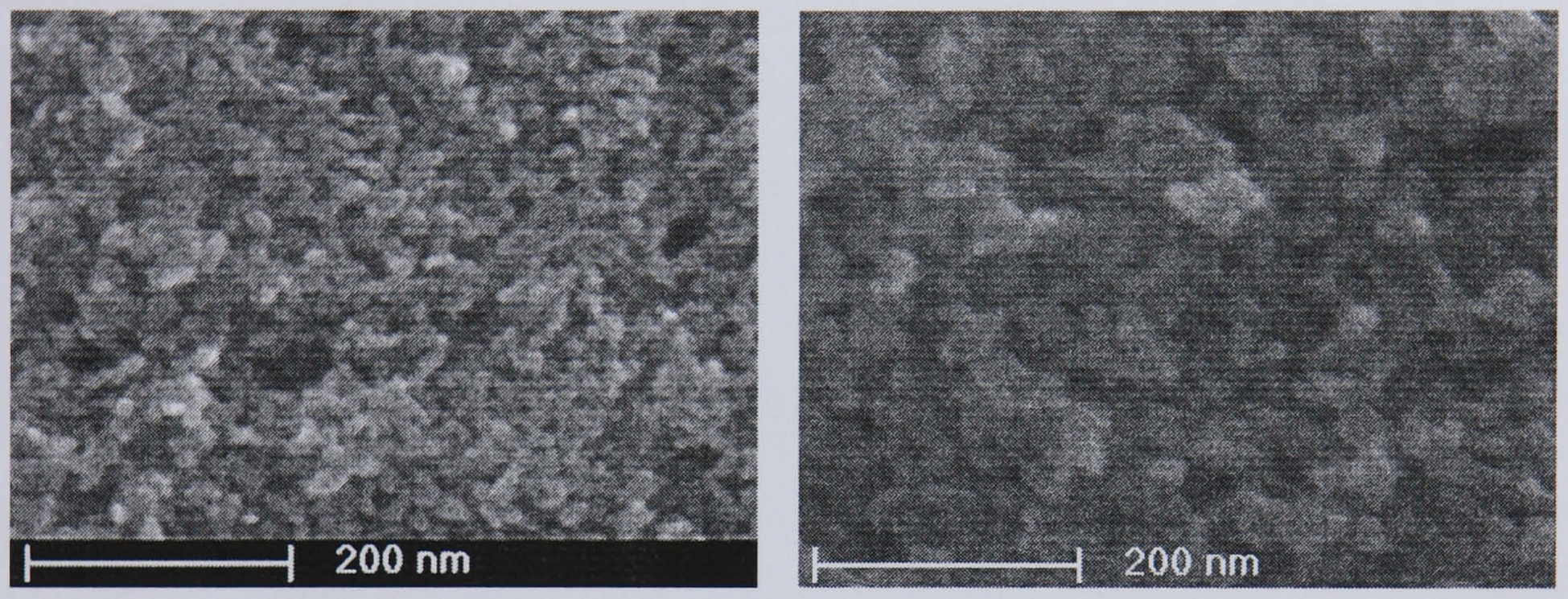


Figure 5.8 SEM *micrographs of TiO_2 colloidal films (~ 140-200 nm thicknesses) with different particle sizes (a) IC, (b) ECN, (c) ECN* and (d) P25.*

Figure 5.8 shows typical SEM micrographs of the TiO_2 colloidal films. IC film has uniform distribution of small particles of about 10-15 nm in diameter, while ECN film has slightly bigger particles of 20-30 nm diameter. Both ECN* and P25 films show

non-uniform distributions of particle sizes and contain some quite large particles (> 50 nm). P25 film appears to have the highest porosity of these films. The colour of the IC films was transparent, whereas the other films were milky. The milky colour of the films is due to the presence of large particles, causing strong scattering of visible light, while the smaller particle size in the IC films cause negligible scattering. According to measurements by Sarmimala Hore[142], the BET surface area of the particles in IC films is higher than the ECN film (see table 5.2).

Table 5.2 *Dimension of nanoparticles in films prepared from ECN and IC pastes*

Porous TiO_2	Particle diameters (nm)	BET surface area (m^2/g) [142]	d*BET** (nm)[142]
IC	10-15	145	11
ECN	20-30	66	24

** Assuming that the particles are spherical, the average diameter, d_{BET}^* is back-calculated from the BET surface area. (The surface area was calculated using BET isotherms obtained from nitrogen absorption and desorption on the TiO_2 films[142])*

5.3.2 Polymer uptake

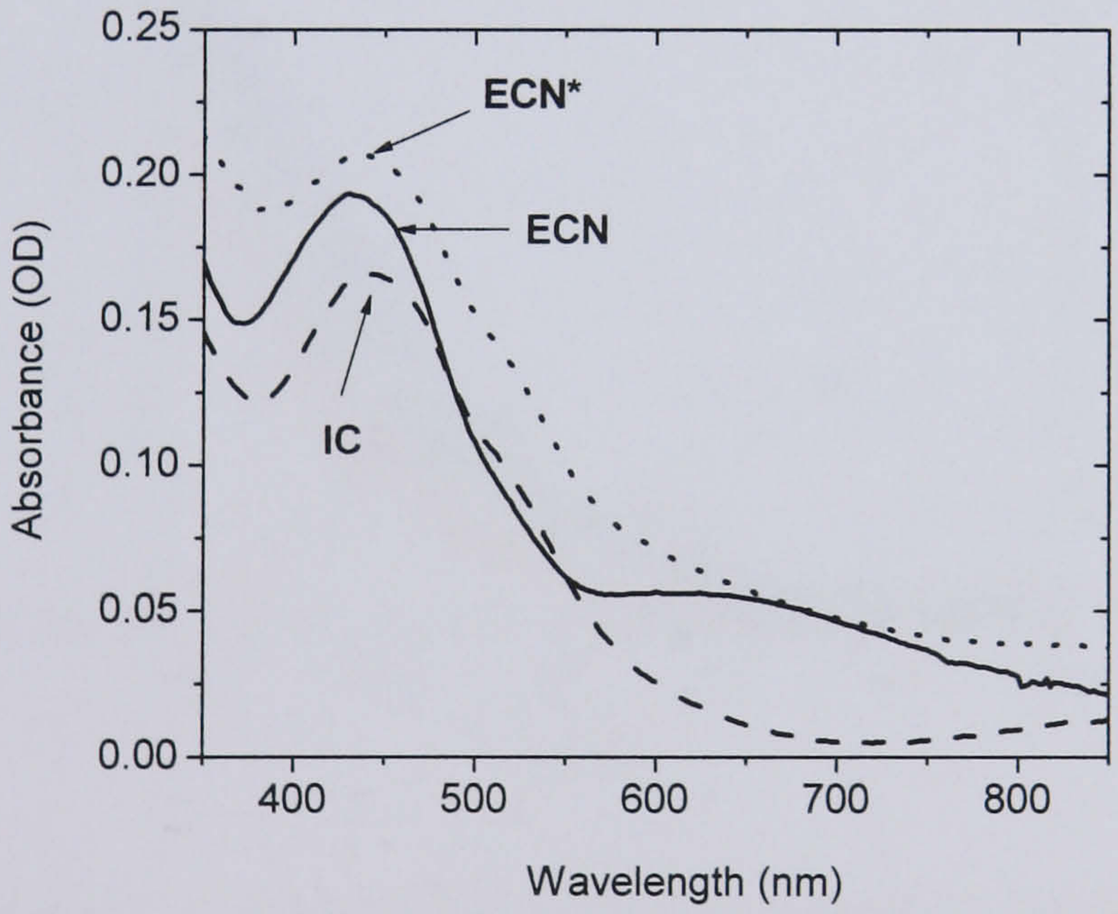


Figure 5.9 *UV-VIS optical absorption spectra of porous TiO_2 films [ECN (solid line), ECN* (dotted line) and IC (dashed line) of thickness about 120 nm, after dipping in TPD (4M)-MEH-M3EH-PPV / C_6H_5Cl (1 mg/ml) solutions for 18 hrs at 60 ^{0}C. The apparent absorption beyond 600 nm may be due to scattering by the larger TiO_2 colloidal particles.*

Figure 5.9 compares the optical density of porous TiO_2 electrodes of thickness about 120 nm following dip-coating in TPD (4M)-MEH-M3EH-PPV / C_6H_5Cl (1 mg/ml) polymer solutions for 18 hrs at 60 ^{0}C. The absorbance spectra of all the polymer

dip-coated TiO_2 films resemble the sum of the absorption spectra of polymer and TiO_2, except there is an apparent absorption beyond 600 nm for all dip coated films except IC film. This is probably due to scattering by the larger particles or interference effects. The absorption spectrum dip-coated P25 film has also showed higher apparent absorption (not shown in Figure 5.9) and this is also attributed to scattering by the larger particles of P25 film. Polymer uptake of ECN and ECN* films is higher than IC film. Originally we believed the higher polymer uptake was due to larger pore size in the ECN films, which may be expected on account of the larger particle size. However, very recent porosity measurements of IC and ECN film[142] indicate a lower porosity for ECN than IC paste (IC ~ 62 % and ECN ~ 45 %). Therefore the reasons for the higher uptake are not well known, and further studies are needed to address this point. However, the ECN paste is prepared according to basic procedures[106]. The ECN films are therefore expected to have basic properties which may favour polymer attachment.

5.3.3 Charge recombination kinetics

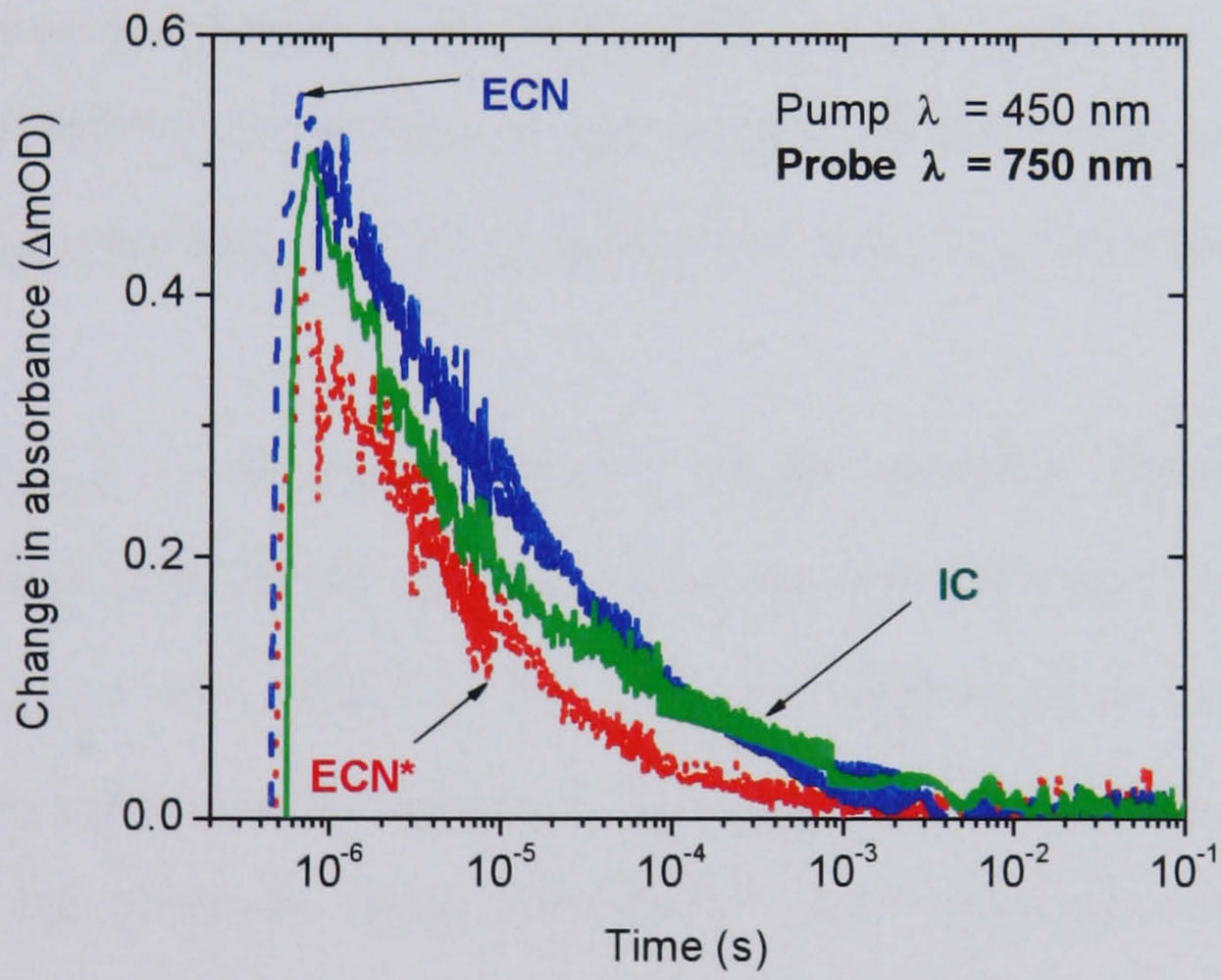


Figure 5.10 *Transient absorption kinetics following photoexcitation of ITO / HBL / porous TiO_2 / TPD(4M)-MEH-M3EH-PPV polymer using different TiO_2 films (IC-solid line, ECN-dashed line, ECN*- dotted line). The excitation density was about 30 μJ / pulse / cm^2 (corresponding to 1.3×10^{14} incident photons / pulse / cm^2). The samples were illuminated through the TiO_2 side. The transient absorption is assigned to hole-polarons in the polymer and the decay to interfacial recombination between electrons in the TiO_2 and hole-polarons in the polymer.*

Figure 5.10 shows the transient absorption kinetics for porous TiO_2 / TPD (4M)-MEH-M3EH-PPV at a probe wavelength of 750 nm under excitation by pulses of intensity ~ 30 μJ / pulse / cm^2 respectively. The transient absorption signals of the

structures with IC, ECN and ECN* paste films are shown by solid, dash and dotted lines in this figure. We have performed detailed transient absorption studies on pristine TPD (4M)-MEH-M3EH-PPV polymer film as control experiments (λ_{pump} = 450 nm and λ_{probe} = 750 nm) as described in the chapter 3 and 4. These studies reveal no evidence of any absorption feature, which could be assigned to the triplet, for instance, on the time scale of charge recombination dynamics (0.1 μs - 100 ms). Therefore, the decay in absorbance as a function of time after the excitation is attributed to recombination of hole polarons in the polymer with electrons to the TiO_2.

Figure 5.10 shows that the shape and magnitude of the transient absorption signals are almost identical for the structures made with IC and ECN films. The recombination time of the both structure made with ECN and IC films are similar, while structure made with the ECN* film showed faster kinetics and a smaller transient absorption signal than the other two. The structure made with P25 film showed very fast kinetics and a very weak transient absorption signal and is not shown in Figure 5.10. The charge separation yield should depend on the change in absorbance (ΔOD) of the TiO_2 / polymer structure relative to the optical density (OD) at the pump wavelength. The charge separation yield can be defined as the ratio of the number of hole polarons created to the number of photons absorbed. The yield should therefore be proportional to $\frac{\Delta OD}{\left(1-10^{-OD(\lambda_{pump})}\right)}$,

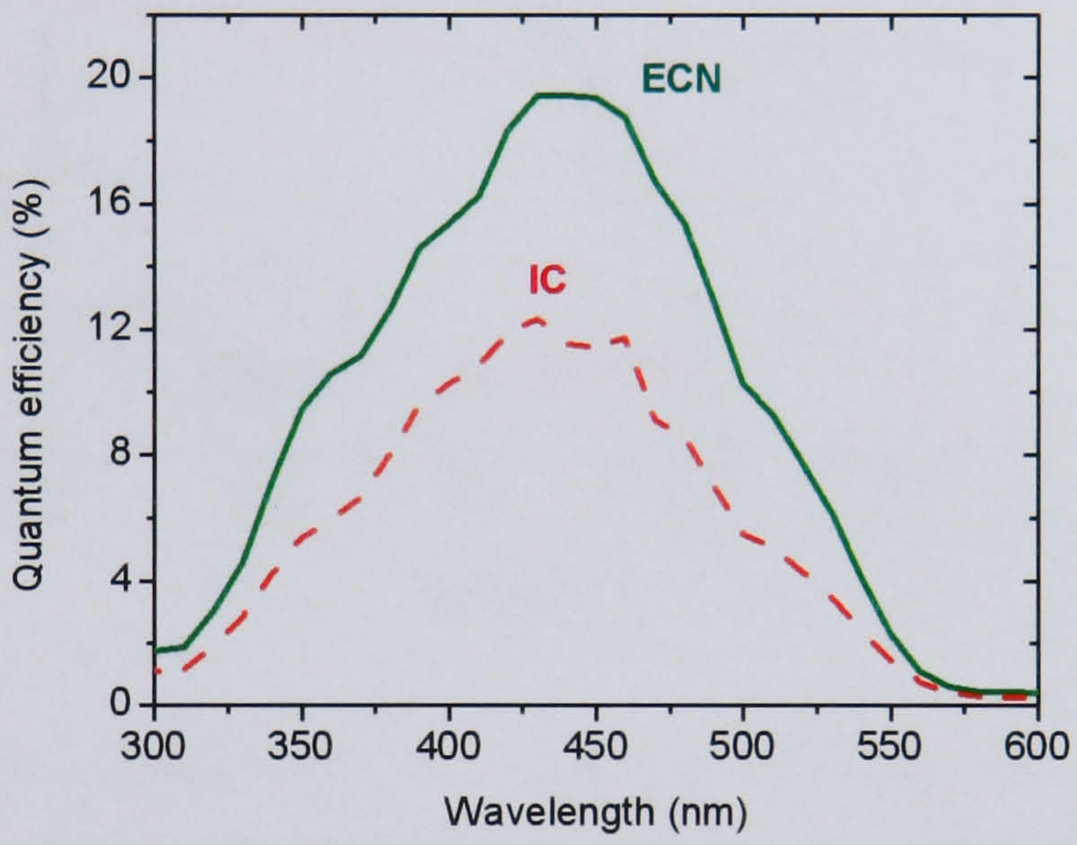
$OD(\lambda_{pump})$ is the optical density of the structure. Relative values of the charge separation yield for the different structures were estimated from the measured values of $OD(\lambda_{pump})$ and ΔOD of the structure. The relative charge separation yield and recombination time of the structures made with IC paste and ECN paste were similar, while the structure made with ECN* paste showed about 50 % smaller charge separation yield and faster recombination time than IC and ECN paste structures. A slightly higher charge separation yield is observed for the IC paste than ECN paste structure. This is probably due to the higher surface area of the due to smaller particle sizes.

5.3.4 J-V characteristics

Figure 5.11 (a) and (b) shows EQE spectra and J-V characteristics for two devices, one made with IC film and the other with ECN film, under AM1.5 equivalent illumination (100mWcm^{-2}). Both devices (without PEDOT:PSS layer) are made with TPD (4M)-MEH-M3EH-PPV polymer as described in the section 2.2. The inset of

Figure 5.11 (b) shows the corresponding dark J-V characteristics of the devices. The ECN film device shows a higher EQE spectrum and J_{SC} compared to the IC film device. The peak EQE of the ECN film device is about 19 % at 440 nm. The higher EQE and J_{SC} (Figure 5.11 (b)) in the device made with ECN film is probably due to better polymer uptake by the ECN film (see Figure 5.9) attributed due to larger pore volume. The open circuit voltage (V_{OC}), however, is lower by about 0.1 V in the ECN film device than in the IC film device. The overall efficiencies of these two devices are about the same. The inset to Figure 5.11 (b) shows that the forward-bias dark current for the ECN film device is an order of magnitude higher (10 times at +2 V) than for the IC film device. Device made with ECN* showed poorer performance than any of these devices.

(a)



(b)

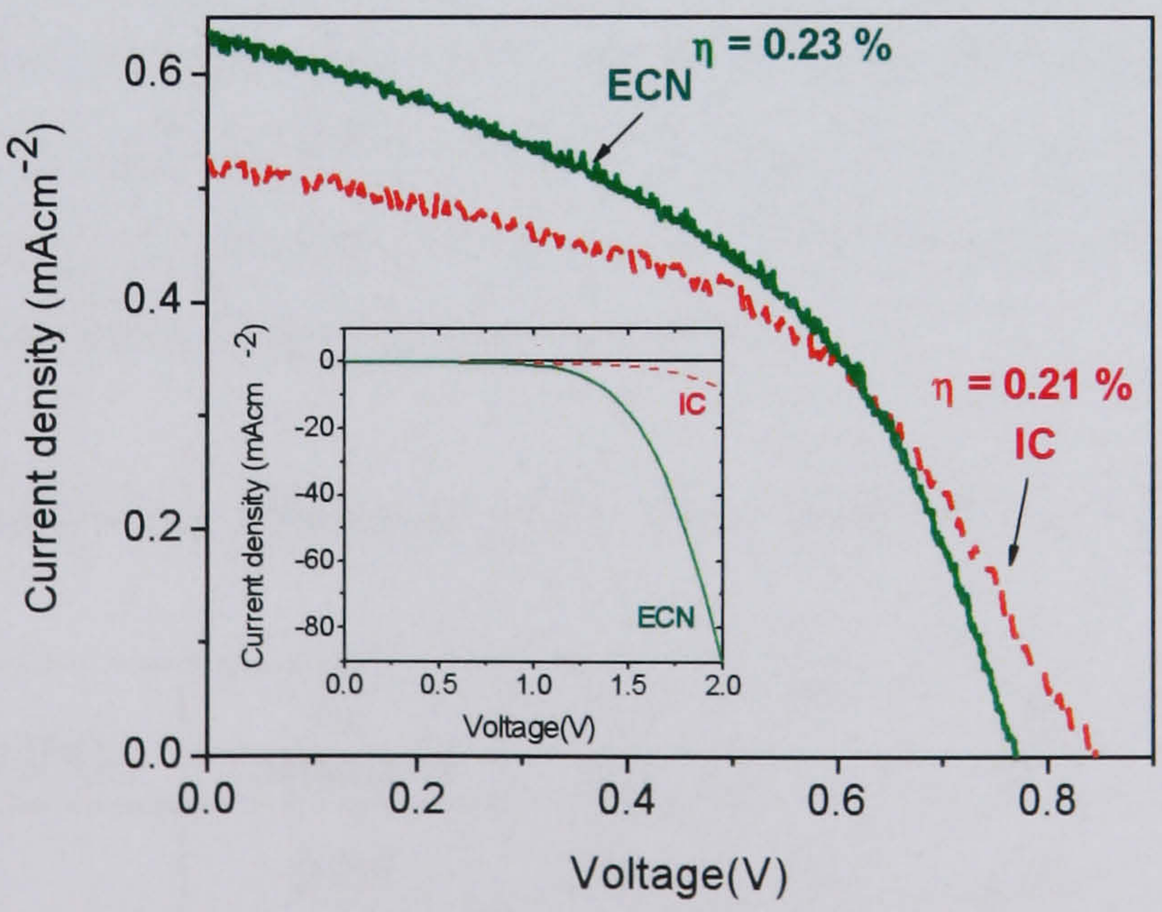


Figure 5.11 *(a) External quantum efficiency spectra and (b) Current density vs voltage (J - V) characteristics under A.M. 1.5 conditions (1 sun) and in the dark (inset) for ITO / dense TiO_2 (50 nm) / porous TiO_2 (140 nm) / TPD (4M)-MEH-M3EH-PPV(70 nm) / Au devices. The solid lines represent results from ECN film and the dashed lines represent IC paste.*

Next we will focus on devices with a PEDOT:PSS layer under the top contact. Figure 5.12 shows the J - V characteristic under A.M. 1.5 conditions (1 sun) for devices containing a PEDOT:PSS layer and different porous TiO_2 layers. The inset to Figure 5.12 shows the optical absorbance of the ECN and IC TiO_2 films of thickness about 120 nm, after dipping in TPD (4M)-MEH-M3EH-PPV / C_6H_5Cl (2 mg/ml) solutions for 18 hrs at 60 ^{0}C. The apparent absorption beyond 600 nm in the dip coated ECN films may be due to scattering or interference effects.

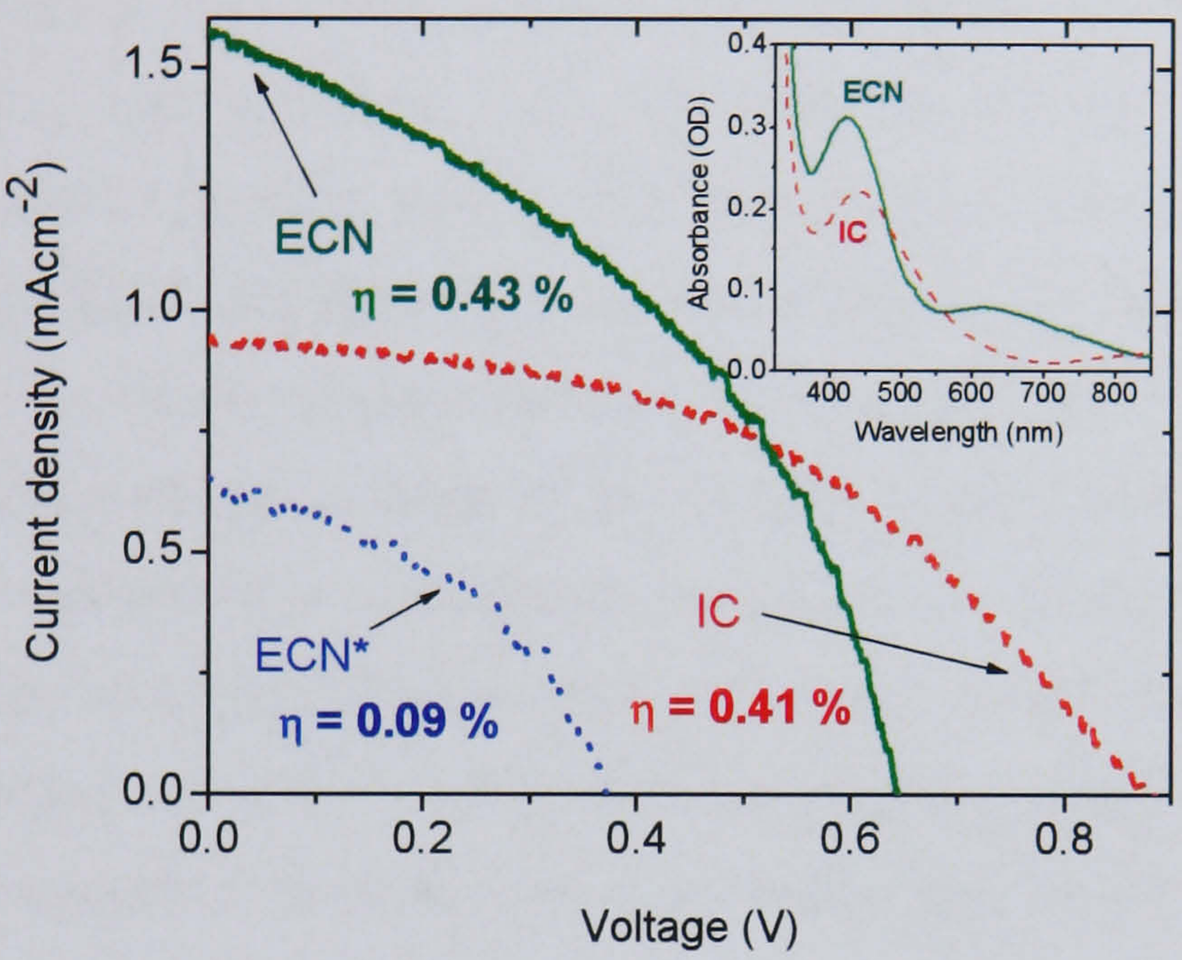


Figure 5.12 *J - V characteristic under A.M. 1.5 conditions (1 sun) for ITO / dense TiO_2 (50 nm) / porous TiO_2 (120 nm) / TPD (4M)-MEH-M3EH-PPV (60 nm) / **PEDOT:PSS** / Au devices with different porous TiO_2 layers (ECN- solid line, IC-dashed line and ECN*-dotted line). Inset shows UV-VIS optical absorption spectra of porous TiO_2 films of thickness about 120 nm, after dipping in TPD (4M)-MEH-M3EH-PPV / C_6H_5Cl (2 mg/ml) solutions for 18 hrs at 60 ^{0}C. The apparent absorption beyond 600 nm in the dip coated ECN films may be due to scattering by the larger TiO_2 colloidal particles or to interference effects.*

Table 5.3 *The photovoltaic parameters of the device presented in Figure 5.12 under AM1.5 conditions*

Porous TiO_2	J_{SC} (mAcm^{-2})	V_{OC} (V)	FF	η (%)
IC	0.95	0.86	0.49	**0.41**
ECN	1.58	0.64	0.43	**0.43**
ECN*	0.65	0.38	0.38	**0.09**

Table 5.3 summarises the photovoltaic parameters of the devices presented in Figure 5.12 under AM 1.5 conditions. The V_{OC} of these devices is consistent with the

trend in recombination kinetics observed through transient absorption measurements discussed above. The recombination time and V_{OC} appear to increase with decreasing particle sizes.

Figure 5.12 further shows that the device made with ECN film produced J_{SC} well over 1 $mAcm^{-2}$, while the device with IC film device shows a higher open circuit voltage of almost 0.9 V. Both devices show over 0.4 % power conversion efficiency under AM 1.5 conditions. The higher J_{SC} of 1.6 $mAcm^{-2}$ obtained for the ECN film device compared to the IC film device is attributed due to better polymer uptake by the ECN film (see, inset of Figure 5.12). However, the V_{OC} of the ECN film device is significantly lower by, about 0.25 V, than that of the IC film device. The dark current observed in the ECN film device is much higher than in the device IC film device. This suggests that the interfacial recombination may be dominant in device with ECN film. However the recombination times of the structures made with IC paste and ECN are similar. The reduced V_{OC} is therefore not related to recombination but it may be explained partly in terms of higher electron injection. It has been found[143] that electron injection is higher in Al_2O_3 / P3HT composite structures made with larger pore size of Al_2O_3 film compared to structure made with smaller pore size of Al_2O_3 film. Since ECN paste film has higher pore size compared to IC paste film, it is expected the electron injection may be higher in ECN film compared to IC paste film.

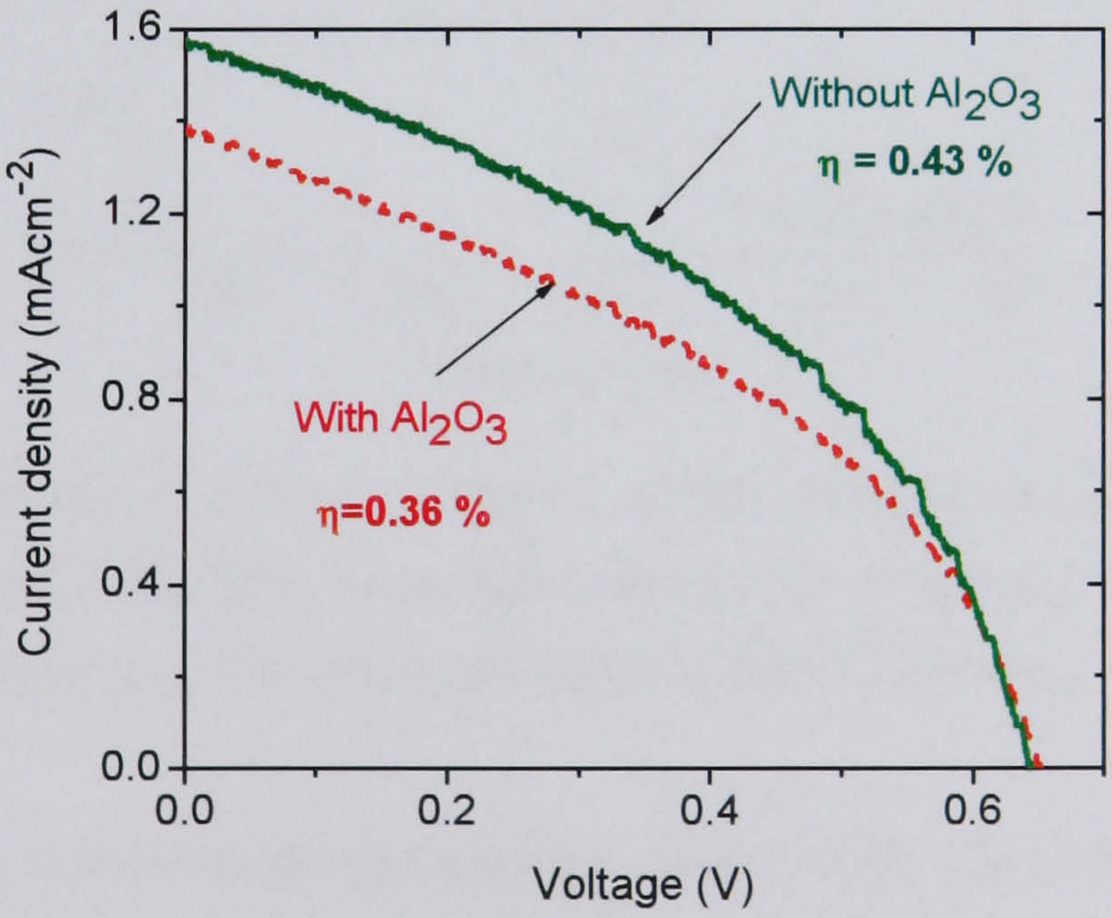


Figure 5.13 *J-V characteristic under A.M. 1.5 conditions (1 sun) for ITO / dense TiO_2 (50 nm) / porous TiO_2 (ECN - 120 nm) / Al_2O_3 / TPD (4M)-MEH-M3EH-PP (60 nm) / PEDOT:PSS / Au device (dashed line) in comparison with a similar device without the alumina layer (solid line).*

In order to improve V_{OC} in devices with ECN film, we introduced a thin insulating alumina layer prior to dip and spin coating the polymer. Figure 5.13 shows the effect of

the alumina layer on a device made with ECN film. However, there is no significant enhancement of V_{OC} with respect to the control device. Moreover, J_{SC} diminishes while there is only a small increase in fill factor, resulting an overall decrease in power conversion efficiency. The reason for the lower J_{SC} in devices with alumina coated ECN film is not clear, but it is appears to related interfacial chemistry between TiO_2 microstructure and the coated alumina.

In order to study the effect of TiO_2 microstructure on device performance of TiO_2 / polymer further, we selected P3HT polymer to combine with ECN and IC porous layers. P3HT has been identified as promising hole conductor material due to its good spectral response (peak absorption at 550 nm) and high hole-mobility ($\mu_{TOF} = 3\times10^{-4}$ $cm^2V^{-1}s^{-1}$ at 2.5×10^5 V/cm[86]). However, the maximum efficiency reported for TiO_2 / Poly(3-alkyl thiophene) is only 0.06 % under AM 1.5 conditions[17,72,73,89] and peak external quantum efficiency is 10 % at 550 nm[70,144]. Here, we improve the device performance by using multilayer device structure.

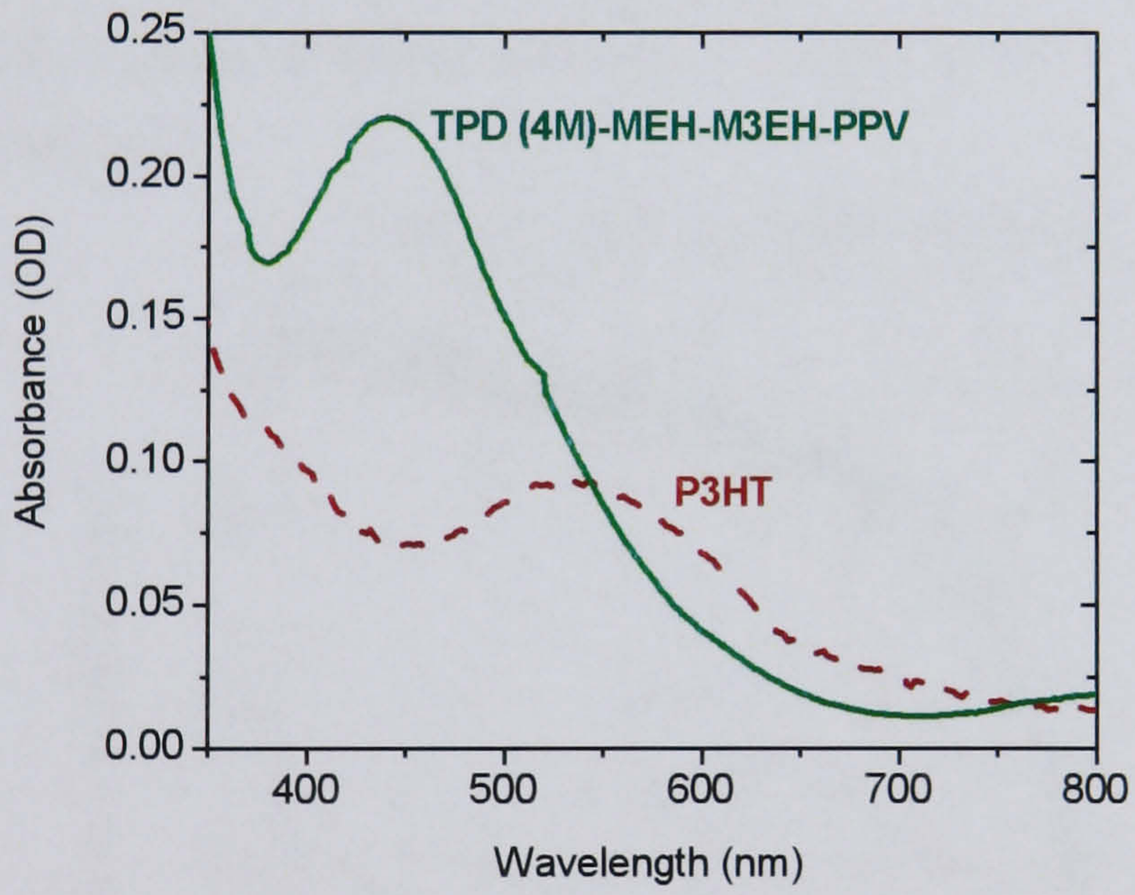


Figure 5.14 *UV-VIS optical absorption spectra of TiO_2 nanoporous films (IC, 120 nm thick) dipped into the polymer / C_6H_5Cl (~2 mg/ml) solutions for 18 hrs at 60^0C. The polymers used were P3HT (dashed line) and TPD (4M)-MEH-M3EH-PPV (solid lines)*

Figure 5.14 compares the optical absorbance of IC films of thickness about 120 nm, after dipping in two different polymer solutions [P3HT and TPD (4M)-MEH-M3EH-PPV each dissolved in C_6H_5Cl (2 mg/ml)] for 18 hrs at 60 ^{0}C. The P3HT polymer shows a poorer uptake by TiO_2 than the TPD (4M)-MEH-M3EH-PPV polymer. We improved the polymer uptake by increasing the temperature of the P3HT dipping solution. Figure 5.15 compares the optical absorbance of IC and ECN films of thickness about 120 nm, after dipping in P3HT polymer / C_6H_5Cl (1 mg/ml) solutions

for 18 hrs at about 120 ^{0}C and spin coating P3HT polymer. In contrast to TPD (4M)-MEH-M3EH-PPV polymer (see, Figure 5.9), P3HT polymer uptake by IC film is better than by ECN film.

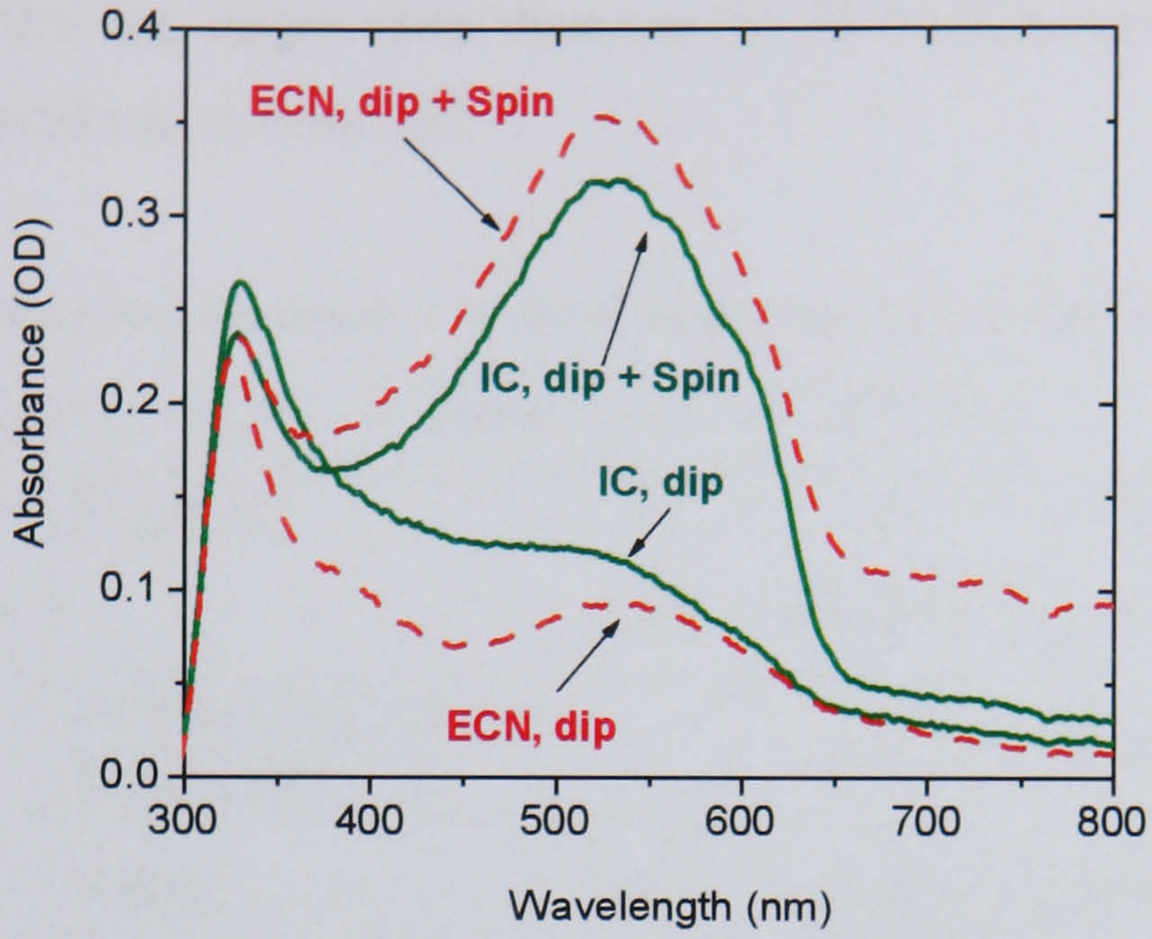


Figure 5.15 *UV-VIS optical absorption spectra of different types of TiO_2 films (~120 nm thick) dipped into P3HT / C_6H_5Cl (1 mg/ml) solutions for 18 hrs at about 120 ^{0}C. (ECN film-dashed line, IC film –solid line).*

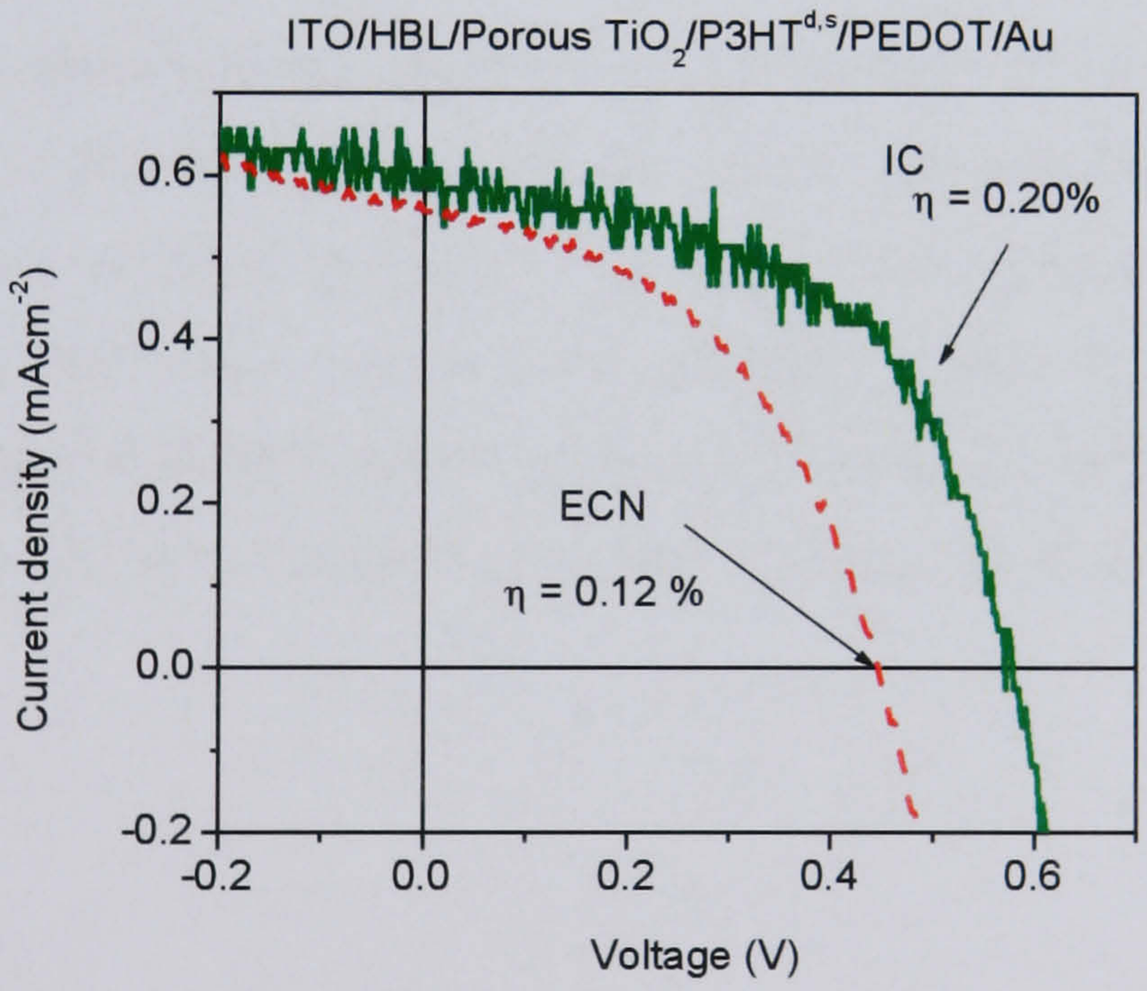


Figure 5.16 *J-V characteristic under A.M. 1.5 conditions (1 sun) for an ITO / dense TiO_2 (50 nm) / porous TiO_2 (120 nm) / P3HT (60 nm) / Au device made with different TiO_2 films. (IC film-solid line, ECN film-dashed line).*

Figure 5.16 compares the performance of two TiO_2 / P3HT polymer devices, made with IC and ECN films, respectively. The TiO_2 (IC) / P3HT device shows much better fill factor and V_{OC}, resulting in higher efficiency than TiO_2 (ECN) / P3HT device. The higher fill factor and J_{SC} observed in TiO_2 (IC) / P3HT device is probably due to the

better polymer uptake by the IC film during the dipping process (see Figure 5.15). The lower V_{OC} observed in the TiO_2 (ECN) / P3HT device compared to the TiO_2 (IC) / P3HT device is probably due to a combination of shorter exciton diffusion length of P3HT polymer and the larger pore diameter of ECN film (see, Table 5.4) where germinate recombination is dominant.

Table 5.4 *The photovoltaic parameters of the devices presented in Figure 5.12 & 5.16 together with the exciton diffusion length L_d and pore sizes of the TiO_2 films.*

Porous TiO_2	Size (nm)	Polymer	L_d (nm)	J_{SC} ($mAcm^{-2}$)	V_{OC} (V)	FF	η (%)
IC	< 10	TPD (4M)-MEH-M3EH-PPV	15	0.95	0.86	0.49	**0.41**
IC	**< 10**	**P3HT**	**05**	**0.62**	**0.58**	**0.56**	**0.20**
ECN	**> 20**	TPD (4M)-MEH-M3EH-PPV	**15**	**1.58**	**0.64**	**0.43**	**0.43**
ECN	> 20	P3HT	05	0.56	0.45	0.47	**0.12**

Table 5.3 summaries the photovoltaic parameters of the devices presented in Figure 5.12 and 5.16, in comparison with the exciton diffusion length of the polymers and the pore sizes of the TiO_2 films. The device performance correlates with the microstructure of the films and exciton diffusion length of the polymers. The observation suggests that optimisation of TiO_2 / polymer device performance requires both a fine scale of TiO_2 microstructure and a long exciton diffusion length in the polymer.

5.4 Role of hole- and electron-blocking layers

Here we study the role of the dense TiO_2 and the spin coated layer in the multilayer device. Figure 5.18 (a) shows the J-V characteristics for TiO_2 (IC) / P3HT devices with and without a dense TiO_2 layer under AM 1.5 conditions. The inset to Figure 5.18 shows that the device without a dense TiO_2 produced a higher dark current than the device with the dense layer. This higher dark current appears to be responsible for the lower V_{OC} when the HBL is absent. Similar behaviour is observed for devices made with ECN film, as shown in Figure 5.19 (a). A schematic representation of the ITO / HBL (dense TiO_2) / porous TiO_2: polymer^d / polymer^s / PEDOT:PSS / Au device is shown Figure 5.19 (b). Lower dark currents in devices with dense layers suggest that the dense layer suppresses the hole transfer from the HOMO of the polymer to the ITO electrode as illustrated in Figure 5.19 (c). Such hole transfer is possible with many hole-transporting polymers, and ITO is often used as the hole-injecting or hole-collecting electrode in LEDs or solar cells. The dense layer serves to block this hole-transfer.

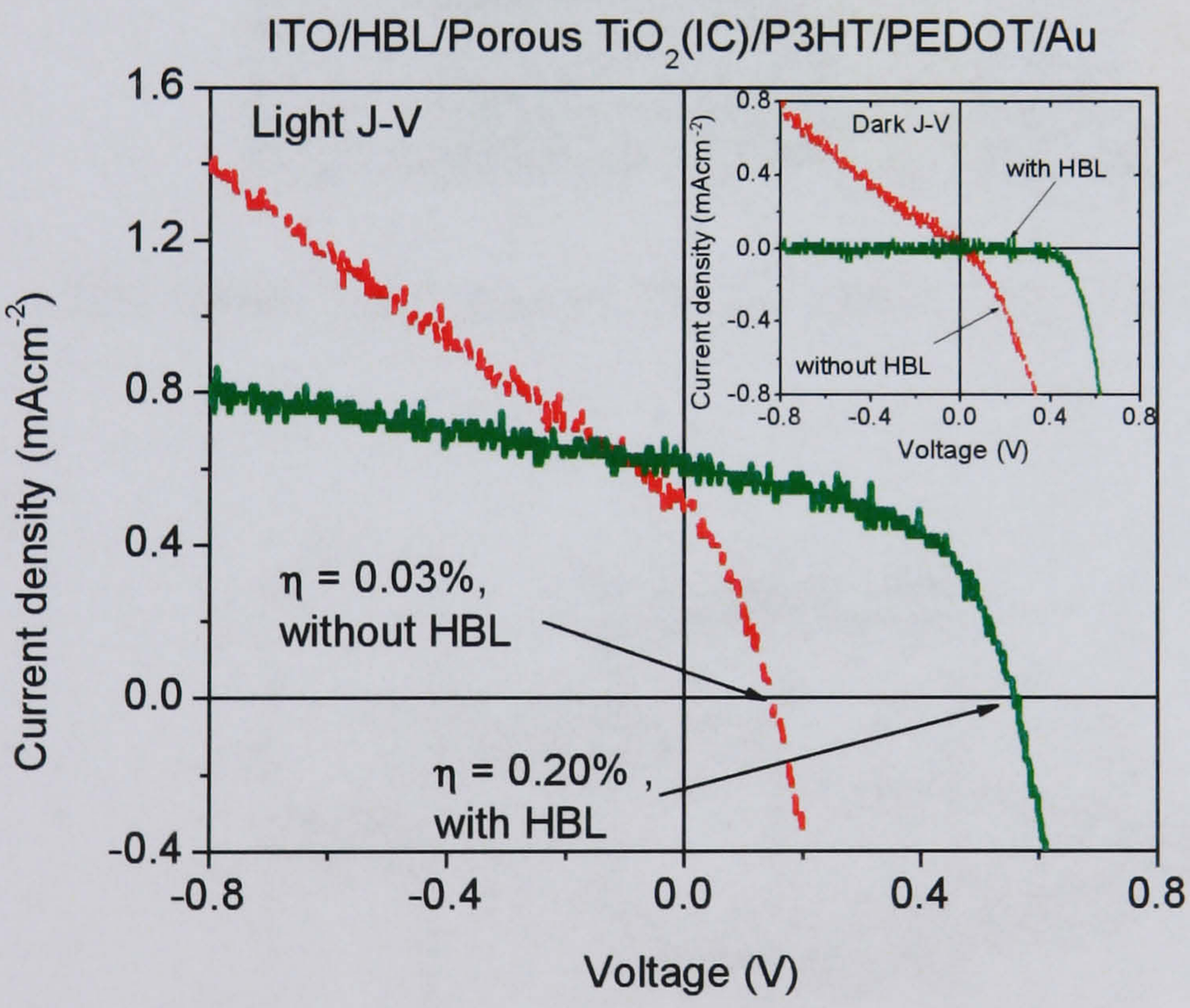
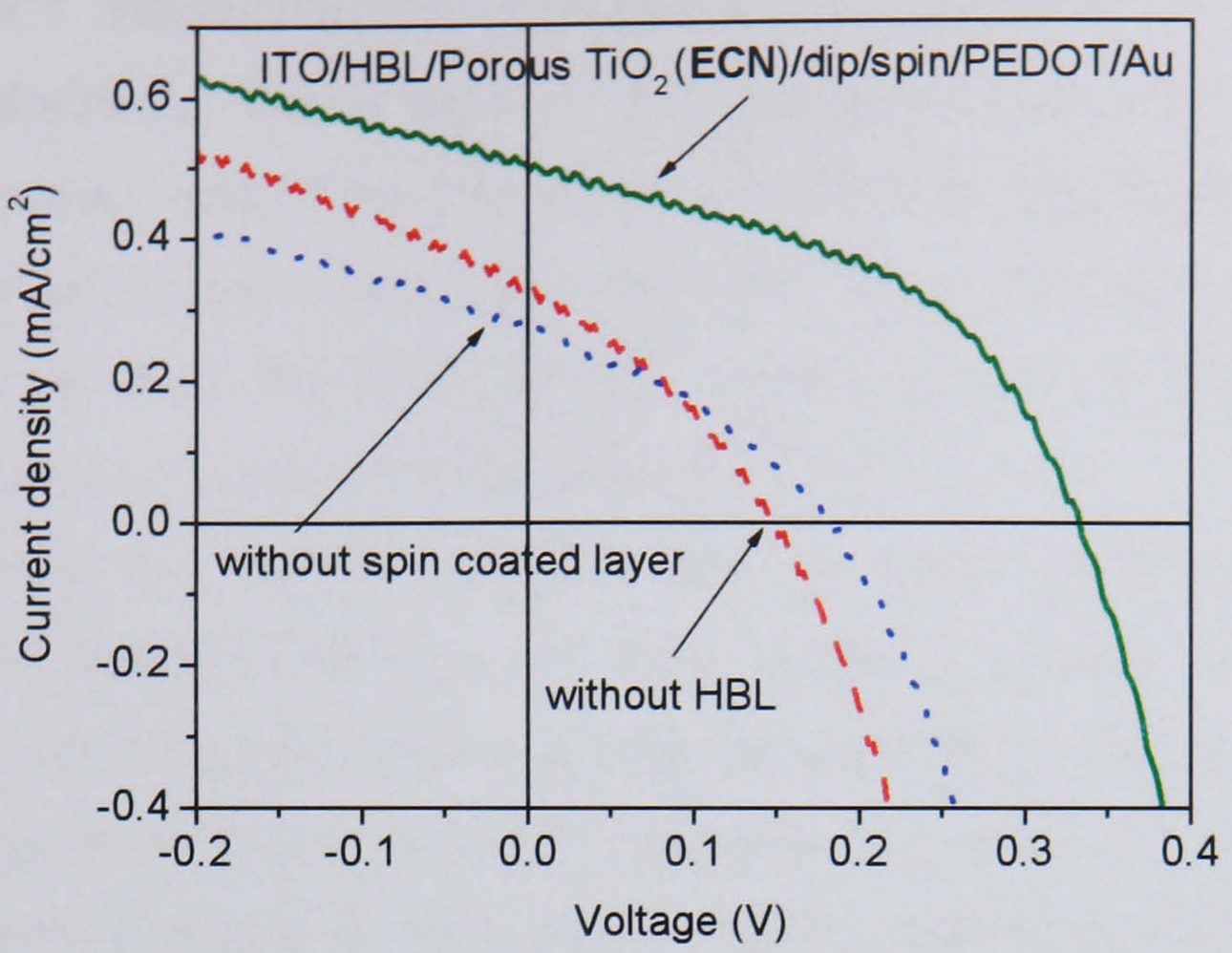


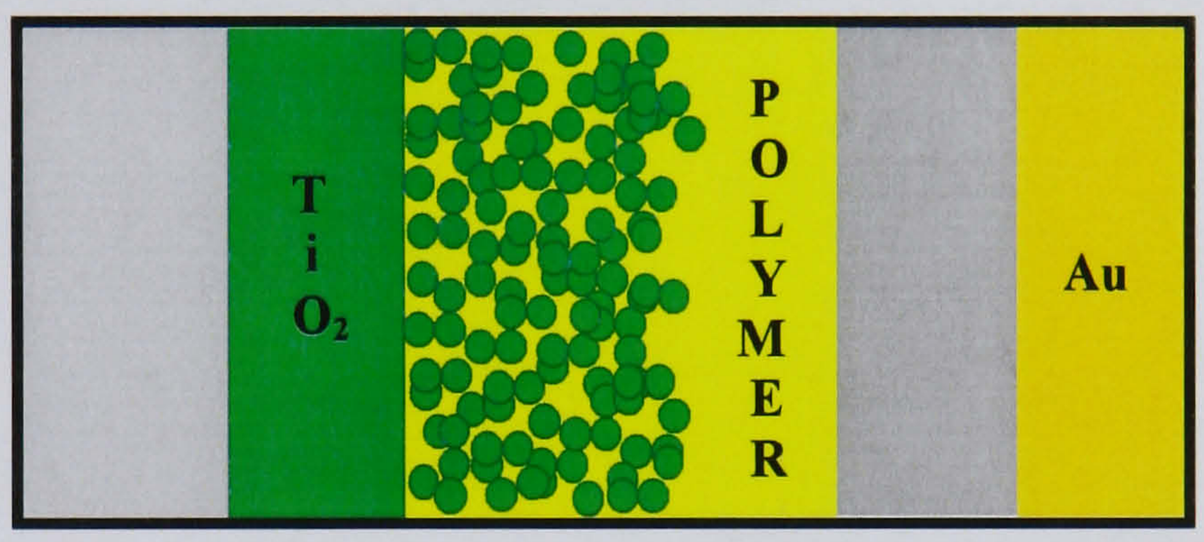
Figure 5.18 *J-V characteristics for an ITO / dense TiO_2 (HBL) / porous TiO_2 (IC) /P3HT^d /P3HT^s / PEDOT:PSS / Au device in comparison with an identical device with no dense TiO_2 layer under AM 1.5 conditions and in dark (inset).*

Figure 5.19 (a) further shows that the device without spin-coated layer also shows lower V_{OC} and lower J_{SC}. The lower J_{SC} is explained by polymer content and lower optical absorption. A lower V_{OC} in dip-coated only devices was also observed in TiO_2 / F8T2 polymer devices, as described in chapter 3, and in TiO_2 / MEH-DOO-PPV

(a)



(b)



ITO / dense TiO_2 / porous TiO_2:polymer^d / polymer^s / PEDOT / Au

(c)

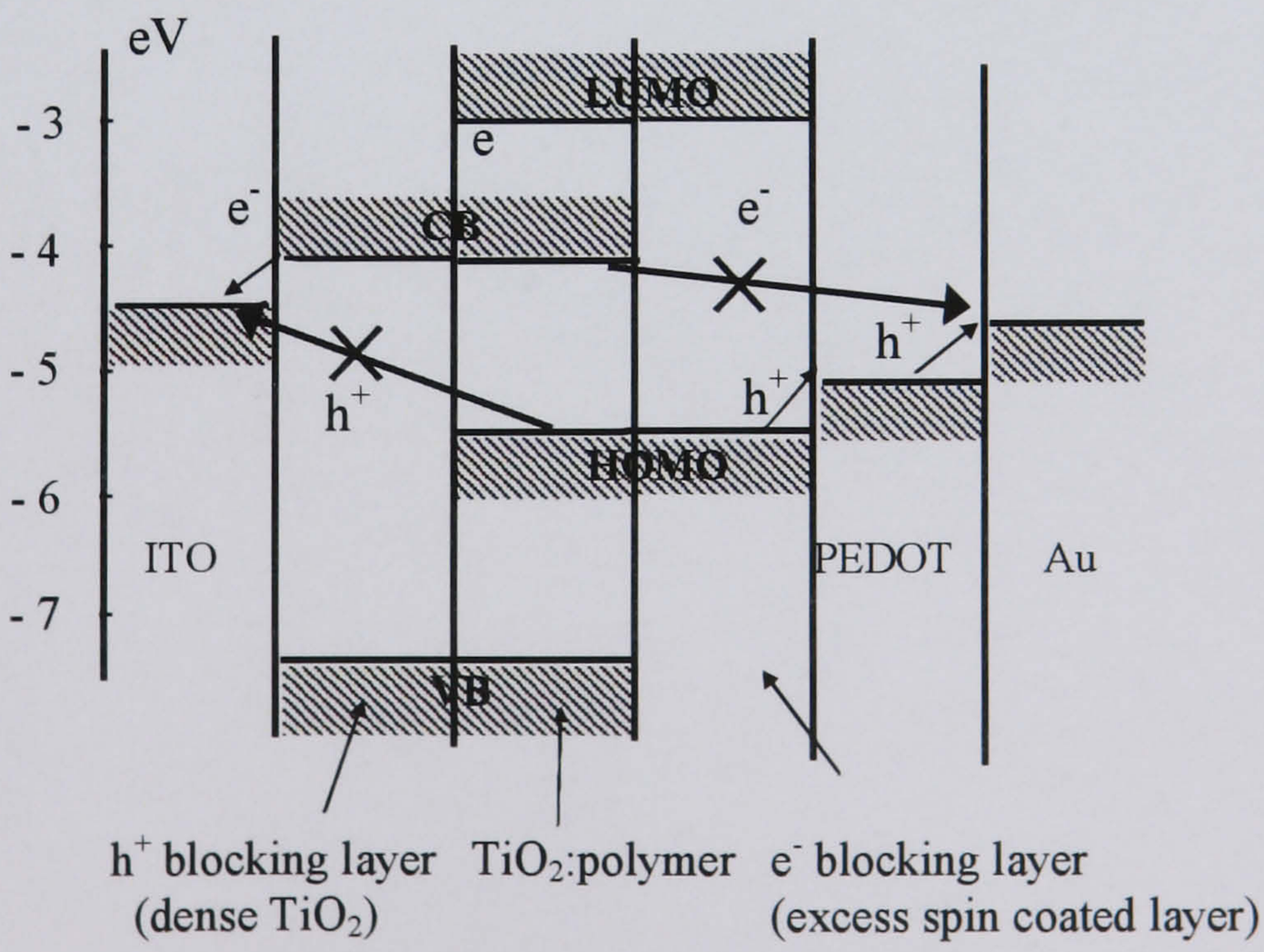


Figure 5.19 *(a) J-V characteristics, (b) Schematic diagram and (c) proposed electronic energy-level diagram for ITO / HBL (dense TiO_2) / porous TiO_2: polymer^d / polymer^s / PEDOT:PSS / Au devices.*

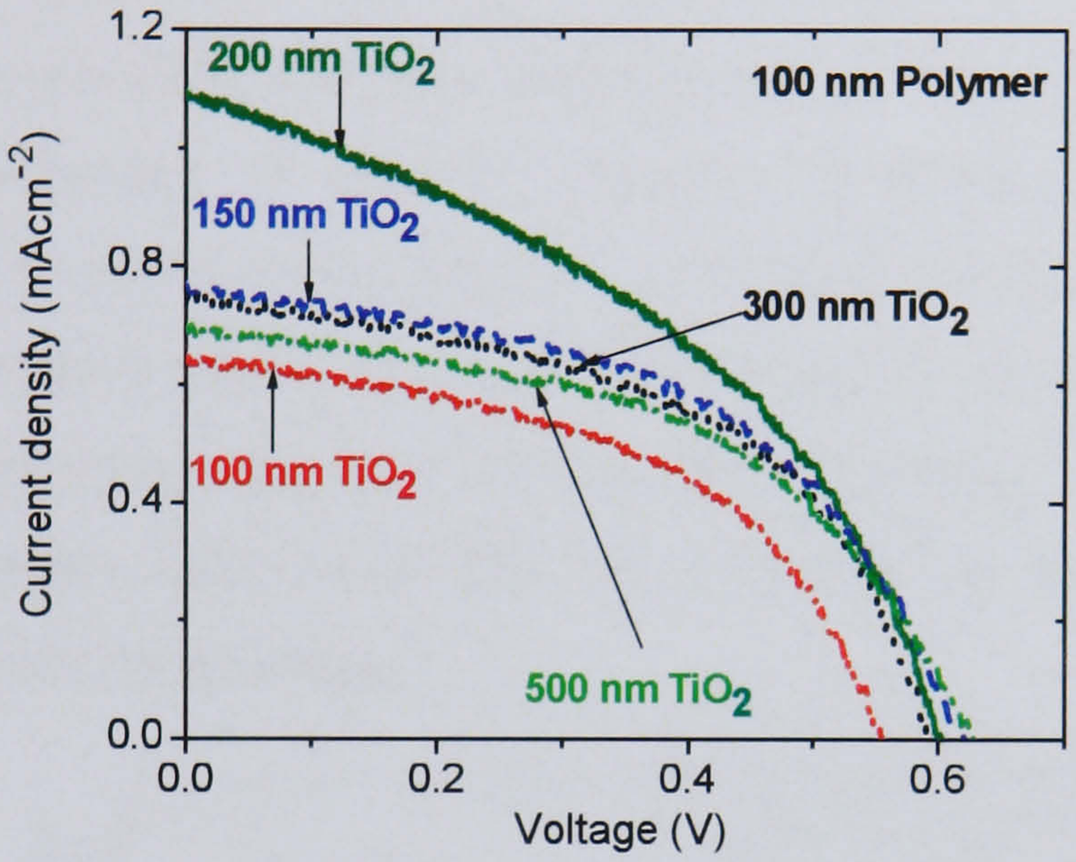
polymer device[145]. These observations suggest that the spin-coated layer is vital to for higher V_{OC} and also $J_{SC.}$ Excess polymer layer appears to block back electron transfer from the conduction band of the TiO_2 to the Au electrode causing short circuits. The excess polymer layer acts as an electron blocking layer. We found the PEDOT:PSS layer has also blocked the back electron transfer in TiO_2 / F8T2 device. The PEDOT:PSS layer also acts as an electron blocking layer.

In summary, we observe strong effects on device performance both from introduction of a PEDOT:PSS layer and from the use of electron and hole blocking layers. We found that the performance of TiO_2 / polymer devices is highly dependent on the pore diameter or particle size of TiO_2 relative to the exciton diffusion length of the polymer. In all these studies, we found TiO_2 (ECN) / TPD (4M)-MEH-M3EH-PPV is the best combination (see, table 5.4) and showed power conversion efficiency of 0.43 % under 1 sun.

5.5 Optimising active layer thickness

In order to optimise the device structure, we focus on the combination of ECN TiO_2 paste and TPD (4M)-MEH-M3EH-PPV polymer. As shown in the previous sections, this combination has the best combined optoelectronic properties among studied polymers. The standard device structure was ITO / HBL (dense TiO_2) / porous TiO_2 (ECN) / polymer^d / polymer^s / PEDOT:PSS / Au. The first study was to optimise the thickness of the active layers.

(a)



(b)

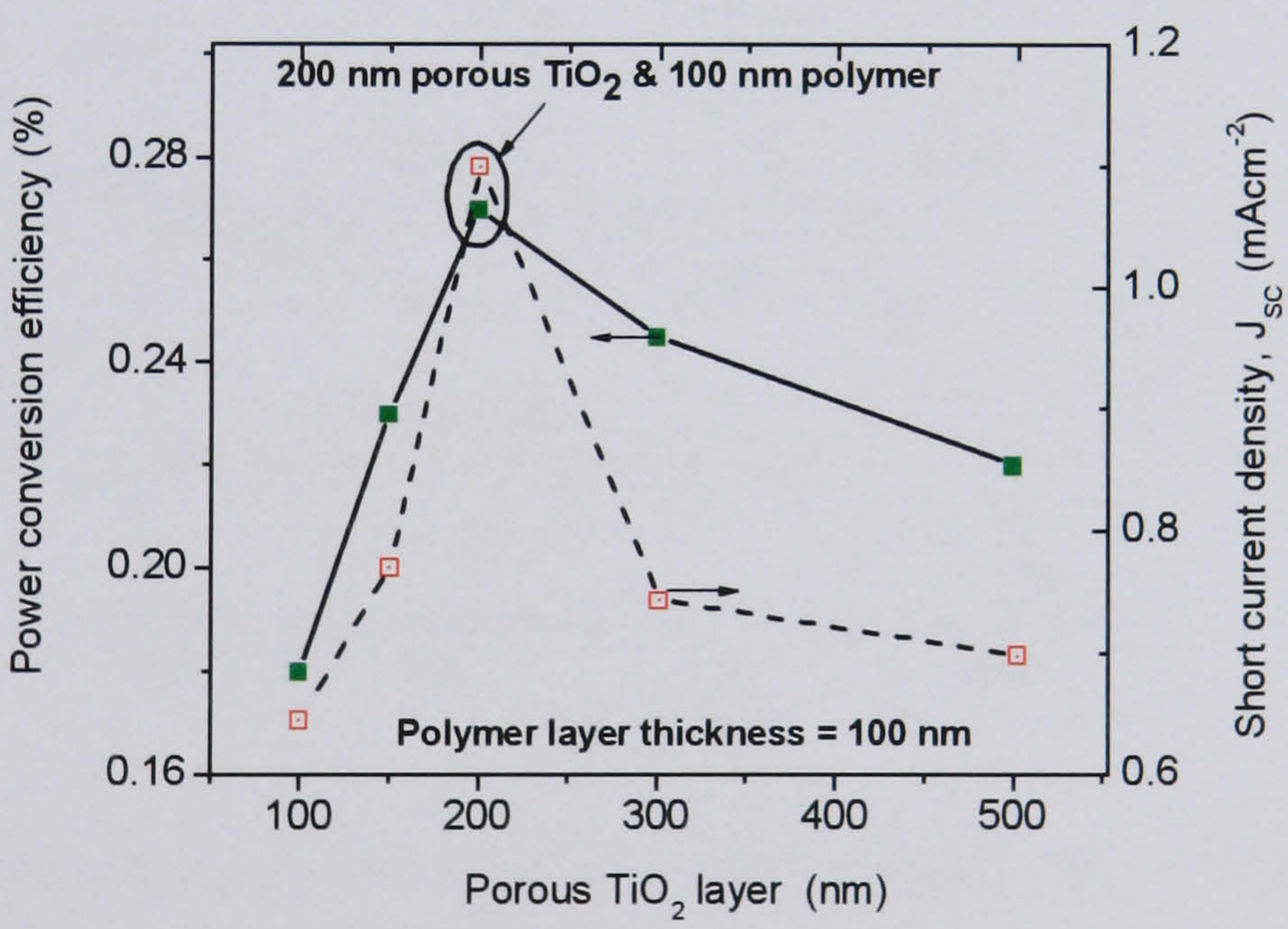


Figure 5.20 *(a) Current density vs voltage characteristics (under A.M. 1.5 conditions (1 sun)) for devices with different porous layer thicknesses for a constant polymer thickness (100nm). (b) The AM 1.5 short circuit current densities and power conversion efficiencies for the corresponding devices.*

Figure 5.20 (a) shows the J-V characteristics under AM 1.5 conditions for devices with different porous TiO_2 layer thicknesses, from 100 nm to 500 nm and a fixed spin coated polymer thickness of 100 nm. Figure 5.20 (b) shows the short circuit current

densities and power conversion efficiencies of the corresponding devices as a function of the porous TiO_2 layer thickness. The figures show that the short circuit current density depends strongly on the thickness of the porous TiO_2 active layers, while the open circuit voltage and fill factor depend weakly on layer thickness. The short circuit current density and power conversion efficiency are maximum when the ratio of the porous TiO_2 layer thickness to the effective polymer layer thickness is about 2:1. This result is reasonable, since there should be enough polymer to fill the pores at this ratio, assuming that the porosity of the TiO_2 films is 45 %[146]. Excess porous TiO_2 in comparison to polymer layer thickness would be expected to create voids in the devices and reduce the efficiency of the hole transport. The data show that excess TiO_2 decreases the short circuit current density, while open circuit voltage and fill factor remain approximately the same. Excess polymer would be expected to cause losses by optical filtering and series resistance. The data show that using less than 200 nm porous TiO_2. With a polymer thickness of 100 nm decreases both the short circuit current density and the open circuit voltage.

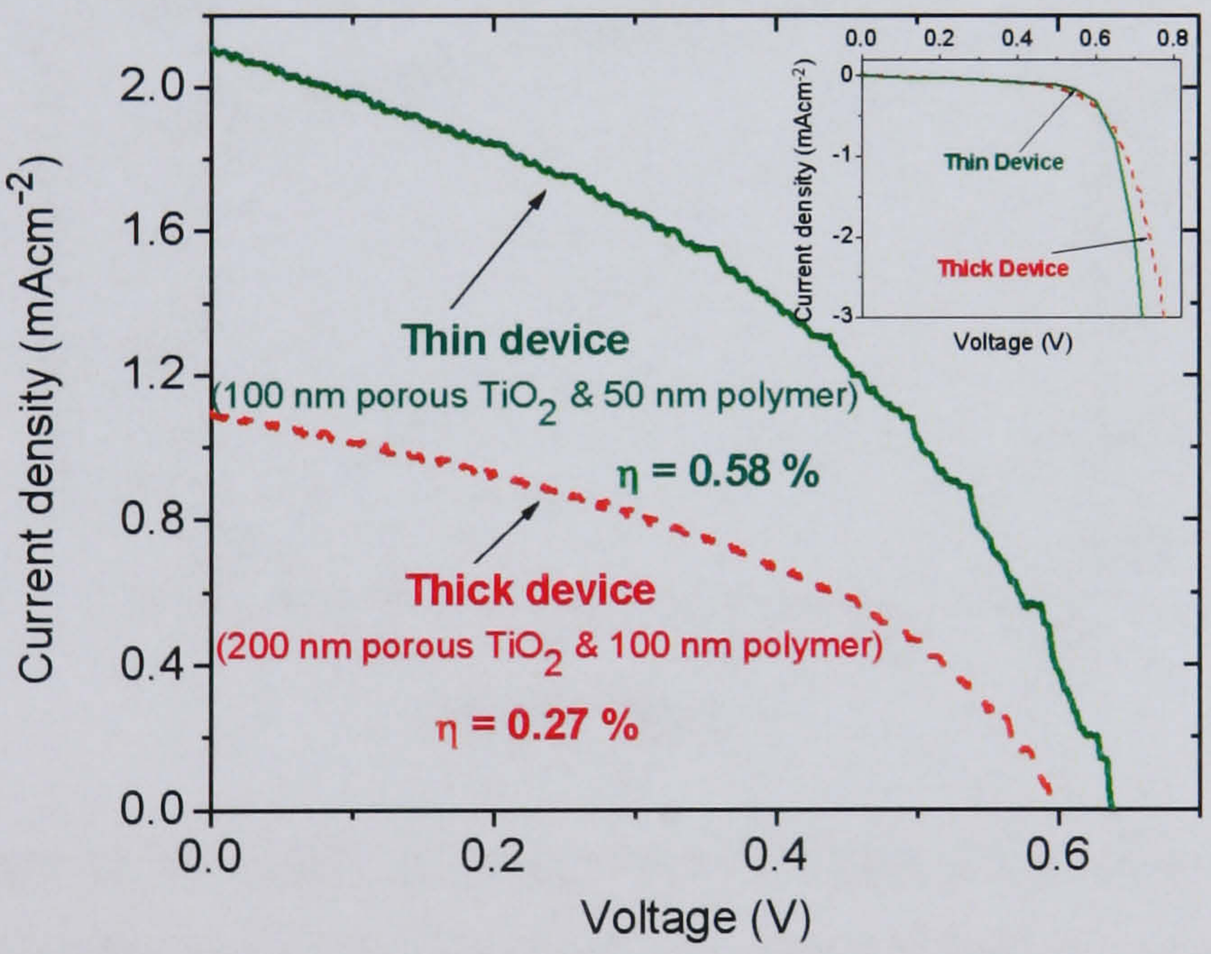
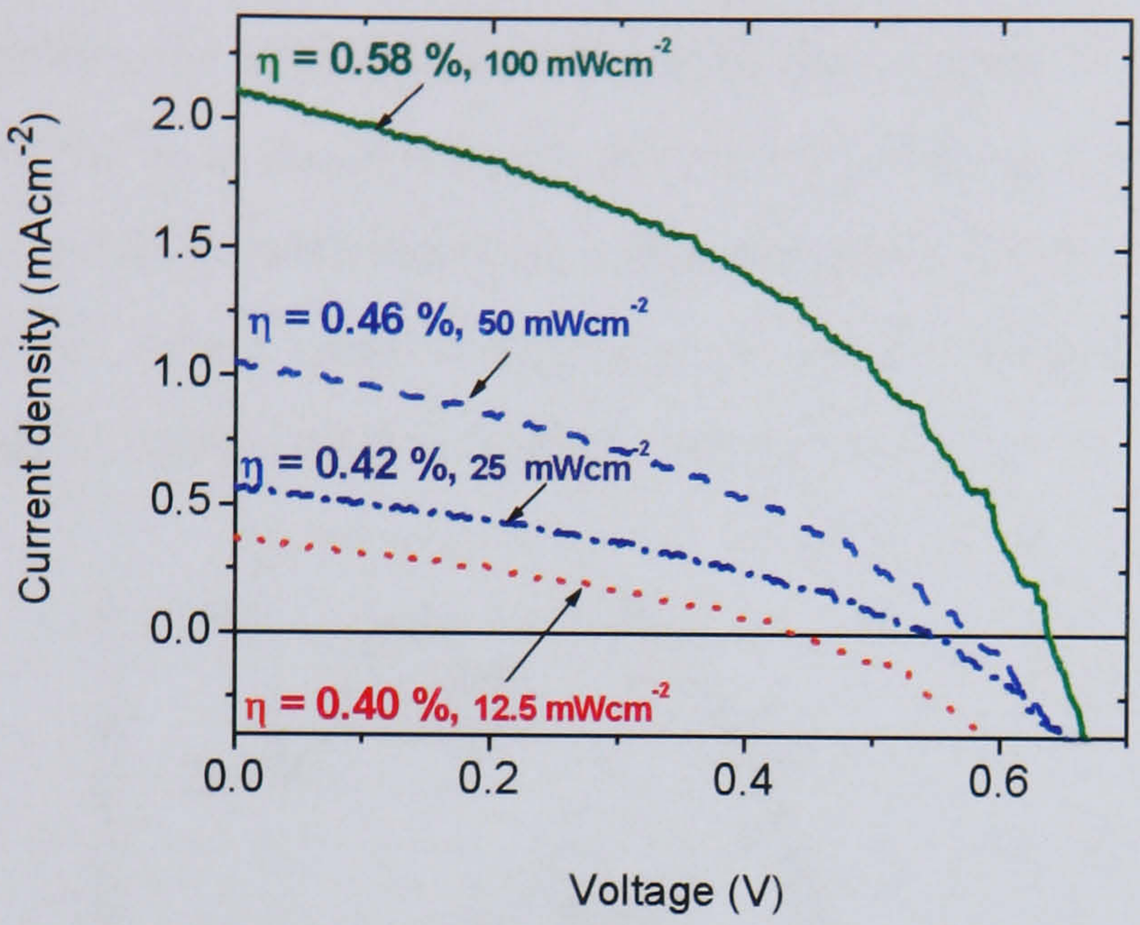


Figure 5.21 *J-V characteristics for for both thick (200 nm porous TiO_2, 100 nm polymer) and thin (100 nm porous TiO_2, 50 nm polymer) multilayer devices under A.M. 1.5 conditions (1 sun) and in the dark (inset).*

Next, keeping the optimum ratio of 2:1 for the porous TiO_2 to polymer layer thicknesses, the effect of total device thickness was studied. Figure 5.21 compares the J-V characteristics for thick (200 nm porous TiO_2, 100 nm polymer) and thin (100 nm porous TiO_2, 50 nm polymer) devices under AM 1.5 conditions. The thin device shows an open circuit voltage V_{OC} of 0.64 V, a short circuit current density J_{SC} of 2.1 mA cm^{-2} and a fill factor of 0.43. Its resulting AM 1.5 power conversion efficiency, 0.58 %, is

more than twice that of the thick device, which was only 0.27 %. The higher efficiency may be attributed to a reduced series resistance for the thinner TiO_2 and polymer layers, and to improved charge collection efficiency.

(a)



(b)

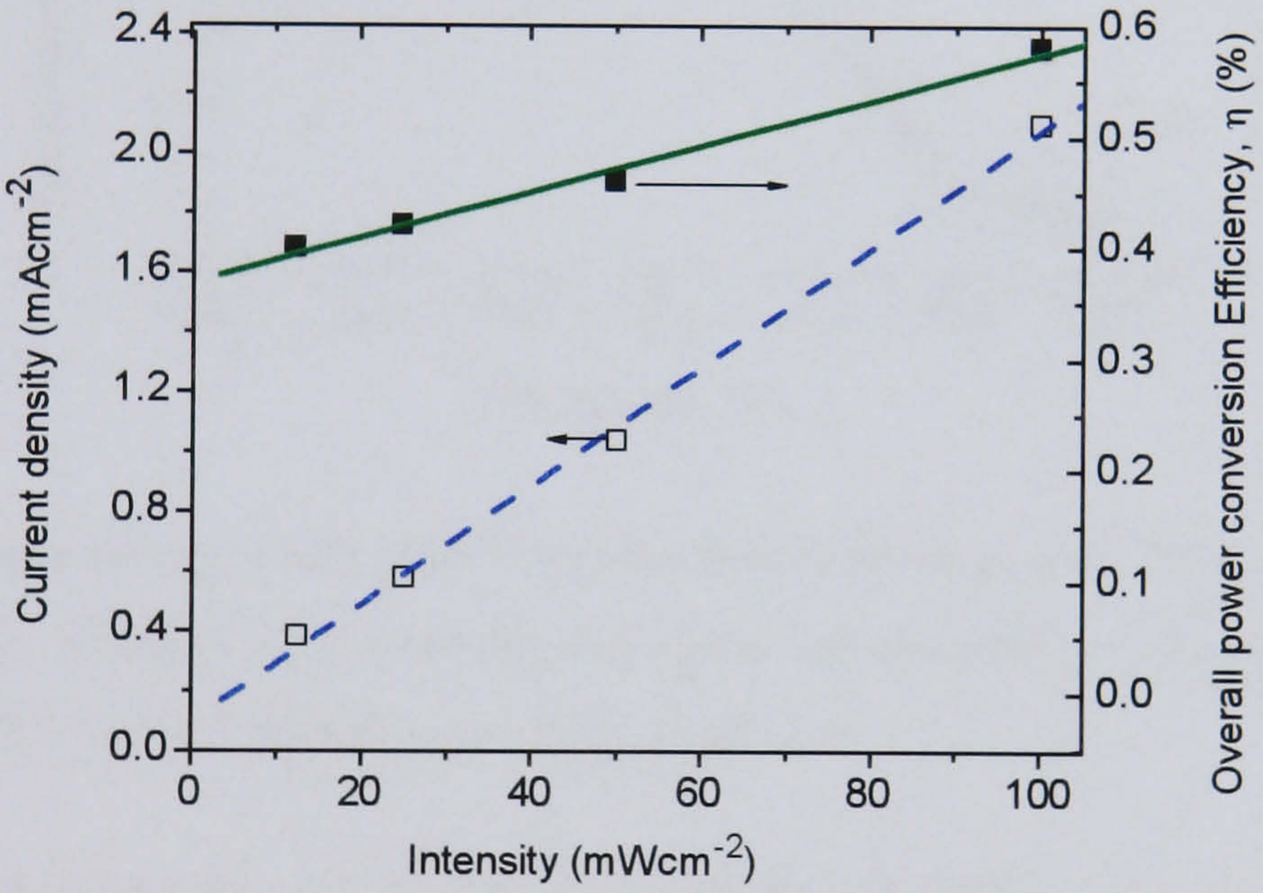


Figure 5.22 (a) *Current density vs voltage characteristics, (b) Short circuit current density and power conversion efficiency of the best device as a function light intensities. (J_{SC} - open square, dashed line and η-filled square, solid line)*

We have also examined the effect of light intensity on the photovoltaic performance of the best device using simulated AM 1.5 irradiation and neutral density filters. Figure 5.22 (a) and (b) show the current density - voltage characteristics, short circuit current density and power conversion efficiency of the best device as a function light intensities. Figure 5.22 (a) and (b) show that both V_{OC} and J_{SC} increase with increasing light intensity and both J_{SC} and η show linear intensity dependence and no tendency to saturate up to the AM 1.5 intensity of 100 $mWcm^{-2}$. The linear dependence

of the device short circuit current density indicates that bimolecular recombination losses are minimal compared to charge collection at short circuit.

Figure 5.23 shows the external quantum efficiency, EQE spectrum of the thin device together with the absorption spectrum of the polymer. The EQE spectrum of the device resembles the absorption spectrum of the polymer film on spectrosil and reaches maximum of 40 % at the maximum absorption of the polymer. Integrating the product of the measured EQE with the photon flux density of the AM1.5 solar spectrum yields a maximum short circuit current density of about 2.5 $mAcm^{-2}$, which is consistent with the measured J_{SC} under AM1.5 conditions of 2.1 mA cm^{-2}.

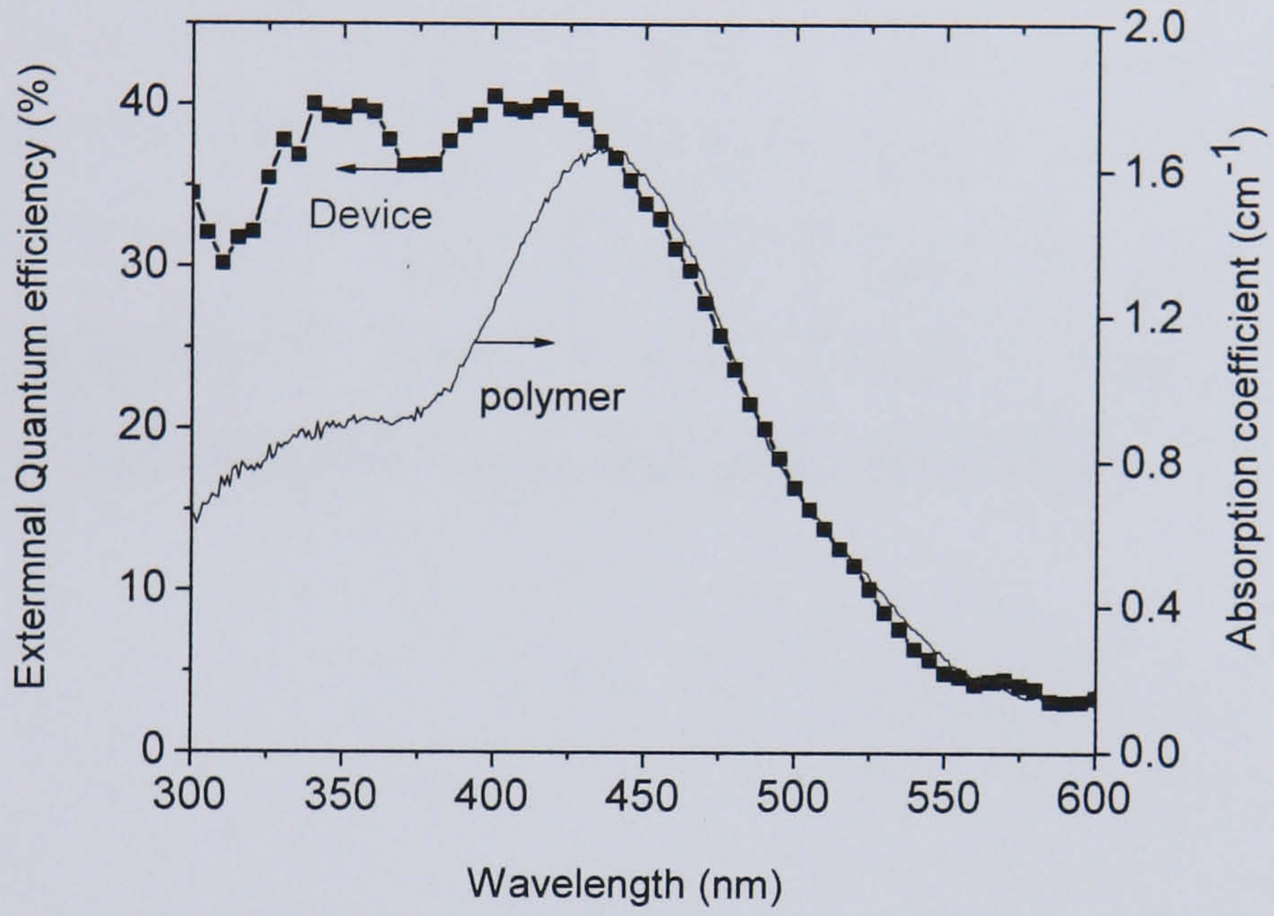


Figure 5.23 *Quantum efficiency spectrum of the thin (100 nm porous TiO_2, 50 nm polymer) multilayer device (filled squares) and the corresponding absorption spectrum of a TPD (4M)-MEH-M3EH-PPV polymer film on spectrosil (solid line)*

Table 5.5 compares the performance characteristics of our devices with the best previously reported hybrid TiO_2 / polymer devices under AM1.5 illumination. The reported efficiency values for TiO_2 / P3HT polymer devices are about three times smaller than TiO_2 / PPV polymer devices and the best previously reported[73] value for a TiO_2 / P3HT polymer device is 0.06 % under AM 1.5 conditions. Our best TiO_2 / P3HT polymer device shows an efficiency over three times higher than previously reported TiO_2 / polythiophene devices under 1 sun. The improved performance of TiO_2 / P3HT device is largely attributed to device design.

Our best TiO_2 / TPD (4M)-MEH-M3EH-PPV device shows over 2 $mAcm^{-2}$ while previously reported J_{SC} values are a few hundred μAcm^{-2}. The efficiency of our device is three times higher than the best previously reported efficiency for any hybrid TiO_2 / polymer device under 1 sun. The better performance of this device compared to

previously reported hybrid TiO_2 / polymer devices may be attributed to improvements in device design, polymer pore penetration, and the specific properties of the polymer, including its hole mobility and ability to sensitise TiO_2.

Table 5.5 *Comparison of the performance (under AM 1.5condition – 1 sun) of our devices with that of the best previously reported hybrid TiO_2 / polymer solar cells.*

Polymer	J_{SC} ($mAcm^{-2}$)	V_{OC} (V)	FF	**η (%)**	Reference
P3HT	0.31	0.49	0.40	**0.06**	[73]
P3HT	0.64	0.58	0.54	**0.20**	This work
MEH-PPV	0.40	1.10	0.42	**0.18**	[16]
MDMO-PPV	0.60	0.51	0.42	**0.19***	[20]
TPD-M3EH-MEH-PPV	2.10	0.64	0.43	**0.58**	This work

**Performance under 70 $mWcm^{-2}$, while others under 100 $mWcm^{-2}$.*

5.6 Summary

We have addressed the effect of microstructure of the porous TiO_2 film, the film thickness, the type of metal oxide (TiO_2, ZnO and SnO_2) and surface treatment of the TiO_2 (with alumina or dye coatings) on the performance of polymer / metal oxide devices. We have reported the first working polymer / metal oxide device using SnO_2 nanocrystalline. The SnO_2 / polymer device produced good short circuit current density J_{SC} of 0.48 mA cm^{-2} and open circuit voltage V_{OC} of 0.75 V under AM 1.5 conditions. The corresponding overall power conversion efficiency was 0.17 %. The performance is comparable to previously reported TiO_2 / polymer devices.

We studied the device performance of polymer / TiO_2 devices as a function of the thickness, microstructure and surface treatment of the porous TiO_2. We found that interfacial recombination can be reduced by treating the TiO_2 surface with a thin insulating Al_2O_3 layer. The alumina layer increases device efficiency more than 25 %. We have also found that the performance of TiO_2 / polymer devices is highly dependent on the pore diameter or particle size of TiO_2 relative to the exciton diffusion length of the polymer. Performance is also strongly affected by the active layer thickness and the relative thicknesses of the porous TiO_2 and polymer. We observe strong effects on device performance both from introduction of a PEDOT:PSS layer and from the use of electron and hole blocking layers.

Finally we report high efficiency multilayer hybrid TiO_2 / polymer solar cells based on nanocrystalline TiO_2 and a TPD containing MEH-PPV polymer. The optimised device has peak external quantum efficiency $\approx$ 40 % at the polymer's maximum absorption wavelength and yields a short circuit current density $\geq$ 2 mA cm^{-2} for air mass (AM) 1.5 conditions (100 mW cm^{-2}, 1 sun). The AM 1.5 open circuit voltage reaches 0.64 V and the fill factor 0.43, resulting in an overall power conversion efficiency of 0.58 %. The best TiO_2 / P3HT multilayer device showed an overall power conversion efficiency of 0.2 % under AM 1.5 conditions.

Although the reported efficiencies here are greater than any previously published values for TiO_2 / polymer solar cells, they are still lower than for polymer-fullerene solar cells, largely on account of relatively low J_{SC} values. Possible reasons may be the poor electron mobility of the porous TiO_2 (~ 10^{-6} to 10^{-7} cm^2/Vs, as measured by TOF and described in the next chapter), the pore size of the nanostructure which may still allow exciton quenching despite the relatively long exciton diffusion length of MEH-PPV polymers, or the optical transparency of the TiO_2 which contributes nothing to light harvesting.

Chapter 6

Charge transport in porous TiO_2

This chapter focuses on measurements of electron mobility in nanostructured TiO_2 films prepared by different routes (chemical and physical deposition routes) and relation to their microstructure. Time of flight mobility measurement techniques have been employed for this purpose.

6.1 Abstract

Three different techniques namely, electrostatic assisted vapour deposition (**ESAVD**), sputter deposition (**SD**) and sol-gel deposition (doctor blading of **colloidal** TiO_2 paste), have been employed to deposit porous TiO_2 films on ITO substrates. Sputter deposited films had lower porosity (~10% and 36% for normal-, and oblique (60°)-angle deposited films) compared to ~50% for films deposited by the two other techniques. All the films prepared by these techniques exhibited only the anatase phase as confirmed by X-ray diffraction (XRD) analysis. Scanning electron microscopic (SEM) studies show that sputter deposited films have rod shaped (columnar) particles, while others have a random distribution of TiO_2 particles.

The electron mobilities in the films were measured using the time-of-flight (TOF) technique. The electron transients for these films are very dispersive and the electron mobilities of all the porous TiO_2 films are in the range of 10^{-7} to 10^{-6} cm^2/Vs in the low field region (<55,000 Vcm^{-1}). We found a negative field dependence of electron mobility in each type of porous TiO_2 film. This behaviour is consistent with a model, due to Takashima *et al.*, involving a heterogeneous field distribution. The electron mobilities in the columnar TiO_2 films prepared by reactive sputtering were consistently

higher than in the films prepared by the two other techniques and the mobility values appear to be independent of the porosity of the columnar films. The relationship between the mobility and film morphology is discussed with the aid of SEM studies.

6.2 Introduction

Porous TiO_2 materials have attracted significant interest for more than a decade due to their applications in photocatalyisis, electrochromism, and gas sensing[8,42,147] as well as dye sensitized photovoltaic (PV) devices. Interest in the application of porous TiO_2 to hybrid TiO_2/polymer photovoltaic devices has also grown in recent years.

The performance of porous TiO_2 based PV devices is influenced by the charge transport properties of the porous TiO_2. Although the large surface-to-volume ratio of porous nanocrystalline TiO_2 leads to efficient charge separation in TiO_2 based PV devices, this porosity may adversely affect charge transport in this material, and so may limit the performance of such devices. The nature of charge transport in porous TiO_2 materials is determined by the ambient environment, microscopic structure and morphology. Eppler *et al.*[133,148] reported that there is large variation of dark conductivity and photoconductivity of the porous TiO_2 in different ambient conditions. Nelson[149] recently suggested a simple rate equation model incorporating trapping, recombination and scavenging which describes the gross features of the photoconductive behaviour of TiO_2 in solvent as well as gaseous ambient.

In this work, we study the relationship between charge transport and morphology of porous TiO_2 films prepared by different methods. Different fabrication processes for porous TiO_2 films result in different film morphology, which in turn affects the charge transport. We employ TOF mobility measurements for photoelectrical characterization and SEM & XRD measurements for structural characterization of the porous TiO_2 films prepared by different routes.

6.3 Experimental details

Three different techniques namely, doctor blading of sol-gel colloidal TiO_2 paste, electrostatic assisted chemical vapour deposition (ESAVD) and D.C. reactive sputtering have been employed to deposit thin TiO_2 films on ITO substrates. The sol-gel processed colloidal films were prepared at Dr. James Durrant's laboratory, Department of Chemistry, Imperial College London, while EASVD and sputtered films were prepared by Dr. Xianghui Ho and Dr. Jo Hamphsire respectively, at Prof. K. L. Choy's laboratory, Department of Materials, Imperial College London.

The colloidal TiO_2 films were prepared by doctor blading the TiO_2 colloidal paste (prepared at Imperial College) onto an ITO conducting glass substrate as described in section 2.4. The films were then sintered at 450°C for 30 minutes to remove the polymeric binder (polyethylene glycol (PEG)), and create a continuous network of nanoparticles.

The details of the EASVD film preparation used here are similar to those reported elsewhere[150]. The ESAVD technique involves spraying atomized precursor droplets across an electric field where the droplets undergo decomposition and/or chemical reaction in the vapour phase close to the heated substrate.

The DC reactive magnetron sputtered samples were prepared under the following conditions: the base pressure was 2×10^{-5} Torr, the argon pressure was 4×10^{-3} Torr and a current of 6 *A* (400 V) was applied to the titanium target (99.99 % purity). The deposition time was 140 minutes. The oxygen was controlled by an optical emission feedback loop by controlling the degree of poisoning of the titanium target. The TiO_2 films were stable at 25 % of the original metal emission value. Two sets of films were sputter-deposited: (i) normal angle incidence (SD90), and (ii) 60°-oblique angle incidence (SD60) between the plane of the substrate and the direction of the molecular beam.

The porosity of the EASVD and SD TiO_2 films was estimated using the weighing method, i.e., the substrates were weighed before and after deposition of the films. From the dimensions of the film (substrate surface area and thickness of the film) the bulk densities and hence porosities were determined, using 3.9 gcm^{-3} as the theoretical density of anatase TiO_2[151]. The thickness of all the films was measured using a Tencor Alpha-Step 200 profilometer. The ESAVD film had an average thickness of 3.4 μm and ~ 50 % porosity, whilst the colloidal film was 4.0 μm thick and ~ 50 % porous. The SD90 film had an average thickness of 4.7 μm and porosity ~ 10 %, while the SD60

film was 4.6 μm thick and ~ 36 % porous. The difference in porosity of the two sputtered deposited films can be explained when we consider that during oblique-angle deposition some areas of the substrate are shielded or shadowed by the initial island growth of the evaporated material resulting in more porous structure.

The structural studies (SEM & XRD) of the porous TiO_2 films were carried out at the Department of Materials with a visiting academic Prof. Bernard. O. Aduda. X-ray diffraction (XRD) characterizations were conducted using a Philips PW1700 Series X-ray diffractometer with CuK_α (λ = 0.15405 nm) radiation from a secondary crystal monochromator (accelerating voltage = 40kV and current = 40mA). A high-resolution scanning electron microscope (LEO 1525) was employed for micrographs of the porous TiO_2.

The TOF mobility measurement was performed on the samples after evaporating Au as a top contact as described in section 2.7. Each sample consisted of six devices of area 4.2 mm^2 and the devices were illuminated through the ITO. Initial measurements were carried out on colloidal films with the excellent guidance of Dr. Theo Kreouzis, while the measurements of other films were taken with Prof. Bernard O. Aduda.

Photocurrent transient measurements were taken both in air and vacuum. For measurements in vacuum, the chamber was evacuated to less than 10^{-4} Torr. In some cases (air ambient) the injected current was very high and therefore the dark current had to be subtracted with an additional home built differential amplifier.

6.4 Results and discussions

We will first discus the TOF measurements of the TiO_2 colloidal samples and then compare this result with the measurements of the other samples in relations to their microstructure using SEM images.

6.4.1 TOF measurements of colloidal films

Depending on the polarity of the applied voltage either positive or negative carriers can be drawn into the sample during photoexcitation. The attempt to draw the hole by applying positive voltage to the illuminated transparent electrode was not successful even at very high voltage. This observation indicates that the hole-mobility of porous TiO_2 is very low. A photocurrent transient was observed when a negative voltage was applied to the illuminated ITO. This photocurrent transient is due to electron transport.

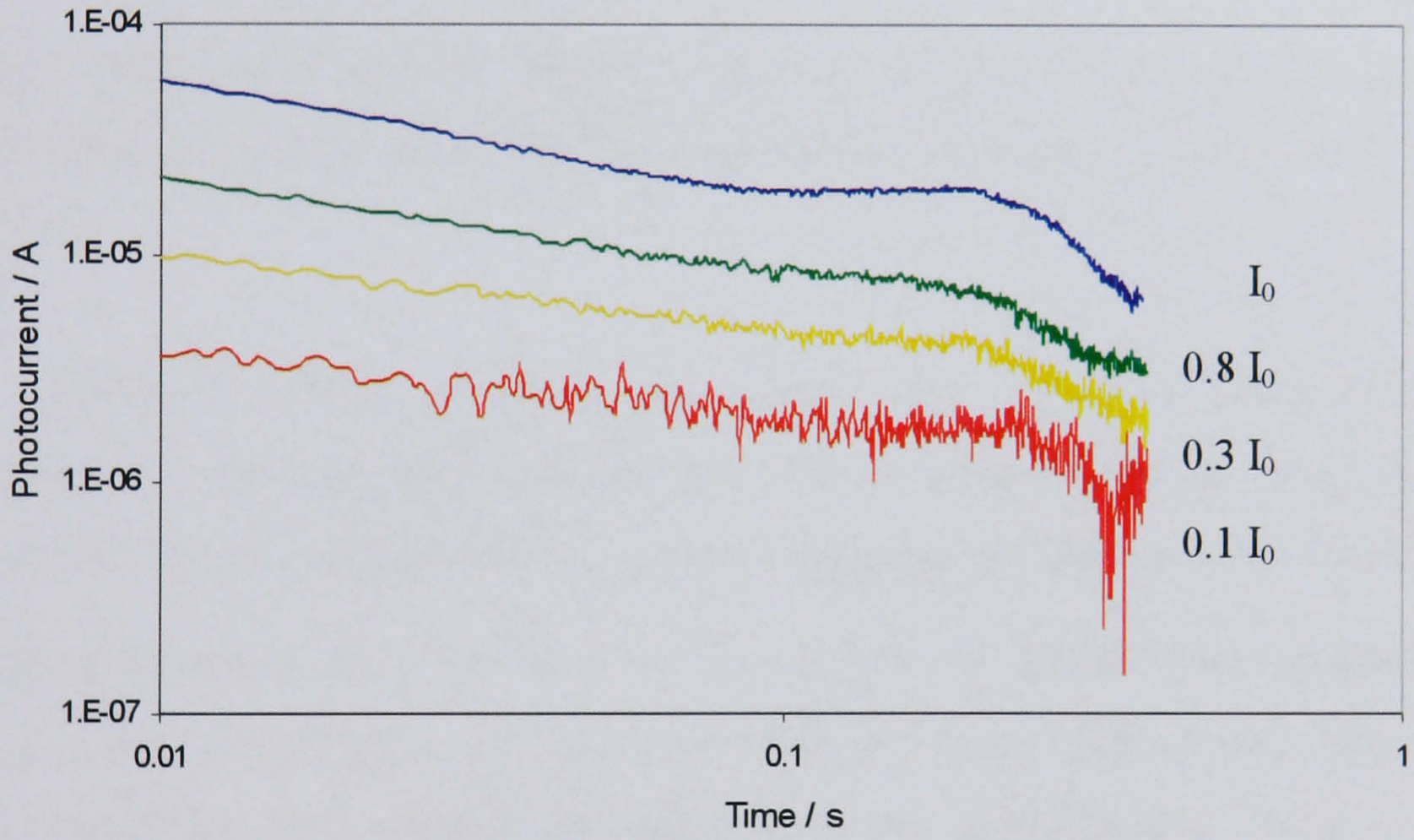


Figure 6.1 *Double logarithmic plot of a set of electron photocurrent transients for a colloidal TiO_2 film in air at different laser light intensities ($I_0 \sim 100\ mJcm^{-2}$, $\lambda = 355\ nm$).*

Figure 6.1 shows a double logarithmic plot of the electron photocurrent transients for a colloidal porous TiO_2 film in air at different laser light intensities. At higher intensity, the photocurrent transient shows a bump like feature. This is attributed to space charge. The photogenerated charge overwhelms the charge on the electrodes so that space charge limited transport dominates over the drift current at higher intensity. The bump like feature is almost eliminated by reducing the laser light intensity. In previous TOF studies[152,153] of porous TiO_2, the transit time of the electron in porous TiO_2 was determined in the space-charge-limited- current (SCLC) region, where the peak current (t_P) in the photocurrent transient can be related to the transit time through

t_T = 1.25 t_P. However, at high intensity, trap saturation and recombination becomes important[154] and the transport mechanism may be different. Therefore, in our studies, the photocurrent transients were taken in the limit of low intensity, avoiding the space charge limited current region.

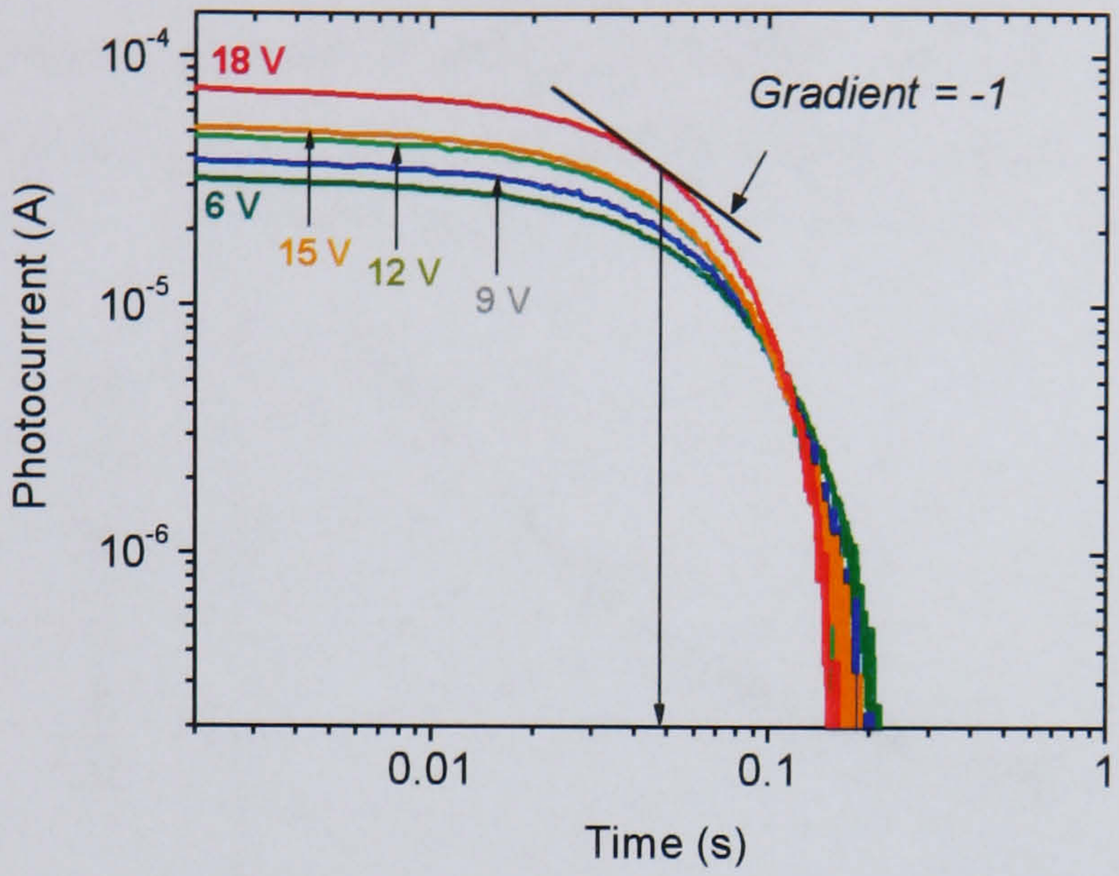


Figure 6.2 *Double logarithmic plot of the electron photocurrent transient for a colloidal TiO_2 film of thickness 4 μm in air at different bias with laser light intensity of about 23 $mJcm^{-2}$ (λ = 355 nm).*

Figure 6.2 shows a double logarithmic plot of several electron photocurrent transient for the colloidal TiO_2 film in air at different biases. Each photocurrent transients shows a change from a slower decrease in photocurrent at short time towards a strong decrease [$i(t) \propto t^{-p}$, p > 1] at long time. The decrease of photocurrent at longer times gets stronger with increasing voltage. Although the transit time gets shorter with increasing bias voltage, the position of the characteristic "knee", marking the intersection of the short time and long time asymptotes on a log-log scale, is hard to define. Therefore we used two different methods[129] to determine the transit time, t_T. The first was to estimate the position of the knee, and the second was to find the time at which the gradient of the double logarithmic plot equals to -1, as shown in the Figure 6.2. The transit times obtained by the two methods agree to within about 20 % in the case of a transient with well-defined asymptotes and consequently we remark that this may be an adequate means of estimating the characteristic transit time in very dispersive materials[129]. The mobility values of the electron with different applied voltage, U are determined by using the usual expression $\mu = \frac{d^2}{V t_T}$, where d is the thickness of the sample.

The electron mobility of the porous colloidal TiO_2 (50 % porosity) is 4.4×10^{-7} cm^2/Vs at 1.5×10^4 V/cm. The value is in reasonable agreement with reported values[152,153], while lower than the value of 6×10^{-4} cm^2/Vs deduced from the effective diffusion coefficient[153] for transport in electrolyte contacted colloidal TiO_2 films. The room temperature electron mobility of porous TiO_2 is, however, much lower than electron mobility of crystalline anatase TiO_2 which is about 1 cm^2/Vs [155].

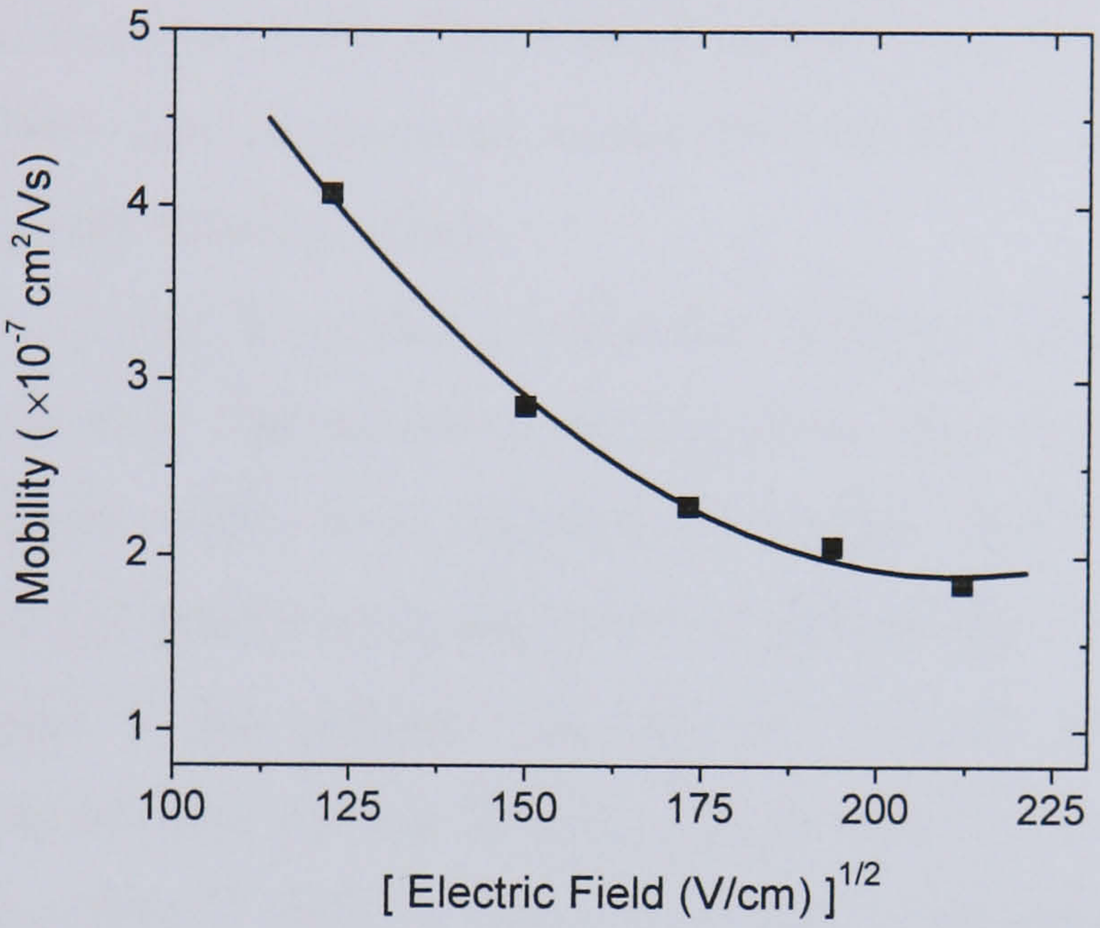


Figure 6.3 *Electron mobility vs applied field for the colloidal TiO_2 film* in air.

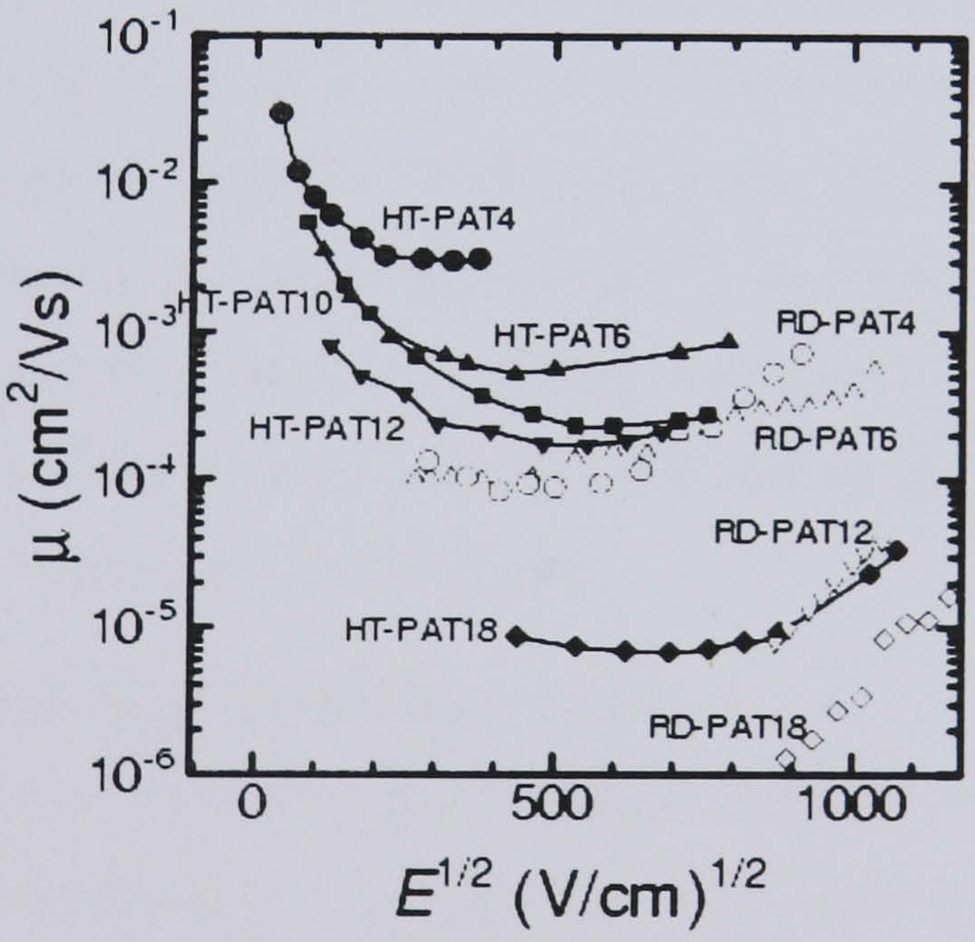


Figure 6.4 *Mobility vs applied field for several* poly(alkylthiophene) [PAT] polymer materials[156].

We observed a delayed response of the dark current to the applied voltage and no photocurrent transient below an applied voltage of 3 V. These observations suggest that porous TiO_2 has a lot of traps. The low mobility value observed in porous TiO_2 may therefore be attributed partly to the blocking of charge transfer by trapped space charge.

We expect a higher trap density in porous materials than in bulk films because of the higher probability of surface defects. It is therefore likely that the electric field in the porous TiO_2 sample is not homogenously distributed during the mobility measurement. If the electric field is not uniform, then the extracted mobility value is not accurate. It has been suggested[152] that defects near the surface of the nanoparticles are the most probable candidates for the limitation of the carrier transport in porous TiO_2. Recombination of carriers is the other loss of mechanism and becomes dominant at high intensity. All these loss mechanisms would need to be incorporated into a model in order to find the real mobility values.

Figure 6.3 shows the extracted electron mobility values in porous TiO_2 with increasing electric field. The electron mobility values show negative field dependence in the low field region unlike most disordered materials. Dittrich *et al.*[152] have reported that the value of μ is practically independent of applied bias voltage (V) for V < 10-15 V, but for higher V the mobility (μ) starts to decrease. A similar negative field dependence of mobility in the low field region has also been found in some conjugated polymers such as F8T2[136], P3HT[157] and several other poly(alkylthiophene) polymers of various chain lengths[156] (see Figure 6.4).

It is normally expected that the mobility should be field-independent, or possibly *increase* with electric field in the case of a field assisted hopping mechanism. One possible explanation for negative field dependence of mobility is a high degree of configurational (rather than energetic) disorder[119]. An alternative mechanism leading to reduced apparent mobility may be increasing bimolecular recombination with applied bias. A third is the redistribution of electric field due to the background charge carrier density. This will be discussed further below

6.4.2 Heterogeneous field distribution model

In estimation of mobility, it is normally assumed that the electric field is uniform in the sample. Takashima *et al.*[156] proposed a model of heterogeneous field distribution for a simplified Schottky junction of metal and semiconductor (see Figure 6.5). In the Schottky junction semiconductor structures, the external bias is mainly dropped across a depletion layer of field-dependent thickness d', leaving a field-free 'bulk' region of thickness $(d - d')$ adjacent to the ohmic contact at applied biases smaller than some critical value V_C. (In our case, the depletion region is expected to form next to the interface between gold contact and the n-type TiO_2). The depleted region has a low conductivity σ_d relative to that of the undepleted bulk material, σ_b (i.e., $\sigma_d << \sigma_b$).

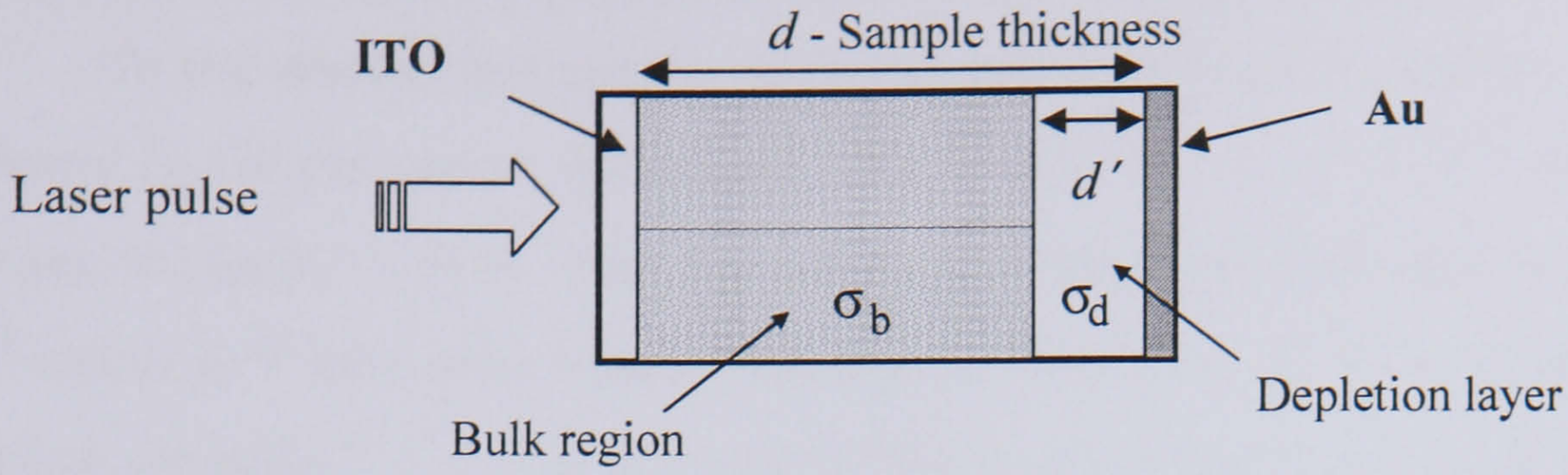


Figure 6.5 *Model of heterogeneous field distribution for a simplified Schottky junction of metal and semiconductor*[156].

The apparent transit time (t_T) of the carriers can then be approximated by

$$t_T = \frac{\left[1+\left(\frac{\sigma_b}{\sigma_d}\right)\left(\frac{d'}{d}\right)\right]d^2}{\mu V} \qquad (6.1)$$

so that the effective bias (V_{eff}) experienced by the carriers is

$$V_{eff} = \frac{V}{\left[1+\left(\frac{\sigma_b}{\sigma_d}\right)\left(\frac{d'}{d}\right)\right]} \qquad (6.2)$$

where $d' = \left(\frac{2\varepsilon\varepsilon_0}{en_0}\right)^{1/2} (V - V_{BI})^{1/2}$, ε is the dielectric permittivity, ε_o is the permittivity of free space, n_0 the equilibrium carrier density, e the electronic charge and V_{BI} the Schottky barrier height or built-in bias. (In TOF experiments, V is normally > V_C). V_C is the bias at which the film is just depleted and is given by $V_C = \frac{en_0 d^2}{2\varepsilon\varepsilon_0} + V_{BI}$. As bias is reduced below V_C, d' decreases and the transit time increases more slowly than $1/V$, with the effect that the mobility, defined from $\mu = \frac{d^2}{V_{eff}\ t_T}$, appears to increase. Thus the negative-field dependence of μ in the low field region can be attributed to the bias dependent depletion width.

Juska *et al.*[158] proposed a similar explanation for negative field-dependent mobility in the low field region as measured by TOF. They argued that high equilibrium carrier densities and the resulting redistribution of electric field inside the sample cause the transit time to exceed the dielectric relaxation time ($\tau_{rel} = \frac{\varepsilon\varepsilon_0}{ep_0\mu}$) and the necessary condition for TOF, ($\tau_{rel} >> t_T$) may not fulfilled. The apparent mobility approaches the true mobility only when $V >> V_C$.

To test whether our samples lie in the regime of negative apparent mobility we estimate U_C for our system. Substituting the values $\varepsilon = 114$, $n_o \sim 10^{16}$ cm^{-3}[159] and $d = 4.0$ μm, we get $V_C \approx 18$ V. This may be considered a lower limit since lower values of ε[158] and of n_o[128] have been reported for anatase. This value of V_C is comparable to the applied voltages ($V = 3 - 25$ V) used during the experiments and so the criterion for accurate mobility measurement by TOF ($V >> V_C$) is not satisfied. Under these circumstances, our results may be explained and the true mobility estimated using Takashima's model. If the barrier height $V_{BI} << V$ ($V_{BI} \sim 0.4$ V for ITO / TiO_2 / Au), so that $d' \propto V^{1/2}$ Takshima's[156] expression for t_T can be written

$$t_T V = \Psi V^{1/2} + d^2/\mu \qquad (6.3)$$

where Ψ is a constant given by $\Psi = \frac{\sigma_b d}{\sigma_d}\left(\frac{2\varepsilon\varepsilon_0}{en_0}\right)^{1/2}$. (6.4)

To test the behaviour predicted by equation 6.3, we plot $t_T U$ vs $U^{1/2}$. The linear behaviour of the plot of $t_T V$ vs $V^{1/2}$ (Figure 6.6) confirms that the equation 6.3 is followed for the colloidal TiO_2 sample. The electron mobility of the colloidal TiO_2 estimated from the intercept the plot is 6.5×10^{-7} cm^2/Vs. This is comparable to the value obtained from the usual equation $\mu = \frac{d^2}{V t_T}$.

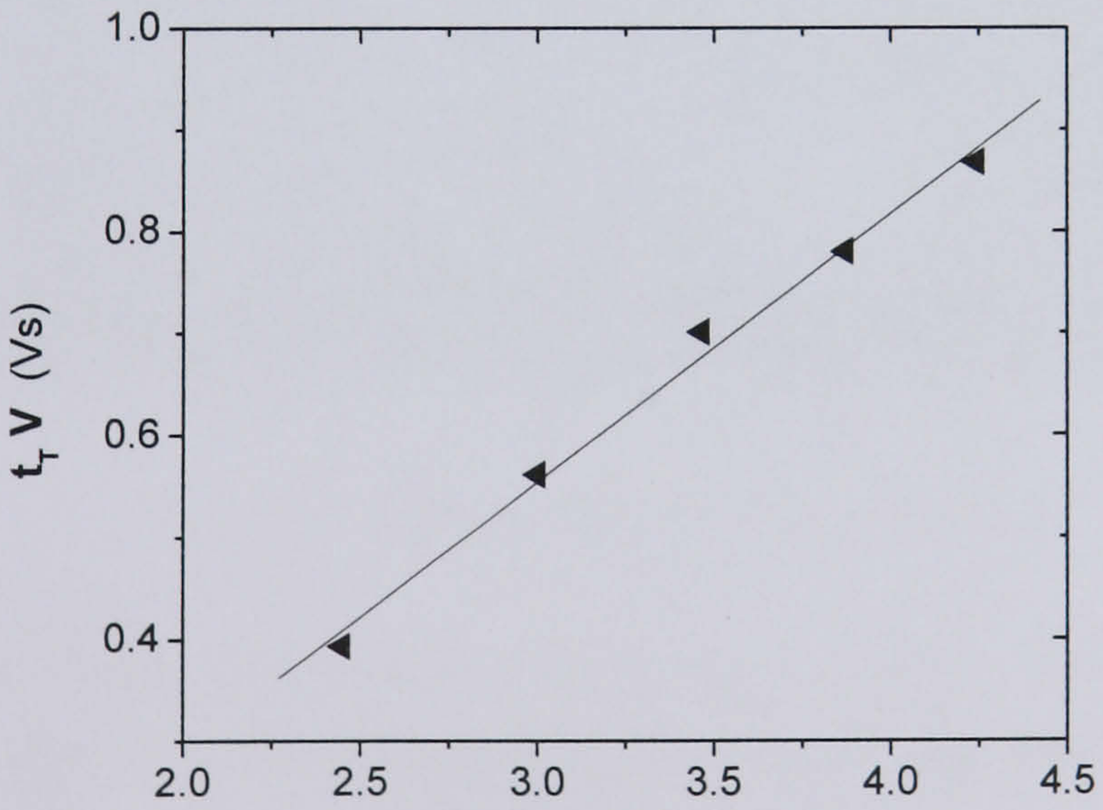


Figure 6.6 The *plot of $t_T V$ vs $V^{1/2}$ for a colloidal TiO_2 film.*

Electron photocurrent transient in colloidal TiO_2 were also observed in vacuum at different bias. However, no transit time could be defined for the transients in vacuum. Relatively higher photocurrents were observed in vacuum compared to air. This may be attributed to the absence of surface adsorbed molecular oxygen which acts as an

electron scavenger. Removal of oxygen extends the electron lifetime and results in higher photocurrent in vacuum. A similar observation has already been reported[133,148] through photoconductivity measurement in porous TiO_2.

6.4.3 Effect of morphology on electron mobility of porous TiO_2

In this section we will discuss the effect of morphology on carrier mobility in porous TiO_2. SEM, XRD and TOF flight measurements of physical deposited porous TiO_2 films were done with Prof. Bernard O. Aduda.

6.4.3.1 XRD measurements

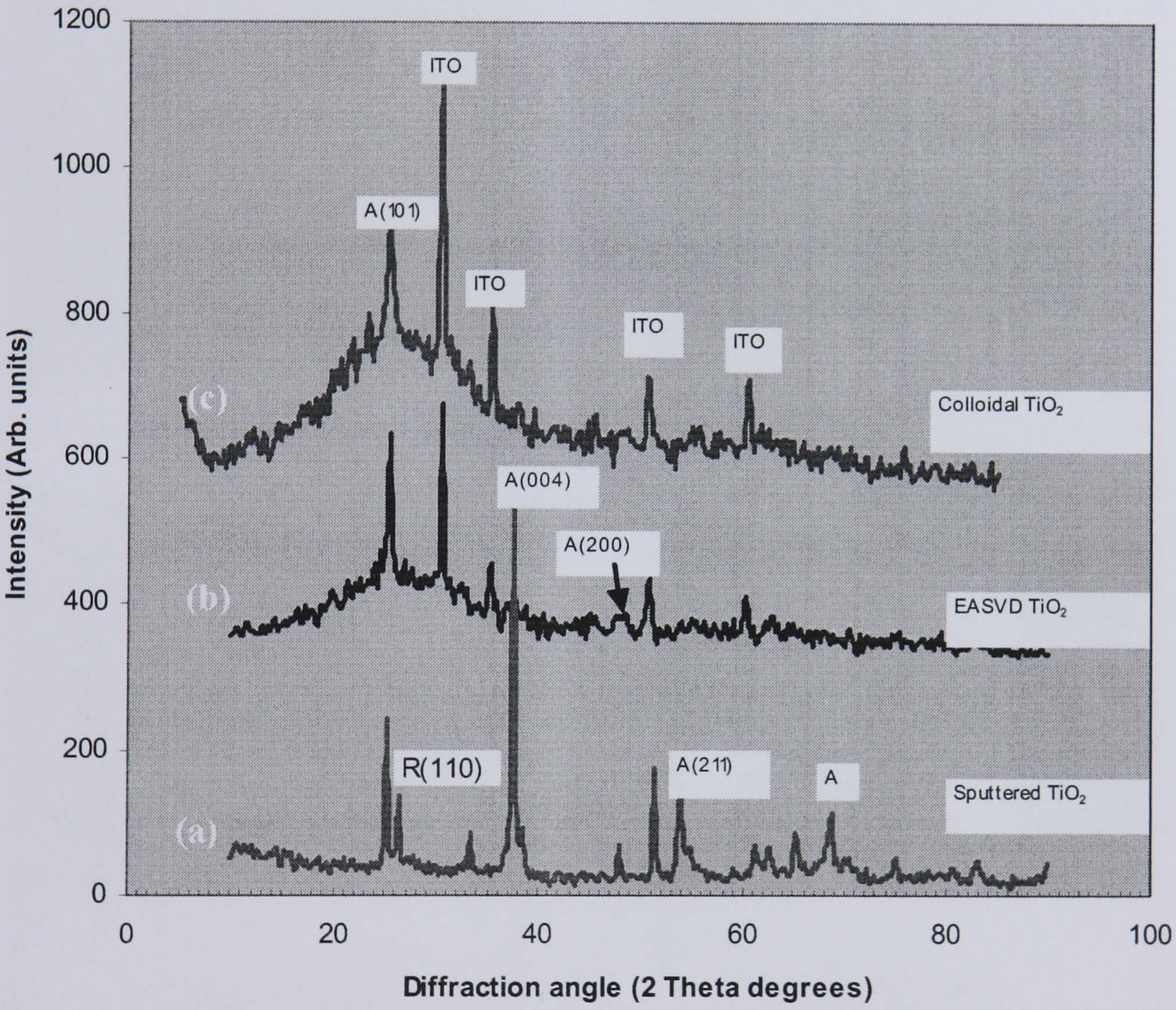


Figure 6.7 *X-ray diffraction patterns of TiO_2 films prepared by different techniques on ITO substrates: (a) sputtering (b) electrostatic assisted vapour deposition (EASVD) (c) doctor blading of colloidal TiO_2.*

X-Ray diffraction analysis (see Figure 6.7) of all the samples indicated that they comprised mainly anatase with little (sputtered) or no rutile phase detected. From the widths of the reflection line A (101), we can infer that the crystallites of the colloidal TiO_2 were the finest, with those of the sputtered TiO_2 being the coarsest.

6.4.3.2 SEM measurements

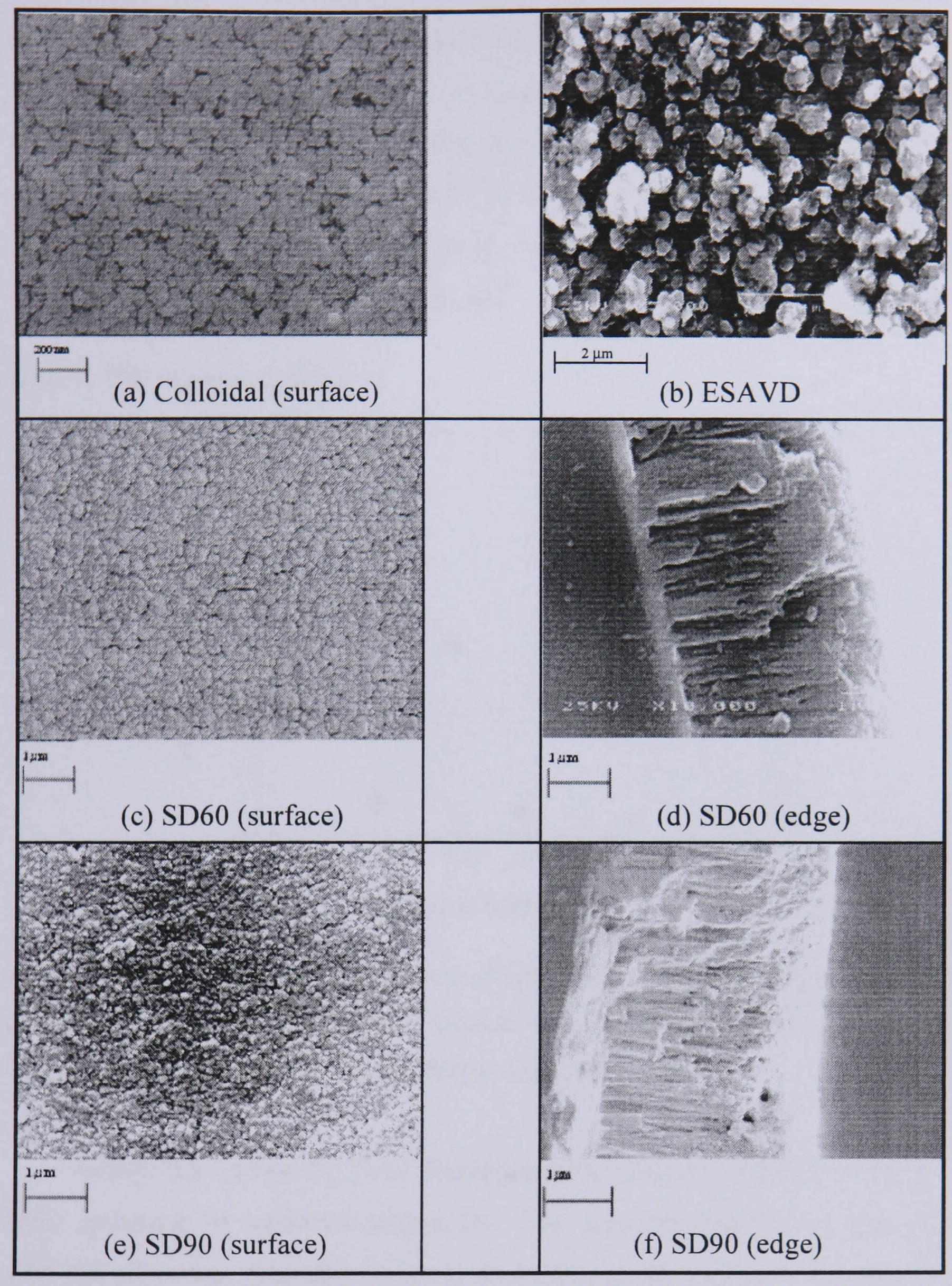


Figure 6.8 *SEM micrographs of the TiO_2 films prepared by different techniques: colloidal film (a) surface, electrostatic spray assisted vapour (ESVAD) film (b) surface, sputter deposited-oblique angle 60-degrees (SD60) (c) surface (d) edge and sputter deposited-oblique angle 90-degrees (SD90) (e) surface (f) edge.*

Figure 6.8 shows typical scanning electron micrographs (surface and edge) of the ESAVD, colloidal and sputtered TiO_2 films. Notable is the high porosity but quite large particles (>500 nm) of the ESAVD film, compared to those in the colloidal film. The sputtered films show a columnar structure with narrower columns for the film deposited at 60° than for the film deposited at normal incidence.

The colour of the colloidal films was transparent, whereas the ESVAD films and sputtered films were milky and slightly dark grey. Oxygen deficient anatase TiO_2 is also known to have a darker colour[159]. The sputtered TiO_2 lost its grey colour when heat treated in air at 500 ^{0}C for 30 minutes, as expected upon oxidation of reduced TiO_2. The milky colour in the case of the ESAVD film may be due to the large particle size (> 500 nm), causing strong scattering of light, while the smaller particle size in the colloidal films cause negligible scattering.

6.4.3.3 TOF measurements

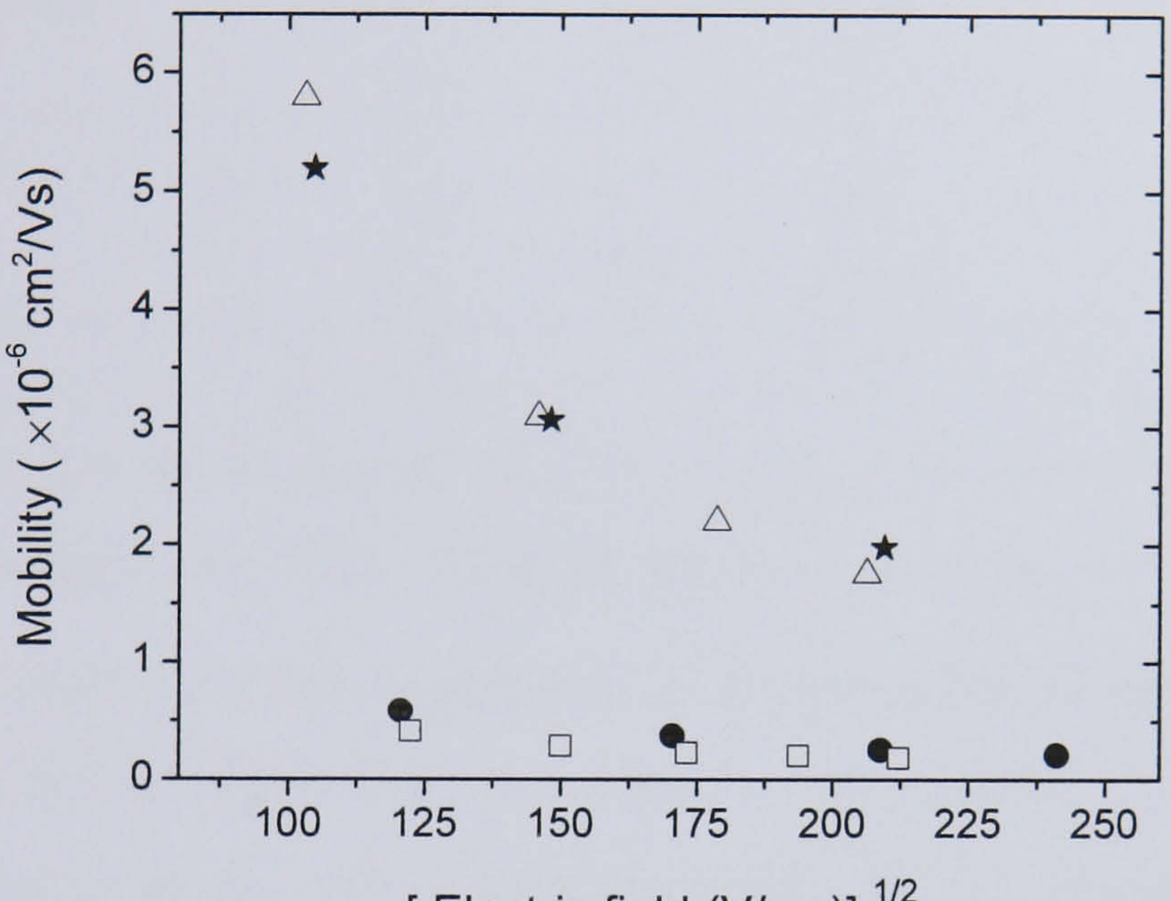


Figure 6.9 *The electric field dependence of mobility in porous TiO_2 films prepared by different techniques: ESVAD (filled circles), colloidal (open squares), sputtered-normal angle (open triangles) and sputtered-60^0-degree oblique angle (filled star).*

Figure 6.9 shows the field dependence of electron mobility in the porous TiO_2 films prepared by different techniques. The electron mobility of the colloidal and ESAVD films was generally lower than for the sputtered films. The mobility value of sputter deposited TiO_2 (5.6×10^{-6} cm^2/Vs) is one order magnitude higher than the other two films. The lower electron mobility in the colloidal and ESAVD films compared to the sputtered ones can be attributed to their observed high porosity, smaller grain size with increased grain boundary and surface area, compared to that of sputter deposited TiO_2 films. It is important to point out that there was no significant difference between the electron mobility values of the sputter deposited films (SD90 and SD60), indicating that in these films the effect of porosity was comparatively small (see table 6.1). Since the films prepared by the ESAVD and colloidal techniques had similar porosity (~

50%), the slightly higher mobility values of the ESAVD films may be attributed to the larger particles, hence fewer grain boundaries, observed in this film. The columnar rod-shaped particles of the sputtered films reduce the number of particle-particle hops required for charge transfer to the substrate, thus enhancing the chances of an electron moving through the electrode without recombining or being trapped.

Table 6.1 *Comparison of electron mobilities, μ_e, of porous TiO_2 films with their porosities. Mobility values are estimated from usual expression and the intercept of the plots of $t_T V$ vs $V^{1/2}$ (Takashima's model).*

Porous TiO_2 film	Porosity (%)	μ_e ($\times 10^{-7}$cm^2/Vs) @ 1.5×10^4 V/cm	μ_e ($\times 10^{-7}$cm^2/Vs) by Takashima's model
Colloidal	50	5.0	6.5
ESVAD	50	6.7	6.6
SD 60	36	42.0	56.0
SD 90	10	44.0	56.0

Figure 6.9 shows that all the porous TiO_2 films show negative field dependence electron mobility in low field. We again applied Takashima's model and the plots of $t_T V$ vs $V^{1/2}$ for these TiO_2 films are shown in Figure 6.10. The linear behaviour confirms that equation 6.3 is followed for our samples. The mobility values of the various TiO_2 films estimated from the intercepts are 6.6×10^{-7} cm^2/Vs for electrostatic spray assisted vapour deposited films, 5.6×10^{-6} cm^2/Vs for sputter deposited TiO_2 (both normal and oblique angle deposition). These values are comparable to those obtained from the usual equation $\mu = \frac{d^2}{V\ t_T}$. (see table 6.1).

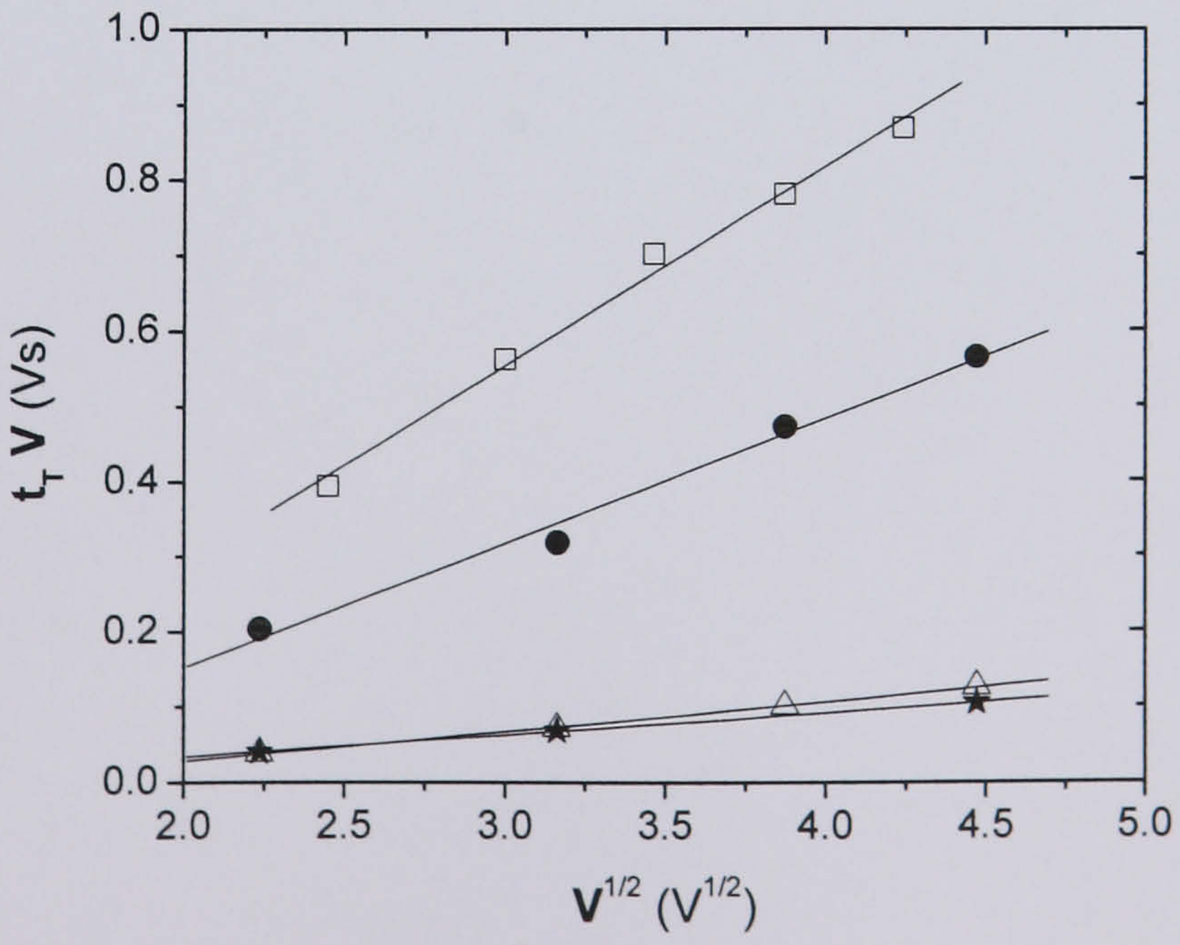


Figure 6.10 *The plot of t_T U versus $U^{1/2}$ for porous TiO_2 (anatase) prepared by different techniques: ESVAD (filled circles), colloidal (open squares), sputtered-normal angle (open triangles) and sputtered-60^0-degree oblique angle (filled star).*

6.5 Summary

We have found that the electron mobility measured by the TOF technique for porous TiO_2 is in the range of 10^{-7} to 10^{-6} cm^2/Vs, and is dependent on the morphology of the film. Columnar TiO_2 films have higher electron mobility than porous films with random distribution of TiO_2 particles. This could be due to the fact that charge carriers in the columnar films, with the columns aligned nearly in the direction of the field may be able to gain kinetic energy from the applied field along the column axis which minimizes recombination and scattering, resulting in higher mobility. Solar cells made with columnar nanostructured TiO_2 with suitable dimension may therefore offer better device performance than randomly distributed TiO_2 particles.

Chapter 7

Conclusions and Future Works

7.1 Conclusions

The conclusions of this thesis are divided into four sections, namely optimisation of device design, the effects of polymer optoelectronic properties, microstructure, metal oxides and metal oxide coating on device performance as well as charge transport of porous TiO_2.

7.1.1 Optimisation of device design of multilayer hybrid polymer / metal oxide combinations

We presented a novel device design and criteria for optimisation of multilayer hybrid polymer / metal oxide solar cells. Most of the device design and process of device optimisation for this thesis was done with TiO_2 and a fluorene-bithiophene (F8T2) polymer material combination. Efficient photo-induced charge transfer is observed from F8T2 to the TiO_2 film, while interfacial recombination is relatively slow (10 ms -100 μs). A study of different top contact material in TiO_2 / F8T2 bi-layer device reveals that high work function materials must be used for efficient charge (holes) collection in hybrid polymer / metal oxide devices. Inserting a thin (~100 nm) porous layer of TiO_2 into a planar bi-layer TiO_2 / polymer structure increases EQE by a factor of five, but the device performances are limited by poor fill factor. Polymer infiltration into the pores of thin (< 150 nm) porous TiO_2 films is achieved by a dip-coating step without any additional melt processing steps, while additional surface treatment of TiO_2 and melting of the polymer was needed to achieve polymer penetration into the pores for thicker TiO_2 films. Device performance is improved by reducing the thickness of both TiO_2 and polymer layers, which may be explained by reduced series resistance and

reduced optical filtering. A dip coating layer improves polymer infiltration and fill factor of the device and improve overall performance by 50 % in thin devices. Although the device with a dip coated layer alone offers photovoltaic action, a spin coated layer is essential for better device performance. The second spin-coated layer is required to fill the pores, thus increasing optical density and improving film uniformity. The polymer layer thickness should be optimised to minimise losses to optical filtering. Devices with F8T2 polymer and Au contacts suffer from poor fill factor and short circuit current density. Comparison with other polymer-interface combinations suggests that this is due to an energy mismatch at the interface, and that contacts which allow good hole-injection tend to lead to higher fill factors in this system. The introduction of PEDOT:PSS layer between polymer / metal contact improve both the J-V characteristics and the short circuit current density by over 50 %. Power conversion efficiency of this improved multilayer device is, 0.21 %, three times greater than the device without either the dip coated polymer layer or PEDOT:PSS layer.

7.1.2 The effect of polymer optoelectronics properties

We studied the effects of the optoelectronic properties of the polymer, and of PEDOT:PSS insertion under the top contact, on the performance of polymer-TiO_2 hybrid systems. A comparison of the exciton transport, charge transport and light harvesting properties of three different MEH-PPV based polymers and a fluorene-bithiophene polymer was made. The performance of the corresponding photovoltaic devices was also assessed. Our results established that the short circuit current density is limited primarily by the photogeneration rate, and by the quality of the interfaces, rather than by the hole-transport properties of the polymer. Through a study of the sensitisation process and device design we confirm that excellent polymer infiltration into the porous metal oxide could be achieved by dip coating, and that including a PEDOT:PSS layer beneath the top Au contact improves the short circuit photocurrent in all cases. We note that the qualitatively similar effect of PEDOT:PSS on the performance of devices using these polymers with different chemical structure shows that the mechanism responsible is quite general and is unlikely to result from an anomalous interaction between polymer and PEDOT:PSS. Instead, it seems that the roles of the PEDOT:PSS layer in improving hole injection and improving the quality of the interface are responsible.

7.1.3 The effect of microstructure of metal oxides

We reported the first efficient working polymer / metal oxide device using nanocrystalline SnO_2. The SnO_2/polymer device produced a promising short circuit current density J_{SC} of 0.48 mA cm^{-2} and open circuit voltage V_{OC} of 0.75 V under AM 1.5 conditions. The corresponding overall power conversion efficiency was 0.17 %.

We studied the performance of polymer / TiO_2 devices as a function of the thickness, microstructure and surface treatment of the porous TiO_2. We found that interfacial recombination can be reduced by treating the TiO_2 surface with a thin insulating Al_2O_3 layer. The alumina layer can increases device performance by more than 25 %. We have also found that the performance of TiO_2 / polymer devices is highly dependent on the pore diameter or particle size of TiO_2 relative to the exciton diffusion length of the polymer, on the active layer thickness and on the relative volumes of the porous TiO_2 and polymer. We observe strong effects on device performance both from introduction of a PEDOT:PSS layer and from the use of electron and hole blocking layers.

Finally we report high efficiency multilayer hybrid TiO_2 / polymer solar cells based on nanocrystalline TiO_2 and a TPD containing MEH-PPV polymer. The optimised device has peak external quantum efficiency ≈ 40 % at the polymer's maximum absorption wavelength and yields a short circuit current density ≥ 2 mA cm^{-2} for air mass (AM) 1.5 conditions (100 mW cm^{-2}, 1 sun). The AM 1.5 open circuit voltage reaches 0.64 V and the fill factor 0.43, resulting in an overall power conversion efficiency of 0.58 %. The best TiO_2 / P3HT multilayer device showed an overall power conversion efficiency of 0.2 % under AM 1.5 conditions.

7.1.4 Charge transport of TiO_2

We have found that the electron mobility measured by the time-of-flight technique for porous TiO_2 is in the range of 10^{-7} to 10^{-6} cm^2/Vs, and is dependent on the morphology of the film. Columnar TiO_2 films have higher electron mobility than porous films with random distribution of TiO_2 particles. This could be due to the fact that charge carriers in the columnar films, with the columns aligned nearly in the direction of the field may be able to gain kinetic energy from the applied field along the column axis which minimizes recombination and scattering, resulting in higher mobility. Solar cells made with columnar nanostructured TiO_2 with suitable dimension may therefore offer better device performance than randomly distributed TiO_2 particles.

7.2 Suggestions for Future Works

In this section, we present some suggestions for future work to optimise the performance of hybrid metal oxide / polymer photovoltaic devices.

7.2.1 Fabrication and Characterization of metal oxide : polymer blend device

Although our best multilayer devices show short circuit current density, J_{SC} over 2 $mAcm^{-2}$, this value is still low compared best polymer / fullerene solar cells. One of the reasons for the lower J_{SC} short circuit current density is lower interfacial area. It is interesting to study the solar cells made by spin casting a mixture of smaller size TiO_2 nanoparticles (< 10 nm) and the high mobility MEH-PPV polymer. In this blend device, a high work function electrode, (ITO/PEDOT:PSS) as to collect the holes, and a low work function electrode (LiF / Al) as a electron collector can be used. There are number factors such as solvent, quenching weight % of TiO_2, particle sizes which can be varied. Photoluminescence measurement of TiO_2: polymer blend as a function of wt or volume % of TiO_2 nanocrystals should be done to find the optimum volume or weight % of TiO_2 for efficient photovoltaic application. The advantage of this approach is the possibility of reducing the metal oxide volume fraction and hence increasing optical depth.

7.2.2 Charge transport in TiO_2 / polymer composite

We discussed the charge transport of porous TiO_2 films and polymer films separately. The nature of charge transport of the carriers in the TiO_2 / polymer composite may be different from pure films. Therefore, it would be interesting to study the charge transport properties of metal oxide / polymer composites and metal oxide / polymer blends with different weight % of metal oxides nanocrystals.

7.2.3 Metal oxide nanorods / polymer devices

From our time-of-flight measurement of porous TiO_2 in chapter 6, we found that columnar TiO_2 films have higher electron mobility than porous films with random distribution of TiO_2 particles. Solar cells made with columnar nanostructured TiO_2 with suitable dimension may therefore offer better device performance than randomly distributed TiO_2 particles. The future studies may therefore be focussed on devices having different metal oxide rods and polymer.

7.2.4 Studies of origin of open circuit voltage in TiO_2 / polymer devices

Although there are a few studies to address the origin of the open circuit voltage of polymer / fullerene solar cell, there is no such study of hybrid metal oxide device. It would be interesting to find a relationship between open circuit voltage, V_{OC} of hybrid TiO_2 / polymer device and the ionization potential of the polymer, the electron affinity and doping level of the metal oxide, and the work function of the top contact. A similar study can be made of the effect of polymer ionization potential on J-V characteristics of TiO_2 / polymer devices.

7.2.5 Control of interface

Our group more recently applied[160] self assembled monolayers (SAMs) of molecules with permanent dipole moment to control device performance of a polymer LED by modulating the Fermi level of the ITO electrode. Although Gratzel's group[78] has already applied SAMs with different dipole moments to modify interface of TiO_2 and spiro-MeOTAD to control the dark current, there is no report on effect of dipole on hybrid solar cell performance to date. It would be interesting to modify the surface of the metal oxide with SAMs and find the effect of SAM molecules on improvement polymer penetration in polymer / metal oxide structure, as well as on the open circuit voltage and J-V characteristics.

References

[1] International Energy Outlook 2004, (US Energy Information Administration, http://www.eia.doe.gov/oiaf/ieo/world.html).

[2] C. J. Campbell and J. H. Laherrere, "Preventing the next oil crunch - The end of cheap oil", Sci.Am. **278** (3), 77-83 (1998).

[3] Survey of Energy Resources, (World Energy Council, http://www.worldenergy.org/wec-geis/publications/reports/ser/solar/solar.asp).

[4] International Energy Agency, (http://www.iea.org/).

[5] M. D. Archer and R. Hill, *Clean electricity from photovoltaics*, First ed. (Imperial College Press, London, 2001), p.844.

[6] Photovoltaic Power Systems Programme, (International Energy Agency, http://www.iea-pvps.org/).

[7] M. A. Green, "Crystalline silicon photovoltaic cells", Adv. Mater. **13** (12-13), 1019-1022 (2001).

[8] M. Gratzel, "Photoelectrochemical cells", Nature **414** (6861), 338-344 (2001).

[9] J. Nelson, "Organic photovoltaic films", Curr. Opin. Solid State Mat. Sci. **6** (1), 87-95 (2002).

[10] C. J. Brabec, N. S. Sariciftci, and J. C. Hummelen, "Plastic solar cells", Adv. Funct. Mater. **11** (1), 15-26 (2001).

[11] J. J. M. Halls and R.H. Friend, in *Clean Electricity from Photovoltaics*, edited by M.D. Archer and R.D. Hill (Imperial College Press, London, 2001), pp. 377-445.

[12] P. Schilinsky, C. Waldauf, C.V. Ossietzky, and C. J. Brabec, "Printed plastic solar cells with power efficiencies of 5 %", Proc. SPIE Int. Soc. Opt. Eng. (2004).

[13] J. G. Xue, S. Uchida, B. P. Rand, and S. R. Forrest, "4.2 % efficient organic photovoltaic cells with low series resistances", Appl. Phys. Lett. **84** (16), 3013-3015 (2004); L. Schmidt-Mende (Private communication).

[14] W. U. Huynh, J. J. Dittmer, and A. P. Alivisatos, "Hybrid nanorod-polymer solar cells", Science **295** (5564), 2425-2427 (2002).

[15] N. C. Greenham, X. G. Peng, and A. P. Alivisatos, "Charge separation and transport in conjugated polymer cadmium selenide nanocrystal composites studied by photoluminescence quenching and photoconductivity", Synth. Met. **84** (1-3), 545-546 (1997).

[16] A. J. Breeze, Z. Schlesinger, S. A. Carter, and P. J. Brock, "Charge transport in TiO2/MEH-PPV polymer photovoltaics", Phys. Rev. B **6412** (12), 125205 (2001).

[17] M. Kaneko, K. Takayama, S. S. Pandey, W. Takashima, T. Endo, M. Rikukawa, and K. Kaneto, "Photovoltaic cell using high mobility poly(alkylthiophene)s and TiO_2", Synth. Met. **121** (1-3), 1537-1538 (2001).

[18] J. S. Salafsky, "Exciton dissociation, charge transport, and recombination in ultrathin, conjugated polymer-TiO_2 nanocrystal intermixed composites", Phys. Rev. B **59** (16), 10885-10894 (1999); L. H. Slooff, M. M. Wienk, and J. M. Kroon, "Hybrid TiO_2 : polymer photovoltaic cells made from a titanium oxide precursor", Thin Solid Films **451-52**, 634-638 (2004).

[19] T. J. Savenije, J. M. Warman, and A. Goossens, "Visible light sensitisation of titanium dioxide using a phenylene vinylene polymer", Chem. Phys. Lett. **287** (1-2), 148-153 (1998).

[20] P. A. van Hal, M. M. Wienk, J. M. Kroon, W. J. H. Verhees, L. H. Slooff, W. J. H. van Gennip, P. Jonkheijm, and R. A. J. Janssen, "Photoinduced electron transfer and photovoltaic response of a MDMO-PPV : TiO_2 bulk-heterojunction", Adv. Mater. **15** (2), 118-121 (2003).

[21] A. C. Arango, S. A. Carter, and P. J. Brock, "Charge transfer in photovoltaics consisting of interpenetrating networks of conjugated polymer and TiO_2 nanoparticles", Appl. Phys. Lett. **74** (12), 1698-1700 (1999).

[22] A. C. Arango, L. R. Johnson, V. N. Bliznyuk, Z. Schlesinger, S. A. Carter, and H. H. Horhold, "Efficient titanium oxide/conjugated polymer photovoltaics for solar energy conversion", Adv. Mater. **12** (22), 1689-1692 (2000).

[23] Q. Fan, B. McQuillin, D. D. C. Bradley, S. Whitelegg, and A. B. Seddon, "A solid state solar cell using sol-gel processed material and a polymer", Chem. Phys. Lett. **347** (4-6), 325-330 (2001).

[24] H. Ishii, K. Sugiyama, E. Ito, and K. Seki, "Energy level alignment and interfacial electronic structures at organic metal and organic organic interfaces", Adv. Mater. **11** (8), 605-625 (1999).

[25] J. H. Burroughes, D. D. C. Bradley, A. R. Brown, R. N. Marks, K. Mackay, R. H. Friend, P. L. Burns, and A. B. Holmes, "Light-Emitting-Diodes Based on Conjugated Polymers", Nature **347** (6293), 539-541 (1990).

[26] M. Theander, A. Yartsev, D. Zigmantas, V. Sundstrom, W. Mammo, M. R. Andersson, and O. Inganas, "Photoluminescence quenching at a polythiophene/C-60 heterojunction", Phys. Rev. B **61** (19), 12957-12963 (2000).

[27] G. Yu, J. Gao, J. C. Hummelen, F. Wudl, and A. J. Heeger, "Polymer Photovoltaic Cells - Enhanced Efficiencies Via a Network of Internal Donor-Acceptor

Heterojunctions", Science **270** (5243), 1789-1791 (1995); J. J. M. Halls, C. A. Walsh, N. C. Greenham, E. A. Marseglia, R. H. Friend, S. C. Moratti, and A. B. Holmes, "Efficient Photodiodes from Interpenetrating Polymer Networks", Nature **376** (6540), 498-500 (1995).

[28] G. Yu and A. J. Heeger, "Charge Separation and Photovoltaic Conversion in Polymer Composites with Internal Donor-Acceptor Heterojunctions", J. Appl. Phys. **78** (7), 4510-4515 (1995).

[29] C.W. Tang, "Two-layer organic photovoltaic cell", Appl. Phys. Lett. **48**, 183-185 (1986).

[30] J. J. M. Halls, K. Pichler, R. H. Friend, S. C. Moratti, and A. B. Holmes, "Exciton diffusion and dissociation in a poly(p- phenylenevinylene) / C-60 heterojunction photovoltaic cell", Appl. Phys. Lett. **68** (22), 3120-3122 (1996).

[31] S. A. Carter, M. Angelopoulos, S. Karg, P. J. Brock, and J. C. Scott, "Polymeric anodes for improved polymer light-emitting diode performance", Appl. Phys. Lett. **70** (16), 2067-2069 (1997).

[32] K. Petritsch, "Organic Solar cell Architectures", Ph.D. Thesis, University of Cambridge, 2000.

[33] H.B. Michaelson, "The workfunction of the elements and its periodicity", J. Appl. Phys. **48**, 4729-4733 (1977).

[34] A. Ioannidis, J. S. Facci, and M. A. Abkowitz, "Evolution in the charge injection efficiency of evaporated Au contacts on a molecularly doped polymer", J. Appl. Phys. **84** (3), 1439-1444 (1998).

[35] A. J. Campbell, D. D. C. Bradley, and H. Antoniadis, "Quantifying the efficiency of electrodes for positive carrier injection into poly(9,9-dioctylfluorene) and representative copolymers", J. Appl. Phys. **89** (6), 3343-3351 (2001).

[36] D. Poplavskyy, T. Kreouzis, A. J. Campbell, J. Nelson, and D.C.C. Bradley, "Injection and charge transport in polyfluorene polymers", Mater. Res. Soc. Symp. Proc. **725**, 61 (2002).

[37] D. Poplavskyy, "Hole injection and transport in organic semiconductor", Ph.D. Thesis, University of London, 2003.

[38] J. Nelson, "Solar energy - Solar cells by self-assembly?", Science **293** (5532), 1059-1060 (2001).

[39] J. Rostalski and D. Meissner, "Monochromatic versus solar efficiencies of organic solar cells", Sol. Energy Mater. Sol. Cells **61** (1), 87-95 (2000).

[40] K. Yoshino, K. Tada, A. Fujii, E. M. Conwell, and A. A. Zakhidov, "Novel photovoltaic devices based on donor-acceptor molecular and conducting polymer systems", IEEE Trans. Electron Devices **44** (8), 1315-1324 (1997).

[41] J. Nelson, *The Physics of Solar cells*. (Imperial College Press, 2003).

[42] M. K. Nazeeruddin, A. Kay, I. Rodicio, R. Humphrybaker, E. Muller, P. Liska, N. Vlachopoulos, and M. Gratzel, "Conversion of Light to Electricity by Cis-X2bis(2,2'-Bipyridyl- 4,4'-Dicarboxylate)Ruthenium(Ii) Charge-Transfer Sensitizers (X = Cl-, Br-, I-, Cn-, and Scn-) on Nanocrystalline TiO_2 Electrodes", J. Am. Chem. Soc. **115** (14), 6382-6390 (1993).

[43] K. Tennakone, Grra Kumara, I. R. M. Kottegoda, and V. P. S. Perera, "An efficient dye-sensitized photoelectrochemical solar cell made from oxides of tin and zinc", Chem. Commun. (1), 15-16 (1999).

[44] F. Cao, G. Oskam, and P. C. Searson, "A Solid-State, Dye-Sensitized Photoelectrochemical Cell", J. Phys. Chem. **99** (47), 17071-17073 (1995).

[45] U. Bach, D. Lupo, P. Comte, J. E. Moser, F. Weissortel, J. Salbeck, H. Spreitzer, and M. Gratzel, "Solid-state dye-sensitized mesoporous TiO_2 solar cells with high photon-to-electron conversion efficiencies", Nature **395** (6702), 583-585 (1998).

[46] J. Kruger, R. Plass, L. Cevey, M. Piccirelli, M. Gratzel, and U. Bach, "High efficiency solid-state photovoltaic device due to inhibition of interface charge recombination", Appl. Phys. Lett. **79** (13), 2085-2087 (2001).

[47] J. Kruger, R. Plass, M. Gratzel, and H. J. Matthieu, "Improvement of the photovoltaic performance of solid-state dye- sensitized device by silver complexation of the sensitizer cis- bis(4,4 '-dicarboxy-2,2 ' bipyridine)-bis(isothiocyanato) ruthenium(II)", Appl. Phys. Lett. **81** (2), 367-369 (2002).

[48] S. A. Haque, Y. Tachibana, R. L. Willis, J. E. Moser, M. Gratzel, D. R. Klug, and J. R. Durrant, "Parameters influencing charge recombination kinetics in dye-sensitized nanocrystalline titanium dioxide films", J. Phys. Chem. B **104** (3), 538-547 (2000).

[49] S. A. Haque, Y. Tachibana, D. R. Klug, and J. R. Durrant, "Charge recombination kinetics in dye-sensitized nanocrystalline titanium dioxide films under externally applied bias", J. Phys. Chem. B **102** (10), 1745-1749 (1998).

[50] S. A. Haque, T. Park, C. Xu, S. Koops, N. Schulte, R. J. Potter, A. B. Holmes, and J. R. Durrant, "Interface engineering for solid-state dye-sensitized nanocrystalline solar cells: The use of ion-solvating hole- transporting polymers", Adv. Funct. Mater. **14** (5), 435-440 (2004); S. A. Haque, T. Park, A. B. Holmes, and J. R.

Durrant, "Transient optical studies of interfacial energetic disorder at nanostructured dye-sensitised inorganic/organic semiconductor heterojunctions", ChemPhysChem **4** (1), 89-93 (2003).

[51] E. Palomares, J. N. Clifford, S. A. Haque, T. Lutz, and J. R. Durrant, "Slow charge recombination in dye-sensitised solar cells (DSSC) using Al_2O_3 coated nanoporous TiO_2 films", Chem. Commun. (14), 1464-1465 (2002).

[52] E. Palomares, J. N. Clifford, S. A. Haque, T. Lutz, and J. R. Durrant, "Control of charge recombination dynamics in dye sensitized solar cells by the use of conformally deposited metal oxide blocking layers", J. Am. Chem. Soc. **125** (2), 475-482 (2003).

[53] J. N. Clifford, E. Palomares, M. K. Nazeeruddin, M. Gratzel, J. Nelson, X. Li, N. J. Long, and J. R. Durrant, "Molecular control of recombination dynamics in dye-sensitized nanocrystalline TiO_2 films: Free energy vs distance dependence", J. Am. Chem. Soc. **126** (16), 5225-5233 (2004).

[54] J. Nelson, S. A. Haque, D. R. Klug, and J. R. Durrant, "Trap-limited recombination in dye-sensitized nanocrystalline metal oxide electrodes", Phys. Rev. B **6320** (20), 205321 (2001).

[55] J. Nelson, "Continuous-time random-walk model of electron transport in nanocrystalline TiO_2 electrodes", Phys. Rev. B **59** (23), 15374-15380 (1999).

[56] R. L. Willis, C. Olson, B. O'Regan, T. Lutz, J. Nelson, and J. R. Durrant, "Electron dynamics in nanocrystalline ZnO and TiO_2 films probed by potential step chronoamperometry and transient absorption spectroscopy", J. Phys. Chem. B **106** (31), 7605-7613 (2002).

[57] M. Thelakkat, C. Schmitz, and H. W. Schmidt, "Fully vapor-deposited thin-layer titanium dioxide solar cells", Adv. Mater. **14** (8), 577-581 (2002).

[58] P. Peumans, V. Bulovic, and S. R. Forrest, "Efficient photon harvesting at high optical intensities in ultrathin organic double-heterostructure photovoltaic diodes", Appl. Phys. Lett. **76** (19), 2650-2652 (2000).

[59] P. Peumans and S. R. Forrest, "Very-high-efficiency double-heterostructure copper phthalocyanine/C-60 photovoltaic cells", Appl. Phys. Lett. **79** (1), 126-128 (2001).

[60] T. M. Brown, J. S. Kim, R. H. Friend, F. Cacialli, R. Daik, and W. J. Feast, "Built-in field electroabsorption spectroscopy of polymer light- emitting diodes incorporating a doped poly(3,4-ethylene dioxythiophene) hole injection layer", Appl. Phys. Lett. **75** (12), 1679-1681 (1999).

[61] C. J. Brabec, S. E. Shaheen, C. Winder, N. S. Sariciftci, and P. Denk, "Effect of LiF/metal electrodes on the performance of plastic solar cells", Appl. Phys. Lett. **80** (7), 1288-1290 (2002).

[62] M. M. Wienk, J. M. Kroon, W. J. H. Verhees, J. Knol, J. C. Hummelen, P. A. van Hal, and R. A. J. Janssen, "Efficient methano 70 fullerene / MDMO-PPV bulk heterojunction photovoltaic cells", Angew. Chem.-Int. Edit. **42** (29), 3371-3375 (2003); F. Padinger, C. J. Brabec, T. Fromherz, J. C. Hummelen, and N. S. Sariciftci, "Fabrication of large area photovoltaic devices containing various blends of polymer and fullerene derivatives by using the doctor blade technique", Opto-Electron. Rev. **8** (4), 280-283 (2000); Y. Kim, S. A. Choulis, S. Cook, J. R. Durrant, J. Nelson, and D. D. C. Bradley, Appl. Phys. Lett. (submitted).

[63] M. Granstrom, K. Petritsch, A. C. Arias, A. Lux, M. R. Andersson, and R. H. Friend, "Laminated fabrication of polymeric photovoltaic diodes", Nature **395** (6699), 257-260 (1998).

[64] N. C. Greenham, X. G. Peng, and A. P. Alivisatos, "Charge separation and transport in conjugated- polymer / semiconductor-nanocrystal composites studied by photoluminescence quenching and photoconductivity", Phys. Rev. B **54** (24), 17628-17637 (1996).

[65] T. J. Savenije, M. J. W. Vermeulen, M. P. de Haas, and J. M. Warman, "Contactless determination of the efficiency of interfacial charge separation in a TiO_2 / phenylene vinylene polymer junction", Sol. Energy Mater. Sol. Cells **61** (1), 9-18 (2000).

[66] P. A. van Hal, M. P. T. Christiaans, M. M. Wienk, J. M. Kroon, and R. A. J. Janssen, "Photoinduced electron transfer from conjugated polymers to TiO_2", J. Phys. Chem. B **103** (21), 4352-4359 (1999).

[67] J. S. Salafsky, W. H. Lubberhuizen, and R. E. I. Schropp, "Photoinduced charge separation and recombination in a conjugated polymer-semiconductor nanocrystal composite", Chem. Phys. Lett. **290** (4-6), 297-303 (1998).

[68] J. S. Salafsky, H. Kerp, and R. E. I. Schropp, "Microwave photoconductivity, photovoltaic properties and architecture of a polymer-semiconductor nanocrystal composite", Synth. Met. **102** (1-3), 1256-1258 (1999).

[69] K. M. Coakley, Y. X. Liu, M. D. McGehee, K. L. Frindell, and G. D. Stucky, "Infiltrating semiconducting polymers into self-assembled mesoporous titania films for photovoltaic applications", Adv. Funct. Mater. **13** (4), 301-306 (2003).

[70] K. M. Coakley and M. D. McGehee, "Photovoltaic cells made from conjugated polymers infiltrated into mesoporous titania", Appl. Phys. Lett. **83** (16), 3380-3382 (2003).

[71] D. Gebeyehu, C. J. Brabec, N. S. Sariciftci, D. Vangeneugden, R. Kiebooms, D. Vanderzande, F. Kienberger, and H. Schindler, "Hybrid solar cells based on dye-sensitized nanoporous TiO_2 electrodes and conjugated polymers as hole transport materials", Synth. Met. **125** (3), 279-287 (2001); P. A. van Hal, M. M. Wienk, J. M. Kroon, and R. A. J. Janssen, "TiO_2 sensitized with an oligo(p-phenylenevinylene) carboxylic acid: a new model compound for a hybrid solar cell", J. Mater. Chem. **13** (5), 1054-1057 (2003).

[72] C. L. Huisman, A. Goossens, and J. Schoonman, "Aerosol synthesis of anatase titanium dioxide nanoparticles for hybrid solar cells", Chem. Mat. **15** (24), 4617-4624 (2003).

[73] A. Watanabe and A. Kasuya, "Effect of atmosphere on the open circuit photovoltage of nanoporous TiO_2 / poly(3-hexylthiophene) heterojunction solar cell", Thin Solid Films (accepted).

[74] J. Nelson, M. Eppler, D. Poplavskyy, P. Ravirajan, D.C.C. Bradley, J.R. Durrant, and S. A. Haque, "Conjugated fluorene copolymers as hole transport materials in polymer-metal oxide photovoltaic devices", Proc. 201st Meeting of The Electrochemical Society, (2002).

[75] A. F. Nogueira, I. Montanari, J. Nelson, J. R. Durrant, C. Winder, and N. S. Sariciftci, "Charge recombination in conjugated polymer / fullerene blended films studied by transient absorption Spectroscopy", J. Phys. Chem. B **107** (7), 1567-1573 (2003); A. F. Nogueira, M. A. De Paoli, I. Montanari, R. Monkhouse, J. Nelson, and J. R. Durrant, "Electron transfer dynamics in dye sensitized nanocrystalline solar cells using a polymer electrolyte", J. Phys. Chem. B **105** (31), 7517-7524 (2001).

[76] I. Montanari, A. F. Nogueira, J. Nelson, J. R. Durrant, C. Winder, M. A. Loi, N. S. Sariciftci, and C. Brabec, "Transient optical studies of charge recombination dynamics in a polymer / fullerene composite at room temperature", Appl. Phys. Lett. **81** (16), 3001-3003 (2002).

[77] N. A. Anderson, E. C. Hao, X. Ai, G. Hastings, and T. Q. Lian, "Ultrafast and long-lived photoinduced charge separation in MEH-PPV / nanoporous semiconductor thin film composites", Chem. Phys. Lett. **347** (4-6), 304-310 (2001).

[78] J. Kruger, U. Bach, and M. Gratzel, "Modification of TiO_2 heterojunctions with benzoic acid derivatives in hybrid molecular solid-state devices", Adv. Mater. **12** (6), 447-451 (2000).

[79] M. Abkowitz, J. S. Facci, and J. Rehm, "Direct evaluation of contact injection efficiency into small molecule based transport layers: Influence of extrinsic factors", J. Appl. Phys. **83** (5), 2670-2676 (1998).

[80] I. H. Campbell, D. L. Smith, C. J. Neef, and J. P. Ferraris, "Charge transport in polymer light-emitting diodes at high current density", Appl. Phys. Lett. **75** (6), 841-843 (1999).

[81] S. Tuladhar (personal communication).

[82] E. Lebedev, T. Dittrich, V. PetrovaKoch, S. Karg, and W. Brutting, "Charge carrier mobility in poly(p-phenylenevinylene) studied by the time-of-flight technique", Appl. Phys. Lett. **71** (18), 2686-2688 (1997).

[83] D. Poplavskyy and J. Nelson, "Nondispersive hole transport in amorphous films of methoxy- spirofluorene-arylamine organic compound", J. Appl. Phys. **93** (1), 341-346 (2003).

[84] M. Redecker, D. D. C. Bradley, M. Inbasekaran, W. W. Wu, and E. P. Woo, "High mobility hole transport fluorene-triarylamine copolymers", Adv. Mater. **11** (3), 241-246 (1999).

[85] W. Takashima, S. S. Pandey, T. Endo, M. Rikukawa, N. Tanigaki, Y. Yoshida, K. Yase, and K. Kaneto, "Photocarrier transports related to the morphology of regioregular poly(3-hexylthiophene) films", Thin Solid Films **393** (1-2), 334-342 (2001).

[86] S. A. Choulis, Y. Kim, J. Nelson, D. D. C. Bradley, M. Giles, M. Shkunov, and I. McCulloch, Applied Physics Letters (to be published).

[87] S. S. Pandey, W. Takashima, T. Endo, M. Rikukawa, and K. Kaneto, "Poly(3-butylthiophene): conjugated polymer with record high TOF mobility", Synth. Met. **121** (1-3), 1561-1562 (2001).

[88] D. Hertel, H. Bassler, U. Scherf, and H. H. Horhold, "Charge carrier transport in conjugated polymers", J. Chem. Phys. **110** (18), 9214-9222 (1999).

[89] D. Gebeyehu, C. J. Brabec, F. Padinger, T. Fromherz, S. Spiekermann, N. Vlachopoulos, F. Kienberger, H. Schindler, and N. S. Sariciftci, "Solid state dye-sensitized TiO_2 solar cells with poly(3- octylthiophene) as hole transport layer", Synth. Met. **121** (1-3), 1549-1550 (2001).

[90] J. E. Kroeze, T. J. Savenije, M. J. W. Vermeulen, and J. M. Warman, "Contactless determination of the photoconductivity action spectrum, exciton diffusion length, and charge separation efficiency in polythiophene-sensitized TiO_2 bilayers", J. Phys. Chem. B **107** (31), 7696-7705 (2003).

[91] J. E. Kroeze (personal communication).

[92] S. Luzzati, M. Basso, M. Catellani, C. J. Brabec, D. Gebeyehu, and N. S. Sariciftci, "Photo-induced electron transfer from a dithieno thiophene-based polymer to TiO_2", Thin Solid Films **403**, 52-56 (2002).

[93] N. A. Anderson, E. C. Hao, X. Ai, G. Hastings, and T. Q. Lian, "Subpicosecond photoinduced electron transfer from a conjugated polymer to SnO_2 semiconductor nanocrystals", Physica E **14** (1-2), 215-218 (2002).

[94] J. E. Kroeze and T. J. Savenije, "The application of a low-bandgap conjugated oligomer for the sensitization of SnO_2 and TiO_2", Thin Solid Films **451-52**, 54-59 (2004).

[95] W. J. E. Beek, M. M. Wienk, and R. A. J. Janssen, "Efficient hybrid solar cells from zinc oxide nanoparticles and a conjugated polymer", Adv. Mater. **16** (12), 1009-1013 (2004).

[96] S. Alem, R. de Bettignies, J. M. Nunzi, and M. Cariou, "Efficient polymer-based interpenetrated network photovoltaic cells", Appl. Phys. Lett. **84** (12), 2178-2180 (2004).

[97] F. Padinger, R. S. Rittberger, and N. S. Sariciftci, "Effects of postproduction treatment on plastic solar cells", Adv. Funct. Mater. **13** (1), 85-88 (2003).

[98] H. Sirringhaus, R. J. Wilson, R. H. Friend, M. Inbasekaran, W. Wu, E. P. Woo, M. Grell, and D. D. C. Bradley, "Mobility enhancement in conjugated polymer field-effect transistors through chain alignment in a liquid-crystalline phase", Appl. Phys. Lett. **77** (3), 406-408 (2000).

[99] H. Sirringhaus, N. Tessler, and R. H. Friend, "Integrated optoelectronic devices based on conjugated polymers", Science **280** (5370), 1741-1744 (1998).

[100] P. Coppo, M. Turner, D. C. Cupertino, and S.G. Yeast, "Investigation of the electronic properties of cyclopentadithiophene polymers and copolymers", Proc. Mat.Res.Soc.Symp. **771**, L4.9.1-L4.9.4 (2003).

[101] M. Inbasekaran (private communication).

[102] H. Sirringhaus, P. J. Brown, R. H. Friend, M. M. Nielsen, K. Bechgaard, B. M. W. Langeveld-Voss, A. J. H. Spiering, R. A. J. Janssen, E. W. Meijer, P. Herwig, and

D. M. de Leeuw, "Two-dimensional charge transport in self-organized, high-mobility conjugated polymers", Nature **401** (6754), 685-688 (1999).

[103] H. H. Horhold, H. Tillmann, C. Bader, R. Stockmann, J. Nowotny, E. Klemm, W. Holzer, and A. Penzkofer, "MEH-PPV and dialkoxy phenylene vinylene copolymers. Synthesis and lasing characterization", Synth. Met. **119** (1-3), 199-200 (2001).

[104] S. Pfeiffer and H. H. Horhold, "Synthesis of soluble MEH-PPV and MEH-PPB by HORNER condensation polymerization", Synth. Met. **101** (1-3), 109-110 (1999).

[105] W. Holzer, A. Penzkofer, H. Tillmann, D. Raabe, and H. H. Horhold, "Photo-physical characterisation and travelling-wave lasing of some TPD-based polymer neat films", Opt. Mater. **19** (2), 283-294 (2002).

[106] M. Spath, P. M. Sommeling, J. A. M. van Roosmalen, H. J. P. Smit, N. P. G. van der Burg, D. R. Mahieu, N. J. Bakker, and J. M. Kroon, "Reproducible manufacturing of dye-sensitized solar cells on a semi-automated baseline", Prog. Photovoltaics **11** (3), 207-220 (2003).

[107] K. Westermark, H. Rensmo, H. Siegbahn, K. Keis, A. Hagfeldt, L. Ojamae, and P. Persson, "PES studies of Ru(dcbpyH(2))(2)(NCS)(2) adsorption on nanostructured ZnO for solar cell applications", J. Phys. Chem. B **106** (39), 10102-10107 (2002).

[108] L. Kavan, B. O'Regan, A. Kay, and M. Gratzel, "Preparation of TiO_2 (anatase) films on electrodes by anodic oxidative hydrolysis of $TiCl_3$", J. Electroanal. Chem. **346** (1-2), 291-307 (1993).

[109] P. Ravirajan, S. A. Haque, J. R. Durrant, D. Poplavskyy, D. D. C. Bradley, and J. Nelson, "Hybrid nanocrystalline TiO_2 solar cells with a fluorene- thiophene copolymer as a sensitizer and hole conductor", J. Appl. Phys. **95** (3), 1473-1480 (2004).

[110] P. Ravirajan, S. A. Haque, D. Poplavskyy, J. R. Durrant, D. D. C. Bradley, and J. Nelson, "Solid state solar cell made from nanocrystalline TiO_2 with a fluorene-thiophene copolymer as a hole conductor", Proc. SPIE Int. Soc. Opt. Eng. **5215**, 226-236 (2004).

[111] L. Kavan and M. Gratzel, "Highly Efficient Semiconducting TiO_2 Photoelectrodes Prepared by Aerosol Pyrolysis", Electrochim. Acta **40** (5), 643-652 (1995).

[112] J. Huang, P. F. Miller, J. C. de Mello, A. J. de Mello, and D. D. C. Bradley, "Influence of thermal treatment on the conductivity and morphology of PEDOT/PSS films", Synth. Met. **139** (3), 569-572 (2003).

[113] P. Scott, (Oregon Medical Laser Center, US http://omlc.ogi.edu/spectra/icg/).

[114] J. R. Durrant, "Transient Absorption Spectroscopy of Photosystem II", Ph.D. Thesis, University of London, 1992.

[115] S. A. Haque, "Charge Recombination Kinetics in Dye-Sensitized Nanocrystalline Titanium Dioxide solar cells", Ph.D. Thesis, University of London, 2000.

[116] J. N. Clifford, "Control of electron transfer dynamics in dye sensitized solar cells", Ph.D. Thesis, University of London, 2003.

[117] W. E. Spear, "Drift mobility techniques for the study of electrical transport properties in insulating solids", Journal of Non-Crystalline Solids **1**, 197 (1969).

[118] A. J. Campbell, D. D. C. Bradley, H. Antoniadis, M. Inbasekaran, W. S. W. Wu, and E. P. Woo, "Transient and steady-state space-charge-limited currents in polyfluorene copolymer diode structures with ohmic hole injecting contacts", Appl. Phys. Lett. **76** (13), 1734-1736 (2000).

[119] H. Bassler, "Charge transport in disordered organic photoconductors", Phys. Stat. Sol. (b) **175**, 15 (1993).

[120] H. Scher and E. W. Montroll, "Anomalous transit- time dispersion in amorphous solids", Phys. Rev. B **12**, 2455 (1975).

[121] I. D. Baikie, Robert Gordon University, (http://www2.rgu.ac.uk/subj/skpg/kpintro.htm).

[122] J. S. Kim, B. Lagel, E. Moons, N. Johansson, I. D. Baikie, W. R. Salaneck, R. H. Friend, and F. Cacialli, "Kelvin probe and ultraviolet photoemission measurements of indium tin oxide work function: a comparison", Synth. Met. **111**, 311-314 (2000).

[123] W. N. Hansen and K. B. Johnson, "Work function measurements in gas ambient", Surface Science **316** (3), 373-382 (1994).

[124] W. N. Hansen and G. J. Hansen, "Standard reference surfaces for work function measurements in air", Surface Science **481** (1-3), 172-184 (2001).

[125] M. G. Harrison, J. Gruner, and G. C. W. Spencer, "Analysis of the photocurrent action spectra of MEH-PPV polymer photodiodes", Phys. Rev. B **55** (12), 7831-7849 (1997).

[126] X. Crispin, S. Marciniak, W. Osikowicz, G. Zotti, A. W. D. Van der Gon, F. Louwet, M. Fahlman, L. Groenendaal, F. De Schryver, and W. R. Salaneck, "Conductivity, morphology, interfacial chemistry, and stability of poly(3,4-ethylene dioxythiophene)-poly(styrene sulfonate): A photoelectron spectroscopy study", J. Polym. Sci. Pt. B-Polym. Phys. **41** (21), 2561-2583 (2003).

[127] G. G. Malliaras, J. R. Salem, P. J. Brock, and C. Scott, "Electrical characteristics and efficiency of single-layer organic light-emitting diodes", Phys. Rev. B **58** (20), R13411-R13414 (1998).

[128] G. Rothenberger, D. Fitzmaurice, and M. Gratzel, " Spectroscopy of Conduction-Band Electrons in Transparent Metal-Oxide Semiconductor-Films - Optical Determination of the Flat-Band Potential of Colloidal Titanium-Dioxide Films", J. Phys. Chem. **96** (14), 5983-5986 (1992).

[129] B. O. Aduda, P. Ravirajan, K. L. Choy, and J. Nelson, "Effect of morphology on electron drift mobility in porous TiO_2", International Journal of Photoenergy **6** (3), 141-147 (2004).

[130] J. Kruger, R. Plass, M. Gratzel, P. J. Cameron, and L. M. Peter, "Charge transport and back reaction in solid-state dye- sensitized solar cells: A study using intensity-modulated photovoltage and photocurrent spectroscopy", J. Phys. Chem. B **107** (31), 7536-7539 (2003).

[131] A. F. Nogueira, I. Montanari, J. Nelson, C. Winder, N. S. Sariciftci, C. Brabec, and J. R. Durrant, "Charge recombination dynamics in a polymer / fullerene bulk heterojunction studied by transient absorption spectroscopy", Synth. Met. **137** (1-3), 1505-1506 (2003).

[132] K. Petritsch and R. H. Friend, "Ultrathin organic photovoltaic devices", Synth. Met. **102** (1-3), 976-976 (1999).

[133] A. Eppler, "Charge transport of nanocrystalline titanium oxide and its use in solar cells", Ph.D. Thesis, University of London, 2004.

[134] J. Nelson, J. Kirkpatrick, and P. Ravirajan, "Factors limiting the efficiency of molecular photovoltaic devices", Phys. Rev. B **69** (3), 035337 (2004).

[135] M. Grell, M. Redecker, K. S. Whitehead, D. D. C. Bradley, M. Inbasekaran, E. P. Woo, and W. Wu, "Monodomain alignment of thermotropic fluorene copolymers", Liq. Cryst. **26** (9), 1403-1407 (1999).

[136] R. Rawcliffe (Private communication).

[137] T. Park, "Organic hole transport materials for dye-sensitised photo cells", Ph.D. Thesis, University of Cambridge, 2002.

[138] S. A. Choulis, J. Nelson, Y. Kim, D. Poplavskyy, T. Kreouzis, J. R. Durrant, and D. D. C. Bradley, "Investigation of transport properties in polymer / fullerene blends using time-of-flight photocurrent measurements", Appl. Phys. Lett. **83** (18), 3812-3814 (2003).

[139] C. J. Brabec, A. Cravino, D. Meissner, N. S. Sariciftci, T. Fromherz, M. T. Rispens, L. Sanchez, and J. C. Hummelen, "Origin of the open circuit voltage of plastic solar cells", Adv. Funct. Mater. **11** (5), 374-380 (2001); V. D. Mihailetchi, P. W. M. Blom, J. C. Hummelen, and M. T. Rispens, "Cathode dependence of the open-circuit voltage of polymer : fullerene bulk heterojunction solar cells", J. Appl. Phys. **94** (10), 6849-6854 (2003).

[140] A. Kay and M. Gratzel, "Dye-sensitized core-shell nanocrystals: Improved efficiency of mesoporous tin oxide electrodes coated with a thin layer of an insulating oxide", Chem. Mat. **14** (7), 2930-2935 (2002).

[141] G. R. R. A. Kumara, K. Tennakone, V. P. S. Perera, A. Konno, S. Kaneko, and M. Okuya, "Suppression of recombinations in a dye-sensitized photoelectrochemical cell made from a film of tin IV oxide crystallites coated with a thin layer of aluminium oxide", J. Phys. D-Appl. Phys. **34** (6), 868-873 (2001).

[142] S. Hore, E. Palomares, H. J. P. Smit, N. J. Bakker, P. Comte, P. Liska, R. Thampi, J. M. Kroon, A. Hinsch, and J. R. Durrant, J. Mater.Chem. (accepted).

[143] M. D. McGehee, K. M. Coakley, Y. Liu, and C. Goh, "Optimising the nanostructure inorganic - organic hybrid photovoltaic cells", Proc. SPIE Int. Soc. Opt. Eng. (2004).

[144] J. Liu, E. N. Kadnikova, Y. Liu, M. D. McGehee, and J. M. J. Frechet, "Polythiophene Containing Thermally Removable Solubilizing Groups Enhances the Interface and the Performance of Polymer-Titania Hybrid Solar Cells", Journal of the American Chemical Society Communication) **126** (31), 9486-9487 (2004).

[145] M. Mohr (private communication).

[146] C. J. Barbe, F. Arendse, P. Comte, M. Jirousek, F. Lenzmann, V. Shklover, and M. Gratzel, "Nanocrystalline titanium oxide electrodes for photovoltaic applications", J. Am. Ceram. Soc. **80** (12), 3157-3171 (1997).

[147] R. Konenkamp, *Photoelectrical properties and Applications of low mobility semiconductor*. (Spinger publishing group, New york).

[148] A. Eppler, I. N. Ballard, and J. Nelson, "Charge transport in porous nanocrystalline titanium dioxide", Physica E **14** (1-2), 197-202 (2002).

[149] J. Nelson, A. M. Eppler, and I. M. Ballard, "Photoconductivity and charge trapping in porous nanocrystalline titanium dioxide", J. Photochem. Photobiol. A-Chem. **148** (1-3), 25-31 (2002).

[150] J. D. Vyas and K. L. Choy, "Structural characterisation of thermal barrier coatings deposited using electrostatic spray assisted vapour deposition method", Materials

Science and Engineering a-Structural Materials Properties Microstructure and Processing **277** (1-2), 206-212 (2000).

[151] J. Szczyrbowski, G. Brauer, M. Ruske, J. Bartella, J. Schroeder, and A. Zmelty, "Some properties of TiO_2 layers prepared by medium frequency reactive sputtering", Surf. Coat. Technol. **112** (1-3), 261-266 (1999).

[152] T. Dittrich, J. Weidmann, V. Y. Timoshenko, A. A. Petrov, F. Koch, M. G. Lisachenko, and E. Lebedev, "Thermal activation of the electronic transport in porous titanium dioxides", Mater. Sci. Eng. B-Solid State Mater. Adv. Technol. **69**, 489-493 (2000).

[153] T. Dittrich, E. A. Lebedev, and J. Weidmann, "Electron drift mobility in porous TiO_2 (anatase)", Phys. Status Solidi A-Appl. Res. **165** (2), R5-R6 (1998).

[154] R. Konenkamp and I. Rieck, "Electrical properties of Schottky diodes on nano-porous TiO_2 films", Mater. Sci. Eng. B-Solid State Mater. Adv. Technol. **69**, 519-521 (2000).

[155] L. Forro, O. Chauvet, D. Emin, L. Zuppiroli, H. Berger, and F. Levy, "High-Mobility N-Type Charge-Carriers in Large Single-Crystals of Anatase (TiO_2)", J. Appl. Phys. **75** (1), 633-635 (1994).

[156] W. Takashima, S. S. Pandey, T. Endo, M. Rikukawa, and K. Kaneto, "Effects of regioregularity on carrier transport in poly(alkylthiophene) films with various alkyl chain lengths", Current Applied Physics **1** (1), 90-97 (2001).

[157] A. J. Mozer and N. S. Sariciftci, "Negative electric field dependence of charge carrier drift mobility in conjugated, semiconducting polymers", Chem. Phys. Lett. **389** (4-6), 438-442 (2004).

[158] G. Juska, K. Genevicius, K. Arlauskas, R. Osterbacka, and H. Stubb, "Charge transport at low electric fields in pi-conjugated polymers", Phys. Rev. B **65** (23), 0233208 (2002).

[159] K. Takeuchi, I. Nakamura, O. Matsumoto, S. Sugihara, M. Ando, and T. Ihara, "Preparation of visible-light-responsive titanium oxide photocatalysts by plasma treatment", Chem. Lett. (12), 1354-1355 (2000).

[160] S. Khodabakhsh, D. Poplavskyy, S. Heutz, J. Nelson, D. D. C. Bradley, H. Murata, and S.T Jones, Adv. Funct. Mater. (submitted).

Appendix - List of Publications and conference abstracts

List of journal papers:

[1] Hybrid nanocrystalline TiO_2 solar cells with a fluorene--thiophene copolymer as a sensitizer and hole conductor, **P. Ravirajan**, S. A. Haque, J. R. Durrant, D. Poplavskyy, D. D. C. Bradley, and J. Nelson, *Journal of Applied Physics* **95** (2004) 1473 - 1480.

[2] Nanoporous TiO_2 solar cells sensitized with a fluorene-thiophene copolymer, **P. Ravirajan**, S. A. Haque, D. Poplavskyy, J. R. Durrant, D. D. C. Bradley, and J. Nelson, *Thin Solid Film* **451-452** (2004) 624 - 629.

[3] Factors limiting the efficiency of molecular photovoltaic devices, J. Nelson, J. Kirkpatrick, and **P. Ravirajan**, *Physical Review B* **69** (2004) 035337.

[4] Effect of morphology on electron drift mobility in porous TiO_2, B. O. Aduda, **P. Ravirajan**, K. L. Choy, and J. Nelson, *International Journal of Photoenergy* **6** (2004) 141-147.

[5] The effect of polymer optoelectronic properties on the performance of multilayer hybrid polymer/TiO_2 solar cell, **P. Ravirajan**, S. A. Haque, J. R. Durrant, D. D. C. Bradley and J. Nelson, *Advanced Functional Materials* (accepted).

[6] Efficient Charge Collection in Hybrid Polymer / TiO_2 Solar Cell using PEDOT:PSS as a Hole Collector, **P. Ravirajan**, S. A. Haque, J. R. Durrant, S. J. P. Smith, J. M. Kroon, D. D. C. Bradley and J. Nelson, *Applied Physics Letter* (submitted).

List of conference papers (refereed):

[1] Solid state solar cell made from nanocrystalline TiO_2 with a fluorene-thiophene copolymer as a hole-conductor, **P. Ravirajan**, S. A. Haque, D. Poplavskyy, J. R. Durrant, D. D. C. Bradley, and J. Nelson, *Proc. SPIE Int. Soc. Opt. Eng.* **5215**, (2004) 226 - 236.

[2] Photovoltaic devices based on nanocrystalline TiO_2 and a fluorene-thiophene copolymer, **P. Ravirajan**, S. A. Haque, D. Poplavskyy, J. R. Durrant, D. D. C. Bradley, and J. Nelson, *Proc. 3rd World Conference on Photovoltaic Energy Conversion (WCPEC3)* (2003) S1P-A7-11.

[3] Efficient hybrid polymer / TiO_2 solar cells using a multilayer structure, **P. Ravirajan**, S. A. Haque, J. R. Durrant, D. D.C.Bradley, and J. Nelson, *Proc. SPIE Int. Soc. Opt. Eng.* (in press)

List of conference abstracts:

[1] Characterisation of solar cells made from nanocrystalline TiO_2 and a fluorene-thiophene copolymer, **P. Ravirajan**, Saif A.Haque, Dmitry Poplavskyy, James R. Durrant, Donal D.C.Bradley and Jenny Nelson, *The 2002 Annual Conference of the British Association for Crystal Growth,* The University of Liverpool, 8 - 10 September 2002.

[2] Characterisation of thin film nanocrystalline TiO_2 solar cells with fluorene-thiophene copolymer as a hole conductor, **P. Ravirajan**, Saif A.Haque, Dmitry Poplavskyy, James R. Durrant, Donal D.C.Bradley, and Jenny Nelson, *Bi-annual conference of the Solar Energy Society,* Loughborough University, April 3-4, 2003.

[3] Photovoltaic Device based on nanocrystalline TiO_2 and a fluorene-thiophene copolymer, **P. Ravirajan**, S. A. Haque, D. Poplavskyy, J. R. Durrant, D. D.C.Bradley, and J. Nelson, *Discussion Meeting on Functional Mechanisms in Organic and Dye sensitised Solar cells*, Imperial College London, London, July 9-10, 2003.

[4] Polymer-fullerne blend and polymer-TiO_2 hybrid solar cells, **P.Ravirajan,** S. A. Choulis, S. A. Haque, J. Nelson, J. R. Durrant and D. D. C.Bradley, *Science Bazaar on Organic and Dye Sensitized solar cells*, Linz, Austria, September 18-19, 2003.

[5] Multi-layer solar cells based on nanoporous TiO_2 and a fluorene-thiophene copolymer,**P. Ravirajan**, S. A. Haque, J. R. Durrant, D. D.C.Bradley, and J. Nelson, *MRS Fall Meeting,* Boston, USA, December 1-5, 2003.

[6] Efficient hybrid polymer / TiO_2 solar cell using PEDOT:PSS as hole collector, **P. Ravirajan**, S. A. Haque, J. R. Durrant, D. D.C.Bradley, and J. Nelson, *SCELL 2004*, Badajoz, Spain, May 13-15th, 2004.

[7] Improvement of charge collection in hybrid polymer / TiO_2 solar cell using PEDOT:PSS as hole collector, **P. Ravirajan**, S. A. Haque, J. R. Durrant, D. D.C.Bradley, and J. Nelson, *15th International Conference on Photochemical Conversion and Storage of Solar Energy* (IPS-15), Paris, France, July 4-9, 2004.

[8] Metal oxide / polymer nanocomposite films for light-driven deoxygenation and solar cells, A. M. Peiró, C. Colombo, **P. Ravirajan**, L. Xiao, G. Doyle , A. Mills, J. Nelson, J. R. Durrant, *15th International Conference on Photochemical Conversion and Storage of Solar Energy (IPS-15),* Paris, France, July 4-9, 2004.

BIBL. LONDIN.